Development of Local Hybrid Functionals for Time-Dependent Density Functional Theory

vorgelegt von
Diplom-Chemiker
Toni Mike Maier
geb. in Berlin

Von der Fakultät II - Mathematik und Naturwissenschaften
der Technischen Universität Berlin
zur Erlangung des akademischen Grades

Doktor der Naturwissenschaften
– Dr. rer. nat. –

genehmigte Dissertation

Promotionsausschuss:

Vorsitzender:	Prof. Dr. Arne Thomas
Gutachter:	Prof. Dr. Martin Kaupp
Gutachter:	JProf. Dr. Thomas Körzdörfer

Tag der wissenschaftlichen Aussprache: 07. November 2016

Berlin 2016

Danksagung

Diesen Abschnitt meiner Arbeit möchte ich dazu nutzen, mich bei einigen Menschen zu bedanken, die mich während der letzten, knapp 4 Jahre bei dem Vorhaben „Doktorarbeit“ entweder direkt oder auch indirekt unterstützt haben und damit nicht unerheblich zur Fertigstellung der vorliegenden Arbeit beigetragen haben.

Allen voran gilt mein Dank meinem Betreuer *Prof. Dr. Martin Kaupp*, besonders für das entgegengebrachte Vertrauen während meiner Arbeit an diesem höchstinteressanten Projekt, welches mir Einblicke in viele verschiedene Bereiche der aktuellen Forschung gewährte. Vor allem für die Möglichkeit, dass ich meine Arbeit an dem Projekt frei nach eigenen Interessen gestalten sowie eigenen Ideen nachgehen und diese auch umsetzen konnte, bin ich besonders dankbar. Nicht zu vergessen sind auch die unzähligen, wissenschaftlichen Diskussionen, die zum Teil auch weiter über mein eigentliches Thema hinaus gingen und mir somit eine breitere Sichtweise auf das gesamte Feld der Quantenchemie ermöglichten.

JProf. Dr. Thomas Körzdörfer danke ich dafür, dass er sich als Zweitgutachter für die Begutachtung meiner Arbeit zur Verfügung gestellt hat.

Weiterhin danke ich *Dr. Hilke Bahmann* für die Unterstützung rund um die Implementierung von lokalen Hybriden in TURBOMOLE sowie für viele wertvolle Diskussionen. Bei *Dr. Alexey Arbuznikov* bedanke ich mich ebenfalls für die vielen fruchtbaren Diskussionen, vor allem über Dichtefunktionaltheorie und lokale Hybridfunktionale im Speziellen.

Bei unseren Nachwuchsquantenchemikern *Matthias Haasler*, *Robin Grotjahn* und *Casper Schattenberg* bedanke ich mich für die gute Zusammenarbeit bei ihren Projekten rund um das Thema lokale Hybridfunktionale, sei es im Rahmen von Bachelor- und Masterarbeiten oder Forschungspraktika. Ich hoffe, dass ihr dabei genauso viel Spaß habt beziehungsweise hattet und mindestens genauso viel gelernt habt wie ich auch.

Für die Unterstützung beim Erledigen lästiger bürokratischer Aufgaben beziehungsweise für die Hilfe in technischen Angelegenheiten möchte ich mich bei *Nadine Rechenberg* und *Heidi Grauel* bedanken. Dem Land Berlin danke ich für die finanzielle Unterstützung durch das Elsa-Neumann Stipendium.

Ich danke auch allen anderen aktuellen und ehemaligen Mitgliedern des Arbeitskreises, die für die stets entspannte und spaßige Betriebsathmosphäre gesorgt haben, sowohl während aber auch nach der eigentlichen Arbeit. Meinen ehemaligen Bürokollegen *Dr. Manuel Renz* und *Dr. Matthias Parthey* sowie der aktuellen Besetzung von C073g, *Sascha Klawohn* und *Anja Greif*, sei dafür Dank ausgesprochen, dass sie jeden noch so flachen Kommentar meinerseits stets mit Fassung ertragen und mir am nächsten Tag trotzdem immer wieder zugehört haben. Manuel, sowohl die zwei zusätzlichen Bildschirme als auch der gut sortierte Rollcontainer, den du hinterlassen hast, haben sich als sehr praktisch erwiesen, danke also auch dafür. Nicht zu vergessen sind auch die Vielzahl an Spieleabenden an Mittwoch- und/oder Donnerstagabenden, an denen von kurzen Zweistundenbrettspielen bis zu Neuerscheinungen alles vertreten war. Für viele interessante Partien möchte ich mich hier bei *Sascha Klawohn*, *Kolja Theilacker*, *Martin Enke*, *Sebastian Gohr*, *Casper Schattenberg*, *Dr. Rober Mueller* und *Dr. Johannes Schraut* bedanken.

Abschließend möchte ich meinen beiden Eltern, *Olaf Maier* und *Christiane Maier*, einen herzlichen Dank aussprechen. Dank eurer unermüdlichen Versorgung mit Kaffee und warmen Mahlzeiten, natürlich weit jenseits des Mensastandards, sind viele Wochenenden nicht zu reiner Arbeitszeit verkommen. Ein offenes Ohr für Probleme zu haben, die erst einmal mehrstündige Erklärungen bedürfen, ist auch nicht selbstverständlich. Dafür und für eure permanente Unterstützung gebührt euch mein größter Dank.

„Nur wer erwachsen wird und Kind bleibt, ist ein Mensch.“

Erich Kästner

Abstract

The present work is concerned with the advancement of the relatively recent class of local hybrid functionals. The first part of the work addresses the conjunction of local hybrid functionals with linear-response time-dependent density functional theory (TDDFT), which is the most widely used quantum chemical method for excited-state calculations. Besides a detailed derivation of the required formulas, the implementation into the quantum chemical program TURBOMOLE is presented, which, due to the use of an efficient semi-numerical integration scheme, exhibits even a higher efficiency than the previous global hybrid TDDFT implementation. Based on the new implementation, the current work also features the first evaluation of local hybrid functionals with respect to their performance for vertical excitation energies. Here, local hybrid functionals have crystallized as a promising approach for the description of many particularly difficult excitation classes, e.g. core, Rydberg as well as triplet valence excitations.

The second part of the work addresses the development of new local hybrid functionals. Besides the new semi-local pig and tpig type calibration functions, which have been constructed on the basis of a novel derivation scheme, a new local mixing function and a modified self-interaction-reduced LDA correlation functional, referred to as gt-LMF and sirPW92*, respectively, have been proposed. This is accompanied by a novel optimization procedure for the determination of suitable CF parameters. While the new CFs effectively mitigate known issues caused by the gauge problem, the potential of the new LMF has been illustrated with respect to thermochemical and vertical-excitation test sets. Especially atomization energies are significantly improved compared to standard global hybrids and other local hybrid functionals.

Zusammenfassung

Die vorliegende Arbeit beschäftigt sich mit der Weiterentwicklung von lokalen Hybridfunktionalen auf dem Feld der Dichtefunktionaltheorie. Im ersten Abschnitt der Arbeit wird auf die Verknüpfung von lokalen Hybridfunktionalen mit der zeitabhänigen Dichtefunktionaltheorie eingegangen, welche in ihrem linearen Responseformalismus die meistverwendete quantenchemische Methode zur Berechnung angeregter elektronischer Zustände darstellt. Neben einer detaillierten Herleitung aller benötigten Formeln wird die Implementierung in das quantenchemische Programm TURBOMOLE beschrieben, welche aufgrund des verwendeten seminumerischen Integrationsschemas eine höhere Effizienz als die bisherige Implementierung globaler Hybridfunktionale aufweist. Unter Verwendung der neuen Implementierung wird zusätzlich die erste detaillierte Untersuchung lokaler Hybridfunktionale bezüglich ihrer Leistungsfähigkeit zur Beschreibung angeregter elektronischer Zustände vorgenommen. Hierbei haben sich lokale Hybridfunktionale vor allem als vielversprechender Ansatz zur Beschreibung schwieriger Anregungsklassen erwiesen, so zum Beispiel für Kern-, Rydberg- und Triplettvalenzanregungen.

Im zweiten Abschnitt der Arbeit wird die Entwicklung neuer lokaler Hybridfunktionale behandelt. Neben den neuen semilokalen Kalibrierungsfunktionen vom pig und tpig Typ, welche auf der Grundlage eines neuartigen Herleitungsschemas entwickelt wurden, wurden eine neue lokale Mischfunktion, die gt-LMF, sowie eine modifizierte Variante des selbstwechselwirkungsreduzierten LDA Korrelationsfunktionals, welches als sirPW92* bezeichnet wird, vorgestellt. Zusätzlich wurde ein neuartiges Optimierungsschema zur Bestimmung geeigneter Kalibrierungsfunktionsparameter entwickelt. Während die neuen Kalibrierungsfunktionen ermöglichen, Folgen des Eichursprungsproblems effektiv zu reduzieren, wurde das Potential der neuen gt-LMF anhand thermochemischer Testsätze sowie mittels Anregungsenergietestsätzen untersucht. Vor allem für Atomisierungsenergien konnte hierbei eine signifikante Verbesserung im Vergleich zu herkömmlichen globalen und anderen lokalen Hybridfunktionalen erzielt werden.

List of Publications

[1] T. M. Maier, H. Bahmann and M. Kaupp, *"Efficient Semi-Numerical Implementation of Global and Local Hybrid Functionals for Time-Dependent Density Functional Theory"*, *J. Chem. Theory Comput.* **11**, 4226 (2015).

[2] T. M. Maier, H. Bahmann, A. V. Arbuznikov and M. Kaupp, *"Validation of Local Hybrid Functionals for TDDFT Calculations of Electronic Excitation Energies"*, *J. Chem Phys.* **144**, 074106 (2016).

[3] T. M. Maier, M. Haasler, A. V. Arbuznikov and M. Kaupp, *"New Approaches for the Calibration of Exchange-Energy Densities in Local Hybrid Functionals"*, *Phys. Chem. Chem. Phys.* **18**, 21133 (2016).

Copyrights

- Chapters 3 and 4 as well as tables and graphics within are reproduced with permission from T. M. Maier, H. Bahmann and M. Kaupp, *J. Chem. Theory Comput.* **11**, 4226 (2015). Copyright 2016 American Chemical Society.
- Chapter 5 as well as tables and graphics within are reproduced with permission from T. M. Maier, H. Bahmann, A. V. Arbuznikov and M. Kaupp, *J. Chem. Phys.* **144**, 074106 (2016) and with the permission of AIP Publishing.
- Chapter 6 as well as tables and graphics within are reproduced from T. M. Maier, M. Haasler, A. V. Arbuznikov and M. Kaupp, *Phys. Chem. Chem. Phys.* **18**, 21133 (2016) with permission from the PCCP Owner Societies.
- Appendix A is partly reproduced from T. M. Maier, M. Haasler, A. V. Arbuznikov and M. Kaupp, *Phys. Chem. Chem. Phys.* **18**, 21133 (2016) with permission from the PCCP Owner Societies.

Contents

List of Abbreviations

AC	adiabatic connection
AE	atomization energy
AO	atomic orbital
BLAS	basic linear algebra subprograms
BO	Born-Oppenheimer
CASPT	complete-active-space perturbation theory
CASSCF	complete-active-space self-consistent field
CC	coupled-cluster
CF	calibration function
CI	configuration interaction
CIS	configuration interaction singles
COSX	chain-of-spheres exchange
CT	charge transfer
DFT	density functional theory
DORI	density overlap regions indicator
EA	electron affinity
EOM-CC	equation-of-motion coupled-cluster
FDO	functional derivatives with respect to occupied orbitals
GEA	gradient expansion approximation

GGA	generalized gradient approximation
GTO	Gaussian-type orbital
HF	Hartree-Fock
HOMO	highest occupied molecular orbital
IP	ionization potential
KS	Kohn-Sham
LCAO	linear combination of atomic orbitals
LDA	local-density approximation
LH	local hybrid
LinK	linear-scaling exact exchange
LMF	local mixing function
LSDA	local-spin-density approximation
LUMO	lowest unoccupied molecular orbital
MAE	mean absolute error
MCSCF	multi-configurational self-consistent field
ME	mean error
MO	molecular orbital
MP	Møller-Plesset
MRCC	multi-reference coupled-cluster
MRCI	multi-reference configuration interaction
MS-CASPT	multi-state complete-active-space perturbation theory
MS-MRCI	multi-state multi-reference configuration interaction
MSE	mean signed error

NDC	non-dynamical correlation
OEP	optimized effective potential
PES	potential energy surface
PS	pseudospectral
RASSCF	restricted-active-space self-consistent field
RHF	restricted Hartree-Fock
RI	resolution-of-identity
RPA	random-phase approximation
RS	range-separated / range-separation
SCF	self-consistent field
SE	Schrödinger equation
SMP	shared-memory multi-processing
SR	short range
STO	Slater-type orbital
TDA	Tamm-Dancoff approximation
TDDFT	time-dependent density functional theory
TDHF	time-dependent Hartree-Fock
TDKS	time-dependent Kohn-Sham
TDOEP	time-dependent optimized effective potential
UEG	uniform electron gas
UHF	unrestricted Hartree-Fock
X2C	exact two-component
XC	exchange-correlation

1. Introduction

In modern quantum chemistry, time-dependent density functional theory (TDDFT) within its linear-response formalism represents the method of choice, when it comes to the calculation of excited states of large molecular systems.[1] Besides an excellent ratio between accuracy and computational effort,[2] TDDFT constitutes a robust black-box method, which thus can be efficiently used in routine calculations to tackle chemical problems. Therefore, TDDFT is applied in a wide range of different fields, ranging from material research[3–6] to biophysics.[1] Nevertheless, the quality of TDDFT calculations strongly depends on the choice of the exchange-correlation (XC) functional, potential and kernel. Apart from the usually applied adiabatic approximation for the kernel, which enables the utilization of approximations to the ground-state XC functional, but allows only the computation of singly excited states,[1] conventional semi-local XC functionals exhibit substantial errors, for example for the description of core excitations, Rydberg states and most charge-transfer (CT) excitations.[7–12] Although state-of-the-art XC functionals, as e.g. global and range-separated hybrid functionals,[8,13,14] which feature a constant or an interelectronic distance-dependent admixture of exact exchange, respectively, significantly mitigate these issues, problems are not completely solved, yet.

Another relatively recent class of XC functionals are local hybrid functionals (local hybrids),[15] which feature a real-space-dependent admixture of exact exchange employing a so-called local mixing function (LMF). Despite the ambiguity arising due to the local exact-exchange admixture, known as gauge problem,[16] local hybrids have been shown to be able to provide significant improvements over standard XC functionals concerning ground-state properties, as e.g. atomization energies and barrier heights.[17,18] Regarding excited-state calculations, for which local hybrids represent a potentially advantageous approach, neither a TDDFT implementation nor a theoretical formulation of the adiabatic local hybrid XC kernel have been available at the beginning of the present work, so that an evaluation of local hybrids for their performance with respect to excited-state calculations was not possible so far.

The main objective of the present work is to close this gap between local hybrid functionals and TDDFT. Based on an introduction of the underlying theoretical background,

in particular concerning TDDFT and local hybrid functionals, the adiabatic local hybrid XC kernel will be derived first, followed by a detailed description and evaluation of the implementation of the local hybrid XC kernel into the quantum chemical program package TURBOMOLE.[19] Here, special attention will be paid to an efficient implementation to retain the high efficiency provided by the existing TDDFT implementation of TURBOMOLE.[20] Based on the new implementation, the first evaluation of a broader range of existing local hybrid functionals for the calculation of vertical excitation energies will be presented, illustrating their performance in comparison to other successful XC functionals. In the second part of the work, the development of local hybrid functionals is expedited. In particular, this concerns the two integral parts of local hybrids, i.e. the LMF, and the calibration function (CF),[21] which shall correct errors caused by gauge issues. For both building blocks, new approaches regarding their construction as well as suitable optimization procedures will be presented. Besides the conjunction of local hybrids and TDDFT, the present work thus also provides state-of-the-art developments of local hybrid functionals.

2. Theoretical Background

In this chapter, the theoretical background required for the understanding of the derivation and implementation of the local hybrid exchange-correlation kernel and for the construction of novel local hybrid functionals is described. Starting with some basic quantum chemical concepts given by the Schrödinger equation and Hartree-Fock theory, concepts and approximations in density functional theory will be described in detail, with a special focus on local hybrid functionals, which respresent the main topic of the present work. Being directly related to the derivations and implementation, respectively, time-dependent density functional theory and concepts of integral evaluation are also described. Throughout the entire work, atomic units are used.

2.1. Fundamental Quantum Chemistry

2.1.1. Schrödinger Equation

The fundamental equation in non-relativistic quantum chemistry is the time-dependent Schrödinger equation (SE),[22] which describes the quantum dynamics of a many-particle system represented by the wavefunction Ψ. For molecules, i.e. systems of N_N atomic nuclei and N_e electrons with the spatial coordinates $\mathbf{R}$ and $\mathbf{r}$, respectively, it reads

$$\hat{H}\left(\mathbf{r},\mathbf{R},t\right)\Psi\left(\mathbf{r},\mathbf{R},t\right)=\mathrm{i}\frac{\partial}{\partial t}\Psi\left(\mathbf{r},\mathbf{R},t\right)\ , \tag{2.1}$$

with the Hamilton operator[23,24]

$$\begin{aligned}\hat{H}\left(\mathbf{r},\mathbf{R},t\right)=&\hat{T}_N\left(\mathbf{R}\right)+\hat{T}_e\left(\mathbf{r}\right)+\hat{V}_{NN}\left(\mathbf{R}\right)+\\&\hat{V}_{Ne}\left(\mathbf{r},\mathbf{R}\right)+\hat{V}_{ee}\left(\mathbf{r}\right)+\hat{V}_{ext}\left(t\right)\end{aligned} \tag{2.2}$$

containing the kinetic energy operators $\hat{T}$ and the potential energy operators $\hat{V}$. The indices N and e denote nuclei and electrons, respectively, while $\hat{V}_{ext}$ stands for an external time-dependent potential, e.g. a laser pulse or an electromagnetic field. $\hat{V}_{NN}$ and

$\hat{V}_{ee}$ thus describe nucleus-nucleus and electron-electron repulsion, while $\hat{V}_{Ne}$ denotes the nucleus-electron attraction potential. Note that the three aforementioned potentials are multiplicative, while the kinetic energy operators represent non-multiplicative differential operators. This can be seen in a more explicit form of $\hat{H}$

$$\begin{aligned}\hat{H}\left(\mathbf{r},\mathbf{R},t\right) = &-\frac{1}{2}\sum_{A}^{N_N}\frac{1}{m_A}\nabla_A^{\mathrm{T}}\nabla_A - \frac{1}{2}\sum_{i}^{N_e}\nabla_i^{\mathrm{T}}\nabla_i + \sum_{A}^{N_N}\sum_{B>A}^{N_N}\frac{Z_A Z_B}{|\mathbf{R}_A-\mathbf{R}_B|} \\ &-\sum_{A}^{N_N}\sum_{i}^{N_e}\frac{Z_A}{|\mathbf{R}_A-\mathbf{r}_i|} + \sum_{i}^{N_e}\sum_{j>i}^{N_e}\frac{1}{|\mathbf{r}_i-\mathbf{r}_j|} + \hat{V}_{ext}\left(t\right)\ , \end{aligned} \tag{2.3}$$

with the iteration variables A, B for nuclei and i, j for electrons as well as the nuclear mass m_A and nuclear charge Z_A (for the Ath atom). Without an external time-dependent potential, i.e. $\hat{V}_{ext} = 0$, $\hat{H}$ becomes time-independent, so that the wavefunction Ψ can be separated into a time-independent part with a time-dependent oscillating prefactor of constant frequency ω

$$\Psi\left(\mathbf{r},\mathbf{R},t\right) = \mathrm{e}^{-\mathrm{i}\omega t}\Psi\left(\mathbf{r},\mathbf{R}\right)\ , \tag{2.4}$$

which leads to the time-independent Schrödinger equation for stationary states

$$\hat{H}\left(\mathbf{r},\mathbf{R}\right)\Psi\left(\mathbf{r},\mathbf{R}\right) = E\left(\mathbf{r},\mathbf{R}\right)\Psi\left(\mathbf{r},\mathbf{R}\right)\ , \tag{2.5}$$

with E being the eigenvalue of $\hat{H}$, thus describing the total energy of the system.

(2.5) can be further simplified applying the Born-Oppenheimer (BO) approximation, also known as clamped-nuclei approximation.[25,26] It states that, due to the large difference between electron and atomic masses, the motion of electrons and atomic nuclei can be separated. Pictorially, the electrons move in a field of fixed nuclei, while the nuclei move in an averaged field of fast moving electrons. Formally, this is realized by the separation of the Hamilton operator and the wavefunction into an electronic and a nuclear part

$$\hat{H}\left(\mathbf{r},\mathbf{R}\right) = \hat{H}_e\left(\mathbf{r},\mathbf{R}\right) + \hat{H}_N\left(\mathbf{R}\right) \tag{2.6}$$

$$\Psi\left(\mathbf{r},\mathbf{R}\right) = \Psi_e\left(\mathbf{r},\mathbf{R}\right)\Psi_N\left(\mathbf{R}\right)\ , \tag{2.7}$$

with the nuclear and electronic Hamiltonians

$$\hat{H}_N(\mathbf{R}) = \hat{T}_N(\mathbf{R}) + \hat{V}_{NN}(\mathbf{R}) \tag{2.8}$$

$$\hat{H}_e(\mathbf{r},\mathbf{R}) = \hat{T}_e(\mathbf{r}) + \hat{V}_{ee}(\mathbf{r}) + \hat{V}_{Ne}(\mathbf{r},\mathbf{R}) \ . \tag{2.9}$$

For a set of fixed atomic coordinates, i.e. $\hat{T}_N = 0$ and $\hat{V}_{NN} = const.$, one gets the electronic Schrödinger equation

$$\hat{H}_e(\mathbf{r};\mathbf{R})\,\Psi_e(\mathbf{r};\mathbf{R}) = E_e(\mathbf{R})\,\Psi_e(\mathbf{r};\mathbf{R}) \tag{2.10}$$

with the electronic energy E_e and a remaining parametrical dependency on the nuclear spatial coordinates $\mathbf{R}$ (denoted by the separator ;). Note that the total energy of the molecule (for fixed nuclei) is simply the sum of E_e and the constant nucleus-nucleus potential, both depending parametrically on $\mathbf{R}$. This dependence gives rise to the popular concept of potential energy surfaces (PES).[27] Similar to the time-independent case, the BO approximation can be applied to the time-dependent Schrödinger equation, thus leading to the time-dependent electronic SE[28,29]

$$\hat{H}_e(\mathbf{r},t;\mathbf{R})\,\Psi(\mathbf{r},t;\mathbf{R}) = \mathrm{i}\frac{\partial}{\partial t}\Psi(\mathbf{r},t;\mathbf{R}) \ . \tag{2.11}$$

Despite the reduction of the molecular SE to a pure electronic problem by the BO approximation, analytical solutions of the time-independent electronic SE (2.10) are only accessible for the hydrogen atom and for other one-electron systems. For all other molecules, approximate solutions have to be found.

2.1.2. Hartree-Fock Theory

One of the most basic approximations for the solution of the time-independent electronic Schrödinger equation (2.10) is the Hartree-Fock (HF) method, also known as mean-field approximation.[30] In this approach, the electronic wavefunction is approximated as a so-called Slater determinant Φ, i.e. an antisymmetrized product of one-particle wavefunctions, the spin orbitals ϕ. For an N electron system, the normalized Slater determinant

reads

$$\Psi \approx \Phi\left(\mathbf{x}_1, \mathbf{x}_2, \ldots, \mathbf{x}_N\right) = \frac{1}{\sqrt{N!}} \begin{vmatrix} \phi_1\left(\mathbf{x}_1\right) & \phi_1\left(\mathbf{x}_2\right) & \cdots & \phi_1\left(\mathbf{x}_N\right) \\ \phi_2\left(\mathbf{x}_1\right) & \phi_2\left(\mathbf{x}_2\right) & \cdots & \phi_2\left(\mathbf{x}_N\right) \\ \vdots & \vdots & \ddots & \vdots \\ \phi_N\left(\mathbf{x}_1\right) & \phi_N\left(\mathbf{x}_2\right) & \cdots & \phi_N\left(\mathbf{x}_N\right) \end{vmatrix} . \tag{2.12}$$

By default, it provides the correct symmetry for the exchange of two electrons and obeys the Pauli exclusion principle.[31] For the construction of Φ, a set of $M \geq N$ orthonormal spin orbitals $\{\phi_p\}$ is used, while only the N occupied orbitals appear in the Slater determinant. The spin orbitals themselves are products of a spin function and a spatial wavefunction $\varphi\left(\mathbf{r}\right)$, the molecular orbital (MO). While the spin functions form an orthonormal basis, which is represented by the functions $\alpha\left(s\right)$ and $\beta\left(s\right)$, only spatial orbitals of same spin have to be orthonormal, since orthonormality of spin orbitals with different spin is already ensured by the spin functions. Without restrictions for spatial orbitals of different spin (unrestricted Hartree-Fock (UHF)), the spin orbitals are given by

$$\left\{\phi_p\left(\mathbf{x}\right)\right\} = \begin{cases} \alpha\left(s\right)\varphi_{q,\alpha}\left(\mathbf{r}\right) \\ \beta\left(s\right)\varphi_{q,\beta}\left(\mathbf{r}\right) \end{cases}, q = 1, \ldots, \frac{M}{2} , \tag{2.13}$$

with $\varphi_{q,\sigma}$ denoting the qth MO arising from a σ spin orbital. Hence, the one-electron density matrices D^{σ}_{pq} in the MO basis[32] are given by

$$D^{\sigma}_{ij} = \delta_{ij} \tag{2.14}$$

$$D^{\sigma}_{ia} = D^{\sigma}_{ai} = D^{\sigma}_{ab} = 0 , \tag{2.15}$$

thus satisfying the idempotency condition

$$D^{\sigma}_{pq} = \sum_r D^{\sigma}_{pr} D^{\sigma}_{rq} . \tag{2.16}$$

As usual, the indices $i, j, \ldots$ are used for occupied, $a, b, \ldots$ for virtual and $m, n, \ldots$ for general orbitals. The calculation of the energy expectation value of the Slater determinant Φ for the electronic Hamilton operator (2.9) then gives its energy in density matrix

notation[33]

$$E_{SD} = \sum_{\sigma} \sum_{pq} h_{pq}^{\sigma} D_{pq}^{\sigma} + \frac{1}{2} \sum_{\sigma} \sum_{pqrs} \left[\left(g_{pqrs}^{\sigma\sigma} - g_{psrq}^{\sigma\sigma} \right) D_{rs}^{\sigma} + g_{pqrs}^{\sigma\sigma'} D_{rs}^{\sigma'} \right] D_{pq}^{\sigma} \,, \tag{2.17}$$

which matches the Hartree-Fock energy only for the optimized set of spin orbitals. Note that σ' is no separate spin variable, but denotes the opposite spin of σ. The core Hamilton matrix

$$h_{pq}^{\sigma} = \int \varphi_{p,\sigma}^{*}(\mathbf{r}) \left[-\frac{1}{2} \nabla^{\mathrm{T}} \nabla - \sum_{A} \frac{Z_A}{|\mathbf{r} - \mathbf{R}_A|} \right] \varphi_{q,\sigma}(\mathbf{r}) \, \mathrm{d}\mathbf{r} \tag{2.18}$$

contains the expressions for the kinetic energy and the electron-nucleus attraction, respectively, while the electron-electron interaction is captured by the matrix

$$g_{pqrs}^{\sigma\varsigma} = \int \int \frac{\varphi_{p,\sigma}^{*}(\mathbf{r}_1) \, \varphi_{q,\sigma}(\mathbf{r}_1) \, \varphi_{r,\varsigma}^{*}(\mathbf{r}_2) \, \varphi_{s,\varsigma}(\mathbf{r}_2)}{|\mathbf{r}_1 - \mathbf{r}_2|} \mathrm{d}\mathbf{r}_1 \mathrm{d}\mathbf{r}_2 \,, \tag{2.19}$$

which appears with normal index order g_{pqrs} and exchanged index order g_{psrq}. After multiplication with the density matrix $\mathbf{D}$, the former term respresents the classical Coulomb repulsion of charged particles, while the latter one is the non-classical exchange interaction arising due to the antisymmetry of the wavefunction.

While (2.17) gives the energy of a Slater determinant built from an arbitrary set of orthonormal MOs, it provides no rule for the determination of the set of MOs giving the lowest energy. Therefore, the energy (2.17) is minimized by variation[34] with respect to the molecular orbitals, resulting in the Hartree-Fock equations

$$\sum_{r} \left[F_{pr}^{\sigma} D_{rq}^{\sigma} - D_{pr}^{\sigma} F_{rq}^{\sigma} \right] = 0 \,, \tag{2.20}$$

with the Fock matrix elements F_{mn} in the MO basis

$$F_{mn}^{\sigma} = h_{mn}^{\sigma} + \sum_{rs} \left[\left(g_{mnrs}^{\sigma\sigma} - g_{msrn}^{\sigma\sigma} \right) D_{rs}^{\sigma} + g_{mnrs}^{\sigma\sigma'} D_{rs}^{\sigma'} \right] \,. \tag{2.21}$$

Additionally imposing the canonical condition

$$F_{pq}^{\sigma} = \epsilon_{p}^{\sigma} \delta_{pq} \,, \tag{2.22}$$

results in the canonical Hartree-Fock equations, which uniquely define an optimal set of orthonormal molecular orbitals, occupied as well as virtual. Nevertheless, the Hartree-

Fock equations cannot be solved directly, since the Fock matrix, which determines the optimal density matrix and thus the MOs, depends itself on the density matrix. Hence, (2.20) and (2.22) have to be solved in an iterative procedure until self-consistency for the molecular orbitals is achieved. The eigenvalues ϵ_p^σ for the optimized set of MOs are then interpreted as orbital energies of the pth MO and are related to the Hartree-Fock energy via

$$E_{HF} = \frac{1}{2} \sum_\sigma \sum_{pq} \left[\epsilon_p^\sigma + h_{pq}^\sigma \right] D_{pq}^\sigma \ . \tag{2.23}$$

Note that the given equations for the unrestricted HF method reduce to the restricted HF (RHF) equations in the case of a closed-shell singlet state ($N_\alpha = N_\beta$) with equal spatial orbitals for α and β spin. The introduction of a basis set, e.g. an atomic orbital basis (see Sec. 2.5.1), leads to the well known Pople-Nesbet (unrestricted)[35] and Roothaan-Hall (restricted) equations, respectively.[36,37]

2.1.3. Electron Correlation

One important concept in quantum chemistry, which is related to the Hartree-Fock method, is the so-called electron correlation.[38,39] Assuming a product of single-particle wavefunctions, i.e. the Hartree product

$$\Psi \left(\mathbf{x}_1, \mathbf{x}_2, \ldots, \mathbf{x}_N \right) = \prod_i^N \phi_i \left(\mathbf{x}_i \right) \ , \tag{2.24}$$

the electron-electron interaction reduces to the classical Coulomb interaction of electron densities. Hence, in this independent particle model, every electron interacts only with the averaged charge of all electrons, which is regarded as uncorrelated motion of the electrons. As a consequence, two electrons are allowed to come close together and even have the same spatial coordinates without being affected explicitly by each other's charge, resulting in a too large repulsive electron-electron interaction. The exact wavefunction on the other hand considers the correlated motion of the electrons, thus preventing the electrons from having the same position. According to the variational principle,[34] the energy of the exact wavefunction is thus lower than that of the independent particle wavefunction (2.24). The difference between the independent and the correlated motion of electrons is known as electron correlation, where the Fermi correlation incorporates effects caused by the antisymmetry of the wavefunction, while the Coulomb correlation describes the explicit charge interaction of the electrons.

In the case of the Hartree-Fock method, the wavefunction is not approximated by the independent particle wavefunction but a Slater determinant, which is an antisymmetrized product of single-particle wavefunctions. In contrast to the Hartree product, the antisymmetry of the electronic wavefunction is correctly described. As a consequence, the motion of the electrons in the Hartree-Fock method is not completely uncorrelated. Regarding (2.17), the classical Coulomb interaction is reduced by the exchange term in the case of identical spins, describing correctly the Fermi correlation. Hence, the exchange term also cancels the spurious Coulomb interaction of an electron with itself (orbital indices $p = q = r = s$), known as self-interaction error.[40,41] Since exchange is a direct result of the antisymmetry of the wavefunction and is already described by a single determinant, it is conventionally excluded from the term 'electron correlation' and denoted as exchange, which leads to the definition of electron correlation by Löwdin[38]

$$E_{corr} = E_{exact} - E_{HF} \; . \tag{2.25}$$

In this definition of the correlation energy, two different effects are included, the dynamical and the static or non-dynamical correlation.[39] While the dynamical correlation describes the Coulomb correlation explained before, static correlation refers to near-degeneracy effects between different configurations, leading to strong interactions between them.

In wavefunction theory, both types of correlation can be captured by the inclusion of more than a single determinant for the description of the wavefunction. This can be done by expanding the wavefunction in terms of excited Hartree-Fock determinants, leading to so-called single-reference methods[42] such as Møller-Plesset perturbation theory (MP), configuration interaction (CI) and coupled-cluster theory (CC).[42] Usually, the major part of the dynamical correlation can be described by these methods, while CI and CC methods also include parts of the static correlation. Note that a complete CI or CC expansion leads to a numerically exact solution of the Schrödinger equation and thus covers all correlation effects.

Nevertheless, in some cases Hartree-Fock orbitals are a poor description for the real system, especially for systems with strong static correlation, where due to near-degeneracy effects, the selection of a single Slater determinant according to the aufbau principle is not sufficient. In these cases, which are usually called multi-reference systems, the spin orbitals can be optimized for a multi-determinantal wavefunction. This multi-configurational self-consistent field method (MCSCF)[42] is usually applied within a complete or a restricted space of active orbitals, leading to the CASSCF or RASSCF method, respectively. While these methods already describe the major part of the static correlation, the remaining

dynamical correlation has to be determined by methods using the multi-determinantal wavefunction as reference,[42] e.g. complete-active-space perturbation theory (CASPT), multi-reference CI (MRCI) or multi-reference CC (MRCC). For many of the methods mentioned, extensions for the description of excited states exist, too, e.g. equation of motion coupled-cluster (EOM-CC),[43] multi-state MRCI (MS-MRCI)[44] and CASPT (MS-CASPT).[45]

While wavefunction methods can be systematically improved by adding more determinants to the description, the major bottleneck is their increasing calculation cost, which has an unfavorable scaling with respect to system size, so that accurate calculations are often restricted to small or medium sized molecules.

2.2. Density Functional Theory

2.2.1. Basics

An alternative approach for the solution of the electronic Schrödinger equation is provided by density functional theory (DFT).[46] Instead of the wavefunction Ψ, the electron density ρ is used as basic quantity for the description of a system. It describes the probability of finding an electron (with arbitrary spin) in an infinitesimal small volume element of real space. For an N electron system, ρ thus integrates to the total electron number

$$\int \rho\left(\mathbf{r}\right) \mathrm{d}\mathbf{r} = N \; . \tag{2.26}$$

In terms of the normalized wavefunction Ψ, the electron density is thus defined as

$$\rho\left(\mathbf{r}\right) \equiv \rho\left(\mathbf{r}_1\right) = N \int \Psi^*\left(\mathbf{x}_1, \ldots, \mathbf{x}_N\right) \Psi\left(\mathbf{x}_1, \ldots, \mathbf{x}_N\right) \mathrm{d}s_1 \mathrm{d}\mathbf{x}_2 \ldots \mathrm{d}\mathbf{x}_N \; . \tag{2.27}$$

While the wavefunction represents a rather complex object with a dependence on $4N$ variables ($3N$ spatial and N spin variables), the electron density depends only on the three spatial coordinates. Furthermore, ρ is directly accessible by experiments, e.g. X-ray diffraction or electron microscopy.

The first theoretical legitimization for the description of the energy as a functional of the electron density was given by Hohenberg and Kohn in 1964.[47] In their first theorem, they proved by *reductio ad absurdum* the one-to-one mapping between an external potential and the ground-state electron density. Since the external potential, which is the electron-nucleus attraction potential V_{Ne} in the case of molecules (cf. (2.3) and (2.9)), also fixes the

electronic Hamiltonian, the electronic energy is a unique functional of ρ, which is given by

$$E_0 = E[\rho_0] = T[\rho_0] + E_{ee}[\rho_0] + E_{Ne}[\rho_0] \tag{2.28}$$

for the ground-state electron density ρ_0, where T, E_{ee} and E_{Ne} denote the energy functionals of the kinetic energy, the electron-electron repulsion and the electron-nucleus attraction, respectively. A variational principle for the determination of the ground-state electron density ρ_0 is provided by the second Hohenberg-Kohn theorem [47] and in a slightly different formulation by the constrained-search approach of Levy. [48] In the formulation of Levy, the variational search is given by

$$E[\rho_0] = \min_{\rho \to N} \left(F[\rho] + \int \hat{V}_{Ne} \rho(\mathbf{r}) \, \mathrm{d}\mathbf{r} \right) , \tag{2.29}$$

where the universal functional F is defined by the constrained-search formula

$$F[\rho] = \min_{\Psi \to \rho} \left\langle \Psi \left| \hat{T} + \hat{V}_{ee} \right| \Psi \right\rangle . \tag{2.30}$$

However, in DFT, the universal functional F is expressed as an explicit density functional rather than a constrained search, so that the minimization in (2.29) depends only on the electron density. Hence, the electron-electron interaction E_{ee} and the kinetic energy T as part of F also have to be expressed as explicit density functionals

$$F[\rho] = T[\rho] + E_{ee}[\rho] . \tag{2.31}$$

A consequence of (2.29) is that the energy expectation value calculated with a trial density ρ has to be larger than or equal to the energy obtained with the exact ground-state density

$$E[\rho] = F[\rho] + E_{Ne}[\rho] \geq E[\rho_0] , \tag{2.32}$$

which is similar to the variational principle in wavefunction theory. [34] Nevertheless, this variational principle holds true completely only for the exact universal functional F, which, unfortunately, is not known and thus has to be approximated. While (2.32) holds true even for an approximated F, with ρ_0 being its optimized ground-state electron density, the energy expectation value $E[\rho_0]$ might be lower than the real ground-state energy E_0. Hence, DFT is variational with respect to the electron density but not with respect to the choice of the approximated universal functional.

The central problem in conventional DFT is thus to find a viable approximation for the universal functional. Unfortunately, besides the electron-nucleus attraction E_{Ne}, only the classical Coulomb repulsion of the electrons J is known exactly

$$E_{Ne}[\rho] = -\sum_A Z_A \int \frac{\rho(\mathbf{r})}{|\mathbf{r} - \mathbf{R}_A|} \mathrm{d}\mathbf{r} \tag{2.33}$$

$$J[\rho] = \frac{1}{2} \int\int \frac{\rho(\mathbf{r}_1)\,\rho(\mathbf{r}_2)}{|\mathbf{r}_1 - \mathbf{r}_2|} \mathrm{d}\mathbf{r}_1 \mathrm{d}\mathbf{r}_2 \ . \tag{2.34}$$

The remaining density functionals of the kinetic energy and of the non-classical electron-electron interaction on the other hand have to be approximated, where the kinetic energy represents the larger part with respect to the total energy. The application of model functionals like the one of Thomas and Fermi[49,50] revealed that the major problems, e.g. the false prediction of unbound ground states of molecules, are related to the approximated kinetic energy functional. While more elaborated explicit density functionals including gradient corrections could reproduce the exact kinetic energy slightly more accurately,[51] the alternative indirect approach of Kohn and Sham,[52] which circumvents the construction of an explicit density functional for the kinetic energy, became the standard approach in today's density functional theory.

2.2.2. Kohn-Sham DFT

In their approach of 1965, Kohn and Sham (KS) introduced a fictitious non-interacting reference system of electrons moving in an effective, local potential, the KS potential, so that it yields, by definition, the same electron density as the interacting system.[52–54] Since the wavefunction for a non-interacting system is known exactly, i.e. a Slater determinant (2.12), its kinetic energy T_s and electron density can be calculated directly from the MOs

$$T_s[\{\varphi_p\}] = -\frac{1}{2} \sum_\sigma \sum_{pq} D^\sigma_{pq} \int \varphi^*_{p,\sigma}(\mathbf{r})\, \nabla^{\mathrm{T}} \nabla \varphi_{q,\sigma}(\mathbf{r})\, \mathrm{d}\mathbf{r} \tag{2.35}$$

$$\rho(\mathbf{r}) = \sum_\sigma \rho_\sigma(\mathbf{r}) = \sum_\sigma \sum_{pq} D^\sigma_{pq} \varphi^*_{p,\sigma}(\mathbf{r})\, \varphi_{q,\sigma}(\mathbf{r}) \ , \tag{2.36}$$

with the density matrices thus being defined as in (2.14) and (2.15). On the basis of the non-interacting kinetic energy T_s, Kohn and Sham reexpressed the energy functional (2.28) as

$$E[\rho] = T_s[\{\varphi_p\}] + J[\rho] + E_{xc}[\rho] + E_{Ne}[\rho] \ . \tag{2.37}$$

In contrast to conventional DFT, the problem of finding the exact ground-state density is thus shifted to the problem of finding the orbitals of a non-interacting system, which yields the exact ground-state density. The advantage of the KS approach is that the kinetic energy of the non-interacting system T_s can be calculated exactly via (2.35), while it has to be approximated in conventional DFT. The presumably small remaining difference to the real kinetic energy T is then merged with the non-classical electron-electron interaction, i.e. exchange and correlation, into the exchange-correlation (XC) functional

$$E_{xc}[\rho] = T[\rho] - T_s[\{\varphi_p\}] + E_{ee}[\rho] - J[\rho] \ . \tag{2.38}$$

The XC energy defined in (2.38) has to be distinguished from the definition of exchange and correlation in section 2.1.3. While the definition in wavefunction theory is based on the Hartree-Fock approximation and thus the optimized HF orbitals, the XC energy is calculated for a fictitious set of orbitals, called KS orbitals, which by definition gives the exact ground-state density. Hence, the amount of exchange and correlation is different from the definitions in wavefunction theory, although the considered effects are similar. Besides the XC energy, all other parts of the total energy are calculated exactly in KS DFT. In comparison to conventional DFT, a far lesser part of the total energy thus has to be approximated, explaining the significantly enhanced accuracy of KS DFT. Nevertheless, the introduction of an orbital basis for the exact calculation of T_s, which is only an implicit functional of the density, lifts the simplicity of dealing with explicit density functionals, resulting in a higher computational cost. As for F (cf. Eq. (2.31)) in conventional DFT, knowledge of the exact XC functional gives the exact ground-state energy of the system, rendering KS DFT an in principle exact theory. However, in real-life calculations, approximations have to be made.

A generalization of the approach of Kohn and Sham was given by Levy and coworkers.[55] Instead of constructing a non-interacting reference system, they introduced a fully or partially interacting reference system, which can be described by a single Slater determinant. Similar to KS DFT, an energy functional

$$E[\rho] = T_s[\{\varphi_p\}] + J[\rho] + E_{xc}[\{\varphi_p\}] + E_{Ne}[\rho] \tag{2.39}$$

can be formulated. In contrast to the KS approach, exact orbital exchange and correlation contributions defined by the reference system may enter the energy functional, leading to a possible explicit orbital dependence of the XC functional. Nevertheless, only the electron density of the reference system equals the density of the fully interacting system, while

MOs and thus the density matrix in general are not equivalent.[56] In this sense, the HF method can be regarded as a special case in the framework of generalized KS DFT, in which complete exact orbital exchange

$$E_x^{ex}\left[\{\varphi_p\}\right] = \sum_\sigma E_{x,\sigma}^{ex} = -\frac{1}{2}\sum_\sigma \sum_{pqrs} g_{psrq}^{\sigma\sigma} D_{pq}^\sigma D_{rs}^\sigma \tag{2.40}$$

is used as approximate XC functional (without a correlation contribution). Nevertheless, the generalized KS scheme simply reduces to the original KS approach in the case of a non-interacting reference system.

In both approaches, KS as well as generalized KS DFT, a set of KS orbitals that gives the minimal energy has to be found. Analogously to the HF method, the energy functional has to be minimized with respect to the MOs rather than the electron density. Applying a variation of the MOs thus simply reduces to the canonical single-particle equations (2.20) and (2.22), which in the context of KS DFT are called Kohn-Sham equations. Equivalently, the matrix $\mathbf{F}^\sigma$ is called Kohn-Sham matrix and, in the general case of orbital-dependent XC functionals, is given by (cf. Eq. (2.21) for the HF case)

$$F_{mn}^\sigma = h_{mn}^\sigma + \sum_{rs}\left[g_{mnrs}^{\sigma\sigma} D_{rs}^\sigma + g_{mnrs}^{\sigma\sigma'} D_{rs}^{\sigma'}\right] + \frac{\delta E_{xc}}{\delta D_{mn}^\sigma} \,. \tag{2.41}$$

While derivatives with respect to the density matrix (or equivalently functional derivatives with respect to molecular orbitals) are needed for the treatment of explicitly orbital-dependent XC functionals within the generalized KS framework, a treatment within conventional KS DFT or within the optimized effective potential (OEP) method[57] gives a semi-local or local XC potential v_{xc}, i.e. the first functional derivative with respect to the electron density. Derivatives with respect to the density matrix can thus be reexpressed as

$$\frac{\delta E_{xc}}{\delta D_{mn}^\sigma} = \int \varphi_{m,\sigma}^*(\mathbf{r})\, v_{xc}^\sigma(\mathbf{r})\, \varphi_{n,\sigma}(\mathbf{r})\, \mathrm{d}\mathbf{r} = \int \varphi_{m,\sigma}^*(\mathbf{r})\, \frac{\delta E_{xc}}{\delta \rho_\sigma(\mathbf{r})} \varphi_{n,\sigma}(\mathbf{r})\, \mathrm{d}\mathbf{r} \,. \tag{2.42}$$

A detailed discussion of functional derivatives will be given in chapter 3.

2.2.3. Adiabatic Connection and Exchange-Correlation Hole

While KS DFT rigorously ensures the existence of the XC functional, it basically gives no explicit expression or prescription for the construction of E_{xc}. The latter was first provided by the adiabatic connection (AC) formalism.[58–61] Here, the non-interacting

reference system of KS DFT is connected to the fully interacting system by means of a coupling strength parameter λ ranging between 0 and 1 and thus describing the amount of explicit electron-electron interaction

$$\hat{H}_\lambda = \hat{T} + \lambda \hat{V}_{ee} + \hat{V}_{ex}^\lambda \,, \tag{2.43}$$

with a λ-dependent external potential $\hat{V}_{ex}^\lambda$. Along this connection, the system is described by the λ-dependent wavefunction Ψ^λ giving the exact ground-state density of the interacting system, irrespective of the coupling strength parameter. In this sense, the AC formalism shows similarities to generalized KS, which also allows partially-interacting reference systems. Nevertheless, in the AC formalism, the wavefunction Ψ^λ is generally not restricted to a single Slater determinant. Connecting the limiting cases of the AC, i.e. the non-interacting ($\lambda = 0$) and the fully interacting ($\lambda = 1$) system, leads to an explicit expression for the XC functional

$$E_{xc}\left[\rho\right] = \frac{1}{2} \int \frac{\rho_2^{avg}\left(\mathbf{r}_1, \mathbf{r}_2\right) - \rho\left(\mathbf{r}_1\right)\rho\left(\mathbf{r}_2\right)}{\left|\mathbf{r}_1 - \mathbf{r}_2\right|} \mathrm{d}\mathbf{r}_1 \mathrm{d}\mathbf{r}_2 \tag{2.44}$$

in terms of the coupling-strength-averaged pair density [62]

$$\rho_2^{avg}\left(\mathbf{r}_1, \mathbf{r}_2\right) = \int_0^1 \rho_2^\lambda\left(\mathbf{r}_1, \mathbf{r}_2\right) \mathrm{d}\lambda \,, \tag{2.45}$$

with the λ-dependent pair density being defined as

$$\rho_2^\lambda\left(\mathbf{r}_1, \mathbf{r}_2\right) = N\left(N-1\right) \int \left[\Psi^\lambda\right]^*\left(\mathbf{x}_1, \ldots, \mathbf{x}_N\right) \Psi^\lambda\left(\mathbf{x}_1, \ldots, \mathbf{x}_N\right) \mathrm{d}s_1 \mathrm{d}s_2 \mathrm{d}\mathbf{x}_3 \ldots \mathrm{d}\mathbf{x}_N \,. \tag{2.46}$$

It should be mentioned that, although (2.44) defines the XC functional purely in terms of a non-classical electron-electron interaction, the difference between the non-interacting and the exact kinetic energy (see (2.38)) is implicitly included via the coupling strength integration in (2.45).

An XC functional can also be directly introduced through the concept of the so-called XC hole. [63] It is defined as the conditional pair density associated with the difference in (2.44) [62]

$$\rho_{xc}\left(\mathbf{r}_1, \mathbf{r}_2\right) = \frac{\rho_2^{avg}\left(\mathbf{r}_1, \mathbf{r}_2\right)}{\rho\left(\mathbf{r}_1\right)} - \rho\left(\mathbf{r}_2\right) \tag{2.47}$$

and is related to the exchange-correlation functional via

$$E_{xc}\left[\rho\right] = \frac{1}{2}\int \frac{\rho\left(\mathbf{r}_1\right)\rho_{xc}\left(\mathbf{r}_1,\mathbf{r}_2\right)}{\left|\mathbf{r}_1-\mathbf{r}_2\right|}\mathrm{d}\mathbf{r}_1\mathrm{d}\mathbf{r}_2 \ . \tag{2.48}$$

All non-classical effects considered by the XC functional can thus be attributed to the XC hole. Hence, $\rho_{xc}\left(\mathbf{r}_1,\mathbf{r}_2\right)$ can be formally regarded as a non-classical density that reduces the electron density $\rho\left(\mathbf{r}_2\right)$ around the reference electron at $\mathbf{r}_1$, so that the effective density $\rho_{xc}\left(\mathbf{r}_1,\mathbf{r}_2\right)+\rho\left(\mathbf{r}_2\right)$ interacting with the reference electron density $\rho\left(\mathbf{r}_1\right)$ results in the exact electron-electron interaction energy. While the problem of finding a suitable approximation is simply shifted from the XC functional to ρ_{xc}, the formulation in terms of the XC hole has the major advantage that some properties of the XC hole that have turned out to be crucial for the performance of the resulting approximate XC functionals are known exactly.[64] Among others, the normalization of the XC hole to -1 for every reference coordinate $\mathbf{r}_1$ has proven to be of major importance

$$\int \rho_{xc}\left(\mathbf{r}_1,\mathbf{r}_2\right)\mathrm{d}\mathbf{r}_2 = -1 \ . \tag{2.49}$$

This normalization, also known as sum rule, simply reflects the antisymmetry of the wavefunction arising due to the Pauli principle. Hence, it is usually attributed as an effect of exchange, which is described by the Fermi hole ρ_x, while the remaining correlation effects are included in the Coulomb hole ρ_c, so that the complete XC hole is conveniently decomposed into a sum of the Fermi and the Coulomb hole. As a consequence of this separation, the Fermi and the Coulomb hole have to obey the sum rules

$$\int \rho_x\left(\mathbf{r}_1,\mathbf{r}_2\right)\mathrm{d}\mathbf{r}_2 = -1 \tag{2.50}$$

$$\int \rho_c\left(\mathbf{r}_1,\mathbf{r}_2\right)\mathrm{d}\mathbf{r}_2 = 0 \ , \tag{2.51}$$

respectively. In the case of the Fermi hole, further properties can be deduced from exact orbital exchange (2.40). Hence, the Fermi hole has to exhibit the on-top value[65]

$$\rho_x\left(\mathbf{r}_1,\mathbf{r}_1\right) = -\frac{1}{2}\rho\left(\mathbf{r}_1\right) \ , \tag{2.52}$$

with a zero slope for vanishing interelectronic distances, i.e. $\mathbf{r}_1 = \mathbf{r}_2$, while the exact on-top value in the spin-resolved case is

$$\rho_{x,\sigma}\left(\mathbf{r}_1,\mathbf{r}_1\right) = -\rho_\sigma\left(\mathbf{r}_1\right) \ . \tag{2.53}$$

Furthermore, ρ_x has to be negative over the entire space. In contrast, the Coulomb hole has a cusp for vanishing interelectronic distances,[66] whereas the exact on-top value is unknown. In addition, ρ_c is not bound to negative values and even has to exhibit positive values to satisfy the sum rule (2.51).

While the XC hole is a six-dimensional quantity in general, the electron-electron interaction operator $\hat{V}_{ee}$ depends only on the distance of two electrons. Hence, it is sufficient to consider a spherically averaged XC hole with a dependence on one electron coordinate $\mathbf{r}_1$ and the interelectronic separation coordinate $|\mathbf{r}_1 - \mathbf{r}_2|$, with its properties being essentially the same as for the original XC hole.

2.2.4. Approximate Exchange-Correlation Functionals

As already pointed out, the only unknown fragment in KS DFT is the XC functional. On the basis of theoretical concepts as, e.g., the adiabatic connection[67,68] and the exchange-correlation hole,[64,65,69] various approximations have been developed during the last decades.[62,70] A categorization of these approximate XC functionals was first introduced by Perdew and Schmidt,[71] who established the so-called Jacob's Ladder of approximate XC functionals. Starting from the Hartree world, i.e. the absence of an XC functional, Perdew and Schmidt proposed five rungs of approximations with increasing accuracy and complexity, peaking in the heaven of chemical accuracy. Meanwhile, extensions[72] of the original scheme and classifications from a more implementational point of view[73] have also been proposed.

Similarly to the XC hole, approximations to the XC functional are usually separated into an exchange and a correlation functional E_x and E_c, respectively

$$E_{xc}\left[\rho\right] = E_x\left[\rho\right] + E_c\left[\rho\right] \ . \tag{2.54}$$

Conveniently, these functionals are either expressed as integrals of the energy density $e_{x/c}$ or the energy density per particle $\epsilon_{x/c}$ multiplied by the electron density

$$E_{x/c} = \int \rho\left(\mathbf{r}\right) \epsilon_{x/c}\left(\mathbf{r}\right) \mathrm{d}\mathbf{r} = \int e_{x/c}\left(\mathbf{r}\right) \mathrm{d}\mathbf{r} \ . \tag{2.55}$$

In the case of the exchange functional, it is known from exact orbital exchange (2.40) that only electrons with same spin interact with each other, so that E_x can be expressed as a

functional of ρ_α and ρ_β that can be split into separate spin functionals

$$E_x\left[\rho_\alpha, \rho_\beta\right] = E_{x,\alpha}\left[\rho_\alpha\right] + E_{x,\beta}\left[\rho_\beta\right] \ . \tag{2.56}$$

The link between the exchange functional depending on the total density $E_x\left[\rho\right]$ and $E_x\left[\rho_\alpha, \rho_\beta\right]$ is given by the spin scaling relation

$$E_x\left[\rho_\alpha, \rho_\beta\right] = \frac{1}{2}\left\{E_x\left[2\rho_\alpha\right] + E_x\left[2\rho_\beta\right]\right\} \ . \tag{2.57}$$

Due to this spin scaling relation, notations of the exchange functional as $E_x\left[\rho\right]$ and $E_x\left[\rho_\alpha, \rho_\beta\right]$ are equivalent, and both are in common use in the literature.[62] In the case of the correlation functional, the predominant contribution usually stems from the interaction of spin densities with opposite spin. The correlation functional can thus be equivalently expressed as functional of the spin densities $E_c\left[\rho_\alpha, \rho_\beta\right]$ or as functional of the total electron density and the spin polarization $E_c\left[\rho, \zeta\right]$ with

$$\zeta\left(\mathbf{r}\right) = \frac{\rho_\alpha\left(\mathbf{r}\right) - \rho_\beta\left(\mathbf{r}\right)}{\rho_\alpha\left(\mathbf{r}\right) + \rho_\beta\left(\mathbf{r}\right)} \ . \tag{2.58}$$

Throughout this work, exchange and correlation are denoted as spin-resolved functionals $E_x\left[\rho_\alpha, \rho_\beta\right]$ and $E_c\left[\rho_\alpha, \rho_\beta\right]$, respectively. Consistent to the subject of the present work, approximate exchange functionals are in the focus of the discussion.

The most basic approximation, which represents the first rung on the Jacob's Ladder, is the local-density approximation (LDA), or local-spin-density approximation (LSDA)[61] in the spin-unrestricted case. As model system, the three-dimensional uniform electron gas (UEG), i.e. a system with constant electron density and a homogeneously distributed positive background charge to ensure neutrality, is employed. The exchange functional for the UEG, which is also known as Slater-Dirac exchange, can be derived exactly and is given by[52,74,75]

$$E_{x,\sigma}^{LDA} = -\frac{3}{2}\left(\frac{3}{4\pi}\right)^{1/3}\int \rho_\sigma^{4/3}\left(\mathbf{r}\right)\mathrm{d}\mathbf{r} \ . \tag{2.59}$$

In contrast, correlation functionals on the basis of the UEG, e.g. the functionals of Vosko, Wilk and Nusair (VWN[76]) and Perdew and Wang (PW92[77]) as the most popular ones, could be only obtained by fitting analytic expressions to accurate reference data, e.g. quantum Monte Carlo results.[78] The common characteristic of all LDA functionals, either exchange or correlation, is the sole dependence on the electron density ρ, or the spin

densities ρ_α and ρ_β in the spin-unrestricted case. Since the LDA bases on the UEG, it works best for systems with an approximately homogeneously distributed electron density, as e.g. simple metalic solids as sodium.[79] Nevertheless, even for inhomogeneous systems as atoms and molecules, the LDA shows a reasonable behavior,[61] which could be attributed to a correct normalization of the XC hole,[58] a negatively bound Fermi hole with a correct on-top value[62] and the fact that only the spherically averaged XC hole, which is reasonably well described by LDA,[63] enters the XC energy. Furthermore, the Coulomb hole obeys the cusp condition, and the exchange functional (2.59) the correct homogeneous coordinate scaling.[80] On the other hand, LDA correlation functionals do not show the exact homogeneous coordinate scaling,[81] and the exchange functional (2.59) does not cancel the spurious self-interaction of electrons (cf. Sec. 2.1.3). Although the LDA is a large improvement over the HF method,[62] with errors for the thermochemical G2/97[82] test set being almost halved, it shows a systematic strong overbinding for molecules,[83] limiting the applicability of LDA for chemical problems.

A straightforward extension of the LDA is the gradient expansion approximation[84] (GEA), which introduces a Taylor expansion of the XC energy in terms of the density gradient, thus taking into account that atoms and molecules are not well represented by the UEG. For the exchange functional, the second-order gradient expansion, simply fixed by dimensional analysis,[85] is given by

$$E_{x,\sigma}^{GEA} = E_{x,\sigma}^{LDA} - \beta \sum_{\sigma} \frac{\gamma_{\sigma\sigma}(\mathbf{r})}{\rho_\sigma^{4/3}(\mathbf{r})} \tag{2.60}$$

with the square of the density gradient

$$\gamma_{\sigma\varsigma}(\mathbf{r}) = \nabla^{\mathrm{T}} \rho_\sigma(\mathbf{r}) \nabla \rho_\varsigma(\mathbf{r}) \ . \tag{2.61}$$

In homogeneous regions, i.e. regions with a vanishing density gradient ($\nabla\rho_\sigma(\mathbf{r}) = 0$), (2.60) correctly reduces to the exact homogeneous limit, i.e. Slater-Dirac exchange. The expansion parameter β can be either determined empirically[85] or deduced from the gradient expansion of the Fermi hole.[86] To second order, the expansion of the spherically averaged spin-resolved Fermi hole is given by

$$\langle \rho_{x,\sigma}(\mathbf{r}_1, \mathbf{r}_2) \rangle = -\rho_\sigma(\mathbf{r}_1) - \frac{1}{6}\left[\nabla^{\mathrm{T}}\nabla\rho_\sigma(\mathbf{r}_1) - 4\tau_\sigma(\mathbf{r}_1) + \frac{1}{2}\frac{\gamma_{\sigma\sigma}(\mathbf{r}_1)}{\rho_\sigma(\mathbf{r}_1)}\right] |\mathbf{r}_1 - \mathbf{r}_2| \ , \tag{2.62}$$

where

$$\tau_\sigma(\mathbf{r}) = \frac{1}{2}\sum_{pq} D^\sigma_{pq} \nabla^{\mathrm{T}} \varphi^*_{p,\sigma}(\mathbf{r})\, \nabla \varphi_{q,\sigma}(\mathbf{r}) \tag{2.63}$$

denotes the kinetic energy density. Substitution of τ by a gradient expansion[87] with respect to the electron density and subsequent partial integration leads to the expression for the GEA exchange (2.60) with $\beta = 0.00293$, which fits empirical findings fairly well.[62,85,88] Obviously, the GEA Fermi hole constitutes the exact on-top value. Nevertheless, it violates the normalization (2.50) and the negativity condition, which have been found to be crucial for the reasonable performance of the LDA.[64] Furthermore, the GEA exchange potential diverges in small density regions, as is the case in the exponential tails of finite systems.[85] Hence, results for real systems are typically worsened with respect to the LDA.

In order to restore the exact hole constraints violated by the GEA, various approaches, that are collectively known as generalized gradient approximation (GGA), have been proposed. All of them have in common that they only depend on the spin densities and their gradients. Two of the first approaches were introduced by Becke[89] and Perdew.[65,90] While Becke considered a model for the limit of large density gradients to introduce correction terms via interpolation, Perdew used cut-off functions to restore the exact hole constraints and refitted the functional to an analytical functional form. Simpler approaches of Becke (B86[91] and B88[92]) and Perdew *et al.* (PBE[93]) utilize a damping function $F(s_\sigma)$ to ensure the exact hole properties. Based on the reduced spin density gradient

$$s_\sigma(\mathbf{r}) = \frac{1}{k}\frac{\gamma^{1/2}_{\sigma\sigma}(\mathbf{r})}{\rho^{4/3}_\sigma(\mathbf{r})}\,, \tag{2.64}$$

with $k = 2\left(6\pi^2\right)^{1/3} \approx 7.79555$, the latter functionals can be expressed generally (although differently denoted in the original works) as

$$E^{GGA}_{x,\sigma} = E^{LDA}_{x,\sigma} - \int \rho^{4/3}_\sigma(\mathbf{r})\, s^2_\sigma(\mathbf{r})\, F(s_\sigma)\, \mathrm{d}\mathbf{r}\,, \tag{2.65}$$

where the damping functions for the two most popular GGA exchange functionals B88 and PBE are given by

$$F^{B88}\left(s_\sigma\right) = \frac{\beta k^2}{1 + 6\beta k s_\sigma\left(\mathbf{r}\right) \operatorname{asinh}\left(k s_\sigma\left(\mathbf{r}\right)\right)} \tag{2.66}$$

and

$$F^{PBE}\left(s_\sigma\right) = \frac{3}{2}\left(\frac{3}{4\pi}\right)^{1/3} \cdot \frac{\kappa\mu}{\kappa + \mu s_\sigma^2\left(\mathbf{r}\right)} \tag{2.67}$$

respectively. Note that, for a constant damping function, (2.65) simply reduces to GEA exchange. For the determination of the free parameters, i.e. β for B88 as well as κ and μ for PBE, Becke and Perdew followed two different philosophies. While Perdew fixed the parameters with respect to theoretical constraints such as the Lieb-Oxford bound,[93,94] Becke employed a fit to atomic exchange energies. Functionals of other authors, e.g. the HCTH type functionals[95,96] of Handy and co-workers, which use higher powers of the reduced spin density gradient and thus include more parameters, are optimized with respect to molecular test sets. Despite their formal difference, both approaches consider the underlying physics and lead to adequate parametrizations. Nevertheless, Engel *et al.*[97] could show that GGA exchange functionals, in general, are not able to provide simultaneously the correct asymptotic behavior of the exchange energy density and the exchange potential.

Similarly to the exchange functionals, various GGA correlation functionals have also been proposed, predominantly by Perdew and co-workers. This includes Perdew's correlation functional from 1986 (P86[98]), which is an extension of the one by Langreth and Mehl,[99] the PW91 correlation functional[100] as well as it's successor PBE.[93] For their construction, exact constraints as, e.g., the correct behavior in the limits of a slowly or rapidly varying density and uniform coordinate scaling were used. The famous correlation functional of Lee, Yang and Parr (LYP[101,102]) is based on the Colle-Salvetti[103] model for the helium atom.

Due to the inclusion of the density gradient, GEA and GGA functionals contain additional information beyond locality. This is in contrast to the LDA, which considers only purely local effects. Nevertheless, GGA and GEA functionals are not delocalized like exact orbital exchange, i.e. corresponding energy densities at a given point in space depend solely on the quantities evaluated at this point, and are thus usally called semi-local functionals. Functionals at the GEA or GGA level represent the second rung on the Jacob's Ladder.

As can be seen easily from the second-order gradient expansion of the spherically averaged exchange hole (2.62), the gradient expansion of the XC energy does not only depend on the density gradient but also on further quantities such as the Laplacian of the density $\nabla^{\mathrm{T}}\nabla\rho$ and the kinetic energy density τ. Functionals that include at least one of these two quantities, for either exchange or correlation, are called meta-GGAs, thus constituting the third rung in the categorization scheme of Perdew and Schmidt. Since the kinetic energy density depends only implicitly on the electron density via the orbitals, meta-GGAs are usually no explicit density functionals anymore. Nevertheless, they are usually considered as semi-local functionals, too, because the dependence on the orbitals remains semi-local. Recent meta-GGA functionals also include further quantities such as the density overlap regions indicator (DORI),[104] which considers second derivatives of the electron density beyond the Laplacian. With some exceptions, the construction of meta-GGAs generally follows the concepts and philosophies of the GGA construction, presented above, and will be not discussed in detail. Due to the higher flexibility, it is possible to satisfy more physical constraints. For example, one-spin orbital regions can be identified using the ratio between the von Weizsäcker kinetic energy density τ_W[87] and the kinetic energy density τ

$$t_\sigma(\mathbf{r}) = \frac{\tau_{W,\sigma}(\mathbf{r})}{\tau_\sigma(\mathbf{r})} = \frac{1}{8}\frac{\gamma_{\sigma\sigma}(\mathbf{r})}{\tau_\sigma(\mathbf{r})\,\rho_\sigma(\mathbf{r})}\,, \tag{2.68}$$

thus allowing for self-correlation-free functionals and a correct exchange energy for one-electron systems. Amongst the numerous different functionals, there are again some of Perdew and co-workers, namely PKZB,[105] its more advanced succesor TPSS[106,107] as well as MVS[108] and SCAN.[109] Besides some models for strong correlation effects,[110,111] Becke also proposed new approaches for meta-GGA functionals,[112] often as part of hybrid functionals.[69,113] Only to mention a few, further functionals in common use are B97D,[114] τ-HCTH[115] of Handy and co-workers as well as the highly parametrized semi-local functionals of Truhlar and co-workers.[116,117] Also, the Becke-Roussel[118] model for the exchange hole, which is exact for the hydrogen atom, can be regarded as meta-GGA functional, although free parameters in the model have to be determined in an additional optimization procedure, and the homogeneous limit is violated.

In comparison to the LDA, GGA and meta-GGA functionals represent a large improvement. Especially, errors for common atomization energy and reaction barrier height test sets are significantly lowered below 10 kcal/mol.[62] Furthermore, the performance for transition metal complexes is also improved.[119] Nevertheless, even for meta-GGA functionals, the spurious self-interaction error in the exchange contribution to the XC

functional remains and, despite the improvement, calculated atomization energies do not reach chemical accuracy, i.e. 1 kcal/mol.

The next class of functionals on the Jacob's Ladder are explicitly occupied-orbital-dependent functionals, which basically means the inclusion of exact orbital exchange (2.40) and a compatible correlation functional. In global hybrid functionals, first proposed by Becke[120] on the basis of the adiabatic connection theorem (cf. Sec. 2.2.3), the admixture of exact orbital exchange and a local or semi-local exchange functional E_x^{sl} is regulated by a constant mixing parameter c_x leading to the exchange functional

$$E_{x,\sigma}^{GH} = c_x E_{x,\sigma}^{ex} + (1 - c_x)\, E_{x,\sigma}^{sl} \,. \tag{2.69}$$

In the original work,[120] Becke assumed, in a first approximation, a linear interpolation between the interacting and non-interacting reference system, resulting in the half-and-half theory, which fixes c_x to 0.5. While in the originally proposed half-and-half functional, based on LDA exchange and correlation, c_x is also applied as prefactor to the local correlation functional, in GGA-based follow-ups, such as the BHLYP functional, c_x is only used in the exchange functional. A quantification of c_x by Perdew *et al.* on the basis of the AC with additional considerations about perturbation theory gave a mixing parameter of $c_x = 0.25$,[121] which better fits empirical findings[113] than the value of Becke. Nevertheless, also the latter approach and related schemes[122] rely mainly on empirical observations. Since no additional physical constraints can be satisfied by partial admixture of exact orbital exchange, empirical determination of c_x becomes unavoidable.[123] Representatives for simple global hybrids based on GGA or meta-GGA functionals are TPSSh,[124] B95[113] and PBE0.[125] While the latter functional is constructed with the value $c_x = 0.25$ of Perdew *et al.*, the former two functionals rely on an optimization with respect to thermochemical properties as, e.g., atomization energies, barrier heights, electron affinities or ionization potentials.

A popular extension of the global hybrid scheme (2.69) is given by the three-parameter approach introduced by Becke[126]

$$E_{xc}^{B3} = \sum_{\sigma} \left\{ E_{x,\sigma}^{LDA} + c_x \left(E_{x,\sigma}^{ex} - E_{x,\sigma}^{LDA} \right) + c_{nlx} \Delta E_{x,\sigma}^{GGA} \right\} + E_c^{LDA} + c_{nlc} \Delta E_c^{GGA} \,. \tag{2.70}$$

Originally, this so-called B3 scheme was developed in combination with B88 exchange and PW91 correlation, resulting in the thermochemically optimized parameters $c_x = 0.2$, $c_{nlx} = 0.72$ and $c_{nlc} = 0.81$. Nevertheless, it turned out that the same parameter set combined with the LYP functional gives comparable performance, leading to the famous

B3LYP functional.[127] Other popular global hybrid functionals, such as the hybrid variant of the τ-HCTH functional,[115] its descendant BMK,[128] and the Minnesota type functionals of Truhlar and co-workers,[129–132] incorporate many more empirical parameters than the B3 scheme.

While the admixture of exact orbital exchange mitigates the problem of spurious Coulomb self-interaction, only a mixing parameter of $c_x = 1.0$ provides a complete correction. Furthermore, full exact orbital exchange also ensures the correct r^{-1} asymptotic behavior of the potential. On the other hand, 100% exact orbital exchange is less favorable for the description of bonding regions, where semi-local exchange functionals mimicking a certain amount of static correlation are the better choice. Additionally, the exact-exchange Fermi hole is fully delocalized, while the semi-local Coulomb hole is not, providing a less favorable error compensation for the complete XC hole in stretched-bond situations. Hence, only a few, either highly parametrized[131] or rather complicated[133,134] occupied-orbital-dependent functionals use 100% exact orbital exchange everywhere.

Another way of managing the balance between self-interaction correction and static correlation through semi-local exchange is provided by orbital-specific global hybrid functionals,[135,136] which apply different hybrid schemes for different types of orbitals. For example, a distinction between core, valence and Rydberg orbitals lead to the orbital-specific variants of the B3LYP functional of Nakai and co-workers.[137,138] However, such functionals lack invariance to orbital transformations and are not size consistent.

A more popular extension of global hybrids are the so-called range-separated (RS) hybrid functionals.[13,139–142] As the basic step, the electron interaction operator is decomposed with respect to the interelectronic separation coordinate $|\mathbf{r}_1 - \mathbf{r}_2|$, usually choosing the standard error function as splitting operator

$$\frac{1}{|\mathbf{r}_1 - \mathbf{r}_2|} = \frac{1 - \operatorname{erf}(\mu \cdot |\mathbf{r}_1 - \mathbf{r}_2|)}{|\mathbf{r}_1 - \mathbf{r}_2|} + \frac{\operatorname{erf}(\mu \cdot |\mathbf{r}_1 - \mathbf{r}_2|)}{|\mathbf{r}_1 - \mathbf{r}_2|} \,. \tag{2.71}$$

The first and second term on the right-hand side of Eq. (2.71) represent the short- and long-range part of the electron interaction, respectively. The transition between both parts is regulated by the RS parameter μ. In the most simple RS hybrid scheme,[142] short-range exchange is described by a semi-local functional, thus considering static as well as dynamic electron correlation in bonding regions, whereas exact orbital exchange is used in the long-range to ensure the correct asymptotic r^{-1} behavior and to avoid spurious self-interaction in one-electron regions. More advanced RS hybrids[143,144] combine the RS scheme with the global hybrid scheme (2.69), leading to an additional inclusion of short-range exact orbital exchange needed, e.g., for the description of core states. Functionals that use

short-range exact orbital exchange without applying long-range exact exchange[145,146] are usually referred to as screened hybrid functionals. Subsequent extensions proposed, e.g., an increased number of RS parameters,[147] a modified RS scheme,[148] orbital specific RS parameters[149] or non-empirical tuning of the RS parameter.[150–152] As for global hybrid functionals, highly parametrized functionals were also developed.[144,153–155]

The inclusion of exact-exchange contributions, either in global or RS hybrids, to the XC functional has led to a significant improvement over conventional semi-local functionals, with mean absolute errors being below 5 kcal/mol for common thermochemical test sets.[62] More advanced functionals achieve even better results with mean absolute errors around 2-3 kcal/mol and may reach chemical accuracy for selected test sets.[153] However, in comparison to semi-local functionals, calculations using occupied-orbital-dependent XC functionals are significantly slower due to the inclusion of exact orbital exchange, in particular for many applications with periodic boundary conditions. Computation times are comparable to those of the HF method, but include correlation effects, which in wavefunction theory can be considered only using expensive correlation methods such as coupled-cluster theory. One important part, which is still missing in hybrid functionals, is long-range correlation as, e.g., dispersion. A pragmatic solution to retain the good ratio between computational cost and accuracy of hybrid functionals is the *a posteriori* addition of an empirical force-field-like dispersion correction, as done by Grimme.[156] But also several density-based approaches have been developed.[157–163]

The last step on Jacob's Ladder finally allows the inclusion of unoccupied orbitals in the XC functional, which mainly concerns exact correlation contributions of wavefunction theory and thus the correlation functional. Hence, also long-range correlation effects are considered explicitly. The simplest approach is the partial addition of correlation determined by second-order perturbation theory, equivalent to MP2. Popular representatives of these so-called double-hybrid functionals are B2PLYP[164,165] and B2GPPLYP.[166] The inclusion of electron correlation within the random phase approximation (RPA)[167–179] and within the so-called *ab initio* DFT[180] framework is also in active development. Nevertheless, computational costs in all cases significantly exceed those of hybrid functionals, in particular when looking beyond single-point energies.

2.3. Local Hybrid Functionals

2.3.1. Functional Form

A relatively recent class of exchange-correlation functionals on the fourth rung of the Jacob's Ladder of density functional approximations, which is the main topic of the present work, are local hybrid functionals (local hybrids, LHs).[15,181] In contrast to global hybrid functionals, local hybrids feature a local real-space-dependent admixture of exact exchange managed by the local mixing function (LMF) g_σ. This has to be also contrasted to range-separated hybrid functionals, which enable a variable exact-exchange admixture depending on the interelectronic separation. Local hybrid functionals are thus another natural extension of the common global hybrid scheme (2.69), exhibiting the exchange-correlation energy functional (in its most general formulation)

$$E_{xc}^{LH} = \sum_\sigma \int g_\sigma(\mathbf{r}) \cdot e_{x,\sigma}^{ex}(\mathbf{r})\mathrm{d}\mathbf{r} + \sum_\sigma \int [1 - g_\sigma(\mathbf{r})] \cdot \left[e_{x,\sigma}^{sl}(\mathbf{r}) + G_\sigma(\mathbf{r})\right] \mathrm{d}\mathbf{r} + E_c^{sl} \ , \quad (2.72)$$

where $e_{x,\sigma}^{sl}$ and E_c^{sl} denote a semi-local exchange energy density and correlation functional, respectively, while G_σ is a calibration function (CF, see Sec. 2.3.3). The exact exchange energy density in its conventional gauge[21] is given by

$$e_{x,\sigma}^{ex}(\mathbf{r}) = -\frac{1}{2} \sum_{pqrs} D_{pq}^\sigma D_{rs}^\sigma \int \frac{\varphi_{p,\sigma}^*(\mathbf{r})\varphi_{s,\sigma}(\mathbf{r})\varphi_{r,\sigma}^*(\mathbf{r}')\varphi_{q,\sigma}(\mathbf{r}')}{|\mathbf{r} - \mathbf{r}'|}\mathrm{d}\mathbf{r}' \ . \quad (2.73)$$

While the LMF enables a variable amount of exact exchange in different regions of real space, leading to a higher flexibility in comparison to global hybrid functionals, local mixing of exchange in Eq. (2.72) requires the mixing of exchange energy densities rather than integrated exchange energies. Due to an ambiguity in the definition of energy densities in general,[16] this local mixing thus gives rise to the so-called gauge problem, which will be discussed in detail in Sec. 2.3.3.

As for global hybrid functionals,[71,123] the local hybrid XC functional (2.72) can be reformulated in terms of a non-dynamical and dynamical correlation correction to exact orbital exchange[182,183]

$$E_{xc}^{LH} = E_x^{ex} + E_{ndc}^{LH} + E_c^{sl} \ , \quad (2.74)$$

where the local hybrid non-dynamical correlation functional is defined as

$$E_{ndc}^{LH} = \sum_{\sigma} \int [1 - g_\sigma(\mathbf{r})] \cdot \left[e_{x,\sigma}^{sl}(\mathbf{r}) - e_{x,\sigma}^{ex}(\mathbf{r}) + G_\sigma(\mathbf{r}) \right] \mathrm{d}\mathbf{r} \; . \tag{2.75}$$

While local hybrid dynamical correlation is simply determined by a semi-local correlation functional, the exchange energy density difference as well as the LMF and the CF enter the local hybrid non-dynamical correlation functional (2.75). The latter two ingredients represent exclusive building blocks of local hybrid functionals and thus will be discussed in detail in the following sections.

2.3.2. Local Mixing Functions

While the idea of mixing exchange energy densities had been in discussion for some time,[181] it took some years before the first explicit forms for local mixing functions were introduced.[15] Since then, a considerable variety of LMFs has been suggested.

Obviously, as they determine the amount of exact-exchange mixing, all LMFs have to satisfy the necessary condition $0 \leq g_\sigma \leq 1$, as it is also the case for the mixing constant c_x in global hybrid functionals. Besides, other properties of the LMF can be anticipated by identifying exchange-dominated regions,[183] in which exact exchange should be employed to reduce erroneous self-interaction of the semi-local exchange functional, i.e. one-electron and non-uniform high density regions as well as in the rapidly varying limit. In nearly homogeneous regions, as e.g. chemical bonds, vanishing exact exchange contributions should be used to benefit from mimicked static correlation contributions of semi-local functionals.

As a first approach, Jaramillo *et al.*[15] thus proposed the ratio between the von Weizsäcker kinetic energy density τ_W and the kinetic energy density τ, known as inhomogeneity parameter t_σ in the framework of meta-GGA functionals (cf. Eq. (2.68)). While satisfying the abovementioned properties and thus improving results for model systems, atomization energies of the G2 test set are worsened significantly in comparison to common global hybrid functionals (this LMF had been used initially with GGA exchange-energy densities).

Hence, in continuing attempts, empirical parameters have been introduced to improve the performance of this simple LMF. While the consideration of different powers of t_σ[184] did not improve the performance significantly, the introduction of a linear scaling param-

eter, leading to the so-called t-LMF[185]

$$g_\sigma(\mathbf{r}) = a \cdot t_\sigma(\mathbf{r}) = a \cdot \frac{1}{8} \frac{\gamma_{\sigma\sigma}(\mathbf{r})}{\tau_\sigma(\mathbf{r})\,\rho_\sigma(\mathbf{r})} \,, \tag{2.76}$$

led to atomization energies comparable with those of global hybrid functionals, if combined with LDA exchange.[17] Note that the t-LMF features only a fraction (depending on the parameter a) of exact exchange in its upper limit and thus violates the physical constraint for one-electron regions described above. Improved results can thus be partially attributed to some kind of error compensation, as is the case in many global hybrid functionals. Besides, it is noteworthy that, in contrast to the original approach,[15] only simple LDA exchange and correlation are employed. Better performance in comparison to GGA-based local hybrids could be attributed to a less pronounced gauge problem in the case of Slater-Dirac exchange.[182] Hence, many subsequently developed local hybrids are also based on LDA exchange.

Besides the meta-GGA iso-orbital indicator t_σ, other inhomogeneity parameters have also been investigated as ingredients of simple local mixing functions. This includes LMFs based on the reduced spin density gradient (2.64). In contrast to t_σ, s_σ does not exhibit values between 0 and 1. While being always positive, s_σ tends to infinity in low-density regions. Hence, a suitable mapping had to be introduced for use as ingredient of a LMF. Amongst others,[186] an error function has been proposed, giving the LMF

$$g_\sigma(\mathbf{r}) = \mathrm{erf}\left(\beta \cdot s_\sigma(\mathbf{r})\right) \,, \tag{2.77}$$

which will be labeled as s-LMF in the present work. Note that in the original work[186] a slightly different definition of s_σ was used, thus changing the definition of the empirical parameter β. The same error function mapping has been employed in a recently proposed LMF[187] (labeled as z-LMF) based on the parallel spin correlation length

$$z_{\sigma\sigma}(\mathbf{r}) = c_{\sigma\sigma} \cdot \left|\epsilon_{x,\sigma}(\mathbf{r})\right|^{-1} \tag{2.78}$$

introduced by Becke.[112] Both, the s-LMF and z-LMF feature the correct behavior in one-electron regions, i.e. 100% exact orbital exchange. Nevertheless, in high-density regions, e.g. at atomic cores, only low exact-exchange admixture is exhibited, which is in contradiction with the constraint mentioned above. Another LMF developed by de Silva

et al.[188] considers the function

$$\Theta_\sigma(\mathbf{r}) = \frac{\left[\nabla\left(\frac{\nabla\rho_\sigma(\mathbf{r})}{\rho_\sigma(\mathbf{r})}\right)^2\right]^2}{\left(\frac{\nabla\rho_\sigma(\mathbf{r})}{\rho_\sigma(\mathbf{r})}\right)^6} . \tag{2.79}$$

of the DORI[189] as underlying inhomogeneity parameter. A suitable mapping and introduction of an empirical parameter then resulted in the local mixing function (labeled here as Θ-LMF)

$$g_\sigma(\mathbf{r}) = \frac{1}{1 + a \cdot \Theta_\sigma(\mathbf{r})} . \tag{2.80}$$

Like the t-LMF with $a = 1$, the Θ-LMF shows the correct behavior for one-electron, homogeneous and high density regions. In contrast to the iso-orbital indicator t_σ,[190] a reasonable behavior is even guaranteed in the vicinity of orbital nodal planes, since no explicitly orbital-dependent quantities like the kinetic energy density are employed.[188] Combined local and global hybrid mixing schemes, which can be regarded as local hybrids employing a LMF providing a partial constant amount of exact exchange mixing, are also under development.[191]

The original formulation of local hybrid functionals (2.72) suggests that the LMF g_σ should depend only on spin quantities ('spin-channel LMFs'), i.e. the LMF scaling the σ part of exchange depends only on σ quantities. To satisfy the spin scaling relation (2.57), the reformulation (2.74) in terms of non-dynamical correlation formally allows also a consideration of quantities of opposite spin σ' (indicated by prime), since correlation does not have to satisfy the spin scaling relation (2.57). Additional cross-terms arising in the XC functional in comparison to spin-channel LMFs can be thus interpreted as opposite-spin non-dynamical correlation contribution. Accordingly, local mixing functions explicitly considering spin polarization (2.58) have been proposed.[182,192] Another, more straightforward and simple approach for the inclusion of opposite-spin quantities is the concept of so-called 'common LMFs'.[18] Here, spin quantities of spin-channel LMFs are replaced by their total counterparts, e.g. ρ_σ is substituted by $\rho = \rho_\sigma + \rho_{\sigma'}$. For example, this results in the common t-LMF

$$g_\sigma(\mathbf{r}) = a \cdot t(\mathbf{r}) = a \cdot \frac{1}{8}\frac{\gamma_{\sigma\sigma}(\mathbf{r}) + 2\gamma_{\sigma\sigma'}(\mathbf{r}) + \gamma_{\sigma'\sigma'}(\mathbf{r})}{[\tau_\sigma(\mathbf{r}) + \tau_{\sigma'}(\mathbf{r})] \cdot [\rho_\sigma(\mathbf{r}) + \rho_{\sigma'}(\mathbf{r})]} . \tag{2.81}$$

For the construction of a 'common' version of the spin-channel s-LMF (2.77), the reduced spin density gradient (2.64) has to be replaced by the reduced density gradient

$$s(\mathbf{r}) \equiv s_\sigma(\mathbf{r}) = \frac{1}{k'} \frac{\left[\gamma_{\sigma\sigma}(\mathbf{r}) + 2\gamma_{\sigma\sigma'}(\mathbf{r}) + \gamma_{\sigma'\sigma'}(\mathbf{r})\right]^{1/2}}{\left[\rho_\sigma(\mathbf{r}) + \rho_{\sigma'}(\mathbf{r})\right]^{4/3}} , \tag{2.82}$$

with $k' = 2\left(3\pi^2\right)^{1/3} \approx 6.18734$, to ensure that the spin-channel LMF and its 'common' LMF counterpart coincide in the spin-restricted case. While the additional dependence on spin polarization improved atomization energies and slightly deteriorated the performance for reaction barrier heigths,[182] common LMFs in general show a significant improvement for both, but especially for barrier heights, which is partially related to larger exact-exchange admixtures compared to corresponding spin-channel LMFs.[18]

A highly sophisticated approach for the mixing of exact and semi-local exchange energy densities, based on the TPSS meta-GGA,[106,107] is the one of Perdew *et al.*.[183] In their PSTS functional, so-called normal and abnormal regions are defined on the basis of the considerations presented above. Utilizing sophisticated inhomogeneity parameters based on exchange-correlation energy densities, the TPSS Görling-Levy high-density limit,[193] and the exact-exchange energy density in the TPSS gauge (details see Sec. 2.3.3), allowed the identification of these regions and so the construction of a LMF. Together with a small set of empirical parameters optimized against the G2 test set, a performance comparable to that of global hybrid functionals could be achieved for atomization energies, while barrier heights are improved significantly.

Further approaches established a direct connection between semi-local functionals and the local mixing function. For example, Arbuznikov *et al.*[68] derived a scheme based on a local version of the adiabatic connection, showing a direct link between the semi-local correlation functional and the LMF. While these AC type LMFs can be obtained non-empirically from any semi-local correlation functional (originally done for PW91 and PBE correlation), reasonable performance could be only achieved after the introduction of an empirical downshift. A local AC scheme for the construction of a local hybrid has also been used in more recent work.[194] Local mixing functions of Janesko *et al.*,[195,196] based on density matrix similarity metrics, on the other hand, use a relation of the LMF to the underlying exchange functional.

While various approaches for the derivation of local mixing functions have been developed during the last years, it crystallized that the performance of both, LMFs based on simple inhomogeneity parameters as well as more complex LMFs established on theoretical concepts, strongly rely on the introduction of empirical parameters, usually determined

with respect to atomization energy and barrier height test sets, as is the case for global hybrid functionals. Similarly, it is fair to state that a reasonable parameter set and thus empiricism is unavoidable to obtain practically useful LMFs and thus local hybrid functionals.

In the context of local mixing functions, a specialized correlation functional developed by Arbuznikov *et al.*[18] should be mentioned in detail due to its close relation to the local hybrid approach. While the LMF in local hybrid functionals scales locally the amount of exact orbital exchange, the correlation functional is not affected. On the other hand, the reasonable performance of semi-local functionals strongly relies on an error compensation between exchange and correlation functional. Within the local hybrid scheme, this advantageous error compensation is now locally mitigated by the LMF. In detail, in regions of 100% exact exchange, artefacts, e.g. erroneous one-electron self-correlation, of the correlation functional cannot be compensated by the semi-local exchange functional. Accordingly, Arbuznikov *et al.*[18] proposed a local removal of short-range (SR) correlation in these regions to reduce self-correlation, leading to the self-interaction-corrected (sic) PW92 correlation functional

$$E_c^{sicPW92}[\rho_\alpha(\mathbf{r}),\rho_\beta(\mathbf{r})] = E_c^{PW92}[\rho_\alpha(\mathbf{r}),\rho_\beta(\mathbf{r})] - \lambda \sum_\sigma \int t_\sigma(\mathbf{r}) \cdot e_c^{srPW92}[\rho_\sigma(\mathbf{r}),0]\mathrm{d}\mathbf{r} \ , \tag{2.83}$$

with e_c^{srPW92} being the SR part of the PW92 correlation energy density and λ an additional empirical parameter. The good performance of this approach for thermochemistry and barriers in combination with a common t-LMF can be related to a more efficient error compensation featured by the partial removal of self-correlation, which is similar to the mitigation of the self-interaction error in the exchange functional. In combination with the t-LMF, self-interaction-corrected PW92 correlation generally allows larger prefactors a (cf. Eq. (2.76)).

2.3.3. The Gauge Problem

As mentioned in Sec. 2.3.1, local hybrid functionals feature a local admixture of exchange energy densities rather than exchange energies as in global hybrid functionals. Unfortunately, energy densities, in contrast to the integrated energies, are not unambiguously defined.[16,181] That is, a so-called calibration function (CF) G_σ satisfying the condition

$$\int G_\sigma\left(\mathbf{r}\right) \mathrm{d}\mathbf{r} = 0 \ , \tag{2.84}$$

can be added to any energy density without changing the integrated quantity. Usually, differing energy densities integrating to the same energy are considered as constituting different gauge origins (briefly referred as gauges). While unambiguous schemes for the extraction of energy densities from energies on the basis of the potential have been developed for the purpose of comparing different energy densities,[16] standard notations of usual exchange and correlation functionals do not follow this definition. Furthermore, the general ambiguity in the definition of XC energy densities remains. That is, although being unambiguously defined, it cannot be guaranteed that energy densities of different energy functionals exhibit the same gauge origin, whose definition is indeed also rather ambiguous. In the case of common exchange-correlation functionals, which do not consider a local mixing of energy densities, as e.g. semi-local and global hybrid functionals, the gauge origin of the underlying XC energy densities has no influence on the XC energy at all and can thus be chosen arbitrarily without changing the XC energy. Local hybrids including calibrated energy densites on the other hand exhibit the additional integral[197]

$$\int g_\sigma(\mathbf{r}) \cdot G_\sigma(\mathbf{r}) \, \mathrm{d}\mathbf{r} \neq 0 \,, \tag{2.85}$$

which in contrast to the integral over the CF itself (cf. Eq. (2.84)), is not zero in general. Since this additional energy contribution originally has been regarded as main obstacle for their development, the ambiguity of exchange energy densities in local hybrid functionals is often referred to as gauge problem. Note that the CF G_σ occuring in Eqs. (2.75) and (2.85) does not aim to guarantee the correct gauge for the semi-local and exact exchange energy density, e_x^{sl} and e_x^{ex}, respectively, but only corrects for their difference. That is, it aims to ensure the same gauge for both exchange energy densities. It is exactly this difference in the gauges of the mixed exchange energy densities that affects the local hybrid XC functional. Regarding the local hybrid formulation (2.75), the CF and thus the gauge problem can be regarded as part a proper description of non-dynamical correlation. On the other hand, the gauge origin of the total local hybrid XC energy density itself remains ambiguously defined.

While Eq. (2.84) fixes the fundamental property of calibration functions, it provides no distinct rule for their construction. One possible approach, employed by Tao *et al.*,[21] is the construction via the divergence of a vector field $\mathbf{W}_\sigma$

$$G_\sigma(\mathbf{r}) = \nabla^{\mathrm{T}} \cdot \mathbf{W}_\sigma(\mathbf{r}) \,, \tag{2.86}$$

where $\mathbf{W}_\sigma$ is constructed so that G_σ satisfies the most basic properties of exchange energy densities (since the CF may be considered as one of these), i.e. being totally symmetric, invariant with respect to unitary orbital transformations and origin-independent, as well as exhibiting proper coordinate scaling (uniform and/or non-uniform), finiteness everywhere and a sufficiently fast decay in asymptotic regions.[21,197] Accordingly, one particular form for such a vector field was proposed[21]

$$\mathbf{W}_\sigma(\mathbf{r}) = a \cdot \frac{\rho_\sigma(\mathbf{r}) \cdot \tilde{\epsilon}^4_{x,\sigma}(\mathbf{r})}{\tilde{\epsilon}^6_{x,\sigma}(\mathbf{r}) + 4c \cdot \rho^2_\sigma(\mathbf{r})} \cdot \left[\frac{\gamma_{\sigma\sigma}(\mathbf{r})}{\rho_\sigma(\mathbf{r}) \cdot \tau_\sigma(\mathbf{r})}\right]^b \cdot \nabla\tilde{\epsilon}_x(\mathbf{r}) \ , \tag{2.87}$$

with the negative exact-exchange energy density per particle

$$\tilde{\epsilon}_{x,\sigma}(\mathbf{r}) = -\frac{e^{ex}_{x,\sigma}(\mathbf{r})}{\rho_\sigma(\mathbf{r})} \tag{2.88}$$

and the three empirical parameters a, b and c. Another approach, proposed in the same work,[21] is the use of an exact-exchange energy density, obtained by a coordinate transformation of the exact-exchange hole.[198] Given the coordinate transformation parameter $0 \leq \omega \leq 1$, an ω-dependent exact-exchange energy density

$$e^{ex(\omega)}_{x,\sigma}(\mathbf{r}) = -\frac{1}{2}\sum_{pqrs} D^\sigma_{pq} D^\sigma_{rs} \int \frac{\varphi^*_{p,\sigma}(\mathbf{r}^\omega_1)\varphi_{s,\sigma}(\mathbf{r}^\omega_1)\varphi^*_{r,\sigma}(\mathbf{r}^\omega_2)\varphi_{q,\sigma}(\mathbf{r}^\omega_2)}{|\mathbf{u}|} \mathrm{d}\mathbf{u} \ , \tag{2.89}$$

with $\mathbf{r}^\omega_1 = \mathbf{r} + (\omega - 1)\,\mathbf{u}$ and $\mathbf{r}^\omega_2 = \mathbf{r} + \omega\mathbf{u}$ being auxilliary ω-dependent space variables, can be defined. Obviously, $e^{ex(\omega)}_{x,\sigma}(\mathbf{r})$ integrates to the exact-exchange energy (2.40) irrespective of ω. While $\omega = 1$ and $\omega = 0$ give the exact-exchange energy density in its conventional gauge (2.73), $\omega = 0.5$ represents the most localized exact-exchange hole.[198] The substitution of the exact-exchange energy density in the conventional gauge by its coordinate-transformed counterpart can be equivalently expressed as calibration function

$$G_\sigma(\mathbf{r}) = e^{ex}_{x,\sigma}(\mathbf{r}) - e^{ex(\omega)}_{x,\sigma}(\mathbf{r}) \tag{2.90}$$

within the usual local hybrid formulation (2.72). Both approaches have been evaluated in combination with the TPSS meta-GGA exchange functional. It was assumed that, in atoms with a non-degenerate electron configuration, the semi-local and the exact-exchange energy density should be close for every point in space, so that the free parameters of both calibration functions could be directly obtained by a fitting procedure with respect to energy densities. Although both approaches effectively reduced differences of the exchange energy densities, both the coordinate-transformed exchange energy density as well

as the proposed vector field (2.87) require the calculation of computationally expensive quantities, e.g. the gradient and the Laplacian of the exact-exchange energy density.

Another calibration function considering only semi-local quantities such as the electron density and its spatial derivatives, which is thus computationally much less expensive than the previous approaches, was proposed by Arbuznikov *et al.*.[197] Also constructed on the basis of the divergence of a vector field (2.86) under the consideration of basic properties of exchange energy densities (see above), the vector field

$$\mathbf{W}_\sigma(\mathbf{r}) = a \cdot F(s_\sigma) \cdot \frac{\nabla\rho_\sigma(\mathbf{r})}{\rho_\sigma^{1/3}(\mathbf{r})} \tag{2.91}$$

with the damping function

$$F(s_\sigma) = e^{-\beta \cdot s_\sigma(\mathbf{r})} \tag{2.92}$$

was proposed. Being directly optimized together with the LMF with respect to thermochemical test sets, after fixing the damping function parameter by considerations about non-dynamical correlation energies,[197] local hybrid functionals based on GGA exchange and correlation could be obtained, while without calibration LDA-based local hybrids show the best results. It could be shown in addition that these calibrated local hybrids effectively reduce the amount of erroneous non-dynamical correlation in Pauli-repulsion curves of noble-gas dimers in comparison to their uncalibrated counterparts. In combination with an empirical dispersion correction,[199] local hybrids being competitive to the best-performing global hybrid functionals for the large GMTKN30 test set could be obtained.[200–202]

2.4. Time-Dependent DFT

2.4.1. Runge-Gross Theorems

Based on the first Hohenberg-Kohn theorem, DFT as described in Sec. 2.2 constitutes a pure ground-state theory. However, since many chemically relevant problems concern excited states, which are thus usually not accessible within 'traditional' DFT, extensions to excited states have been proposed. Besides approaches like ΔSCF,[203,204] which is restricted to states giving stable solutions of the KS equations such as pseudo ground states separated by symmetry, and constricted variational DFT,[205,206] time-dependent

DFT (TDDFT)[1,207] has become the most popular scheme for the calculation of excited states within a density functional framework.

The basic equation to be solved in TDDFT is the time-dependent electronic Schrödinger equation (2.11). Instead of the time-dependent wavefunction, the quantum dynamics of the many-particle system are described by the time-dependent electron density

$$\rho\left(\mathbf{r},t\right) \equiv \rho\left(\mathbf{r}_1,t\right) = N \int \Psi^*\left(\mathbf{x}_1,\ldots,\mathbf{x}_N,t\right) \Psi\left(\mathbf{x}_1,\ldots,\mathbf{x}_N,t\right) \mathrm{d}s_1 \mathrm{d}\mathbf{x}_2 \ldots \mathrm{d}\mathbf{x}_N \; . \tag{2.93}$$

The formal legitimization of using the time-dependent electron density as basic descriptor was given 1984 by Runge and Gross.[208] They showed by *reductio ad absurdum* that two time-dependent electron densities arising from a common initial state under the influence of two time-dependent external potentials differing by more than a purely time-dependent function always differ, thus providing a one-to-one mapping between the time-dependent electron density and potential as well as the representability of the wavefunction as functional of the density. This first Runge-Gross theorem can be thus regarded as time-dependent analogue to the first Hohenberg-Kohn theorem.

While there exists no minimum principle for the time-dependent Schrödinger equation like for the time-independent case, several formulations of an action principle based on the quantum chemical action integral

$$A = \int_{t_0}^{t_1} \left\langle \Psi \left| \mathrm{i}\frac{\partial}{\partial t} - \hat{H}\left(\mathbf{r},\mathbf{R},t\right) \right| \Psi \right\rangle \mathrm{d}t \tag{2.94}$$

have been proposed, where t_0 and t_1 denote the limits of the considered time interval. Regarding the first Runge-Gross theorem, the action integral (2.94) can be then expressed as density functional

$$A\left[\rho\right] = B\left[\rho\right] - \int_{t_0}^{t_1} \left\langle \Psi \left| \hat{V}_{Ne}\left(\mathbf{r},\mathbf{R}\right) + \hat{V}_{ext}\left(t\right) \right| \Psi \right\rangle \mathrm{d}t \; , \tag{2.95}$$

where $B\left[\rho\right]$ is the universal functional

$$B\left[\rho\right] = \int_{t_0}^{t_1} \left\langle \Psi \left| \mathrm{i}\frac{\partial}{\partial t} - \hat{T}\left(\mathbf{r}\right) - \hat{V}_{ee}\left(\mathbf{r}\right) \right| \Psi \right\rangle \mathrm{d}t \; , \tag{2.96}$$

containing the operator for time evolution, the electronic kinetic energy and the electron-electron interaction, respectively. In their work of 1984,[208] Runge and Gross then pro-

posed the stationarity condition

$$\frac{\delta A\left[\rho\right]}{\delta\rho\left(\mathbf{r},t\right)}=0\ , \tag{2.97}$$

so that the exact time-dependent electron density represents a stationary point of the action integral. Nevertheless, it could be shown that in this definition the action integral leads to a paradox,[207,209,210] i.e., it cannot fulfill the symmetry property of second functional derivatives

$$\frac{\delta^2 A\left[\rho\right]}{\delta\rho\left(\mathbf{r},t\right)\delta\rho\left(\mathbf{r}',t'\right)}=\frac{\delta^2 A\left[\rho\right]}{\delta\rho\left(\mathbf{r}',t'\right)\delta\rho\left(\mathbf{r},t\right)} \tag{2.98}$$

and the causality requirement

$$\frac{\delta^2 A\left[\rho\right]}{\delta\rho\left(\mathbf{r},t\right)\delta\rho\left(\mathbf{r}',t'\right)}=\frac{\delta v\left(\mathbf{r},t\right)}{\delta\rho\left(\mathbf{r}',t'\right)}=0\ \ \text{, if } t<t' \tag{2.99}$$

simultaneously.[211] One solution to resolve this paradox proposed by van Leeuwen[209] introduces a reformulation of the action principle in terms of a Keldysh formalism. A more recent formulation of the action principle by Vignale[210] rehabilitated the original action principle of Runge and Gross by properly taking boundary conditions into account.[207] This has resulted in the Runge-Gross-Vignale action principle

$$\frac{\delta A\left[\rho\right]}{\delta\rho\left(\mathbf{r},t\right)}=\mathrm{i}\frac{\langle\Psi\ |\delta\Psi\rangle}{\delta\rho\left(\mathbf{r},t\right)}\ , \tag{2.100}$$

which often leads to the same conclusions as the original action principle of Runge and Gross.[207,210] Since this is particularly the case in the linear-response regime (see Sec. 2.4.2) used in the present work, the use of the original Runge-Gross action principle is retained here for simplicity.

Analogous to ground-state theory, time-dependent single particle equations in the sense of Kohn-Sham DFT (for details see Sec. 2.2.2) can be established.[208] Introducing a non-interacting time-dependent reference system, the time-dependent electron density is given by

$$\rho_\sigma\left(\mathbf{r},t\right)=\sum_{pq}P_{pq}^{\sigma}\left(t\right)\varphi_{p,\sigma}^{*}\left(\mathbf{r}\right)\varphi_{q,\sigma}\left(\mathbf{r}\right)\ , \tag{2.101}$$

with $\mathbf{P}^\sigma$ being the time-dependent density matrix in the basis of stationary MOs. The universal functional $B_s\left[\rho\right]$ for such a system is exactly known, it is the implicit density

functional

$$B_s[\rho] = \frac{1}{2}\sum_{\sigma}\sum_{pq}\int_{t_0}^{t_1}\int P_{pq}^{\sigma}(t)\,\varphi_{p,\sigma}^{*}(\mathbf{r})\,\nabla^{\mathrm{T}}\nabla\varphi_{q,\sigma}(\mathbf{r})\,\mathrm{d}\mathbf{r}\mathrm{d}t + \mathrm{i}\sum_{\sigma}\sum_{pq}\int_{t_0}^{t_1}\int \frac{\partial P_{pq}^{\sigma}(t)}{\partial t}\varphi_{p,\sigma}^{*}(\mathbf{r})\,\varphi_{q,\sigma}(\mathbf{r})\,\mathrm{d}\mathbf{r}\mathrm{d}t\ . \tag{2.102}$$

Then the action integral of the interacting system reduces to

$$A[\rho] = B_s[\rho] - \frac{1}{2}\sum_{\sigma\varsigma}\int_{t_0}^{t_1}\int\int\frac{\rho_\sigma(\mathbf{r},t)\,\rho_\varsigma(\mathbf{r}',t)}{|\mathbf{r}-\mathbf{r}'|}\mathrm{d}\mathbf{r}\mathrm{d}\mathbf{r}'\mathrm{d}t - \sum_{\sigma}\int_{t_0}^{t_1}\int\left[\hat{V}_{Ne}(\mathbf{r},\mathbf{R}) + \hat{V}_{ext}(t)\right]\rho_\sigma(\mathbf{r},t)\,\mathrm{d}\mathbf{r}\mathrm{d}t - A_{xc}[\rho]\ , \tag{2.103}$$

with

$$A_{xc}[\rho] = B_s[\rho] - B[\rho] - \frac{1}{2}\sum_{\sigma\varsigma}\int_{t_0}^{t_1}\int\int\frac{\rho_\sigma(\mathbf{r},t)\,\rho_\varsigma(\mathbf{r}',t)}{|\mathbf{r}-\mathbf{r}'|}\mathrm{d}\mathbf{r}\mathrm{d}\mathbf{r}'\mathrm{d}t \tag{2.104}$$

being defined as the exchange-correlation part of the action integral. Similarly to the ground-state theory, it contains all non-classical electron-electron interactions as exchange and correlation as well as the difference between the kinetic energy of the interacting system and the non-interacting reference system. As in DFT, the XC action integral in TDDFT is not known exactly, and approximations have to be made. While the exact XC action integral is non-local in time and thus considers so-called memory effects,[207] usually the adiabatic approximation, which assumes locality in time, is applied. As a consequence, approximations derived for ground-state DFT (see Sec. 2.2.4 and 2.3) can be transferred to the TDDFT framework.[1]

The application of the stationary action principle (2.97) finally gives a set of time-dependent single-particle equations, the time-dependent KS (TDKS) equations,[1,208] which in density matrix notation read (cf. Eq. (2.20) for time-independent single-particle equations)

$$\sum_{q}\left\{F_{pq}^{\sigma}(t)\,P_{qr}^{\sigma}(t) - P_{pq}^{\sigma}(t)\,F_{qr}^{\sigma}(t)\right\} = \mathrm{i}\frac{\partial}{\partial t}P_{pr}^{\sigma}(t) \tag{2.105}$$

with the time-dependent KS matrix being defined as

$$F^{\sigma}_{mn}(t) = h^{\sigma}_{mn} + \sum_{rs}\left[g^{\sigma\sigma}_{mnrs}P^{\sigma}_{rs}(t) + g^{\sigma\sigma'}_{mnrs}P^{\sigma'}_{rs}(t)\right] + \frac{\delta A_{xc}[\rho]}{\delta P^{\sigma}_{mn}(t)} + v^{\sigma}_{mn}(t) \ . \tag{2.106}$$

Integrals over the external time-dependent potential $\hat{V}_{ext}$ are denoted as

$$v^{\sigma}_{pq}(t) = \int \hat{V}_{ext}(t)\,\varphi^{*}_{p,\sigma}(\mathbf{r})\,\varphi_{q,\sigma}(\mathbf{r})\,\mathrm{d}\mathbf{r} \ . \tag{2.107}$$

While the TDKS equations can be directly used for the calculation of the time propagation of the density matrix in the field of the time-dependent KS matrix, leading to so-called real-time TDDFT approaches,[212,213] response formalisms operating in the frequency domain represent the more popular approach.[207] Both schemes can be utilized to calculate electronic excitation energies of molecular systems. In particular, the calculation of excitation energies within the linear-response formalism, which represents one of the main topics of the present work, will be outlined in the next section.

2.4.2. Linear Response TDDFT

In linear-response TDDFT,[214–218] electronic excitation energies are calculated by considering the linear response of the electron density to a perturbation induced through a time-dependent external electric field. Initially, i.e. before the external electric field is applied, the molecular system is assumed to be in its ground state. Hence, it can be described by the time-independent (static) KS equations (see Sec. 2.2.2). Switching on the time-dependent perturbation then induces a time-dependent change of the electron density. To first order, i.e. linear response, the time-dependent density matrix is then given by the sum of the ground-state density matrix $\mathbf{D}^{\sigma}$ and the time-dependent first-order change $\Delta\mathbf{P}^{\sigma}(t)$[1,219,220]

$$P^{\sigma}_{mn}(t) = D^{\sigma}_{mn} + \Delta P^{\sigma}_{mn}(t) \ . \tag{2.108}$$

Similarly, the time-dependent KS matrix is given as sum of the static KS matrix and a linear-response term

$$F^{\sigma}_{mn}(t) = F^{\sigma}_{mn} + \Delta F^{\sigma}_{mn}(t) \ , \tag{2.109}$$

where the linear response of the KS matrix

$$\Delta F^{\sigma}_{mn}(t) = \sum_{st,\varsigma} \int \frac{\delta F^{\sigma}_{mn}(t)}{\delta P^{\varsigma}_{st}(t')} \Delta P^{\varsigma}_{st}(t') \, \mathrm{d}t' + v^{\sigma}_{mn}(t) \tag{2.110}$$

includes the reaction of the time-dependent KS matrix to changes of the time-dependent density matrix as well as the time-dependent perturbation through the external electric field, respectively. Within the popular adiabatic approximation (cf. Sec. 2.4.1), which will be used throughout this work, the former term is substituted using[219]

$$\frac{\delta F^{\sigma}_{mn}(t)}{\delta P^{\varsigma}_{st}(t')} \approx \frac{\delta F^{\sigma}_{mn}}{\delta D^{\varsigma}_{st}} \delta(t - t') \ , \tag{2.111}$$

thus allowing the use of approximated XC functionals of time-independent DFT. Insertion of (2.108) and (2.109) into the time-dependent KS equations (2.105) and consideration of first-order perturbation theory then results in

$$\sum_{q} \left\{ F^{\sigma}_{pq} \Delta P^{\sigma}_{qr}(t) - \Delta P^{\sigma}_{pq}(t) F^{\sigma}_{qr} + \Delta F^{\sigma}_{pq}(t) D^{\sigma}_{qr} - D^{\sigma}_{pq} \Delta F^{\sigma}_{qr}(t) \right\} = \mathrm{i} \frac{\partial}{\partial t} \Delta P^{\sigma}_{pr}(t) \ . \tag{2.112}$$

The frequency-dependent linear response of the density matrix $\Delta \mathbf{P}^{\sigma}(\omega)$ can be obtained by inserting Eq. (2.110) into (2.112) and taking the Fourier transform of the resulting equation, which yields within the adiabatic approximation

$$\begin{aligned} \omega \Delta P^{\sigma}_{pr}(\omega) = \sum_{q} \Bigg\{ & F^{\sigma}_{pq} \Delta P^{\sigma}_{qr}(\omega) + \left[\sum_{st,\varsigma} \frac{\delta F^{\sigma}_{pq}}{\delta D^{\varsigma}_{st}} \Delta P^{\varsigma}_{st}(\omega) + \tilde{v}^{\sigma}_{pq}(\omega) \right] D^{\sigma}_{qr} - \\ & \Delta P^{\sigma}_{pq}(\omega) F^{\sigma}_{qr} - D^{\sigma}_{pq} \left[\sum_{st,\varsigma} \frac{\delta F^{\sigma}_{qr}}{\delta D^{\varsigma}_{st}} \Delta P^{\varsigma}_{st}(\omega) + \tilde{v}^{\sigma}_{qr}(\omega) \right] \Bigg\} \ , \end{aligned} \tag{2.113}$$

where $\tilde{v}^{\sigma}_{pq}(\omega)$ denotes the Fourier-transformed perturbation through the electric field. Considering idempotency of the time-dependent density matrix $\mathbf{P}^{\sigma}$, restricts the form of $\Delta \mathbf{P}^{\sigma}$ via the relation[1,220]

$$\Delta P^{\sigma}_{pr}(\omega) = \sum_{q} \left[D^{\sigma}_{pq} \Delta P^{\sigma}_{qr}(\omega) + \Delta P^{\sigma}_{pq}(\omega) D^{\sigma}_{qr} \right] \ , \tag{2.114}$$

in such a way that only occupied-virtual blocks ΔP^{σ}_{ia} and virtual-occupied blocks ΔP^{σ}_{ai} are non-zero. Additionally taking into account Eqs. (2.14), (2.15) and (2.22), i.e. diagonality and integer occupation of the ground-state density matrix as well diagonality of the KS

matrix in the canonical MO basis, respectively, allows a reformulation of Eq. (2.113) into

$$\omega \Delta P^{\sigma}_{ia}(\omega) = \epsilon^{\sigma}_{i} \Delta P^{\sigma}_{ia}(\omega) - \Delta P^{\sigma}_{ia}(\omega) \epsilon^{\sigma}_{a} - \left[\sum_{bj,\varsigma} \frac{\delta F^{\sigma}_{ia}}{\delta D^{\varsigma}_{bj}} \Delta P^{\varsigma}_{bj}(\omega) + \tilde{v}^{\sigma}_{ia}(\omega) \right] \tag{2.115}$$

$$\omega \Delta P^{\sigma}_{ai}(\omega) = \epsilon^{\sigma}_{a} \Delta P^{\sigma}_{ai}(\omega) - \Delta P^{\sigma}_{ai}(\omega) \epsilon^{\sigma}_{i} + \left[\sum_{bj,\varsigma} \frac{\delta F^{\sigma}_{ai}}{\delta D^{\varsigma}_{bj}} \Delta P^{\varsigma}_{bj}(\omega) + \tilde{v}^{\sigma}_{ai}(\omega) \right] . \tag{2.116}$$

Applying an infinitesimally small perturbation $\tilde{v}^{\sigma}_{ia} \approx 0$ and $\tilde{v}^{\sigma}_{ai} \approx 0$, which corresponds to the poles of the density matrix response,[220] the excitation frequencies $\omega_{ia\sigma}$ (the elements of the diagonal matrix ω_{σ}) are then determined as eigenvalues of the spin-resolved Casida's equations[216]

$$\sum_{\varsigma} \begin{pmatrix} \mathbf{L}_{\sigma,\varsigma} & \mathbf{M}_{\sigma,\varsigma} \\ \mathbf{M}^{*}_{\sigma,\varsigma} & \mathbf{L}^{*}_{\sigma,\varsigma} \end{pmatrix} \begin{pmatrix} \mathbf{X}_{\varsigma} \\ \mathbf{Y}_{\varsigma} \end{pmatrix} = \begin{pmatrix} \omega_{\sigma} & \mathbf{0} \\ \mathbf{0} & -\omega_{\sigma} \end{pmatrix} \begin{pmatrix} \mathbf{X}_{\sigma} \\ \mathbf{Y}_{\sigma} \end{pmatrix} , \tag{2.117}$$

where the standard notation $X^{\sigma}_{ia} = \Delta P^{\sigma}_{ai}$ and $Y^{\sigma}_{ia} = \Delta P^{\sigma}_{ia}$ for the density matrix responses, also named transition density matrices, is used.

For a real wave function, which can be assumed in the absence of a magnetic field and of spin-orbit coupling, $\mathbf{L}_{\sigma,\varsigma}$ and $\mathbf{M}_{\sigma,\varsigma}$ are real-valued matrices, so that Eq. (2.117) reduces to a set of linear equations

$$\mathbf{V}^{\pm}_{\sigma} = \omega \left(\mathbf{X} \mp \mathbf{Y} \right)_{\sigma} , \tag{2.118}$$

where the so-called matrix-vector product $\mathbf{V}^{\pm}_{\sigma}$ is defined by

$$\mathbf{V}^{\pm}_{\sigma} = \sum_{\varsigma} \left(\mathbf{L} \pm \mathbf{M} \right)_{\sigma,\varsigma} \left(\mathbf{X} \pm \mathbf{Y} \right)_{\varsigma} . \tag{2.119}$$

The matrices $(\mathbf{L} + \mathbf{M})_{\sigma,\varsigma}$ and $(\mathbf{L} - \mathbf{M})_{\sigma,\varsigma}$, i.e. the electric and magnetic orbital rotation Hessian, respectively, are given by

$$(L + M)_{ia\sigma,jb\varsigma} = \delta_{ij}\delta_{ab}\delta_{\sigma\varsigma} \left(\epsilon^{\sigma}_{a} - \epsilon^{\sigma}_{i} \right) + 2 \cdot g^{\sigma\varsigma}_{iabj} + f^{\sigma\varsigma}_{iabj} + f^{\sigma\varsigma}_{iajb} \tag{2.120}$$

$$(L - M)_{ia\sigma,jb\varsigma} = \delta_{ij}\delta_{ab}\delta_{\sigma\varsigma} \left(\epsilon^{\sigma}_{a} - \epsilon^{\sigma}_{i} \right) + f^{\sigma\varsigma}_{iabj} - f^{\sigma\varsigma}_{iajb} , \tag{2.121}$$

where the four-center integrals $g^{\sigma\varsigma}_{pqrs}$ are defined as in Eq. (2.19). The XC kernel integrals (within the adiabatic approximation) are given as second derivative of the XC energy

with respect to the ground-state density matrix

$$f_{pqrs}^{\sigma\varsigma} = \frac{\delta^2 E_{xc}}{\delta D_{pq}^{\sigma} \delta D_{rs}^{\varsigma}} \,, \tag{2.122}$$

which for semi-local XC functionals is equivalent to (see chapter 3 for details)

$$f_{pqrs}^{\sigma\varsigma} = \int\int \varphi_{p,\sigma}^{*}(\mathbf{r})\, \varphi_{q,\sigma}(\mathbf{r})\, \frac{\delta^2 E_{xc}}{\delta\rho_{\sigma}(\mathbf{r})\, \delta\rho_{\varsigma}(\mathbf{r}')} \varphi_{r,\varsigma}^{*}(\mathbf{r}')\, \varphi_{s,\varsigma}(\mathbf{r}')\, \mathrm{d}\mathbf{r}\mathrm{d}\mathbf{r}' \,. \tag{2.123}$$

Choosing exact orbital exchange without any correlation (cf. Eq. (2.40)) as XC functional, Eq. (2.117) simply reduces to the time-dependent Hartree-Fock (TDHF) equations,[2,221,222] which have the XC kernel integrals

$$f_{pqrs}^{\sigma\varsigma} = -\delta_{\sigma\varsigma} \cdot g_{psrq}^{\sigma\varsigma} \tag{2.124}$$

and will thus be labeled as exact-exchange kernel integrals throughout this work. Note that this has to be distinguished from the frequency-dependent exact-exchange kernel based on the OEP method,[223] also referred to as time-dependent OEP (TDOEP) method, which is not used in the present work. Hence, in the generalized KS framework, TDHF can be regarded as linear-response TDDFT with a distinct choice of the XC functional. Similarly, the CI singles (CIS) method for the calculation of excitation energies is directly related to linear-response TDDFT. Assuming the matrix $\mathbf{M}_{\sigma,\varsigma}$ to be 0, i.e. the Tamm-Dancoff approximation (TDA) to TDDFT,[224] and employing the exact-exchange kernel (2.124) simply results in the CIS equations.[1] The performance of different XC functionals within the linear-response formalism will be highlighted in chapter 5 in comparison to local hybrid functionals, whose TDDFT implementation is one of the main objectives of the present work.

2.5. Evaluation of Molecular Integrals

2.5.1. Basics

Molecular integrals as, e.g., the one- and two-electron integrals (2.18) and (2.19), respectively, are an inherent component in molecular electronic structure calculations, for example in HF, KS DFT and linear response TDDFT. While so far having been generally formulated in terms of molecular orbitals, the implementation in computer programs requires a suitable numerical representation of the MOs. Besides other approaches,[225–229]

MOs of molecular systems are most commonly expanded in a set of atom-centered atomic orbitals (AOs), which is known as LCAO (linear combination of atomic orbitals) ansatz [36]

$$\varphi_{p,\sigma}(\mathbf{r}) = \sum_{\mu}^{N_{BF}} c_{p\mu}^{\sigma} \cdot \chi_{\mu}(\mathbf{r}) \ , \tag{2.125}$$

with N_{BF} being the number of basis functions within the basis set and $c_{p\mu}^{\sigma}$ the expansion coefficient of the pth MO of σ spin in the μth basis function χ_{μ}. The atomic orbitals themselves are usually represented as Cartesian harmonics, either described by Slater-type (STOs) or more often Gaussian-type orbitals (GTOs)

$$\chi_{\mu}(\mathbf{r}) = x^k y^l z^m \cdot \mathrm{e}^{-\beta_{\mu} x^2} \mathrm{e}^{-\beta_{\mu} y^2} \mathrm{e}^{-\beta_{\mu} z^2} \ , \tag{2.126}$$

with β_{μ} being a fixed exponent determined by the basis set as well as k, l and m being integer numbers determining the angular momentum quantum number of the basis function. Note that common basis sets often also include fixed linear combinations of primitive basis functions (2.126), so-called contracted basis functions, for an improved description of molecular orbital shapes without extending the dimensionality of the variational space, which nonetheless only increases the combinatorial complexity of the integral evaluation problem, while the underlying concepts remain unchanged.

In general, electronic structure calculations require the determination of three types of different integrals, i.e. a) simple integrals as the kinetic energy, basis function overlap or dipole integrals, b) integrals over the Coulomb operator $\mathbf{r}^{-1}$ and c) integration of the XC energy densities. In the case of Cartesian GTOs as MO-LCAO representation, which is the most common choice for molecules and will thus be used for illustration, the Gaussian product rule, factorizability of the three-dimensional integrals into separate one-dimensional integrals as well as several recurrence relations between GTOs of different angular-momentum quantum number simplify integral evaluation significantly. [230] As a consequence, simple integrals such as the ones mentioned before, just reduce to integrals of the kind [230]

$$\int_{-\infty}^{\infty} f(x)\, \mathrm{e}^{-x^2} \mathrm{d}x \ , \tag{2.127}$$

where $f(x)$ is a polynomial arising due to the angular-momentum quantum numbers of the involved GTOs as well as due to the type of the calculated molecular integral. High precision numerical solutions for this kind of integrals can be obtained simply with standard Hermite-Gauss quadrature and will thus not be discussed further. In contrast,

integrals over the Coulomb operator, i.e. (2.19) and the second term of (2.18), in general require the additional Laplace transformation of the $\mathbf{r}^{-1}$ operator[231]

$$\frac{1}{|\mathbf{r}|} = \int \mathrm{e}^{-u^2\mathbf{r}^2}\mathrm{d}u \; . \tag{2.128}$$

Applying several further integral transformations[231] finally allows the reduction of the integrals to the calculation of Boys functions of different orders n

$$F_n\left(x\right) = \int_0^1 \mathrm{e}^{-xt^2}t^{2n}\mathrm{d}t \; . \tag{2.129}$$

The two most famous methods for relating integrals over the Coulomb operator to nth order Boys functions are the Obara-Saika[232] and the McMurchie-Davidson scheme.[233] While the former is directly based on recurrence relations of Cartesian Gaussian functions, in the latter, auxilliary Hermite Gaussian functions and expansion coefficients into Cartesian Gaussian functions are introduced to circumvent direct recurrences of Cartesian Gaussian functions. The Boys functions themselves are usually obtained by a combination of pre-tabulation, fitting and use of shifting techniques.[234–236] An alternative direct approach for the calculation of integrals over the Coulomb operator is provided by the Gauss-Rys quadrature,[237–240] which is based on the calculation of roots and weights of orthogonal Rys polynomials determined through the weighting function $\mathrm{e}^{-\alpha\cdot x^2}$ within the integration ranges 0 and 1, with α being a positive parameter depending on the involved GTOs. In practice, roots and weights of these polynomials are commonly determined by the Christoffel formula,[241] finally allowing the calculation of integrals over the Coulomb operator via a numerical quadrature formula.

While generally based on numerical techniques, explicitly via Gauss quadrature or implicitly through the Boys functions, the former integration techniques are commonly referred to as analytical integration, since results usually close to machine precision are obtained. In the case of one-electron integrals, analytical integration has to be performed separately for each pair of basis functions, while two-electron integrals already require a calculation for each basis function quadruple. Formally, the analytical evaluation of these integrals thus scales as N_{BF}^2 and N_{BF}^4, respectively, where integrals over the Coulomb operator in general are more expensive due to the higher computation complexity. Hence, determination of the two-electron integrals (2.19) represents the most expensive part within integral evaluation during a HF, KS DFT or linear-respons TDDFT calculation. Several prescreening techniques[242] have been developed, reducing the scaling of these

four-center integrals in the asymptotic limit to N_{BF}^2 or less in the case of exact-exchange integrals.[243]

In contrast, due to their complex functional form, XC functionals, representing the last class of occuring molecular integrals, cannot be calculated with the analytical integration techniques presented so far. Instead, XC functionals are generally determined by numerical integration on a molecular grid[244–247]

$$E_{xc} = \int e_{xc}\left(\mathbf{r}\right) \mathrm{d}\mathbf{r} \approx \sum_{i}^{n} w_i \cdot e_{xc}\left(\mathbf{r}_i\right) \ , \tag{2.130}$$

where w_i denotes the weight of the ith grid point with Cartesian real-space coordinates $\mathbf{r}_i$. While the molecular grid is conveniently constructed as superposition of atomic grids, appropriately merged via a partitioning function,[245] numerical integration for the atoms is generally performed by separate radial and spherical Gauss quadrature schemes. The most popular choices for the spherical grid are the ones based on a scheme of Lebedev[248] and Gauss-Lobatto quadrature,[247,249] where the former shows a higher efficiency, while the latter represents an open-ended integration scheme.[244] Although the integration interval for the radial grid is $0 \leq r \leq \infty$, related Gauss quadrature schemes as Gauss-Laguerre quadrature do not offer any advantages due to the complex structure of the integrands.[247] Hence, one common procedure is the use of Gauss quadrature within the interval $0 \leq r \leq 1$ as Gauss-Legendre or Gauss-Chebychev quadrature with a subsequent mapping onto the interval $0 \leq r \leq \infty$, introducing a mapping parameter ξ optimized for each atom type.[244]

Having appropriately set up the numerical molecular grid in real space, which defines n grid point coordinates with their related weights, XC functionals presented in Secs. 2.2.4 and 2.3 can be determined using Eq. (2.130). Therefore, the XC energy density and all associated quantities such as the electron density and the kinetic energy density have to be calculated for every grid point. Assuming an atomic orbital basis, the latter two quantities are given by

$$\rho_\sigma\left(\mathbf{r}\right) = \sum_{\mu\nu} D_{\mu\nu}^{\sigma} \cdot \chi_\mu\left(\mathbf{r}\right) \chi_\nu\left(\mathbf{r}\right) \tag{2.131}$$

$$\tau_\sigma\left(\mathbf{r}\right) = \frac{1}{2} \sum_{\mu\nu} D_{\mu\nu}^{\sigma} \cdot \nabla^{\mathrm{T}} \chi_\mu\left(\mathbf{r}\right) \nabla \chi_\nu\left(\mathbf{r}\right) \ , \tag{2.132}$$

respectively, with

$$D^{\sigma}_{\mu\nu} = \sum_{pq} c^{\sigma *}_{p\mu} c^{\sigma}_{q\nu} \cdot D^{\sigma}_{pq} \tag{2.133}$$

being the density matrix within the AO basis. Formally, computation of these quantities thus scales as N^2_{BF} for every grid point, so that the scaling of the XC energy is determined by $n \cdot N^2_{BF}$. Nevertheless, due to the locality of these quantities, scaling of the XC energy reduces to n in the asymptotic limit. In comparison to the expensive four-center integrals, computation cost of the XC functional is thus largely negligible.

2.5.2. Resolution of the Identity

One famous method for the reduction of the calculation cost of the four-center integrals is the resolution of identity (RI) method,[250–252] also known as density fitting.[253–258] The basic idea of the method consists in the expansion of basis function pairs, occuring, e.g., in the four-center integrals (in contrast to Eq. (2.19) in the AO basis)

$$g_{\mu\nu\kappa\lambda} = \int\int \frac{\chi_{\mu}(\mathbf{r})\,\chi_{\nu}(\mathbf{r})\,\chi_{\kappa}(\mathbf{r}')\,\chi_{\lambda}(\mathbf{r}')}{|\mathbf{r}-\mathbf{r}'|} \mathrm{d}\mathbf{r}\mathrm{d}\mathbf{r}' \,, \tag{2.134}$$

in a set of N_{aux} auxilliary basis functions $\tilde{\chi}_{\lambda}$

$$\chi_{\mu}(\mathbf{r})\,\chi_{\nu}(\mathbf{r}) \approx \sum_{\lambda}^{N_{aux}} c^{\lambda}_{\mu\nu} \cdot \tilde{\chi}_{\lambda}(\mathbf{r}) \;, \tag{2.135}$$

where $c^{\lambda}_{\mu\nu}$ denotes the corresponding expansion coefficients. The latter can be determined by minimization with respect to a distinct metric, usually the Coulomb norm[250]

$$\int\int \frac{R_{\mu\nu}(\mathbf{r})\,R_{\mu\nu}(\mathbf{r}')}{|\mathbf{r}-\mathbf{r}'|} \mathrm{d}\mathbf{r}\mathrm{d}\mathbf{r}' \tag{2.136}$$

or the overlap norm[256]

$$\int R_{\mu\nu}(\mathbf{r})\,\mathrm{d}\mathbf{r} \,, \tag{2.137}$$

with

$$R_{\mu\nu}(\mathbf{r}) = \chi_{\mu}(\mathbf{r})\,\chi_{\nu}(\mathbf{r}) - \sum_{\lambda}^{N_{aux}} c^{\lambda}_{\mu\nu} \cdot \tilde{\chi}_{\lambda}(\mathbf{r}) \tag{2.138}$$

being a residue function, describing the difference between the exact and the fitted basis function pair. Application of the Coulomb norm, which is the natural choice for the approximation of integrals over the Coulomb operator and consequently shows the best performance,[256] replaces the analytical evaluation of the four-center integral by

$$g_{\mu\nu\kappa\lambda} \approx \sum_{o\upsilon} \tilde{g}_{\mu\nu o} \cdot \tilde{g}_{\kappa\lambda\upsilon} \cdot \left[\bar{\mathbf{g}}^{-1}\right]_{o\upsilon} \ . \tag{2.139}$$

Hence, integral evaluation is reduced to the calculation of the auxilliary three- and two-center integrals

$$\tilde{g}_{\mu\nu\kappa} = \int\int \frac{\chi_\mu(\mathbf{r})\,\chi_\nu(\mathbf{r}) \cdot \tilde{\chi}_\kappa(\mathbf{r}')}{|\mathbf{r}-\mathbf{r}'|} \mathrm{d}\mathbf{r}\mathrm{d}\mathbf{r}' \tag{2.140}$$

$$\bar{g}_{\mu\nu} = \int\int \frac{\tilde{\chi}_\mu(\mathbf{r}) \cdot \tilde{\chi}_\nu(\mathbf{r}')}{|\mathbf{r}-\mathbf{r}'|} \mathrm{d}\mathbf{r}\mathrm{d}\mathbf{r}' \ , \tag{2.141}$$

respectively. Consequently, the overall scaling of the AO integral evaluation within the RI method in comparison to standard analytical schemes (cf. Sec. 2.5.1) is reduced to $N_{BF}^2 \cdot N_{aux}$, which is determined by the computation of the three-center integrals.

Based on the RI approximation of the four-center integrals within the AO basis, Coulomb and exact exchange integrals are given by

$$\sum_{\mu\nu\kappa\lambda} g_{\mu\nu\kappa\lambda} \cdot D_{\mu\nu}^\sigma D_{\kappa\lambda}^\sigma \approx \sum_{o\upsilon} \left[\bar{\mathbf{g}}^{-1}\right]_{o\upsilon} \cdot \sum_{\mu\nu} \tilde{g}_{\mu\nu o} D_{\mu\nu}^\sigma \cdot \sum_{\kappa\lambda} \tilde{g}_{\kappa\lambda\upsilon} D_{\kappa\lambda}^\sigma \tag{2.142}$$

$$\sum_{\mu\nu\kappa\lambda} g_{\mu\lambda\kappa\nu} \cdot D_{\mu\nu}^\sigma D_{\kappa\lambda}^\sigma \approx \sum_{o\upsilon} \left[\bar{\mathbf{g}}^{-1}\right]_{o\upsilon} \cdot \sum_{\mu\nu} D_{\mu\nu}^\sigma \cdot \sum_{\kappa\lambda} \tilde{g}_{\mu\lambda o} \tilde{g}_{\kappa\nu\upsilon} D_{\kappa\lambda}^\sigma \ , \tag{2.143}$$

respectively. Due to the multiplication with AO density matrices, in the following also called contraction, additional steps influencing the overall scaling behavior of the RI method have to be considered. In the case of the Coulomb integrals (2.142), each three-center integral is only contracted with one density matrix, so that contraction has to be done only once for each auxilliary basis function. Accordingly, an overall scaling of $N_{BF}^2 \cdot N_{aux}$ is achieved. In contrast, the two three-center integrals are connected by the density matrices in the case of exact exchange integrals (2.143). Hence, multiplication of the three-center integrals with the density matrices has to be performed for each pair of auxilliary basis functions, leading to a scaling of $N_{BF}^2 \cdot N_{aux}^2$. Note that direct use of the expansion coefficients $c_{p\mu}^\sigma$ instead of the AO density matrix leads to a slightly different but similar formal scaling, which also depends on the number of occupied orbitals N_{occ}.[251,252]

While application of the RI method to Coulomb integrals, called RI-J method, thus provides a reduced scaling compared to analytical integration schemes, application to exact exchange, known as RI-K method, does not provide an improved scaling behavior. Furthermore, it could be shown that RI-K additionally requires larger auxilliary basis sets to ensure adequate accuracy. RI-K nonetheless reduces the calculation cost compared to analytical schemes, which is related to a smaller prefactor arising mainly due to the reduced scaling of the integral evaluation within the AO basis.[251] Hence, the RI method is predominantly used for the approximation of Coulomb integrals. Especially in KS DFT[250,251] and linear-response TDDFT calculations[259,260] employing semi-local XC functionals, overall calculation costs are significantly reduced by the RI-J method.

2.5.3. Semi-Numerical Integration

Another approach aiming for a reduced computation cost of four-center integrals is the pseudospectral (PS) method introduced by Friesner.[261–264] In the PS method the four-center integrals are factorized in a way that the integration can be done in two different spectral representations, i.e. in electronic and in real space,

$$g_{\mu\nu\kappa\lambda} \approx \sum_{i}^{n} w_i \cdot Q_\mu\left(\mathbf{r}_i\right) A_{\kappa\lambda}\left(\mathbf{r}_i\right) \chi_\nu\left(\mathbf{r}_i\right) \ . \tag{2.144}$$

While the real-space integration in (2.144) is done numerically as for the integration of XC functionals, elements of the $\mathbf{A}$ matrix

$$A_{\kappa\lambda}\left(\mathbf{r}_i\right) = \int \frac{\chi_\kappa\left(\mathbf{r}\right)\chi_\lambda\left(\mathbf{r}\right)}{\left|\mathbf{r}_i - \mathbf{r}\right|} \mathrm{d}\mathbf{r} \ , \tag{2.145}$$

which represents two-center integrals calculated for a distinct real-space coordinate $\mathbf{r}_i$, are evaluated analytically (cf. Sec. 2.5.1). The transformation between both integration spaces is handled by the transformation vector

$$Q_\mu\left(\mathbf{r}_i\right) = \sum_{\kappa\lambda}^{N_{BF}} S_{\mu\kappa} \cdot \left[\tilde{\mathbf{S}}^{-1}\right]_{\kappa\lambda} \cdot \chi_\lambda\left(\mathbf{r}_i\right) \ , \tag{2.146}$$

where

$$S_{\mu\nu} = \int \chi_\mu(\mathbf{r})\,\chi_\nu(\mathbf{r})\,\mathrm{d}\mathbf{r} \tag{2.147}$$

$$\tilde{S}_{\mu\nu} = \sum_j^n w_j \cdot \chi_\mu(\mathbf{r}_j)\,\chi_\nu(\mathbf{r}_j) \tag{2.148}$$

denote the elements of the analytically and numerically evaluated overlap matrix, respectively. To account for the incompleteness of both integration spaces, the basis set is augmented by orthogonal, so-called de-aliasing functions. Scaling of the PS method is determined by the calculation of the **A** matrix and its multiplication with the basis functions, which both have to be done for every grid point and thus formally scale as $n \cdot N_{BF}^2$.

A simplification of the PS method is achieved by applying the transformation vector

$$Q_\mu(\mathbf{r}_i) = \chi_\mu(\mathbf{r}_i)\ . \tag{2.149}$$

Evaluation of four-center integrals within the AO basis is then reduced to

$$g_{\mu\nu\kappa\lambda} \approx \sum_i^n w_i \cdot \chi_\mu(\mathbf{r}_i)\,\chi_\nu(\mathbf{r}_i)\,A_{\kappa\lambda}(\mathbf{r}_i)\ , \tag{2.150}$$

usually referred to as semi-numerical integration, which accordingly exhibits the same formal scaling as the PS method. Coulomb and exact-exchange integrals within the semi-numerical scheme are thus given by

$$\sum_{\mu\nu\kappa\lambda} g_{\mu\nu\kappa\lambda} \cdot D_{\mu\nu}^\sigma D_{\kappa\lambda}^\sigma \approx \sum_i^n w_i \cdot \rho_\sigma(\mathbf{r}_i) \cdot \sum_{\mu\nu} A_{\mu\nu}(\mathbf{r}_i)\,D_{\mu\nu}^\sigma \tag{2.151}$$

$$\sum_{\mu\nu\kappa\lambda} g_{\mu\lambda\kappa\nu} \cdot D_{\mu\nu}^\sigma D_{\kappa\lambda}^\sigma \approx \sum_i^n w_i \cdot \sum_{\mu\nu\kappa\lambda} \chi_\mu(\mathbf{r}_i)\,D_{\mu\nu}^\sigma \cdot A_{\nu\kappa}(\mathbf{r}_i) \cdot D_{\kappa\lambda}^\sigma \chi_\lambda(\mathbf{r}_i)\ , \tag{2.152}$$

respectively. While the contraction of the **A** matrix with the density matrices in both cases formally scales as $n \cdot N_{BF}^2$, it becomes more obvious for the exact exchange, if the summation over the four basis function indices is split into several separate steps, i.e. the contraction of the density matrix with the basis functions

$$B_\mu^\sigma(\mathbf{r}_i) = \sum_\nu D_{\mu\nu}^\sigma \cdot \chi_\nu(\mathbf{r}_i)\ , \tag{2.153}$$

the contraction of $\mathbf{B}^\sigma$ with the $\mathbf{A}$ Matrix

$$G_\mu^\sigma(\mathbf{r}_i) = \sum_\nu A_{\mu\nu}(\mathbf{r}_i) \cdot B_\nu^\sigma(\mathbf{r}_i) \tag{2.154}$$

and finally the scalar product of $\mathbf{B}^\sigma$ and $\mathbf{G}^\sigma$

$$\sum_{\mu\nu\kappa\lambda} g_{\mu\lambda\kappa\nu} \cdot D_{\mu\nu}^\sigma D_{\kappa\lambda}^\sigma \approx \sum_i^n w_i \cdot \sum_\mu B_\mu^\sigma(\mathbf{r}_i) \cdot G_\nu^\sigma(\mathbf{r}_i) \ , \tag{2.155}$$

which results in the exact-exchange integral (2.152). While the latter step only scales as $n \cdot N_{BF}$, the former two also have to be done for every grid point and thus scale as $n \cdot N_{BF}^2$, which thus determines the overall scaling of the density matrix multiplication.

Together with the AO integral evaluation, the semi-numerical as well as the PS method thus exhibit an overall scaling of $n \cdot N_{BF}^2$. Similar to analytical integral evaluation (cf. Sec. 2.5.1), this scaling can be reduced in the asymptotic limit. Introducing integral screenings with respect to basis function overlap and the density matrix, called S- and P-junctions, respectively, lead to the 'chain-of-spheres exchange' (COSX) method,[265–267] which uses the semi-numerical integration scheme exclusively for the calculation of exact exchange. In the asymptotic limit, scaling is reduced to n and is thus in the same order of magnitude as low-scaling analytical integration schemes like the 'linear-scaling exact exchange' (LinK) method.[243]

Besides the PS method, semi-numerical evaluation of Coulomb integrals is not in wide use. As shown by van Wüllen,[268] this is predominantly caused by problems related to the more long-range character of Coulomb compared to exact-exchange integrals, which requires the inclusion of additional basis functions at the atoms to achieve sufficient accuracy and numerical stability. This is related to the procedure in the PS method of adding dealiasing functions. To circumvent the bottleneck of analytical Coulomb integrals nonetheless, semi-numerical exact exchange evaluation as in the COSX method is best combined with RI-J (cf. Sec. 2.5.2).[267]

2.5.4. Non-Standard Integrals in Local Hybrids

Besides the standard integrals discussed so far, local hybrid functionals require the additional evaluation of LMF-weighted exact-exchange integrals, i.e. the first integral in Eq. (2.72). Since exact exchange, usually determined analytically, is now multiplied with the complex-structured LMF, analytical integration schemes are not applicable anymore. On the other hand, numerical integration schemes, suited for the integration of complex func-

tions like the LMF, exhibit problems in the integration over the Coulomb operator due to the singularity at $\mathbf{r}_i = \mathbf{r}_j$. Hence, the non-standard integrals in local hybrids are best determined through a semi-numerical approach

$$\int g_\sigma(\mathbf{r}) \cdot e_x^{ex}(\mathbf{r})\,\mathrm{d}\mathbf{r} \approx \sum_i^n w_i \cdot g_\sigma(\mathbf{r}_i) \cdot e_{x,\sigma}^{ex}(\mathbf{r}_i) \ . \tag{2.156}$$

In the first implementation of local hybrid functionals by Jaramillo *et al.*,[15] the evaluation of the exact-exchange energy density was related to the localized HF method of Görling and della Salla,[269] which uses an RI approximation, leading to

$$e_{x,\sigma}^{ex}(\mathbf{r}_i) \approx \sum_{\mu\nu} \tilde{Q}_{\mu\nu}^\sigma \cdot \chi_\mu(\mathbf{r}_i)\,\chi_\nu(\mathbf{r}_i) \tag{2.157}$$

with

$$\tilde{Q}_{\mu\nu}^\sigma = \frac{1}{2}\sum_{\upsilon o}\left[\left[\mathbf{S}^{-1}\right]_{\mu\upsilon} D_{o\nu}^\sigma \cdot \sum_{\kappa\lambda} g_{\upsilon\lambda\kappa o} \cdot D_{\kappa\lambda}^\sigma + \left[\mathbf{S}^{-1}\right]_{o\nu} D_{\mu\upsilon}^\sigma \cdot \sum_{\kappa\lambda} g_{\upsilon\lambda\kappa o} \cdot D_{\kappa\lambda}^\sigma\right] \ . \tag{2.158}$$

In their implementation of localized local hybrids, Arbuznikov *et al.*[184] directly applied an RI to the local hybrid potential, leading to a slightly different potential than the one obtained by the integration method of Jaramillo *et al.*, which employs the RI approximation on the level of the energy densities.[270] Nevertheless, in both cases the RI approximation either requires large decontracted basis sets or the introduction of an additional auxilliary basis, resulting in a higher computational cost.[270]

Another option is the direct calculation of the exact-exchange energy density in the sense of a semi-numerical integration (cf. Sec. 2.5.3)[270–272]

$$e_{x,\sigma}^{ex}(\mathbf{r}_i) = \sum_\mu B_\mu^\sigma(\mathbf{r}_i) \cdot G_\nu^\sigma(\mathbf{r}_i) \ . \tag{2.159}$$

It could be shown that the semi-numerical local hybrid implementation can compete with global hybrid functionals employing efficient analytical integration.[270]

3. Derivation of the Local Hybrid Exchange-Correlation Kernel

Based on the theoretical background established in the last chapter, this chapter is concerned with the detailed derivation of the adiabatic local hybrid exchange-correlation kernel and related integrals, which are required in linear-response TDDFT. While in the first formulation of the adiabatic local hybrid XC kernel in Ref. 272 formulas have been established in a very brief and compact way, in this work the complete formalism based on the density matrix formulation of KS DFT is discussed. After showing the relation between the density-matrix-based formalism and the usual derivation schemes, the former is explicitly applied to semi-local XC functionals and exact exchange first to introduce shorthand notations used for the ensuing formulation of the local hybrid XC kernel integrals. As a last step, integrals needed for an implementation, i.e. the local hybrid XC matrix-vector products in the atomic orbital basis, are given.

3.1. Relations between Derivation Schemes

Within the density-matrix-based formulation of linear-response TDDFT, as introduced in the last chapter (see Sec. 2.4 for details), adiabatic XC kernel integrals are determined by the second derivative of the XC functional with respect to the ground-state density matrix

$$f_{mnpq}^{\sigma\varsigma} = \frac{\delta^2 E_{xc}}{\delta D_{mn}^{\sigma} \delta D_{pq}^{\varsigma}} \,. \tag{3.1}$$

In the special case of explicit density functionals, for example GGA exchange and correlation, derivatives with respect to the ground-state density matrix can be transformed considering the definition of the ground-state electron density

$$\rho_{\sigma}\left(\mathbf{r}\right) = \sum_{mn} D_{mn}^{\sigma} \varphi_{m,\sigma}^{*}\left(\mathbf{r}\right) \varphi_{n,\sigma}\left(\mathbf{r}\right) \tag{3.2}$$

and its first derivative

$$\frac{\delta\rho_\sigma(\mathbf{r})}{\delta D^\sigma_{pq}} = \varphi^*_{p,\sigma}(\mathbf{r})\,\varphi_{q,\sigma}(\mathbf{r}) \ . \tag{3.3}$$

Eq. (3.1) can be then reexpressed in terms of functional derivatives with respect to the ground-state electron density by applying the functional chain rule twice

$$\begin{aligned}\frac{\delta^2 E_{xc}}{\delta D^\sigma_{mn}\delta D^\varsigma_{pq}} &= \int\int \frac{\delta^2 E_{xc}}{\delta\rho_\sigma(\mathbf{r})\,\delta\rho_\varsigma(\mathbf{r}')}\frac{\delta\rho_\sigma(\mathbf{r})}{\delta D^\sigma_{mn}}\frac{\delta\rho_\varsigma(\mathbf{r}')}{\delta D^\varsigma_{pq}}\mathrm{d}\mathbf{r}\mathrm{d}\mathbf{r}' \\ &= \int\int \frac{\delta^2 E_{xc}}{\delta\rho_\sigma(\mathbf{r})\,\delta\rho_\varsigma(\mathbf{r}')}\varphi^*_{m,\sigma}(\mathbf{r})\,\varphi_{n,\sigma}(\mathbf{r})\,\varphi^*_{p,\varsigma}(\mathbf{r}')\,\varphi_{q,\varsigma}(\mathbf{r}')\,\mathrm{d}\mathbf{r}\mathrm{d}\mathbf{r}' \ . \end{aligned} \tag{3.4}$$

Although Eq. (3.4) represents the formulation of the XC kernel integrals most commonly used in the literature, it only covers the case of explicitly density-dependent XC functionals, which in fact can be circumvented for implicit density functionals by applying the OEP method.[57,223] On the other hand, direct application of expression (3.1), which is used throughout the present work, in general leads to adiabatic XC kernel integrals within the generalized KS framework.

Nevertheless, within the generalized KS framework integrals containing functional derivatives of implicit density functionals with respect to the ground-state electron density are usually reexpressed in terms of functional derivatives with respect to occupied orbitals (FDO),[55,184,273–275] instead of taking derivatives with respect to the ground-state density matrix. While the FDO ansatz represents the natural approach in a density-matrix-free formulation of KS DFT, it apparently lacks a direct connection to derivatives with respect to the density matrix, since the MOs and the ground-state density matrix are only implicitly related via the electron density (3.2). Hence, as part of this work, the FDO ansatz will be reformulated in terms of a density matrix expression, thus showing the direct relation between the FDO ansatz and derivatives with respect to the density matrix.

As a first step, the derivative ofs the electron density with respect to occupied orbitals have to be expressed within the density matrix formalism. In general, two possible derivatives have to be considered, i.e.

$$\frac{\delta\rho_\sigma(\mathbf{r})}{\delta\left[D^\sigma_{mn}\varphi^*_{m,\sigma}(\mathbf{r}')\right]} = \varphi_{n,\sigma}(\mathbf{r})\,\delta(\mathbf{r}-\mathbf{r}') \tag{3.5}$$

and

$$\frac{\delta\rho_\sigma(\mathbf{r})}{\delta\varphi^*_{m,\sigma}(\mathbf{r}')} = \sum_n D^\sigma_{mn}\varphi_{n,\sigma}(\mathbf{r})\,\delta(\mathbf{r}-\mathbf{r}') \ . \tag{3.6}$$

Explicitly applying the restrictions on ground-state density matrices within KS DFT, diagonal elements of the occupied-occupied block of D^σ_{mn} have to be set to 1, while all other elements are 0. Within a density-matrix-free formulation, both equations would thus reduce to the same formula, although being different within the density matrix formalism. Accordingly, the functional chain rule can be used to formulate two different expressions establishing the connection to functional derivatives with respect to the ground-state electron density, that is

$$\frac{\delta E_{xc}}{\delta\left[D^\sigma_{mn}\varphi^*_{m,\sigma}(\mathbf{r})\right]} = \int \frac{\delta E_{xc}}{\delta\rho_\sigma(\mathbf{r}')}\frac{\delta\rho_\sigma(\mathbf{r}')}{\delta\left[D^\sigma_{mn}\varphi^*_{m,\sigma}(\mathbf{r})\right]}\mathrm{d}\mathbf{r}' = \frac{\delta E_{xc}}{\delta\rho_\sigma(\mathbf{r})}\varphi_{n,\sigma}(\mathbf{r}) \tag{3.7}$$

and

$$\frac{\delta E_{xc}}{\delta\varphi^*_{m,\sigma}(\mathbf{r})} = \int \frac{\delta E_{xc}}{\delta\rho_\sigma(\mathbf{r}')}\frac{\delta\rho_\sigma(\mathbf{r}')}{\delta\varphi^*_{m,\sigma}(\mathbf{r})}\mathrm{d}\mathbf{r}' = \frac{\delta E_{xc}}{\delta\rho_\sigma(\mathbf{r})}\sum_n D^\sigma_{mn}\varphi_{n,\sigma}(\mathbf{r}) \ , \tag{3.8}$$

respectively. However, derivatives with respect to the density matrix can be only reexpressed using Eq. (3.7), leading to

$$\frac{\delta E_{xc}}{\delta D^\sigma_{mn}} = \int \frac{\delta E_{xc}}{\delta\rho_\sigma(\mathbf{r})}\varphi^*_{m,\sigma}(\mathbf{r})\,\varphi_{n,\sigma}(\mathbf{r})\,\mathrm{d}\mathbf{r} = \int \frac{\delta E_{xc}}{\delta\left[D^\sigma_{mn}\varphi^*_{m,\sigma}(\mathbf{r})\right]}\varphi^*_{m,\sigma}(\mathbf{r})\,\mathrm{d}\mathbf{r} \ , \tag{3.9}$$

while such a substitution is not possible when considering Eq. (3.8). Hence, only Eq. (3.9) provides an adequate formulation of the FDO within the density matrix formalism, which can be similarly obtained by applying the functional chain rule

$$\frac{\delta E_{xc}}{\delta D^\sigma_{mn}} = \int \frac{\delta E_{xc}}{\delta\left[D^\sigma_{mn}\varphi^*_{m,\sigma}(\mathbf{r})\right]}\frac{\delta\left[D^\sigma_{mn}\varphi^*_{m,\sigma}(\mathbf{r})\right]}{\delta D^\sigma_{mn}}\mathrm{d}\mathbf{r} = \int \frac{\delta E_{xc}}{\delta\left[D^\sigma_{mn}\varphi^*_{m,\sigma}(\mathbf{r})\right]}\varphi^*_{m,\sigma}(\mathbf{r})\,\mathrm{d}\mathbf{r} \ . \tag{3.10}$$

The difference between Eq. (3.8), which represents an inadequate density matrix formulation of the FDO, and the adequate formulation in Eq. (3.7) becomes more obvious and significant only in the case of second derivatives. Therefore, the special cases

$$\frac{\delta^2 E_{xc}}{\delta\left[D^\sigma_{mn}\varphi^*_{m,\sigma}(\mathbf{r})\right]\delta\left[D^\sigma_{pq}\varphi_{q,\sigma}(\mathbf{r}')\right]} = \frac{\delta^2 E_{xc}}{\delta\rho_\sigma(\mathbf{r})\,\delta\rho_\sigma(\mathbf{r}')}\varphi_{n,\sigma}(\mathbf{r})\,\varphi^*_{p,\sigma}(\mathbf{r}') \tag{3.11}$$

and

$$\frac{\delta^2 E_{xc}}{\delta\varphi^*_{m,\sigma}(\mathbf{r})\,\delta\varphi_{n,\sigma}(\mathbf{r}')} = \frac{\delta^2 E_{xc}}{\delta\rho_\sigma(\mathbf{r})\,\delta\rho_\sigma(\mathbf{r}')}\sum_{pq} D^\sigma_{pn}\varphi^*_{p,\sigma}(\mathbf{r}')\,D^\sigma_{mq}\varphi_{q,\sigma}(\mathbf{r}) + \frac{\delta E_{xc}}{\delta\rho_\sigma(\mathbf{r})}\delta(\mathbf{r}-\mathbf{r}')\,D^\sigma_{mn} \tag{3.12}$$

shall be considered. While the former expression, based on the adequate FDO formulation, directly allows the transformation of Eq. (3.4) into

$$\frac{\delta^2 E_{xc}}{\delta D^\sigma_{mn}\delta D^\varsigma_{pq}} = \int\int \frac{\delta^2 E_{xc}}{\delta\left[D^\sigma_{mn}\varphi^*_{m,\sigma}(\mathbf{r})\right]\delta\left[D^\varsigma_{pq}\varphi^*_{p,\sigma}(\mathbf{r}')\right]}\varphi^*_{m,\sigma}(\mathbf{r})\,\varphi^*_{p,\varsigma}(\mathbf{r}')\,\mathrm{d}\mathbf{r}\mathrm{d}\mathbf{r}'\,, \tag{3.13}$$

which thus gives the correct XC kernel integrals within the FDO approach, Eq. (3.12) again is not suited for such a reformulation. In this context, it is noteworthy that Eq. (3.12) compared to Eq. (3.11) even contains an additional term considering a first derivative with respect to the ground-state electron density. This term becomes significant within a density-matrix-free formulation of the FDO ansatz, i.e. when explicitly considering properties of the ground-state density matrix within KS DFT (see above). While the first derivatives in Eqs. (3.7) and (3.8) would become equal in this case, Eqs. (3.11) and (3.12) would still differ due to the additional term in Eq. (3.12). Considering this fact, the FDO within the density-matrix-free formulation, although already proposed by other authors,[273] is not uniquely defined for second derivatives, since no distinction between Eqs. (3.11) and (3.12) would be possible. On the other hand, the density matrix formulation of the FDO ansatz, i.e. Eqs. (3.10) and (3.13), provides a unique definition of the theory and should thus be preferred over the prevalent density-matrix-free formalism.

While having established a consistent formulation of the FDO ansatz within a density matrix formalism, further derivations will be conveniently carried out using derivatives with respect to the density matrix itself, since this directly gives access to the XC kernel integrals without the need of considering functional derivatives of the XC functional with respect to orbitals or associated integral transformations.

3.2. Application of Density Matrix Derivatives

3.2.1. Semi-Local Exchange-Correlation Functionals

As first special case, the calculation of adiabatic XC kernel integrals of semi-local XC functionals will be described in detail. Considering that, besides the electron density

(3.2), semi-local XC functionals may also depend on other semi-local quantities such as the square of the density gradient or the kinetic energy density

$$\gamma_{\sigma\varsigma}(\mathbf{r}) = \nabla^{\mathrm{T}}\rho_{\sigma}(\mathbf{r})\,\nabla\rho_{\varsigma}(\mathbf{r}) \tag{3.14}$$

$$\tau_{\sigma}(\mathbf{r}) = \frac{1}{2}\sum_{mn} D^{\sigma}_{mn}\nabla^{\mathrm{T}}\varphi^{*}_{m,\sigma}(\mathbf{r})\,\nabla\varphi_{n,\sigma}(\mathbf{r}) \ , \tag{3.15}$$

respectively, one can define a set $\mathbb{Q}$ containing all quantities considered by the respective XC functional. In the case of τ-dependent meta-GGAs, as e.g. TPSS, $\mathbb{Q}$ takes the form

$$\mathbb{Q} = \{\rho_{\alpha}, \rho_{\beta}, \gamma_{\alpha\alpha}, \gamma_{\alpha\beta}, \gamma_{\beta\beta}, \tau_{\alpha}, \tau_{\beta}\} \ . \tag{3.16}$$

The relation between derivatives with respect to the density matrix and those with respect to the quantities included in $\mathbb{Q}$ can then be established by applying the functional chain rule extended in the sense of a complete differential, leading to the definition of the semi-local potential operator

$$\hat{d}_{mn,\sigma} = \sum_{Q\in\mathbb{Q}} \int \frac{\delta Q(\mathbf{r}')}{\delta D^{\sigma}_{mn}} \frac{\delta}{\delta Q(\mathbf{r}')} \mathrm{d}\mathbf{r}' \ , \tag{3.17}$$

so that XC potential integrals, i.e. the first functional derivative of the XC functional with respect to the density matrix, can be expressed as

$$\frac{\delta E_{xc}}{\delta D^{\sigma}_{mn}} = \int \hat{d}_{mn,\sigma} e_{xc}(\mathbf{r})\,\mathrm{d}\mathbf{r} \ . \tag{3.18}$$

Note that Eq. (3.17) represents the most general formulation of the potential operator. Depending on the quantities included in the set $\mathbb{Q}$, it thus may take different explicit forms. For example, in the case of τ-dependent meta-GGAs, $\hat{d}_{mn,\sigma}$ acting on a semi-local XC functional explicitly reads

$$\begin{aligned}\hat{d}_{mn,\sigma} e_{xc}(\mathbf{r}) =& \varphi^{*}_{m,\sigma}(\mathbf{r})\,\varphi_{n,\sigma}(\mathbf{r})\,\frac{\delta e_{xc}(\mathbf{r})}{\delta\rho_{\sigma}(\mathbf{r})} + \frac{1}{2}\nabla^{\mathrm{T}}\varphi^{*}_{m,\sigma}(\mathbf{r})\,\nabla\varphi_{n,\sigma}(\mathbf{r})\,\frac{\delta e_{xc}(\mathbf{r})}{\delta\tau_{\sigma}(\mathbf{r})} + \\ & \nabla^{\mathrm{T}}\left[\varphi^{*}_{m,\sigma}(\mathbf{r})\,\varphi_{n,\sigma}(\mathbf{r})\right]\cdot\left[2\nabla\rho_{\sigma}(\mathbf{r})\,\frac{\delta e_{xc}(\mathbf{r})}{\delta\gamma_{\sigma\sigma}(\mathbf{r})} + \nabla\rho_{\sigma'}(\mathbf{r})\,\frac{\delta e_{xc}(\mathbf{r})}{\delta\gamma_{\sigma\sigma'}(\mathbf{r})}\right] \ . \end{aligned} \tag{3.19}$$

Note again that σ' indicates the opposite spin of σ and no separate spin variable. Concatenation of two semi-local potential operators finally gives the semi-local kernel operator

$$\hat{d}_{mn,\sigma}\hat{d}_{pq,\varsigma} = \sum_{Q\in\mathbb{Q}}\sum_{Q'\in\mathbb{Q}}\int\int \frac{\delta Q\left(\mathbf{r}'\right)}{\delta D^{\sigma}_{mn}}\frac{\delta Q'\left(\mathbf{r}''\right)}{\delta D^{\varsigma}_{pq}}\frac{\delta^2}{\delta Q\left(\mathbf{r}'\right)\delta Q'\left(\mathbf{r}''\right)}\mathrm{d}\mathbf{r}'\mathrm{d}\mathbf{r}'' + \sum_{Q\in\mathbb{Q}}\int \frac{\delta^2 Q\left(\mathbf{r}'\right)}{\delta D^{\sigma}_{mn}\delta D^{\varsigma}_{pq}}\frac{\delta}{\delta Q\left(\mathbf{r}'\right)}\mathrm{d}\mathbf{r}' \;, \tag{3.20}$$

allowing the calculation of the semi-local XC kernel integrals as

$$\frac{\delta^2 E_{xc}}{\delta D^{\sigma}_{mn}\delta D^{\varsigma}_{pq}} = \int \hat{d}_{mn,\sigma}\hat{d}_{pq,\varsigma}e_{xc}\left(\mathbf{r}\right)\mathrm{d}\mathbf{r} \;. \tag{3.21}$$

For clarity, this implicit formulation employing semi-local potential operators will be used throughout this work. Explicit formulas for the XC kernel integrals of several XC functionals are well established, can be found in the literature[273,276] and will thus not be discussed further here.

In the context of semi-local XC kernel integrals, the special case of current-density-dependent meta-GGAs shall be discussed in addition. As mentioned by Furche and Bates,[277] the kinetic energy density (3.15) as used in many standard meta-GGAs is not invariant with respect to the gauge transformation. As solution for this problem, the gauge-invariant kinetic energy density[278]

$$\tilde{\tau}_{\sigma}\left(\mathbf{r}\right) = \tau_{\sigma}\left(\mathbf{r}\right) - \frac{1}{2}\frac{\mathbf{j}^2_{\sigma}\left(\mathbf{r}\right)}{\rho_{\sigma}\left(\mathbf{r}\right)} \tag{3.22}$$

has been introduced as substitute for the conventional kinetic energy density in the XC functional, where

$$\mathbf{j}_{\sigma}\left(\mathbf{r}\right) = \frac{1}{2}\sum_{mn} D^{\sigma}_{mn}\left[\nabla\varphi^{*}_{m}\left(\mathbf{r}\right)\varphi_{n}\left(\mathbf{r}\right) - \varphi^{*}_{m}\left(\mathbf{r}\right)\nabla\varphi_{n}\left(\mathbf{r}\right)\right] \tag{3.23}$$

denotes the the paramagnetic current density. For current-free ground states, i.e. in the absence of a magnetic field, $\mathbf{j}_{\sigma}$ becomes exactly 0 due to the symmetry of the ground-state density matrix, so that $\tilde{\tau}_{\sigma}$ and τ_{σ} are identical. For the calculation of semi-local XC potential and kernel integrals of these current-dependent meta-GGAs, the set $\mathbb{Q}$ used in the definition of the semi-local potential operator simply has to be extended by the paramagnetic current density. Nevertheless, since current-density-dependent meta-GGAs depend on the paramagnetic current density only through the gauge-invariant kinetic

energy density, one can set up the following relations

$$\frac{\delta e_{xc}(\mathbf{r})}{\delta \mathbf{j}_\sigma(\mathbf{r})} = \frac{\delta e_{xc}(\mathbf{r})}{\delta \tilde{\tau}_\sigma(\mathbf{r})}\frac{\delta \tilde{\tau}_\sigma(\mathbf{r})}{\delta \mathbf{j}_\sigma(\mathbf{r})} = -\frac{\delta e_{xc}(\mathbf{r})}{\delta \tilde{\tau}_\sigma(\mathbf{r})}\frac{\mathbf{j}_\sigma(\mathbf{r})}{\rho_\sigma(\mathbf{r})} \tag{3.24}$$

$$\begin{aligned}\frac{\delta^2 e_{xc}(\mathbf{r})}{\delta \mathbf{j}_\sigma^2(\mathbf{r})} &= \frac{\delta^2 e_{xc}(\mathbf{r})}{\delta \tilde{\tau}_\sigma^2(\mathbf{r})}\left[\frac{\delta \tilde{\tau}_\sigma(\mathbf{r})}{\delta \mathbf{j}_\sigma(\mathbf{r})}\right]^2 + \frac{\delta e_{xc}(\mathbf{r})}{\delta \tilde{\tau}_\sigma(\mathbf{r})}\frac{\delta^2 \tilde{\tau}_\sigma(\mathbf{r})}{\delta \mathbf{j}_\sigma^2(\mathbf{r})} \\ &= \frac{\delta^2 e_{xc}(\mathbf{r})}{\delta \tilde{\tau}_\sigma^2(\mathbf{r})}\frac{\mathbf{j}_\sigma^2(\mathbf{r})}{\rho_\sigma^2(\mathbf{r})} - \frac{\delta e_{xc}(\mathbf{r})}{\delta \tilde{\tau}_\sigma(\mathbf{r})}\frac{1}{\rho_\sigma(\mathbf{r})}\end{aligned} \tag{3.25}$$

for the first and second derivatives of the XC energy density, respectively. Hence, in the case of a current-free ground state, i.e. $\mathbf{j}_\sigma = 0$, contributions of $\mathbf{j}_\sigma$ to the XC potential integrals vanish. On the other hand, this is not the case for second derivatives of the XC energy density entering the XC kernel integrals, which exhibit the non-vanishing term

$$\frac{\delta^2 e_{xc}(\mathbf{r})}{\delta \mathbf{j}_\sigma^2(\mathbf{r})} = -\frac{\delta e_{xc}(\mathbf{r})}{\delta \tilde{\tau}_\sigma(\mathbf{r})}\frac{1}{\rho_\sigma(\mathbf{r})}\,. \tag{3.26}$$

This additional term, which arises due to the current dependence of the gauge-invariant kinetic energy density even for current-free ground states, is usually referred to as current-density response and should be considered in TDDFT calculations to ensure gauge invariance of calculated excitation energies. Nevertheless, considering the TPSS meta-GGA functional, it could be shown that the influence of the current-density response is minor in most cases.[277]

3.2.2. Exact Exchange

As second special case, density matrix derivatives of exact orbital exchange

$$E_x^{ex} = -\frac{1}{2}\sum_\sigma \int\int \sum_{mnpq} D_{mn}^\sigma D_{pq}^\sigma \cdot w_{mqpn}^{\sigma\sigma}(\mathbf{r},\mathbf{r}')\,\mathrm{d}\mathbf{r}\mathrm{d}\mathbf{r}' \tag{3.27}$$

will be examined in detail. For brevity, especially for later use in the case of local hybrid functionals, the shorthand notation

$$w_{mnpq}^{\sigma\varsigma}(\mathbf{r},\mathbf{r}') = \frac{\varphi_{m,\sigma}^*(\mathbf{r})\varphi_{n,\sigma}(\mathbf{r})\varphi_{p,\varsigma}^*(\mathbf{r}')\varphi_{q,\varsigma}(\mathbf{r}')}{|\mathbf{r}-\mathbf{r}'|} \tag{3.28}$$

for molecular orbital quadruples over the Coulomb operator is introduced. Taking the first derivative of Eq. (3.27) then directly gives

$$\frac{\delta E_x^{ex}}{\delta D_{rs}^{\sigma}} = -\frac{1}{2}\int\int\left[\sum_{mn} D_{mn}^{\sigma}\cdot w_{msrn}^{\sigma\sigma}\left(\mathbf{r},\mathbf{r}'\right)+\sum_{pq} D_{pq}^{\sigma}\cdot w_{rqps}^{\sigma\sigma}\left(\mathbf{r},\mathbf{r}'\right)\right]\mathrm{d}\mathbf{r}\mathrm{d}\mathbf{r}' \;, \tag{3.29}$$

which, after an exchange of summation variables and consideration of the symmetry of $w_{mnpq}^{\sigma\varsigma}\left(\mathbf{r},\mathbf{r}'\right)$ with respect to an exchange of the space variables, reduces to

$$\frac{\delta E_x^{ex}}{\delta D_{rs}^{\sigma}} = -\int\int\sum_{mn} D_{mn}^{\sigma}\cdot w_{msrn}^{\sigma\sigma}\left(\mathbf{r},\mathbf{r}'\right)\mathrm{d}\mathbf{r}\mathrm{d}\mathbf{r}' \;. \tag{3.30}$$

Exact orbital exchange kernel integrals are then determined by second derivatives with respect to the density matrix

$$\frac{\delta^2 E_x^{ex}}{\delta D_{rs}^{\sigma}\delta D_{tu}^{\varsigma}} = -\int\int w_{tsru}^{\sigma\sigma}\left(\mathbf{r},\mathbf{r}'\right)\delta_{\sigma\varsigma}\mathrm{d}\mathbf{r}\mathrm{d}\mathbf{r}' \;, \tag{3.31}$$

which equals Eq. (2.124) given in Sec. 2.4.2. It should be noted that, regarding Eq. (3.31), exact-exchange kernel integrals exhibit only a non-zero value, if derivatives with respect to the same spin variable are taken twice, i.e. $\sigma = \varsigma$.

3.2.3. Local Hybrid Functionals

Based on the just introduced notations for semi-local XC functionals and exact exchange with respect to density matrix derivatives, the local hybrid XC kernel will be derived. Starting from the local hybrid XC functional

$$\begin{aligned} E_{xc}^{LH} = &-\frac{1}{2}\sum_{\sigma}\sum_{mnpq} D_{mn}^{\sigma}D_{pq}^{\sigma}\int\int g_{\sigma}(\mathbf{r})\cdot w_{mqpn}^{\sigma\sigma}\left(\mathbf{r},\mathbf{r}'\right)\mathrm{d}\mathbf{r}'\mathrm{d}\mathbf{r}+ \\ &\sum_{\sigma}\int\left[1-g_{\sigma}(\mathbf{r})\right]\cdot e_{x,\sigma}^{sl}(\mathbf{r})\mathrm{d}\mathbf{r}+\int e_c^{sl}\left(\mathbf{r}\right)\mathrm{d}\mathbf{r} \;, \end{aligned} \tag{3.32}$$

where for simplicity the calibration function is assumed to be added to the semi-local exchange functional $\tilde{e}_{x,\sigma}^{sl}$

$$e_{x,\sigma}^{sl}(\mathbf{r}) \equiv \tilde{e}_{x,\sigma}^{sl}(\mathbf{r}) + G_{\sigma}(\mathbf{r}) \;, \tag{3.33}$$

the local hybrid XC potential integrals are simply given by

$$\begin{aligned}\frac{\delta E_{xc}^{LH}}{\delta D_{rs}^{\varsigma}} =& -\frac{1}{2}\int\int \left[g_{\varsigma}(\mathbf{r}) + g_{\varsigma}(\mathbf{r}')\right] \cdot \sum_{mn} D_{mn}^{\varsigma} w_{msrn}^{\varsigma\varsigma}\left(\mathbf{r},\mathbf{r}'\right) \mathrm{d}\mathbf{r}'\mathrm{d}\mathbf{r} \\ & - \sum_{\sigma}\int\int \hat{d}_{rs,\varsigma} g_{\sigma}(\mathbf{r}) \cdot \left[\frac{1}{2}\sum_{mnpq} D_{mn}^{\sigma} D_{pq}^{\sigma} w_{mqpn}^{\sigma\sigma}\left(\mathbf{r},\mathbf{r}'\right) + e_{x,\sigma}^{sl}(\mathbf{r})\right] \mathrm{d}\mathbf{r}'\mathrm{d}\mathbf{r} \\ & + \sum_{\sigma}\int \left[1 - g_{\sigma}(\mathbf{r})\right] \cdot \hat{d}_{rs,\varsigma} e_{x,\sigma}^{sl}(\mathbf{r})\mathrm{d}\mathbf{r} + \int \hat{d}_{rs,\varsigma} e_{c}^{sl}\left(\mathbf{r}\right) \mathrm{d}\mathbf{r}\ . \end{aligned} \tag{3.34}$$

While the first line in Eq. (3.34) represents the LMF-weighted exact-exchange potential, the second line considers the LMF potential weighted by the difference of the exchange densities. The last two terms constitute the LMF-weighted semi-local exchange potential and the semi-local correlation potential, respectively. Subsequently taking second derivatives with respect to the ground-state density matrix, results in the local hybrid XC kernel integral

$$\begin{aligned}\frac{\delta^2 E_{xc}^{LH}}{\delta D_{rs}^{\varsigma}\delta D_{tu}^{\vartheta}} =& -\frac{1}{2}\int\int \left[g_{\varsigma}(\mathbf{r}) + g_{\varsigma}(\mathbf{r}')\right] \cdot \delta_{\varsigma\vartheta} \cdot w_{tsru}^{\varsigma\varsigma}\left(\mathbf{r},\mathbf{r}'\right) \mathrm{d}\mathbf{r}'\mathrm{d}\mathbf{r} \\ & - \frac{1}{2}\int\int \hat{d}_{tu,\vartheta} \left[g_{\varsigma}(\mathbf{r}) + g_{\varsigma}(\mathbf{r}')\right] \cdot \sum_{mn} D_{mn}^{\varsigma} w_{msrn}^{\varsigma\varsigma}\left(\mathbf{r},\mathbf{r}'\right) \mathrm{d}\mathbf{r}'\mathrm{d}\mathbf{r} \\ & - \frac{1}{2}\int\int \hat{d}_{rs,\varsigma} \left[g_{\vartheta}(\mathbf{r}) + g_{\vartheta}(\mathbf{r}')\right] \cdot \sum_{mn} D_{mn}^{\vartheta} w_{mutn}^{\vartheta\vartheta}\left(\mathbf{r},\mathbf{r}'\right) \mathrm{d}\mathbf{r}'\mathrm{d}\mathbf{r} \\ & - \sum_{\sigma}\int\int \hat{d}_{rs,\varsigma}\hat{d}_{tu,\vartheta} g_{\sigma}(\mathbf{r}) \cdot \left[\frac{1}{2}\sum_{mnpq} D_{mn}^{\sigma} D_{pq}^{\sigma} w_{mqpn}^{\sigma\sigma}\left(\mathbf{r},\mathbf{r}'\right) + e_{x,\sigma}^{sl}(\mathbf{r})\right] \mathrm{d}\mathbf{r}'\mathrm{d}\mathbf{r} \\ & - \sum_{\sigma}\int \left[\hat{d}_{rs,\varsigma} g_{\sigma}(\mathbf{r}) \cdot \hat{d}_{tu,\vartheta} e_{x,\sigma}^{sl}(\mathbf{r}) + \hat{d}_{tu,\vartheta} g_{\sigma}(\mathbf{r}) \cdot \hat{d}_{rs,\varsigma} e_{x,\sigma}^{sl}(\mathbf{r})\right] \mathrm{d}\mathbf{r} \\ & + \sum_{\sigma}\int \left[1 - g_{\sigma}(\mathbf{r})\right] \cdot \hat{d}_{rs,\varsigma}\hat{d}_{tu,\vartheta} e_{x,\sigma}^{sl}(\mathbf{r})\mathrm{d}\mathbf{r} + \int \hat{d}_{rs,\varsigma}\hat{d}_{tu,\vartheta} e_{c}^{sl}\left(\mathbf{r}\right) \mathrm{d}\mathbf{r}\ . \end{aligned} \tag{3.35}$$

As is the case for the integrals of the potential, the LH kernel integrals (3.35) contain several distinct terms, i.e. the LMF-weighted exact-exchange kernel in the first line, the LMF potential weighted by the exact-exchange potential in the following two lines, as well as the LMF-potential-weighted semi-local exchange potential in the fifth line. While the fourth line exhibits the LMF kernel weighted by the difference of the exchange energy densities, the last two terms represent the LMF-weighted semi-local exchange kernel and the semi-local correlation kernel, respectively.

3.3. Local Hybrid Matrix-Vector Products in the Atomic Orbital Basis

While in the last section, the most general formulation of the local hybrid XC kernel integrals was derived, for an implementation into a quantum chemical program, the matrix-vector product (2.119) is required rather than the XC kernel integrals themselves. Furthermore, integrals are generally evaluated within an atomic orbital basis. Hence, for preparing equations for the subsequent implementation, both transformations have to be performed.

Due to the density matrix formalism used for the derivation of the local hybrid XC kernel integrals, integrals in the AO basis are directly accessible by just substituting MO density matrices by AO density matrices and changing MOs into AO basis functions. Basis function indices are denoted by μ, ν, κ and λ, while σ, ς and ϑ are used as independent spin indices. Accordingly, semi-local potential operators in the AO basis are defined as

$$\hat{d}_{\mu\nu,\sigma} = \sum_{Q\in\mathbb{Q}} \int \frac{\delta Q\left(\mathbf{r}\right)}{\delta D^{\sigma}_{\mu\nu}} \frac{\delta}{\delta Q\left(\mathbf{r}\right)} \mathrm{d}\mathbf{r} \;, \tag{3.36}$$

while for clarity, transition density matrices within the AO basis are abbreviated as

$$P^{\sigma}_{\nu\mu} = \left(\mathbf{X}+\mathbf{Y}\right)_{\mu\nu,\sigma} \tag{3.37}$$

$$U^{\sigma}_{\nu\mu} = \left(\mathbf{X}-\mathbf{Y}\right)_{\mu\nu,\sigma} \;, \tag{3.38}$$

representing the symmetric and anti-symmetric part of the transition density matrix, respectively. Considering Eq. (2.119), the XC parts of the matrix-vector products arising from the electric and magnetic orbital rotation Hessian, respectively, are given by

$$V^{xc,+}_{\mu\nu,\sigma} = \sum_{\varsigma} \left[\frac{\delta^2 E^{LH}_{xc}}{\delta D^{\sigma}_{\mu\nu} \delta D^{\varsigma}_{\kappa\lambda}} + \frac{\delta^2 E^{LH}_{xc}}{\delta D^{\sigma}_{\mu\nu} \delta D^{\varsigma}_{\lambda\kappa}} \right] P^{\varsigma}_{\kappa\lambda} \tag{3.39}$$

$$V^{xc,-}_{\mu\nu,\sigma} = \sum_{\varsigma} \left[\frac{\delta^2 E^{LH}_{xc}}{\delta D^{\sigma}_{\mu\nu} \delta D^{\varsigma}_{\kappa\lambda}} - \frac{\delta^2 E^{LH}_{xc}}{\delta D^{\sigma}_{\mu\nu} \delta D^{\varsigma}_{\lambda\kappa}} \right] U^{\varsigma}_{\kappa\lambda} \;. \tag{3.40}$$

Similarly to the evaluation of the local hybrid XC energy, the local hybrid matrix-vector products contain several non-standard integrals, so that an analytical integration is not possible. Following the semi-numerical approach of Sec. 2.5.4, matrix-vector products can

be expressed as local matrix-vector products $v_{\mu\nu,\sigma}^{xc,\pm}(\mathbf{r})$ integrated on a numerical grid

$$V_{\mu\nu,\sigma}^{xc,\pm} = \int v_{\mu\nu,\sigma}^{xc,\pm}(\mathbf{r})\,\mathrm{d}\mathbf{r} \approx \sum_{i}^{n} w_i \cdot v_{\mu\nu,\sigma}^{xc,\pm}(\mathbf{r}_i) \ . \tag{3.41}$$

The local matrix-vector products themselves shall be evaluated within a simple semi-numerical integration scheme as the one employed in the COSX method. Therefore, analytical two-center integrals over the Coulomb operator, i.e. the A matrix

$$A_{\mu\nu}(\mathbf{r}_i) = \int \frac{\chi_\mu(\mathbf{r})\,\chi_\nu(\mathbf{r})}{|\mathbf{r}_i - \mathbf{r}|}\mathrm{d}\mathbf{r} \ , \tag{3.42}$$

are required. Similarly, $v_{\mu\nu,\sigma}^{xc,\pm}(\mathbf{r})$ also depends on the basis function values at the respective grid point. Hence, the basis function vector

$$X_\mu(\mathbf{r}_i) = \chi_\mu(\mathbf{r}_i) \tag{3.43}$$

shall be introduced. Since all quantities required for the evaluation of the local matrix-vector product only depend on one space variable, for clarity, the dependence on $\mathbf{r}$ is omitted in the following formulas.

In terms of the introduced shorthand notations, the symmetric local matrix-vector product for a local hybrid XC functional reads

$$\begin{aligned}
v_{\mu\nu,\sigma}^{LH,+} = &- g_\sigma \cdot \left[X_\mu \left(\mathbf{A}\mathbf{P}^\sigma\mathbf{X}\right)_\nu + \left(\mathbf{A}\mathbf{P}^\sigma\mathbf{X}\right)_\mu X_\nu\right] \\
&- \frac{1}{2}\sum_{\varsigma}\sum_{\kappa\lambda} P_{\kappa\lambda}^{\varsigma} \cdot \left(\hat{d}_{\kappa\lambda,\varsigma} + \hat{d}_{\lambda\kappa,\varsigma}\right) g_\sigma \cdot \left[X_\mu \left(\mathbf{A}\mathbf{D}^\sigma\mathbf{X}\right)_\nu + \left(\mathbf{A}\mathbf{D}^\sigma\mathbf{X}\right)_\mu X_\nu\right] \\
&- \sum_{\varsigma\vartheta}\sum_{\kappa\lambda} P_{\kappa\lambda}^{\vartheta} \cdot \left(\hat{d}_{\kappa\lambda,\vartheta} + \hat{d}_{\lambda\kappa,\vartheta}\right) g_\varsigma \cdot \hat{d}_{\mu\nu,\sigma} e_{x,\varsigma}^{sl} \\
&- \sum_{\varsigma} \hat{d}_{\mu\nu,\sigma} g_\varsigma \cdot \left[2 \cdot \left(\mathbf{X}^{\mathrm{T}}\mathbf{D}^\varsigma\mathbf{A}\mathbf{P}^\varsigma\mathbf{X}\right) + \sum_{\vartheta}\sum_{\kappa\lambda} P_{\kappa\lambda}^{\vartheta} \cdot \left(\hat{d}_{\kappa\lambda,\vartheta} + \hat{d}_{\lambda\kappa,\vartheta}\right) e_{x,\varsigma}^{sl}\right] \\
&- \sum_{\varsigma\vartheta}\sum_{\kappa\lambda} P_{\kappa\lambda}^{\vartheta} \cdot \hat{d}_{\mu\nu,\sigma} \left(\hat{d}_{\kappa\lambda,\vartheta} + \hat{d}_{\lambda\kappa,\vartheta}\right) g_\varsigma \cdot \left[\frac{1}{2}\left(\mathbf{X}^{\mathrm{T}}\mathbf{D}^\varsigma\mathbf{A}\mathbf{D}^\varsigma\mathbf{X}\right) + e_{x,\varsigma}^{sl}\right] \\
&+ \sum_{\varsigma\vartheta}\sum_{\kappa\lambda} (1 - g_\varsigma) \cdot P_{\kappa\lambda}^{\vartheta} \cdot \hat{d}_{\mu\nu,\sigma} \left(\hat{d}_{\kappa\lambda,\vartheta} + \hat{d}_{\lambda\kappa,\vartheta}\right) e_{x,\varsigma}^{sl} \\
&+ \sum_{\varsigma}\sum_{\kappa\lambda} P_{\kappa\lambda}^{\varsigma} \cdot \hat{d}_{\mu\nu,\sigma} \left(\hat{d}_{\kappa\lambda,\varsigma} + \hat{d}_{\lambda\kappa,\varsigma}\right) e_c^{sl} \ .
\end{aligned} \tag{3.44}$$

While the assignment of the different contributions, arising either from the LMF, exchange or correlation functionals, is similar to the one discussed for the local hybrid XC kernel integrals (cf. Sec. 3.2.3), $v^{LH,+}_{\mu\nu,\sigma}$ can be additionally separated into a non-local and a semi-local part, $v^{nl,+}_{\mu\nu,\sigma}$ and $v^{sl,+}_{\mu\nu,\sigma}$, respectively. The former consists of the first two lines in Eq. (3.44), i.e. the LMF-weighted exact-exchange kernel and the LMF-potential-weighted exact-exchange potential, where the LMF potential is contracted with the transition density matrix to form the matrix-vector product. The remaining terms contribute to the semi-local part of the local matrix-vector product. This also includes terms like the exact-exchange-weighted LMF kernel and the LMF-potential-weighted exact-exchange potential, with the exact-exchange potential being contracted with the transition density matrix. Although the latter two terms arise from non-local exact exchange and thus should apparently contribute to the non-local part of $v^{LH,+}_{\mu\nu,\sigma}$, the indices $\mu\nu$ evolve from a semi-local part, e.g. the LMF kernel or the LMF potential, thus contributing to the local matrix-vector product in the same way as pure semi-local functionals. While other classifications of the terms would be also possible, the present one provides the most beneficial partitioning for an implementation into a computer program. Note in addition that there is no contribution of the current-density response, described in Sec. 3.2.1, to $v^{LH,+}_{\mu\nu,\sigma}$ due to the anti-symmetry of the current-density response term with respect to an exchange of the indices of the semi-local potential operator.

Similarly to the symmetric case, the anti-symmetric LH local matrix-vector product reads

$$
\begin{aligned}
v^{LH,-}_{\mu\nu,\sigma} = &- g_\sigma \cdot \left[X_\mu \left(\mathbf{A}\mathbf{U}^\sigma \mathbf{X} \right)_\nu - \left(\mathbf{A}\mathbf{U}^\sigma \mathbf{X} \right)_\mu X_\nu \right] \\
&- \frac{1}{2} \sum_\varsigma \sum_{\kappa\lambda} U^\varsigma_{\kappa\lambda} \cdot \left(\hat{d}_{\kappa\lambda,\varsigma} - \hat{d}_{\lambda\kappa,\varsigma} \right) g_\sigma \cdot \left[X_\mu \left(\mathbf{A}\mathbf{D}^\sigma \mathbf{X} \right)_\nu + \left(\mathbf{A}\mathbf{D}^\sigma \mathbf{X} \right)_\mu X_\nu \right] \\
&- \sum_{\varsigma\vartheta} \sum_{\kappa\lambda} U^\vartheta_{\kappa\lambda} \cdot \left(\hat{d}_{\kappa\lambda,\vartheta} - \hat{d}_{\lambda\kappa,\vartheta} \right) g_\varsigma \cdot \hat{d}_{\mu\nu,\sigma} e^{sl}_{x,\varsigma} \\
&- \sum_\varsigma \hat{d}_{\mu\nu,\sigma} g_\varsigma \cdot \sum_\vartheta \sum_{\kappa\lambda} U^\vartheta_{\kappa\lambda} \cdot \left(\hat{d}_{\kappa\lambda,\vartheta} - \hat{d}_{\lambda\kappa,\vartheta} \right) e^{sl}_{x,\varsigma} \\
&- \sum_{\varsigma\vartheta} \sum_{\kappa\lambda} U^\vartheta_{\kappa\lambda} \cdot \hat{d}_{\mu\nu,\sigma} \left(\hat{d}_{\kappa\lambda,\vartheta} - \hat{d}_{\lambda\kappa,\vartheta} \right) g_\varsigma \cdot \left[\frac{1}{2} \left(\mathbf{X}^\mathrm{T} \mathbf{D}^\varsigma \mathbf{A}\mathbf{D}^\varsigma \mathbf{X} \right) + e^{sl}_{x,\varsigma} \right] \\
&+ \sum_{\varsigma\vartheta} \sum_{\kappa\lambda} (1 - g_\varsigma) \cdot U^\vartheta_{\kappa\lambda} \cdot \hat{d}_{\mu\nu,\sigma} \left(\hat{d}_{\kappa\lambda,\vartheta} - \hat{d}_{\lambda\kappa,\vartheta} \right) e^{sl}_{x,\varsigma} \\
&+ \sum_\varsigma \sum_{\kappa\lambda} U^\varsigma_{\kappa\lambda} \cdot \hat{d}_{\mu\nu,\sigma} \left(\hat{d}_{\kappa\lambda,\varsigma} - \hat{d}_{\lambda\kappa,\varsigma} \right) e^{sl}_c \ . \qquad (3.45)
\end{aligned}
$$

Assuming a current-free ground state and at most a current dependence of the local hybrid functional through the gauge-invariant kinetic energy density, as is the case in current-density-dependent meta-GGAs, the matrix-vector product reduces to

$$\begin{aligned} v^{LH,-}_{\mu\nu,\sigma} = &- g_\sigma \cdot \left[X_\mu \left(\mathbf{A}\mathbf{U}^\sigma \mathbf{X} \right)_\nu - \left(\mathbf{A}\mathbf{U}^\sigma \mathbf{X} \right)_\mu X_\nu \right] \\ &- \sum_\varsigma \sum_{\kappa\lambda} U^\sigma_{\kappa\lambda} \cdot \hat{d}_{\mu\nu,\sigma} \left(\hat{d}_{\kappa\lambda,\sigma} - \hat{d}_{\lambda\kappa,\sigma} \right) g_\varsigma \cdot \left[\frac{1}{2} \left(\mathbf{X}^\mathrm{T} \mathbf{D}^\varsigma \mathbf{A} \mathbf{D}^\varsigma \mathbf{X} \right) + e^{sl}_{x,\varsigma} \right] \\ &+ \sum_\varsigma \sum_{\kappa\lambda} \left(1 - g_\varsigma \right) \cdot U^\sigma_{\kappa\lambda} \cdot \hat{d}_{\mu\nu,\sigma} \left(\hat{d}_{\kappa\lambda,\sigma} - \hat{d}_{\lambda\kappa,\sigma} \right) e^{sl}_{x,\varsigma} \\ &+ \sum_{\kappa\lambda} U^\sigma_{\kappa\lambda} \cdot \hat{d}_{\mu\nu,\sigma} \left(\hat{d}_{\kappa\lambda,\sigma} - \hat{d}_{\lambda\kappa,\sigma} \right) e^{sl}_c \ , \end{aligned} \tag{3.46}$$

where, due to the anti-symmetry with respect to an index exchange of the semi-local potential operator, only the current-density response remains, so that the anti-symmetric part of the semi-local kernel operator explicitly reads

$$\hat{d}_{\mu\nu,\sigma} \left(\hat{d}_{\kappa\lambda,\sigma} - \hat{d}_{\lambda\kappa,\sigma} \right) = -\frac{1}{2} \left(X_\mu \nabla X_\nu - X_\nu \nabla X_\mu \right) \left(X_\kappa \nabla X_\lambda - X_\lambda \nabla X_\kappa \right) \frac{1}{\rho_\sigma} \frac{\delta}{\delta \tilde{\tau}_\sigma} \ . \tag{3.47}$$

Besides the current-density response, only the non-local LMF-weighted exact-exchange kernel in the first line is thus present in Eq. (3.46).

Note that the presented formulas describe the most general case, i.e. considering spin resolution of the density matrices. In the special case of a restricted ground state, i.e. $\mathbf{D}^\alpha = \mathbf{D}^\beta$, the solutions of Eq. (2.118) decompose into a set of singlet and triplet excitations. The respective matrix-vector products can simply be derived by considering the conditions

$$\mathbf{P}^\alpha = \mathbf{P}^\beta \ , \ \mathbf{U}^\alpha = \mathbf{U}^\beta \tag{3.48}$$

for singlet excitations and

$$\mathbf{P}^\alpha = -\mathbf{P}^\beta \ , \ \mathbf{U}^\alpha = -\mathbf{U}^\beta \tag{3.49}$$

for triplet excitations.

4. Implementation

On the basis of the formulas for the local hybrid matrix-vector products derived in the last chapter, this chapter deals with their implementation into a developer's version of the widely used quantum chemical program package TURBOMOLE.[19] After a brief examination of the program structure of the *escf* module, which contains the existing TDDFT implementation of TURBOMOLE, its extension to local hybrid functionals will be discussed. Besides a detailed explanation of the general structure of the new module, special attention will be paid to the efficiency of the implementation. In this context, an efficient matrix-vector multiplication, a generalization of S- and P-junctions to TDDFT and the memory requirements of the semi-numerical scheme within TDDFT will be discussed. In the subsequent technical evaluation of the semi-numerical implementation, its accuracy and timings will be considered. In general, this chapter thus features a more detailed explanation and analysis of the semi-numerical local hybrid TDDFT implementation first presented in Ref. 272 and thus in large parts contain results already presented there.

4.1. Existing Program Structure

Drawing on the efficient implementation of linear-response TDDFT within the TURBOMOLE program package,[20,259,279] the main task of the present work consists in the embedding of the local hybrid matrix-vector products (derivation see chapter 3) into the existing program structure to enable linear-response TDDFT calculations with local hybrid functionals. Therefore, the general structure of the *escf* module including its subroutines shall be analyzed in detail first.

A simplified schematic representation of the *escf* module structure is shown in Fig. 4.1. Starting from the main routine *escf*, which handles most of the general input needed for a TDDFT calculation such as information about the XC functional, the *respon* routine taking care of the most basic features of TDDFT is called. In particular, *respon* and its subroutines handle the read-in and record of the transition density matrices, where each excitation is described by one transition density matrix (in the MO basis) decomposed into its symmetric and anti-symmetric part $\mathbf{V}^+$ and $\mathbf{V}^-$, respectively, the read-in of the

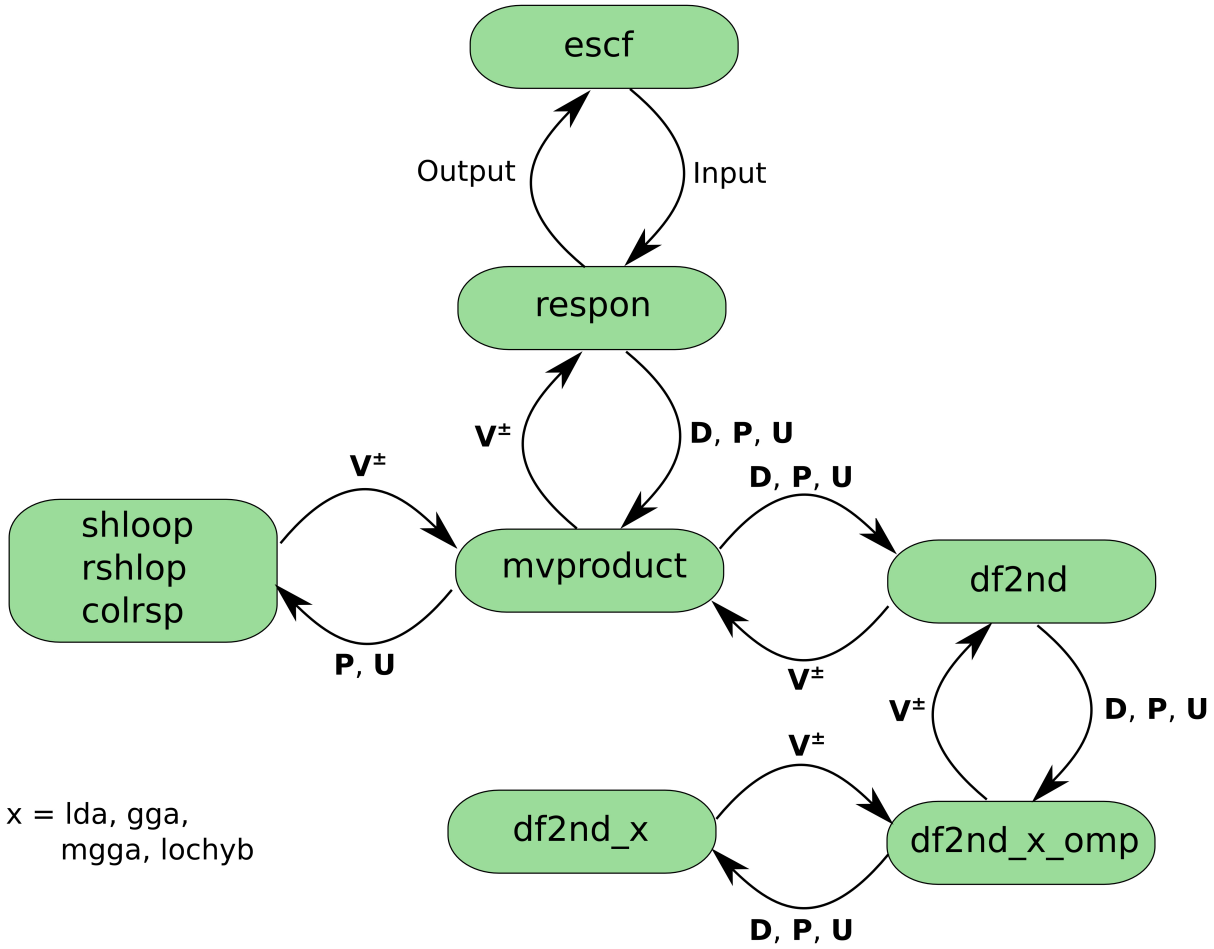

Figure 4.1.: Simplified schematic representation of the general structure of the *escf* module. Beginning from the main routine, the transfer of the density matrices **D**, **P** and **U** as well as the matrix-vector products $\mathbf{V}^{\pm}$ between the particular routines is illustrated (detailed explanations, see text).

ground-state density matrix **D**, as well as the iterative solution of the Casida's equations (2.118).[20,279–281] The latter requires the evaluation of the matrix-vector products (2.119), which are calculated within the *mvproduct* routine on the basis of the handed-over density matrices.

As first step, transition density matrices are transformed into the AO basis, so that they can be directly contracted with the molecular integrals in the AO basis (see Sec. 2.5 for details) to form the required matrix-vector products. Similarly to the direct-SCF method in ground-state DFT calculations,[242] the two-electron integrals themselves are evaluated within the so-called direct-CI method.[282] That is, instead of calculating analytical integrals once and saving them on disk, integrals are recalculated in each iteration step. Thereby, the matrix-vector products can be directly evaluated without storing the

integrals themselves, thus saving disk and main memory, as well as avoiding the repeated read-in of these integrals. The calculation of the Coulomb and the exact-exchange kernel (both calculated analytically) contracted with the transition density matrices is performed by the *rshlop* routine. In the case of semi-local functionals only the Coulomb contribution is required, which in contrast to exact exchange does not contribute to the anti-symmetric matrix-vector product. Hence, either *shloop* or *colrsp*, which both only consider symmetric transition density matrices, is used in these cases for the calculation of the Coulomb part. While in *shloop* integrals are calculated analytically, in *colrsp* the RI approximation is employed.[259] In the case of local hybrid functionals, the exact-exchange contributions to the matrix-vector products have to be calculated on the molecular grid, and thus *shloop* or *colrsp* is used for the Coulomb contribution, too.

Exchange and correlation contributions to the matrix-vector products calculated on the molecular grid are selected and added in the *df2nd* routine, where separate subroutines *df2nd_x* (with *x* being *lda*, *gga*, *mgga* or *lochyb*) for different kinds of XC functionals exist. The respective *df2nd_x_omp* routines handle the SMP (shared-memory multiprocessing). In the case of semi-local functionals, only the transition density matrices **P** and **U** and the precalculated semi-local quantities are handed over to the *df2nd_x* routines, since the ground-state density matrix **D** does not enter the matrix-vector products otherwise, and **D** does not change during the TDDFT calculation. On the other hand, regarding the symmetric and anti-symmetric local hybrid matrix-vector products (3.44) and (3.46), respectively, local hybrids exhibit also non-local contributions, which depend on the ground-state density matrix. Hence, instead of precalculating the semi-local quantities and the ground-state density matrix contracted with the basis function vectors for the whole molecular grid, which indeed requires much more memory than only the storage of the ground-state DFT quantities in the case of semi-local functionals, the ground-state density matrix is handed over to the *df2nd_lochyb* routine in addition to the transition density matrices, and semi-local quantities are recalculated in each iteration. As will be seen later, this does not deteriorate the overall performance.

After having added the XC contributions to the matrix-vector products, they are back-transformed within the *mvproduct* routine into the MO basis, so that the Casida's equations can be solved by the *respon* routine. The computationally most demanding part of such a linear-response TDDFT calculation is the determination of the matrix-vector products,[259] especially the analytical integrals (cf. Sec. 2.5). Hence, an efficient implementation of the latter is of utmost importance. Accordingly, the efficient implementation of the local hybrid matrix-vector products (3.44) and (3.46), which is realized in the *df2nd_lochyb* routine, will be explained and discussed in detail in the following section.

4.2. Implementation of the New Local Hybrid Module

4.2.1. Implementation Details

With the ground-state and transition density matrices being handed over, the *df2nd_lochyb* routine carries out the calculation of the local hybrid matrix-vector products. As described in Sec. 3.3, within the semi-numerical integration scheme, the latter is performed by summing up local matrix-vector products on a molecular grid, which consists of n grid points arranged in grid point batches of a certain size to ensure the optimal balance between the efficiency of the algebraic operations and the efficient use of locality of the semi-local quantities. Furthermore, local matrix-vector products are simultaneously calculated for the set of i excitations, chosen to be calculated by the user, to avoid the recalculation of analytical integrals for each excitation. The calculation of the local matrix-vector products themselves is done by a separation into several basic algebraic steps as is demonstrated by the COSX method (see Sec. 2.5.3 for details). The resulting module structure as implemented in the developer's version of TURBOMOLE is shown in Fig. 4.2. Additionally, formal scalings with respect to basis set size are given.

At the beginning of the TDDFT calculation S-junctions, as used in the COSX method to reduce the calculation cost of the $\mathbf{A}$ matrix and as will be discussed in detail in the following section, are determined once. While this step formally scales as N_{BF}^2, the actual scaling can be reduced to N_{BF} in the limit of large molecules by considering a distance criterium. Furthermore, it exhibits a small prefactor, so that the overall contribution to the calculation cost is negligible.

The actual determination of the local hybrid matrix-vector products begins with the batch-wise iteration over the n grid points, for which the local matrix-vector products (3.44) and (3.46) have to be calculated. For clarity, the dependence of local quantities on the space variable $\mathbf{r}$ is omitted again. Within the iteration over the grid points, all operations that have to be done only once for the set of i excitations are performed first. Initially, the basis function vector $\mathbf{X}$ is determined. Despite the formal linear scaling with the number of basis functions, a constant scaling is achievable for large molecules by applying a distance-based prescreening. Together with a small prefactor, this step thus contributes only little to the overall computational cost. The most important part of this step is the screening of $\mathbf{X}$ for non-zero elements. Therefore, the distinct number of k contributing elements, which do not exhibit zero values for the entire grid batch, is evaluated on the basis of the intermediate vector $\mathbf{X}_{max}$, whose elements are the maximum basis function values on the current grid batch. If higher spatial derivatives of $\mathbf{X}$ are required,

– Determine S-junctions	N_{BF}^2
▷ *Loop over grid points (batch wise):*	
– Evaluate basis function vector $\mathbf{X}$	N_{BF}
– Determine P-junctions	N_{BF}^2
– Perform matrix-vector multiplication $\mathbf{B}^\sigma = \mathbf{D}^\sigma\mathbf{X}$	N_{BF}^2
– Determine ground-state quantities $\mathbb{Q}$	N_{BF}
– Determine XC functional and LMF derivatives	1
– Calculate matrix $\mathbf{A}$	N_{BF}^2
– Perform matrix-vector multiplication $\mathbf{G}^\sigma = \mathbf{A}\mathbf{B}^\sigma$	N_{BF}^2
▷ *Loop over i excitations:*	
– Perform matrix-vector multiplication $\mathbf{B}^{\sigma,+} = \mathbf{P}^\sigma\mathbf{X}$	N_{BF}^2
– Perform matrix-vector multiplication $\mathbf{B}^{\sigma,-} = \mathbf{U}^\sigma\mathbf{X}$	N_{BF}^2
– Perform matrix-vector multiplication $\mathbf{G}^{\sigma,\pm} = \mathbf{A}\mathbf{B}^{\sigma,\pm}$	N_{BF}^2
– Calculate non-local parts of $\mathbf{G}_{nl,i}^{\sigma,\pm}$	N_{BF}
– Calculate semi-local parts of $\mathbf{G}_{sl,i}^{\sigma,\pm}$	1
– Build non-local part $\mathbf{v}_\sigma^{nl,\pm}$	N_{BF}^2
– Build semi-local part $\mathbf{v}_\sigma^{sl,\pm}$	N_{BF}^2

Figure 4.2.: Schematical representation of the individual steps done for the calculation of the local hybrid matrix-vector product as implemented in the *df2nd_lochyb* routine. For each step the formal scaling with respect to the number of basis functions N_{BF} is given in addition.

e.g. in the case of meta-GGAs, also their maximum absolute values are considered for the determination of $\mathbf{X}_{max}$. Due to the locality of the basis function vector, the number of k contributing elements does essentially not scale with the system size, resulting in significantly reduced computation costs in following steps.

In the ensuing step, P-junctions as in the COSX method are determined. While formally scaling as N_{BF}^2, they have to be evaluated only once for each grid batch, and a significant reduction of the scaling can be achieved by an optimized matrix-vector multiplication (see Sec. 4.2.3). Nevertheless, the original scheme for the determination of the P-junctions applied for ground-state calculations[265,270] cannot be used in the case of TDDFT, since $2 \cdot i + 1$ density matrices have to be considered instead of only one ground-state density matrix. Hence, a modified scheme, that is described in detail in Sec. 4.2.2, has to be applied. Next, the ground-state density matrix $\mathbf{D}$ is contracted with the basis function

vectors **X** of the grid point batch

$$B_\mu^\sigma = \sum_\nu D_{\mu\nu}^\sigma \cdot X_\nu \ , \tag{4.1}$$

finally allowing the calculation of the semi-local DFT quantities, e.g.

$$\rho_\sigma = \sum_\mu B_\mu^\sigma \cdot X_\mu \tag{4.2}$$

$$\nabla\rho_\sigma = 2\sum_\mu B_\mu^\sigma \cdot \nabla X_\mu \tag{4.3}$$

$$\tau_\sigma = \frac{1}{2}\sum_\mu \nabla^{\mathrm{T}} B_\mu^\sigma \cdot \nabla X_\mu \ . \tag{4.4}$$

As it is an ordinary matrix-vector multiplication, Eq. (4.1) formally scales as N_{BF}^2. If **B** is only needed for the calculation of semi-local quantities as in Eqs. (4.2) to (4.4), the locality of the basis function vector can be simply used to reduce the scaling to 1, since only the $k \times k$ part of the density matrix is required. Nevertheless, an efficent multiplication scheme (see Sec. 4.2.3) generally reduces the scaling, even in the case of local hybrids, which require the complete **B** vector. In addition, the density matrix does not depend on the space variable **r**, so that efficient BLAS (basic linear algebra subroutines) level 3 algebraic routines can be employed to accelerate the matrix multiplication. Note that for the determination of semi-local quantities needed by meta-GGAs also the first spatial derivatives of the basis function vector have to be contracted with the density matrix. Formal and reduced scaling (considering only k elements of **X**) of the Eqs. (4.2) to (4.4) are N_{BF} and 1, respectively, and accordingly they do not affect the overall cost of the calculation. The latter holds also true for the following calculation of the derivatives of the exchange-correlation functional and the LMF, which requires a constant amount of computation time irrespective of system size. On the other hand, the subsequent determination of the **A** matrix, which represents the most time-consuming part in a ground-state calculation, exhibits a formal scaling of N_{BF}^2, which can be reduced to 1 in the limit of large molecules by considering S- and P-junctions as in the COSX method. S- and P-junctions within a semi-numerical TDDFT calculation will be described in detail in the next section. Following the scheme in Fig. 4.2, the last step that has to be done only once per grid point is the contraction of the **A** matrix with the vector **B**

$$G_\mu^\sigma = \sum_\nu A_{\mu\nu} \cdot B_\nu^\sigma \ . \tag{4.5}$$

Similarly to the matrix-vector multiplication (4.1), Eq. (4.5) exhibits a formal scaling of N_{BF}^2, which can also be reduced by an efficient matrix vector multiplication. In contrast to the density matrix, the **A** matrix is different for each grid point, so that one could only make use of BLAS level 2 routines to perform the algebraic operations, which compared to BLAS level 3 routines provide less acceleration. Since in TURBOMOLE, symmetric matrices are additionally stored in a memory-efficient manner, a rearrangement is necessary to employ BLAS routines. In the case of the **A** matrices, the rearrangement thus would have to be done for each grid point separately. Hence, it turned out that a direct matrix vector multiplication without any rearrangements but consideration of rearranged matrix indices is more efficient than BLAS level 2 routines with a rearrangement.

Since in TDDFT, the excitation energies for the set of i excitations are determined in one run, the actual evaluation of the particular local matrix-vector products is done within an iteration over i excitations. For clarity, the excitation index is omitted in the following formulas. Similar to the ground state density matrix, the basis function vector is contracted first with the transition density matrices **P** and **U**

$$B_\mu^{\sigma,+} = \sum_\nu P_{\mu\nu}^\sigma \cdot X_\nu \tag{4.6}$$

$$B_\mu^{\sigma,-} = \sum_\nu U_{\mu\nu}^\sigma \cdot X_\nu \ , \tag{4.7}$$

which are then multiplied with the **A** matrix, too, to give

$$G_\mu^{\sigma,+} = \sum_\nu A_{\mu\nu} \cdot B_\mu^{\sigma,+} \tag{4.8}$$

$$G_\mu^{\sigma,-} = \sum_\nu A_{\mu\nu} \cdot B_\mu^{\sigma,-} \ . \tag{4.9}$$

Formal scaling and its reduction for large molecules is equal (or at least very similar as will be discussed later) to the ground-state cases (4.1) and (4.5), respectively. Non-local contributions to the local matrix-vector products as defined in Sec. 3.3 are then calculated by multiplying the intermediate $\mathbf{G}_{nl}$ vectors

$$G_{nl,\mu}^{\sigma,+} = -\, g_\sigma \cdot G_\mu^{\sigma,+} - \frac{1}{2} \sum_\varsigma \sum_{\kappa\lambda} P_{\kappa\lambda}^\varsigma \cdot \left(\hat{d}_{\kappa\lambda,\varsigma} + \hat{d}_{\lambda\kappa,\varsigma} \right) g_\sigma \cdot G_\mu^\sigma \tag{4.10}$$

$$G_{nl,\mu}^{\sigma,-} = -\, g_\sigma \cdot G_\mu^{\sigma,-} \tag{4.11}$$

with the basis function vectors

$$v^{nl,+}_{\sigma,\mu\nu} = X_\mu \cdot G^{\sigma,+}_{nl,\nu} + G^{\sigma,+}_{nl,\mu} \cdot X_\nu \tag{4.12}$$

$$v^{nl,-}_{\sigma,\mu\nu} = X_\mu \cdot G^{\sigma,-}_{nl,\nu} - G^{\sigma,-}_{nl,\mu} \cdot X_\nu \ . \tag{4.13}$$

While the first step, i.e. Eqs. (4.10) and (4.11), exhibits a formal scaling of N_{BF}, which for large molecules, is reducable to 1 by applying a simple prescreening for non-zero elements in $\mathbf{G}$, $\mathbf{G}^+$ and $\mathbf{G}^-$, the latter two equations formally scale as N^2_{BF}. Nevertheless, considering the locality of $\mathbf{X}$, i.e. only k non-zero elements, and a prescreening of $\mathbf{G}^+_{nl}$ and $\mathbf{G}^-_{nl}$ for non-zero elements, a scaling of 1 can be achieved in the limit of large molecules, too. Similarly, the remaining semi-local part of the local matrix-vector products is partitioned into

$$v^{sl,+}_{\sigma,\mu\nu} = X_\mu X_\nu \cdot G^{\sigma,+}_{xx,\mu} + \nabla^{\mathrm{T}} \left[X_\mu X_\nu\right] \cdot \mathbf{G}^{\sigma,+}_{dxx,\mu} + \nabla^{\mathrm{T}} X_\mu \nabla X_\nu \cdot G^{\sigma,+}_{dxdx,\mu} \tag{4.14}$$

$$v^{sl,-}_{\sigma,\mu\nu} = \left[\nabla^{\mathrm{T}} X_\mu X_\nu - X_\mu \nabla^{\mathrm{T}} X_\nu\right] \cdot \mathbf{G}^{\sigma,-}_{cdx,\mu} \ , \tag{4.15}$$

where the intermediate vectors $\mathbf{G}^+_{xx}$, $\mathbf{G}^+_{dxx}$, $\mathbf{G}^+_{dxdx}$ and $\mathbf{G}^-_{cdx}$ contain all semi-local terms contributing in their respective way to the local matrix-vector products. In particular, the individual terms have to be collected from the particular semi-local terms in Eqs. (3.44) and (3.46), respectively. While this procedure represents one of the most complex steps in the implementation due to the combinatorial complexity of second derivatives within the semi-local part of local hybrid functionals, the calculation of the intermediate vectors exhibits no scaling with respect to system size and thus contributes only little to the overall computation time. Note that this complexity is significantly enhanced, if additional semi-local quantities are considered (as will be done in a later chapter). On the other hand, Eqs. (4.14) and (4.15) formally scale as N^2_{BF}, which can be reduced to a constant scaling, if the locality of $\mathbf{X}$ is considered.

For the evaluation of the overall scaling behavior and computation cost of the newly implemented routine, the time-determining steps have to be identified first. As for ground-state calculations, the calculation of the $\mathbf{A}$ matrix represents the most time-consuming individual step, followed by its contraction with the $\mathbf{B}$ vectors. In addition, only the contraction of the density matrices with the basis function vectors and the final step in the construction of the matrix-vector products show significant contributions. Nevertheless, in a TDDFT calculation, the $\mathbf{A}$ matrix is contracted with $2 \cdot i + 1$ $\mathbf{B}$ vectors instead of only one within a ground-state calculation. The same holds true for the contraction of the basis function vector with the density matrices and the final step in the construction

of the matrix-vector product, which is equivalent to the last step in the construction of the Fock matrix in ground-state calculations. On the other hand, the **A** matrix has to be determined only once. Hence, in the limit of an infinite number of excitations, the calculation cost for the **A** matrix is negligible in comparison to the other mentioned steps, especially the contraction of the **A** matrix with the **B** vectors. Although in real TDDFT calculations only a limited number of i excitations is considered, the observation for an infinite number of excitations suggests that the influence of the efficiency of the matrix vector multiplication routines is more pronounced. Hence, special attention is paid to an efficient implementation of the matrix vector multiplication, which is described in detail in Sec. 4.2.3. Together with S- and P-junctions (see Sec. 4.2.2), the formal overall scaling of $i \cdot n \cdot N_{BF}^2$ can be then reduced to $i \cdot n$ in the limit of large molecules, i.e. a linear scaling with system size and the number of excitations.

4.2.2. S- and P-Junctions in Linear Response TDDFT

While efficient matrix-vector multiplication plays a more pronounced role in TDDFT than in ground-state calculations with local hybrids, the determination of the **A** matrix remains the most expensive individual step. Hence, its efficiency is of utmost importance. Following the strategy of the COSX method,[265] prescreenings with respect to the basis function overlap and the density matrices, i.e. S- and P-junctions, respectively, can be applied to significantly reduce the scaling with system size and the computation cost. The general idea of both prescreenings is to identify shell pairs that give zero contributions to the **A** matrix (or the **G** vector) for the entire grid batch, before its actual evaluation, so that two-center integrals for these shell pairs can be disregarded. While S- and P-junctions thus avoid the complete iteration over these shell pairs, integral estimates, which are additionally used to reduce the number of analytical integral calculations, require additional steps for each shell pair, so that, despite a large reduction of the computation cost, the formal scaling would not be reduced. Note that similar prescreenings are employed in the analytical evaluation of exact-exchange integrals within the LinK method of Ochsenfeld and co-workers.[243]

Relying on a pure basis function overlap criterium, the determination of S-junctions follows the identical procedure as in ground-state calculations,[265] i.e. constructing an imaginary sphere around each shell, so that outside its radius all basis functions of the respective shell exhibit negligible values (with respect to a certain threshold). Shell pairs with non-overlapping spheres are then disregarded for the evaluation of the **A** matrix. Note that this procedure is comparable to a simple screening with respect to basis function

overlap with the additional assumption that all shells are of s-type, i.e. having an angular momentum quantum number of 0. When only applying S-junctions, the formal scaling of the **A** matrix evaluation is reduced from N_{BF}^2 to a possible linear scaling, which is usually already achieved for medium-sized molecules.

P-junctions on the other hand feature a prescreening with respect to density matrices. In particular, only those shell pairs have to be considered for the evaluation of the **A** matrix, whose shells are connected by the density matrix to any of the k contributing basis functions on the distinct grid batch. This criterium is equivalent to a shell-wise screening of the **B** vector for non-negligible shells (with respect to threshold), followed by the construction of all remaining combinatorially possible shell pairs. In ground-state calculations only one density matrix is needed, so that this screening can be directly done for the **B** vectors on the current grid batch. On the other hand, $2 \cdot i + 1$ density matrices are involved in the case of linear response TDDFT. Here, the simplest procedure would be a common screening of the ground-state **B** vectors as well as all excited state **B** vectors. Nevertheless, since P-junctions have to be calculated before the evaluation of the **A** matrix, and **B** vectors in general shall not be calculated twice, additionally, $2 \cdot i \cdot n_{batch}$ **B** vectors with a dimension of N_{BF} would have to be stored in memory. For a batch size of $n_{batch} = 100$, an excitation number of $i = 50$, $N_{BF} = 1000$ basis functions and double-precision floating-point numbers, this is equivalent to an additional memory requirement of more than 200 MB. For larger molecules or if more excitations are reqired, e.g. for the calculation of X-ray absorption spectra, the additional memory might exceed several GB of main memory. Furthermore, TDDFT calculations in general exhibit larger main memory requirements, so that large additional memory usage is undesirable. The screening of all **B** vectors itself scales as $(2 \cdot i + 1) \cdot n \cdot N_{BF}$.

As alternative to this simple scheme, two memory-efficient procedures have been proposed.[272] In the first method, the $\mathbf{X}_{max}$ vector on the current grid batch is used for the evaluation of the P-junctions instead of all individual basis function vectors. Therefore, the intermediate vectors

$$B^{\sigma}_{max,\mu} = \sum_{\nu} D^{\sigma}_{\mu\nu} \cdot X_{max,\nu} \tag{4.16}$$

$$B^{\sigma,+}_{max,\mu} = \sum_{\nu} P^{\sigma}_{\mu\nu} \cdot X_{max,\nu} \tag{4.17}$$

$$B^{\sigma,-}_{max,\mu} = \sum_{\nu} U^{\sigma}_{\mu\nu} \cdot X_{max,\nu} \ , \tag{4.18}$$

have to be screened. Note that Eqs. (4.16) to (4.18) have to be determined only once per grid batch (and per excitation for the transition density matrices), reducing the prefactor of the screening by a factor of $1/n_{batch}$ compared to the simple method. Furthermore, the intermediate vectors cannot be reused in the subsequent steps, so that on one hand no additional main memory is required, but on the other hand, $2{\cdot}i{+}1$ additional matrix vector multiplications have to be performed for each grid batch, which nonetheless increases the calculation cost of the $\mathbf{B}$ vector evaluation only by a factor of $1 + 1/n_{batch}$. Hence, this additional step neither deteriorates the overall scaling nor the overall computation cost significantly.

Nevertheless, if a large number of excitations have to be calculated, the latter method might exhibit a non-negligible contribution to the overall calculation cost, which can be circumvented by applying the second approximate method for the determination of P-junctions[272] Here, the intermediate density matrix $\mathbf{D}_{max}$, whose elements are the maximum absolute values of all density matrices, is determined first. Multiplication with the $\mathbf{X}_{max}$ vector

$$B^{\sigma}_{max,\mu} = \sum_{\nu} D^{\sigma}_{max,\mu\nu} \cdot X_{max,\nu} \tag{4.19}$$

then allows a screening for non-contributing shell pairs. While the evaluation of $\mathbf{D}_{max}$ formally scales as $i \cdot N_{BF}^2$, consideration of the locality of the basis function vector reduces the scaling to $i \cdot N_{BF}$. Furthermore, this procedure exhibits a very small prefactor. The calculation of the intermediate $\mathbf{B}_{max}$ vector then requires only one additional matrix vector multiplication step per grid batch. Since the latter scales with 1 in the limit of large molecules, if an efficient scheme is utilized (see Sec. 4.2.3), the additional computation cost is almost negligible. As in the first method, no additional main memory is required.

While P-junctions determined with the simple scheme represent the most accurate procedure, the two presented alternative procedures provide only an approximate prescreening. Nevertheless, the latter two methods prevent the additional need of main memory for only a slight increase of the calculation cost. This is achieved by employing the maximum absolute quantities $\mathbf{D}_{max}$ and $\mathbf{X}_{max}$, which also ensures that no shell pairs are falsely disregarded by the approximate P-junctions. On the other hand, few shell pairs might be falsely not disregarded, which happens more likely with the second method. Considering these facts, the first approximate method represents the best compromise between an accurate determination of P-junctions and resource requirements for a moderate number of excitations, while for a large number of excitations the second method is the best choice.

Due to potentially high main memory requirements, the simple scheme is not used in the present implementation.

Evaluating the additional effect of P-junctions on top of S-junctions, the scaling of the **A** matrix calculation is potentially reduced from N_{BF} to 1 in the limit of large molecules, so that an overall linear scaling of n can be expected. While this holds true for ground-state calculations,[265,270] this is not the case for TDDFT calculations in general. Assuming all single excitations allowed by the particular basis set, each occupied molecular orbital would be connected to each virtual orbital by any transition density matrix. Furthermore, many atomic basis functions are already connected by the ground-state density matrix. As a result, almost all basis functions would be connected to each other, so that P-junctions yield only very few shell pairs, e.g. some core-core shell pairs, which can be disregarded for the **A** matrix calculation. In this case, only S-junctions would have a noticeable influence, so that the overall scaling of the **A** matrix evaluation would be $n \cdot N_{BF}$. While this apparently deteriorates linear scaling in local hybrid TDDFT calculations, one has to recall that in the limit of a large number of excitations the contraction of the **A** matrices with the **B** vectors represents the time-determining step, so that the **A** matrix evaluation itself does not determine the overall scaling. In particular, considering an optimized matrix vector multiplication as well as S- and P-junctions, the latter two steps exhibit the competing scalings of $n \cdot i$ and $n \cdot N_{BF}$ in the limit of large molecules. Since the maximum number of excitations i scales faster with system size than the number of basis functions (see Sec. 4.2.4 for an illustrative example), the overall scaling in the limit of all single excitations is determined by $n \cdot i$, which in general is equivalent to linear scaling with respect to the number of basis functions.

Nevertheless, usually only few excitations have to be calculated, so that the **A** matrix evaluation might be one of the time-determining steps. In this case, only few occupied molecular orbitals are connected to some virtual orbitals. Hence, P-junctions generally reduce the overall scaling of the **A** matrix calculation to n in the limit of large molecules, which has to be contrasted to S-junctions, which are already effective for medium-sized molecules. Accordingly, linear scaling $n \cdot i$ is achieved for the case of few excitations as well as in the limit of all single excitations, so that an overall linear scaling for the determination of the local hybrid matrix-vector products is achieved. S- and P-junctions thus also play an important role in linear response TDDFT with local hybrid functionals.

4.2.3. Optimized Matrix Vector Multiplication

As described in the previous sections, scaling and performance of the *df2nd_ lochyb* routine heavily rely on an efficient matrix vector multiplication scheme. In particular, the latter is required for the contraction of the basis function vector with the density matrices and for the contraction of the **B** vectors with the **A** matrices, whereas the former is also needed for the determination of P-junctions. With both operations being a multiplication of a $N_{BF} \times N_{BF}$ matrix with a N_{BF} vector, a scaling of N_{BF}^2 is expected, in general. Nevertheless, based on some properties of the involved vectors and matrices, a constant scaling can be achieved, which is schematically shown in Fig. 4.3.

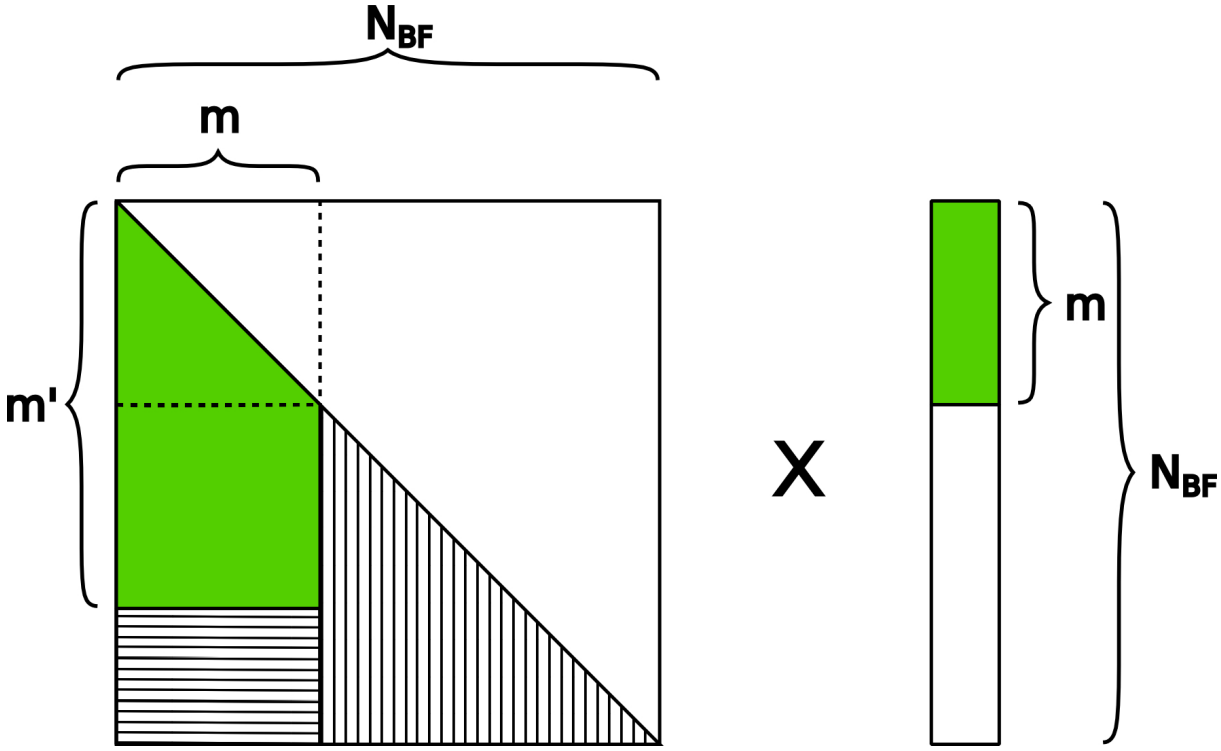

Figure 4.3.: Schematic representation of the optimized matrix vector multiplication scheme for a symmetric (or anti-symmetric) matrix and a vector with only m non-zero elements. The green blocks represent the elements of the matrix and the vector, which have to be considered in the multiplication. The resulting vector exhibits m' non-zero elements.

In particular, all $N_{BF} \times N_{BF}$ matrices involved are either symmetric or anti-symmetric, so that the number of floating point number multiplications, which represents the single time-determining step in a matrix-vector multiplication, is simply reduced from N_{BF}^2 to $\frac{1}{2}\left(N_{BF}^2 + N_{BF}\right)$. The second significant reduction can be made by considering only the m non-zero elements of the vector. In the case of the basis function vector **X**, this directly corresponds to the k contributing elements, while the **B** vectors have to be screened for zero

elements, which scales as N_{BF}. The latter can be accelerated by considering zero elements of the $\mathbf{B}_{max}$ vector, which has to be determined during the evaluation of P-junctions, so that the number of screening steps does not scale with system size anymore. Based on the reduced vector size, the number of floating point number multiplications needed for the matrix vector multiplication further reduces to $m\left(N_{BF} + \frac{1}{2}(1-m)\right)$, which is equivalent to considering the 'complete' trapezoidal part of the matrix (green and horizontally shaded regions in Fig. 4.3).

Last, the particular structure of the involved matrices can be considered additionally. That is, for large systems, the ground-state density matrix as well as the $\mathbf{A}$ matrices exhibit a diagonal band structure, so that many elements far from the diagonal are close to zero. Accordingly, many rows in the 'complete' trapezoidal part of the matrix can be expected to be zero, which holds also true for the transition density matrices, since transition density matrices usually connect only a few molecular orbitals. Applying a prescreening for the m' contributing rows of the 'complete' trapezoidal part, leads to a reduction of floating point number multiplications to $m\left(m' + \frac{1}{2}(1-m)\right)$, where the prescreening for the contraction of the density matrices with the basis function vector can be accelerated by estimating m' on the basis of $\mathbf{B}_{max}$. Regarding Fig. 4.3, application of all described preescreenings results ins a matrix vector multiplication, in which only the green part of the matrix, referred to as reduced trapezoidal part, is involved.

Regarding the reduced trapezoidal matrix vector multiplication, the number of floating point number multiplications does not depend on the number of basis functions, but on m and m', whose scaling in the limit of large molecules thus determines the overall scaling of the matrix vector multiplication. For the contraction of the basis function vector with the density matrices, m is equal to k and thus, exhibits a constant scaling, whereas m' is the number of non-zero elements of the respective $\mathbf{B}$ vector, which according to the mentioned properties of density matrices also does not scale with the system size. For the ensuing step of contracting the $\mathbf{B}$ vectors with the $\mathbf{A}$ matrices, m is equal to m' of the previous step and thus exhibits the same scaling with system size. Due to the diagonal band structure of the $\mathbf{A}$ matrix, the actual m', i.e. the number of non-zero elements in the respective $\mathbf{G}$ vector, shows also a constant scaling. Accordingly, the presented optimized matrix vector multiplication does not only feature a reduction of floating point number multiplications, but also provides a constant scaling for the matrix vector multiplication, so that an overall linear scaling for the evaluation of the local hybrid matrix-vector products is possible.

Technically, the matrix vector multiplication of symmetric matrices is split into two separate parts (see Fig. 4.3), i.e. a symmetric $m \times m$ part and the remaining $m \times (m' - m)$ part, so that symmetric and general BLAS routines can be optimally applied. The same

holds true for the by-hand multiplication of the **A** matrices (for details, see Sec. 4.2.1). On the other hand, the contraction of anti-symmetric density matrices with the basis function vectors is done by using the general matrix vector multiplication BLAS routine for the entire $m \times m'$ block, since no special anti-symmetric routine is available. Consideration of anti-symmetry applying a separate by-hand multiplication of the anti-symmetric $m \times m$ block turned out to be less efficient than the optimized BLAS routine. Nevertheless, the $m \cdot m'$ scaling of the latter step is comparable to the optimal scaling of $m\left(m' + \frac{1}{2}(1-m)\right)$ realized for symmetric matrices.

4.2.4. Memory Dilemma

As presented so far, the implemented *df2nd_lochyb* routine exhibits a linear scaling with respect to the number of grid points and the number of excitations, which is thus comparable to the efficiency of ground-state calculations. Nevertheless, one major drawback compared to the ground-state method is the significantly enhanced memory requirement, which shall be discussed in detail here.

In the *df2nd_lochyb* implementation, several quantities are simultaneously stored for each point of the grid batch, i.e. the basis function vector, three **B** vectors (one for the ground-state and two for the excited state), the respective **G** vectors, the ground-state quantities, derivatives of the LMF and the semi-local XC functional, as well as the **A** matrices. While each vector requires the storage of $n_{batch} \cdot N_{BF}$ double-precision floating-point numbers, ground-state quantities as well as LMF and XC functional derivatives take only a constant amount of memory, which scales as n_{batch}. With $n_{batch} \cdot \frac{1}{2}(N_{BF}^2 + N_{BF})$ stored double-precision floating-point numbers, most main memory is taken by the **A** matrices. Considering a usual TDDFT calculation with 20 excitations, 1000 basis functions and a batch size of $n_{batch} = 100$, the total memory requirement of the routine is around 390 MB, whereas 98% is taken by the **A** matrices. Since it is dominated by the **A** matrices, the amount of required main memory thus scales as $n_{batch} \cdot \frac{1}{2}(N_{BF}^2 + N_{BF})$. Nevertheless, also a large calculation with 4500 basis functions would take less than 8 GB of main memory in this setup, which is still feasible on common computers.

In an alternative possible implementation of the *df2nd_lochyb* routine, which is not implemented in the current developer's version of TURBOMOLE, the storage of the **A** matrices is circumvented by directly contracting them shell-pair-wise with all **B** vectors. In turn, the **B** and **G** vectors of each excitation have to be stored in memory, which in total are $n_{batch} \cdot (3 + 6 \cdot i)$ vectors of size N_{BF} instead of $9 \cdot n_{batch}$ vectors in the implemented version, thus leading to an overall scaling of the memory requirement of $n_{batch} \cdot N_{BF} \cdot$

$(3 + 6 \cdot i)$. Considering again 20 excitations, 1000 basis functions and a batch size of $n_{batch} = 100$, around 100 MB of main memory are required, while the large calculation with 4500 basis functions would need only around 430 MB, which is significantly lower than in the implemented version.

While the alternative version thus apparently exhibits less memory requirements than the implemented one, the memory demand scales linearly with the number of excitations. Hence, there is a cross-over in the memory demand compared to the implemented version, if a large number of excitations is considered, which might be necessary for large molecules or the calculation of complete X-ray absorption spectra. For example, the calculation of 10000 excitations for 1000 basis functions with a grid batch size of $n_{batch} = 100$ requires only 390 MB in the implemented version while more than 44 GB are required within the alternative scheme. Hence, depending on the calculation setup, either scheme might exhibit large memory requirements, which can be referred to as memory dilemma, since one of the two schemes has to be chosen, either the implemented scheme with a quadratic scaling of N_{BF}^2 or the alternative scheme with a scaling of $N_{BF} \cdot i$.

For a decent decision between both schemes, the scaling with respect to the number of basis functions and the number of excitations shall be compared with an increase of the system size. While scaling with the number of basis functions obviously is linear, the number of excitations scales quadratically with system size, if excitations of corresponding character shall be considered. The latter can be illustrated by the example of ethylene. While there is only one π–π^* excitation in the ethylene molecule, doubling of the system size, which is equivalent to the ethylene dimer, results in four separate π–π^* excitations (two of valence and charge-transfer type, respectively). In general, if system size is doubled, the number of occupied and virtual MOs is doubled as well, finally leading to four times the number of excitations. Hence, the implemented scheme scales only quadratically with the sysem size, while the alternative version, despite a smaller prefactor, shows a cubic scaling. Furthermore, due to the generally high computation cost, rarely more than 4500 basis functions are used in calculations with hybrid functionals, so that 8 GB can be regarded as upper bound in the implemented *df2nd_lochyb* routine, while the alternative version might exhibit even larger memory requirements. Accordingly, despite the memory dilemma, which cannot be solved completely, the present implementation represents the best balanced choice with respect to memory requirements.

4.3. Technical Evaluation

4.3.1. Computational Details

While the formal performance of the semi-numerical implementation of the local hybrid matrix-vector products has been extensively discussed in the last sections, the ensuing technical evaluation of the *df2nd_lochyb* routine is concerned with the analysis of its actual accuracy and computation cost for real molecular systems.

In the case of the accuracy analysis, the errors caused by the use of finite numerical integration grids as well as interdependencies between the basis set and the excitation type are investigated.[272] Therefore, a local hybrid with an unscaled t-LMF,[15] i.e. Eq. (2.76) with a factor of $a = 1.0$, in combination with Slater-Dirac exchange[74,75] and VWN correlation[76] is employed. For comparison, semi-numerical TDHF, which is a special case of Eq. (2.72) with $g_\sigma = 1.0$ and $E_c^{sl} = 0$, and the SVWN[74–76] LDA are also considered. Possible basis set effects are investigated using Dunning's correlation consistent basis sets,[283,284] while S- and P-junctions are analyzed separately and are thus switched off for the evaluation of grid-induced errors. Radial and spherical parts of the molecular grids are constructed on the basis of the commonly used Lebedev[248] and Chebyshev[244] grids, respectively, while the function M4 from Ref. 244 with a variable prefactor r_{map} is used for radial mapping. The partitioning function is kept fixed in the form proposed by Becke.[245] Based on the predefined numerical grids within TURBOMOLE,[244] the combination of a 110 point Lebedev and 25 point Chebyshev grid with $r_{map} = 1.0$ is referred to as small grid.

As test case for the analysis, the seven lowest-lying excitations of the CO molecule are used, i.e. three valence and four Rydberg excitations,[272] where the C-O distance of 1.128 Å is taken from Ref. 12. While analytical TDHF results serve as reference for semi-numerical TDHF calculations, the reference values for SVWN and the local hybrid functional are determined using a sufficiently large integration grid, i.e. a 1202 point Lebedev grid together with a 500 point Chebyshev grid and a radial mapping parameter of $r_{map} = 3.0$.[272] Ground-state and excitation energies are converged to $10^{-10} E_h$. The mean absolute deviation in eV between the reference and the (semi-)numerical results, separately determined for valence and Rydberg excitations, serves as measurement for the technical accuracy and will thus be denoted as mean absolute error (MAE). To be considered negligible in comparison to the accuracy of XC functionals with respect to vertical excitation test sets (see chapter 5), an MAE of 0.01 eV is regarded as target accuracy. Nevertheless, slightly larger deviations are still acceptable for many other purposes.

The influence of S- and P-junctions on the accuracy of the semi-numerical integration is determined for the lowest-lying valence excitation (^1B_u) of the decapentaene molecule in all-trans conformation, employing the local hybrid functional described above on the small grid together with the def2-TZVP [285] basis set. On the basis of the absolute error introduced by S- and P-junctions, different thresholds ranging from 10^{-10} a.u. to 10^{-3} a.u. are compared.

For the investigation of computational efficiency, the new semi-numerical implementation is compared to the existing analytical TURBOMOLE implementation by employing the TPSSh [106,107,124] global hybrid functional. Additionally, a local hybrid functional with a scaled t-LMF [185] (prefactor of 0.48) in combination with Slater-Dirac exchange [74,75] and VWN correlation [76] is used to evaluate any overhead arising in the semi-numerical scheme for local compared to global hybrids. [272] For an optimal performance, semi-numerical integration is combined with the RI approximation for Coulomb integrals, [265,267] while the present TURBOMOLE implementation of global hybrid functionals within TDDFT features only analytical four-center integrals.

For the efficiency analysis, the lowest-lying excitation of conjugated polyene chains in all-trans conformation with the molecular formula $C_{2i}H_{2i+2}$ ($i = 1 - 10$) is studied. While for longer polyene chains only the def2-TZVP basis is employed, calculations on the ethylene molecule are carried out with different basis sets, i.e. Dunning's cc-pVXZ, aug-cc-pVXZ and d-aug-cc-pVXZ (X=D,T,Q,5) basis sets [283,284] as well as Ahlrichs' def2-SVP, def2-TZVP and def2-QZVP basis sets, [285] indluding their variants with additional polarization and diffuse basis functions. The small grid and a threshold of 10^{-6} a.u. for S- and P-junctions are applied. All timings are measured on an Intel core i7-3770K processor.

4.3.2. Accuracy

As first step of the accuracy analysis, the basis set dependence of the semi-numerical implementation is investigated. Therefore, the MAE of the CO excitation energies has been determined for the set of Dunning's cc-pVXZ basis sets, with $X = D, T, Q$, as well as for their augmented variants aug-cc-pVXZ and d-aug-cc-pVXZ. In all cases the small grid is employed. Since results for different parent basis set sizes X do not differ qualitatively, effects shall be discussed only for the series of double-ζ basis sets, i.e. cc-pVDZ, aug-cc-pVDZ and d-aug-cc-pVDZ. The respective MAEs for the considered Rydberg and valence excitations are shown in Fig. 4.4. Note again that given MAEs characterize only the accuracy of the numerical grid and are not related to the accuracy of the local hybrid functional itself. While for valence excitations, accurate results with MAEs of less than

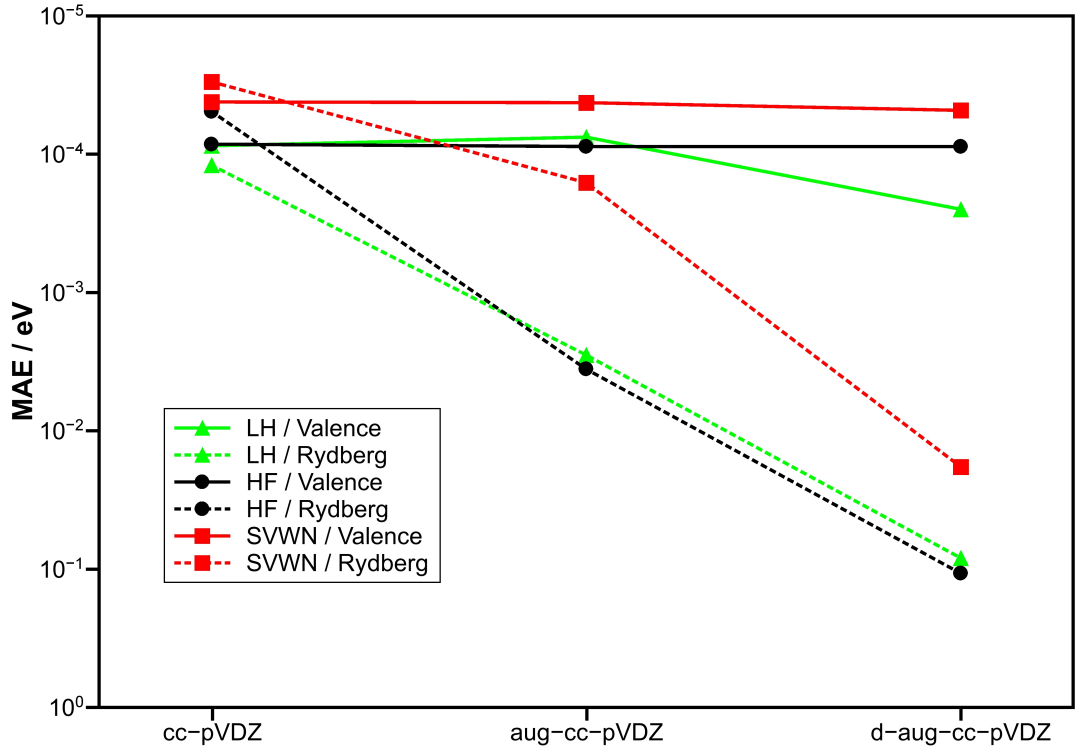

Figure 4.4.: MAE in eV for the low-lying valence and Rydberg excitations of CO for Dunning's double-ζ basis set with increasing basis set augmentation. The small grid is applied.

0.001 eV are obtained with all basis sets, for Rydberg excitations, a significantly decreasing accuracy with respect to basis set augmentation is observed. For the doubly augmented basis set in particular, TDHF and the local hybrid functional exhibit deviations of around 0.1 eV from the reference data, which in fact is one order of magnitude above the target accuracy. Although the behavior is similar for SVWN, the MAE of 0.02 eV with the d-aug-cc-pVDZ basis set is still acceptable due to the generally large underestimation of Rydberg excitations by semi-local functionals (see chapter 5). For the non-diffuse cc-pVDZ basis set on the other hand, Rydberg excitations are as well described as valence excitations. Since augmented basis sets are nonetheless needed for an accurate description of Rydberg excitations, the larger deviations for semi-numerical TDHF and local hybrid results with the chosen grid are investigated further. In particular, the d-aug-cc-pVDZ basis set is used for this purpose (and the remaining grid analysis).

For Rydberg excitations, it is apparently important within the semi-numerical integration scheme to account for the additional space spanned by diffuse basis functions compared to non-diffuse basis sets. Therefore, the numerical grid shall be systematically modified. In this context, the effect of the radial grid parameters, i.e. the number of radial

grid points N_{rad} of the Chebshev grid and the relative radial mapping parameter r_{map}, shall be analyzed first. Therefore, the spherical grid is set to a large 1202 point Lebedev grid, so that numerical errors are predominantly related to the radial grid. The variation of the relative radial mapping parameter r_{map} shifts the center of radial grid points. Values larger than 1.0 give more diffuse grids, while smaller values result in a contracted grid. The screening of r_{map} for a small ($N_{rad} = 25$) and a large ($N_{rad} = 150$) radial grid is shown in Fig. 4.5. While contracted grids expectedly exhibit larger errors, the accuracy for the

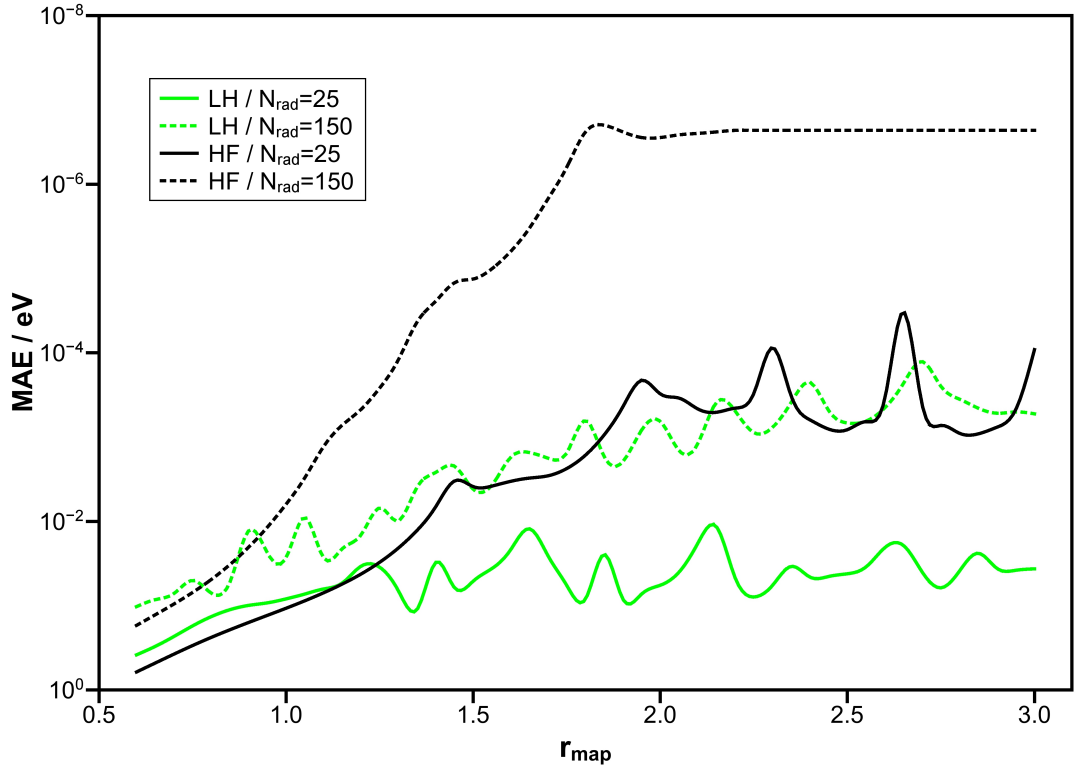

Figure 4.5.: Dependence of the MAE (in eV) on the radial mapping parameter r_{map} for the low-lying CO Rydberg excitations, calculated with the d-aug-cc-pVDZ basis set and a 1202 point Lebedev grid for Chebyshev grids with $N_{rad} = 25$ and $N_{rad} = 150$ radial grid points.

considered Rydberg excitations generally increases for more diffuse grids. In the case of semi-numerical TDHF, the target accuracy is already reached with $r_{map} = 1.0$, if a large radial grid is employed. Convergence is achieved for values larger than $r_{map} = 2.0$. On the other hand, a mapping parameter of $r_{map} = 1.4$ is necessary to reach the target accuracy with the small radial grid, while no convergence with respect to the radial mapping parameter is observed. In the case of the local hybrid functional, the target accuracy cannot be reached with the smaller grid, even by maximizing the mapping parameter, whereas a value of about $r_{map} = 1.5$ is required to obtain accurate results with the large radial

grid. In both cases, the accuracy does not converge with respect to the radial mapping parameter, which results in significant oscillations. Compared to semi-numerical TDHF, the local hybrid functional generally shows a decreased accuracy as well as as a more pronounced sensitivity with respect to r_{map}. Most likely, both phenomena directly arise due to the functional form of local hybrids (see Sec. 2.3.1 for details), where the error is determined by the product of the LMF and the exact-exchange energy density rather than only the exact-exchange energy density. In contrast to semi-numerical TDHF, the LMF features steep changes in certain regions of real space,[286] so that a large number of grid points is required there to ensure an accurate integration of exact exchange. For example, steep changes of the LMF occur between valence and one-electron regions, which in fact are both sampled by Rydberg excitations.[286] Consequently, a more balanced grid is required that accounts for the local exact-exchange admixture and covers the additional space spanned by the diffuse basis functions,[272] which is indeed not achievable by simply shifting the center of the existing grid points.

In addition to the mapping parameter, the dependence on the number of radial grid points N_{rad} is thus investigated. This is illustrated in Fig. 4.6 for a non-diffuse and a diffuse grid with $r_{map} = 1.0$ and $r_{map} = 2.0$, respectively. In combination with the small mapping parameter, semi-numerical TDHF needs a large number of about 125 radial grid points to reach an accuracy of at least 0.01 eV, while already 25 grid points are sufficient for $r_{map} = 2.0$. Despite a strictly decreasing MAE, results for $r_{map} = 1.0$ do not converge for the investigated range of N_{rad}. In addition, the MAEs remain several orders of magnitude above the converged value obtained with the large mapping parameter. On the other hand, the local hybrid functional could not satisfy the accuracy criterion with the non-diffuse grid, whereas with the diffuse grid, it is reached with 55 radial grid points. In both cases, oscillations are observed again, preventing a convergence within the chosen range of N_{rad}. Similar to the screening of r_{map}, this effect is directly related to the functional form of local hybrids.

Based on the findings for the radial grid, the analysis of the dependence on the spherical grid size is performed with a large and diffuse grid ($r_{map} = 2.0$ and $N_{rad} = 150$), to ensure an accuracy of at least 0.01 eV. Besides Rydberg excitations, valence excitations are considered for comparison again. The screening of seven different Lebedev grids with N_{sphe} grid points is shown in Fig. 4.7. For semi-numerical TDHF, the accuracy for Rydberg and valence excitations increases with the number of spherical grid points, where the MAEs converge to values between 10^{-6} eV and 10^{-7} eV. Although exhibiting similarly large errors, local hybrid valence excitations on the other hand do not reach convergence with the largest employed Lebedev grid. Apparently, local hybrid Rydberg excitations are not

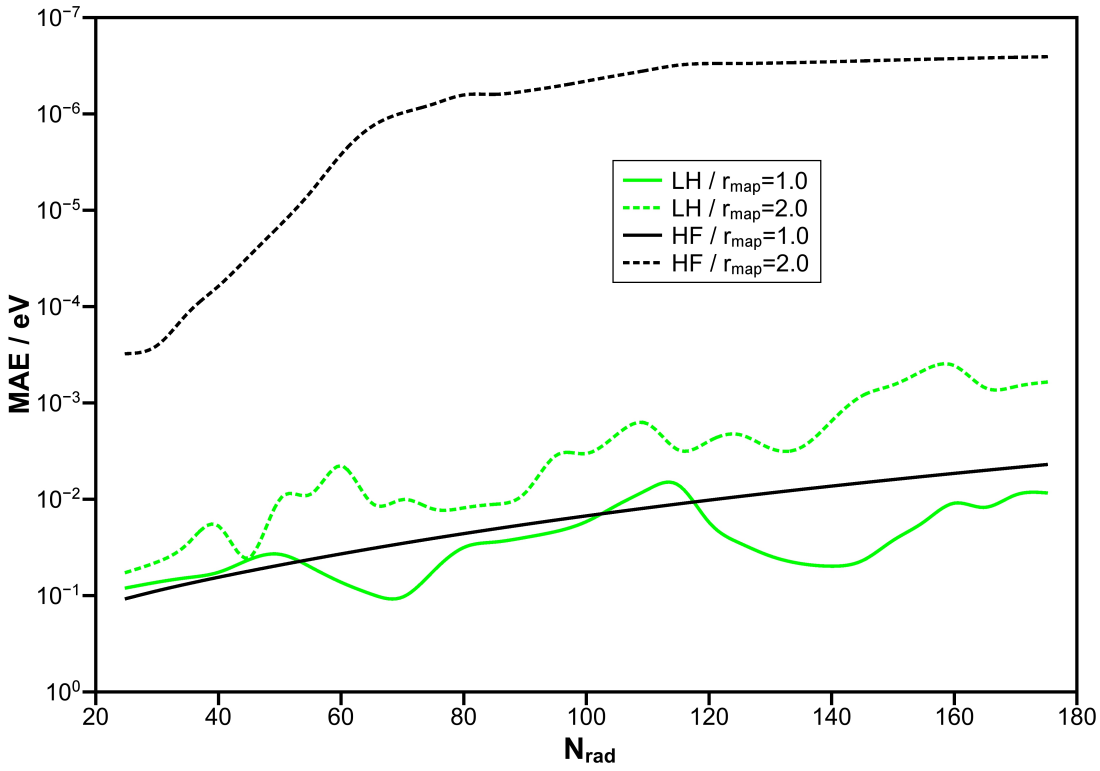

Figure 4.6.: Dependence of the MAE (in eV) on the number of radial grid points N_{rad} (Chebyshev grid) for the low-lying CO Rydberg excitations, calculated with the d-aug-cc-pVDZ basis set and a 1202 point Lebedev grid for the radial mapping parameters $r_{map} = 1.0$ and $r_{map} = 2.0$

affected by an increased spherical grid size. Most probably, their accuracy is limited by regions with steep transitions between local and exact exchange, which in the case of Rydberg excitations, mainly occur in the radial distribution. Hence, Rydberg excitations do not benefit from an increased spherical grid.[272]

The employed example of the seven lowest lying excitations of the CO molecule shows that, for local hybrid calulations, a satisfying accuracy of valence excitations is already achieved with small spherical and radial grids. On the other hand, Rydberg excitations require modifications of the radial grid, when diffuse basis sets are used. Besides a moderate augmentation of the number of radial grid points, the use of diffuse grids, i.e. an increased relative radial mapping parameter r_{map}, is inherently needed to reach a target accuracy beyond 0.01 eV.[272] That is, 'diffuse states require diffuse basis functions and diffuse grids'.[272] Accordingly, a radial mapping parameter of at least $r_{map} = 2.0$ and an additional number of around 20 radial grid points is recommended for the calculation of Rydberg excitations with local hybrid functionals. For higher-lying Rydberg states, most probably even more diffuse and larger grids are required. While semi-numerical

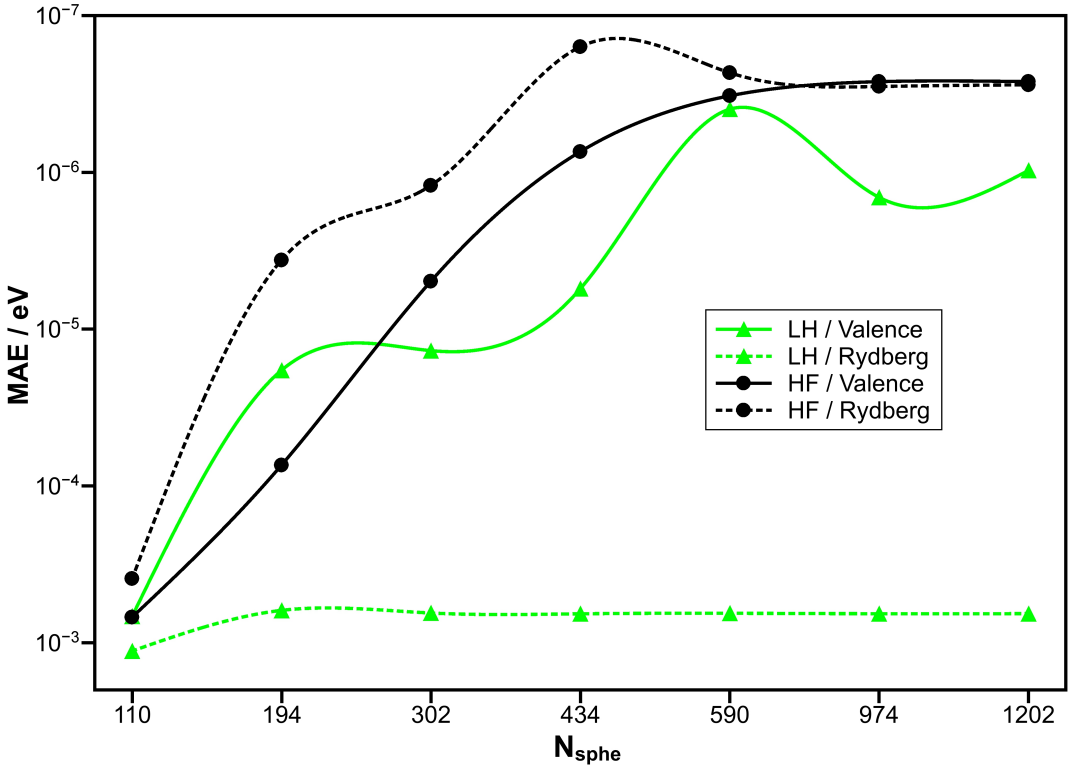

Figure 4.7.: Dependence of the MAE (in eV) on the number of sperical grid points N_{sphe} (Lebedev grid) for the low-lying valence and Rydberg excitations of the CO molecule. A 150 point Chebyshev grid, a mapping parameter $r_{map} = 2.0$ and the d-aug-cc-pVDZ basis set are applied.

TDHF is less sensitive than local hybrid functionals, an overall comparable dependence with respect to the grid parameters could be observed. Hence, other methods employing semi-numerical integration of exact exchange such as the COSX[266] or the pseudospectral method[264] should behave similarly with respect to the numerical grid.

While S- and P-junctions, as discussed in Sec. 4.2.2, formally enable linear scaling of the semi-numerical integration, their actual effectiveness might be limited by accuracy issues. Therefore, the numerical errors introduced separately by both approximations have been evaluated for the decapentaene molecule. In the entire range of screened thresholds between 10^{-3} a.u. and 10^{-10} a.u., use of S-junctions gave stable TDDFT results. For moderate thresholds ranging from 10^{-6} a.u. to 10^{-10} a.u., deviations of around 10^{-5} eV are obtained, while already around one third of the shell pairs of the **A** matrix could be neglected. Looser thresholds resulted in errors of up to 10^{-3} eV, but allowing the neglect of almost half of the **A** matrix shell pairs. S-junctions thus allow substantial computational savings in general.

On the other hand, P-junctions affected calculations only for thresholds looser than 10^{-7} a.u., otherwise no shell pair was neglected for any grid point batch. While thresholds below 10^{-5} a.u. resulted in non-converging TDDFT calculations, with thresholds of 10^{-6} a.u. and 10^{-5} a.u. only less than one shell pair was neglected on average. Accordingly, no significant errors are observed in the latter cases. While P-junctions are thus not very effective for the investigated molecule, larger effects are expected for larger molecules. Nevertheless, thresholds below 10^{-5} a.u. are definitely not recommended due to the deteriorated TDDFT convergence, which limits the effectiveness of P-junctions to very large molecules.

Based on the observed errors, thresholds of 10^{-6} a.u. for both approximations are considered as providing reasonable results.[272] For higher accuracies, thresholds of 10^{-10} a.u. and tighter are recommended.

4.3.3. Timings

As first part of the efficiency analysis of the new implementation, the performance with an extension of system size for a given basis set is evaluated. Therefore, the lowest-lying excitation of conjugated polyene chains of different length is calculated with the def2-TZVP basis set. In contrast to bulkier molecules, polyene chains allow maximal time savings due to non-overlapping basis functions.[272] Since analytical four-center integral calculation features two overlap screenings, compared to only one in the case of the **A** matrix evaluation within the semi-numerical scheme, analytical integration benefits more in this case. Furthermore, the linear growth of the integration grid with respect to system size is unavoidable and the medium-sized def2-TZVP basis does not favor the formal quadratic scaling of the semi-numerical scheme with respect to the number of basis functions. Hence, the chosen model systems represent the worst case for a comparison with an analytical implementation. The CPU times per TDDFT iteration t for the increasing polyene chains as well as fitted scalings with respect to the number of primitive basis functions N_{prim} are shown in Fig. 4.8. Due to large relative errors for small t values, ethylene and butadiene are neglected for the fits. Despite the formal preference of the analytical integration (see above), the semi-numerical scheme is faster for all molecules larger than butadiene, which is accompanied by an additionally better scaling behavior. The overhead of the local hybrid functional compared to the global hybrid is not significant. Note that larger basis sets or non-linear molecules would further increase the preference for the semi-numerical algorithm due to the scaling properties and the less important overlap screening.[272] As P-junctions are not yet effective even for the largest molecule studied, i.e. decapentaene,

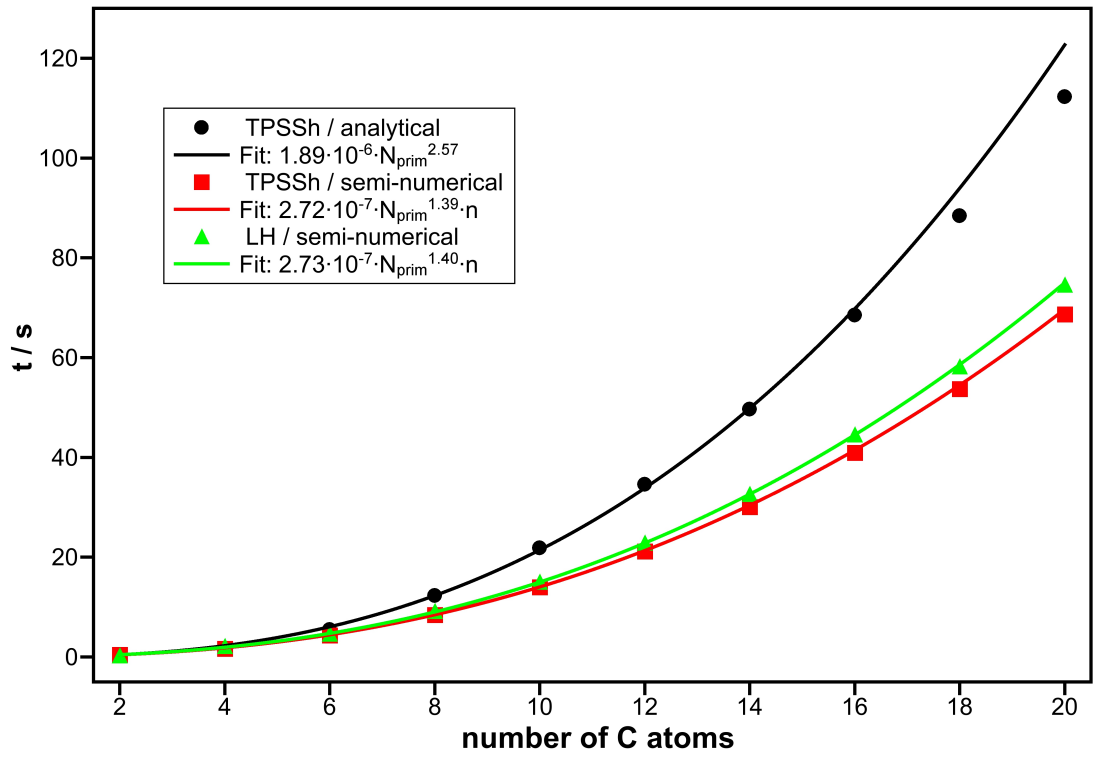

Figure 4.8.: Scaling of the computation time per TDDFT iteration t with respect to the number of C atoms in polyene chains with increasing length using the def2-TZVP basis. The fits with respect to the number of primitive basis functions N_{prim} are done for logarithmic scales.

sub-quadratic scaling is not yet reached for the investigated molecules. Nevertheless, for very large molecules, which are not explicitly considered here, such sub-quadratic scaling is expected for the present semi-numerical implementation.

To evaluate the efficiency with respect to basis set size, timings for the calculation of the lowest-lying excitation of ethylene are measured. Therefore, Dunning's cc-pVXZ, aug-cc-pVXZ and d-aug-cc-pVXZ (X=D,T,Q,5) basis sets, as well as Ahlrichs' def2-type basis sets, i.e. SVP, SVPD, TZVP, TZVPP, TZVPD, TZVPPD, QZVP and QZVPD, are employed. TDDFT iteration times t are shown in Fig. 4.9 with respect to the number of primitive basis functions N_{prim}. Due to its formal quadratic scaling, the increase of only the basis set size favors the semi-numerical integration compared to the analytical algorithm. Furthermore, screenings are naturally not effective for the small ethylene molecule. Accordingly, the semi-numerical integration exhibits only approximately half the scaling of the analytical implementation. Nevertheless, due to the additional scaling of the integral evaluation with respect to the angular momentum quantum number l related to a basis function, i.e. l^5 for two-center and l^{10} for four-center integrals, formal quadratic scal-

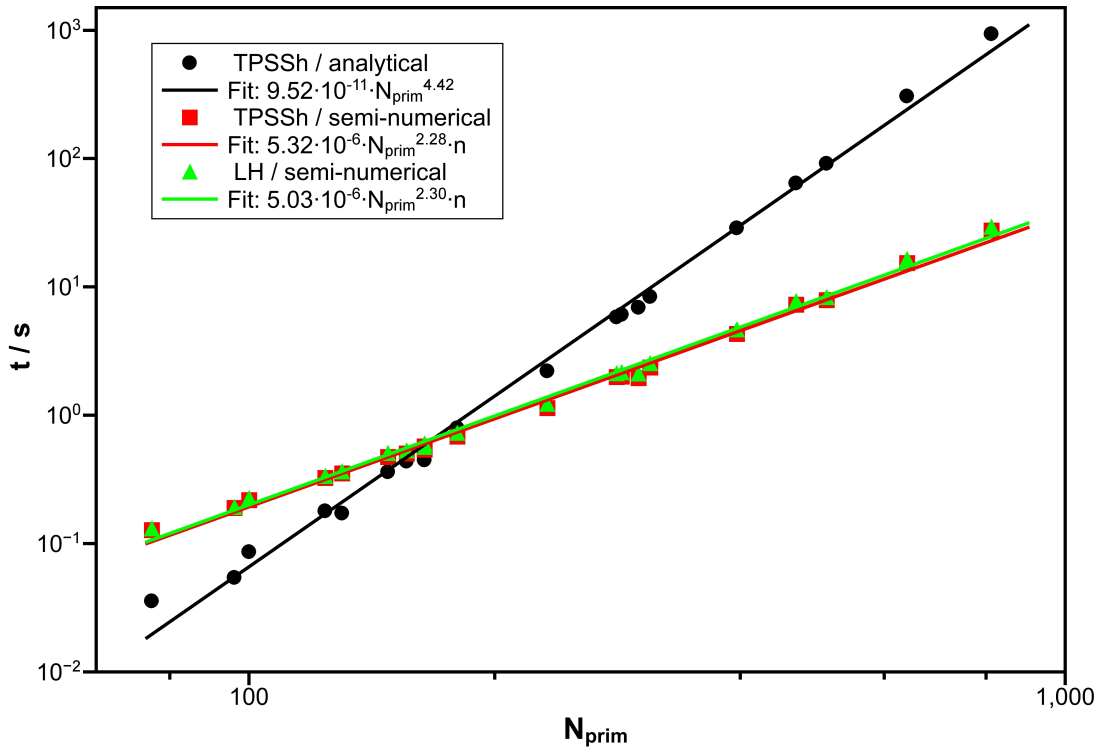

Figure 4.9.: Scaling of computation time per TDDFT iteration t with respect to the number of primitive basis functions N_{prim} for the ethene molecule using different basis sets, i.e Dunning's (d-aug-)cc-pVXZ (X=D,T,Q,5) basis sets and Ahlrichs' def2-type basis sets.

ing could not be reached. Again, no significant overhead is observed for the local hybrid functional.

So far, the efficiency of the new implementation has been investigated only on a single processor. Nevertheless, a shared-memory paralellization has been additionally implemented to enable paralellized calculations on a single node with several processors sharing the same memory. This has been done by an ideal distribution of the grid batches to the distinct processors. Hence, the only step causing an overhead is the last step in the construction of the matrix-vector products, since only one process at a time is allowed to write on the respective array. Nevertheless, in the limit of infinite large molecules, the overall calculation time is almost exclusively determined by the evaluation of the **A** matrices and their contraction with the **B** vectors (cf. Sec. 4.2.1). Hence, the present implementation is virtually ideally parallelized in this case, while for real molecular systems an overhead is expected, which nonetheless mainly depends on the system size of the test case rather than on the quality of the parallelization. Hence, a more detailed analysis of the SMP parallelized version is omitted.

4.4. Conclusions

In the present chapter, the new semi-numerical implementation of local hybrid functionals into the *escf* module of a developer's versions of the quantum chemical program package TURBOMOLE has been presented. Based on a detailed discussion of all individual steps required for the calculation of the local hybrid matrix vector products, it could be shown, that the efficiency of the code depends in particular on an efficient computation of the **A** matrix as well as on an efficient matrix-vector multiplication. While the former could be achieved by extending the conventional determination of P-junctions within ground-state calculations to a larger number of density matrices, for the latter, an optimized procedure employing several prescreenings has been used. Overall, a formal linear scaling could be achieved, while a distinct compromise had to be made with respect to memory requirements due to the simultaneous treatment of many excitations within one TDDFT calculation. During the technical evaluation of the implementation, it thus turned out that the new local hybrid module, if combined with the RI-J approximation for Coulomb integrals, is generally faster than the previous global hybrid TDDFT implementation, where the largest accelerations could be obtained for large basis sets. Despite some additional terms, local hybrids appear to be as efficient as global hybrid functionals with the new semi-numerical implementation. Concerning the accuracy of the semi-numerical implementation, it could be shown that relatively small numerical grids already suffice for an accurate description of most vertical excitations. Here, Rydberg excitations calculated with diffuse basis sets were identified as one exception, since more diffuse grids were needed. This allows the conclusion, that the description of diffuse states generally requires diffuse basis functions and thus also diffuse grids.

5. Validation

Drawing on the efficient TDDFT implementation of local hybrid functionals presented in the last chapter, the present chapter is concerned with the first evaluation of the actual performance of different local hybrid functionals for vertical excitations compared to other popular XC functionals. Therefore, the vertical-excitation test sets of Thiel and co-workers[287–289] as well as those of Tozer and co-workers,[12,290] which cover a large variety of different excitation types including many cases that are prolematic for common XC functionals, have been employed. Additionally, intermolecular charge-transfer (CT) is further investigated using the tetrafluoroethylene ethylene complex.[8,13] Besides, additional effects either related to TDDFT or local hybrid functionals, e.g. to the current-density response, common LMFs and the TDA, are studied in detail, too. The present chapter is thus a reproduction of the results already published in Ref. 286.

5.1. Computational Details

5.1.1. Investigated Vertical Excitations

For a decent analysis of the performance of local hybrid functionals for the calculation of vertical excitation energies within linear-response TDDFT, a broad range of different excitation types shall be investigated. While 'local' valence excitations with single-excitation character are generally well described by most XC functionals, several challenging cases have been discovered. Besides the issue of double excitations and the adiabatic approximation,[1,11] which are both directly related to the general approach of adiabatic linear-response TDDFT rather than the underlying XC functional, conventional functionals usually underestimate charge-transfer,[7–9] Rydberg[10,11] and core excitation energies[12] significantly. The application of hybrid functionals is known to mitigate these problems,[8,14] especially range-separated hybrid functionals[12,144] are a very popular choice to improve upon the excitation energies of CT type, Rydberg and to some extent core excitations.[290] However, as more and more different systems are studied, limitations in the flexibility of range-separated hybrids, typically due to the range-separation parameter, have also be-

come apparent.[150] For example, the optimal range-separation parameter, determined with non-empirical tuning, exhibits a substantial dependence on the system and chromophor size.[150,151] Besides, time-dependent self-interaction corrections represent another attempt towards an improved description of CT excitations.[291,292] Nevertheless, so far no XC functional performs excellently for all kinds of excitations and for very different systems.[286]

For the purpose of comparing the performance of different kinds of XC functionals, one usually relies on distinct vertical-excitation test sets.[293,294] In particular, the test sets of Thiel and co-workers[287–289] as well as those of Tozer and co-workers[12,290] are employed in the present work. The Thiel test set covers a large variety of 167 valence excitations of smaller organic molecules grouped into hydrocarbons, aromatics, carbonyls and nucleobases. In total, 104 singlet and 63 triplet excitations, identified not to exhibit valence-Rydberg mixing and thus not to be affected much by the use of diffuse basis functions, are considered and will therefore be distinguished in the present work. As reference data, best estimates, derived from high-level wavefunction methods such as CC3 and CASPT2 together with the TZVP basis set[295] augmented by information from still higher levels, e.g. larger basis sets with diffuse basis functions,[287] are used. In the revised version of the test set,[289] Thiel and co-workers updated their former theoretical best estimates based on coupled-cluster calculations directly employing an augmented triple-ζ basis set and on new CASPT2 results, which nonetheless only negligibly influences the relative performance of different XC functionals. For simplicity, the original best estimates from Ref. 287 for the TZVP basis set are thus used. Following the evaluation of several XC functionals in Ref. 288, the 1^1B_{3g} state of s-tetrazine is disregarded for the statistical evaluation due to its double-excitation character, which in fact cannot be covered by linear-response TDDFT within the adiabatic approximation. Accordingly, only 166 valence excitations (103 singlet and 63 triplet excitations) are considered. In addition to ground-state excitation energies, energy differences between low-lying excited states have been determined. In total, 27 $S_2 - S_1$, 19 $S_1 - T_1$ and 19 $T_2 - T_1$ energy differences relying on the state ordering of the best estimates in Ref. 287 are considered. Oscillator strengths are disregarded due to larger uncertainties in the currently available benchmark data.

Rydberg and intramolecular CT excitations are in the focus of a test set developed by Tozer and co-workers.[12] In particular, it consists of 13 Rydberg excitations of three small molecules (CO, N_2 and formaldehyde), for which experimental gas phase excitation energies are known, as well as of 14 intramolecular charge-transfer excitations arising from three model peptides, N-Phenylpyrrole, 4-(N,N-dimethylamino)benzonitrile and the HCl

molecule, for which theoretical references are used. In addition, 32 valence excitations of the already considered molecules as well as of polyacetylenes and acenes are also included, which are nonetheless less suited as benchmark compared to those of the larger Thiel test set. Furthermore, only singlet excitations are considered. For some of the test set molecules, new reference values and triplet excitations are given in a later publication.[296] Nevertheless, only a subset of the original test set was considered, so that the original references are used in the present work. Furthermore, triplet excitations of Rydberg and CT character are expected to give similar excitation energies as their singlet counterparts due to their longe-range character.[286] Since for long-range excitations, the difference between singlet and triplet exitations becomes very small, consideration of the respective singlet excitations is sufficient for the purpose of the present benchmark. The more pronounced differences for valence excitations are already covered by the Thiel test set. Accordingly, the original test set together with the primarily used basis sets, i.e. d-aug-cc-pVTZ for CO, N_2 and formaldehyde and cc-pVTZ for all other molecules,[283,284] is employed.[12]

Core excitations are analyzed on the basis of another test set of Tozer and co-workers.[290] While the complete test set features references for core excitations of first- and second-row elements, only first-row element compounds are considered in the present work, since relativistic effects on the respective 1s orbitals are small and can be corrected easily.[286] In contrast, significant basis set and finite-nucleus effects on the relativistic corrections for the 1s orbitals of second-row elements are suggested by test calculations on the H_2S molecule. Since a closer inspection of these effects would be required, which is beyond the scope of the present work, second-row element core excitations are excluded as references. Hence, only the 25 core excitations of first-row elements, divided into 9 core-valence and 16 core-Rydberg type excitations, are considered. For all molecules, Dunning's d-aug-cc-pVTZ basis sets[283,284] are used. Relativistic 1s orbital shifts for the molecules in question are calculated at the HF/aug-cc-pCVQZ-DK[297] level (aug-cc-pVQZ-DK for hydrogen atoms) using the one-component X2C method in its TURBOMOLE implementation.[298,299] While being separately calculated for each molecule, relativistic shifts for a given atom type are similar, i.e. approximately 0.12 eV, 0.24 eV, 0.45 eV and 0.75 eV for C, N, O and F, respectively. One-component X2C TDHF calculations did not show any additional effects. Statistics are provided for core excitation energies with and without relativistic corrections. For all test sets, the molecular structures have either been taken from the references or were recalculated with the methods described therein.

Since intermolecular CT is neither covered by the Tozer nor the Thiel test set, the lowest-lying intermolecular CT excitation of the ethylene tetrafluoroethylene complex

is additionally studied, by stepwise varying the intermonomer distance and comparing results to the exact $1/R$ behavior.[7,13] Monomer structures were optimized at the B3LYP/cc-pVTZ level and are kept frozen. Excitation energies were determined using cc-pVTZ basis sets.

5.1.2. Considered Functionals

For the first assessment of local hybrid functionals with respect to their performance for the calculation of vertical excitation energies, several local hybrids based on Slater-Dirac exchange[74,75] without calibration have been investigated (see Sec. 2.3 for details). In combination with VWN correlation,[76] the spin-channel t-LMF and s-LMF (see Eqs. (2.76) and (2.77), respectively) as well as their common LMF counterparts are applied. To facilitate the discussion and the comparison between the common and the spin-channel scheme, the same parameters are used in both cases. In particular, parameters optimized for the spin-channel LMF with respect to atomization energies are employed, i.e. $a = 0.48$ for the t-LMF[185] and $\beta = 0.277$ for the s-LMF.[186] VWN-based local hybrids are denoted as *Lh*-SVWN.

Additionally, the performance of local hybrids based on self-interaction-corrected PW92 correlation[18] (see Eq. (2.83)) is explored. In combination with the t-LMF, two different approaches for the self-interaction correction are employed, i.e. a self-interaction-free and a self-interaction-reduced scheme, labeled as sifPW92 and sirPW92, respectively. In the self-interaction-free scheme, λ in Eq. (2.83) is set to 1.0 leading to a complete removal of one-electron short-range self-correlation. Setting λ to the prefactor a of the t-LMF reduces the short-range self-correlation locally by the same amount as the LMF removes Coulomb self-interaction in the exchange part, resulting in the self-interaction-reduced scheme. In both cases, a range-separation parameter of $\mu = 0.8$ a.u. is employed for the determination of short-range correlation. Parametrizations optimized for the common t-LMF with respect to atomization energies and reaction barrier heights are used, i.e. $a = 0.709$ for sifPW92 and $a = 0.646$ for sirPW92. For the respective spin-channel LMFs, again the same parameters are applied. The corresponding local hybrids are referred to as *Lh*-SsifPW92 and *Lh*-SsirPW92, respectively.

Given the use of the kinetic energy density, local hybrids containing the t-LMF may exhibit an additional response due to the current density (see Sec. 3.2.1 for details). While local hybrids with the abbreviation *Lh* employ the usual kinetic energy density and thus do not exhibit an additional current-density response, current-dependent local hybrids

abbreviated by *cLH* apply the gauge-invariant kinetic energy density, thus leading to the additional response terms. Use of the Tamm-Dancoff approximation is denoted as (TDA).

For illustration, the spatial behavior of the s-LMF and t-LMF in their respective *Lh*-SVWN and *Lh*-SsirPW92 parametrizations is shown for the CO molecule along the molecular axis (Fig. 5.1). Furthermore, the plot is roughly separated into several real-

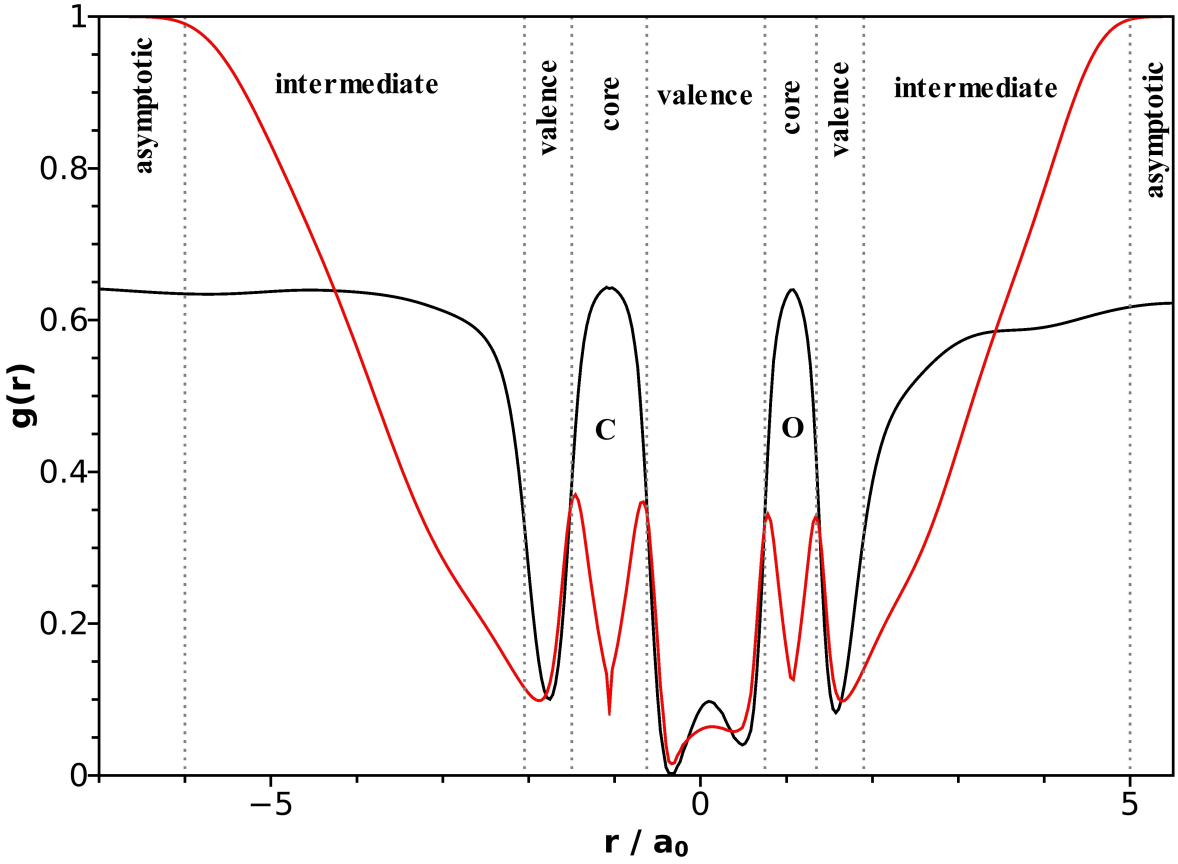

Figure 5.1.: t-LMF (black) and s-LMF (red) ($a = 0.646$ for t-LMF[18] and $\beta = 0.277$ for s-LMF[17]) plotted for the CO molecule along the molecular axis. Different regions in real space are roughly classified into core, valence and asymptotic regions as well as the intermediate space between valence and asymptotic regions.

space regions, i.e. core, valence, asymptotic and intermediate regions between valence and asymptotic regions. Since electronic excitations are usually classified by the types of the involved orbitals, e.g. valence, core or Rydberg orbitals, which themselves can also be roughly related to distinct regions in real space, this approximate separation allows a direct comparison between the LMF behavior and the local hybrid performance for distinct excitation types. Note that the electron density on the border between intermediate and asymptotic region is around 10^{-6} a.u..

To assess the performance of the described local hybrid functionals, various other functionals are considerd for comparison. This includes the semi-local functionals SVWN,[74–76] BLYP,[92,101] PBE[93] and TPSS[106,107] as well as several global hybrid functionals with increasing exact-exchange admixture, i.e. TPSSh (10%),[124] B3LYP (20%),[126,127] PBE0 (25%),[125] BMK (42%),[128] BHLYP (50%),[120] and M06-2X (54%).[130] In some cases, the asymptotic correction to the SVWN potential, i.e. LB94,[300] has also been investigated. In addition, range-separated hybrid functionals covering different ranges of exact exchange and exhibiting different RS parameters are employed. This includes CAM-B3LYP (19%–65%, $\omega = 0.33$),[148] LC-ωPBE (0%–100%, $\omega = 0.40$),[143] and ωB97X-D (22.2036%–100%, $\omega = 0.20$).[154]

All calculations, except those using BMK, M06-2X and the three range-separated hybrids, have been done with the modified developers' version of the TURBOMOLE program package[19] containing local hybrid functionals.[270,272] For the TURBOMOLE calculations, the RI-J approximation for Coulomb integrals[250,259] and semi-numerical integration of exact exchange[270,272] is applied. The latter is generally done on the TURBOMOLE m3 grid, while, according to the findings in Sec. 4.3.2,[272] slighly enhanced and diffuse grids are used for Rydberg and core-Rydberg excitations. Calculations with BMK, M06-2X and the range-separated hybrids have been done with Gaussian 09.[301]

5.2. Results

5.2.1. Valence Excitations: The Thiel Test Set

At first, the performance of the aforementioned local hybrids shall be investigated for the 166 valence excitations of the Thiel test set. While for singlet excitations, local hybrids employing common LMFs exhibit the same exchange-correlation kernel as with the corresponding spin-channel LMF using the same parameters, due to additional cross terms different kernels are obtained in the case of triplet excitations. Since common LMFs are found to always perform better than their spin-channel counterparts, for simplicity only common LMF results are considered in the present section. The detailed comparison between common and spin-channel LMFs is postponed to Sec. 5.2.4. As for all other test sets, the mean absolute error (MAE) and the mean signed error (MSE) are used for statistical analysis. Results for the Thiel test set, grouped by molecule and excitation types, respectively, are provided in Table 5.1 and are graphically displayed in Fig. 5.2.

Although performance of semi-local as well as global and range-separated hybrid functionals for the Thiel test set has already been studied extensively,[288,294,302] results for some

Table 5.1.: Mean absolute errors (MAEs) and mean signed errors (MSEs) (in parentheses) in eV for the valence excitation energies of the Thiel test set calculated with different exchange-correlation functionals. Results are grouped by molecular classes and excitation type, respectively. The numbers of excitations of each subset are given.

Functional	Hydrocarbons	Aromatics	Carbonyls	Nucleobases	Singlets	Triplets	All
	26	89	32	19	103	63	166
SVWN	0.37	0.46	0.55	0.87	0.57	0.41	0.51
	(-0.29)	(-0.37)	(-0.46)	(-0.87)	(-0.49)	(-0.34)	(-0.43)
BLYP	0.43	0.47	0.56	0.86	0.55	0.49	0.53
	(-0.43)	(-0.42)	(-0.50)	(-0.86)	(-0.49)	(-0.49)	(-0.49)
PBE	0.42	0.46	0.57	0.84	0.53	0.50	0.52
	(-0.42)	(-0.40)	(-0.50)	(-0.84)	(-0.46)	(-0.50)	(-0.47)
TPSS	0.41	0.38	0.52	0.67	0.42	0.49	0.45
	(-0.40)	(-0.30)	(-0.39)	(-0.67)	(-0.30)	(-0.49)	(-0.37)
TPSSh	0.45	0.32	0.43	0.36	0.29	0.49	0.37
	(-0.38)	(-0.18)	(-0.33)	(-0.36)	(-0.12)	(-0.49)	(-0.26)
B3LYP	0.45	0.29	0.41	0.21	0.26	0.45	0.33
	(-0.34)	(-0.16)	(-0.31)	(-0.21)	(-0.08)	(-0.45)	(-0.22)
PBE0	0.52	0.30	0.39	0.09	0.23	0.49	0.33
	(-0.35)	(-0.09)	(-0.29)	(-0.05)	(0.03)	(-0.49)	(-0.17)
BMK	0.34	0.28	0.31	0.25	0.32	0.24	0.29
	(-0.02)	(0.15)	(-0.16)	(0.25)	(0.23)	(-0.18)	(0.07)
BHLYP	0.73	0.46	0.46	0.53	0.47	0.58	0.51
	(-0.35)	(0.12)	(-0.13)	(0.53)	(0.40)	(-0.54)	(0.04)
M06-2X	0.32	0.27	0.34	0.25	0.33	0.23	0.29
	(0.10)	(0.18)	(-0.20)	(0.25)	(0.21)	(-0.07)	(0.10)
CAM-B3LYP	0.55	0.30	0.34	0.25	0.29	0.42	0.34
	(-0.22)	(0.02)	(-0.21)	(0.25)	(0.19)	(-0.41)	(-0.04)
LC-ωPBE	0.78	0.42	0.41	0.50	0.44	0.55	0.48
	(-0.23)	(0.11)	(-0.12)	(0.50)	(0.40)	(-0.50)	(0.06)
ωB97X-D	0.47	0.27	0.29	0.24	0.29	0.32	0.30
	(-0.13)	(0.06)	(-0.19)	(0.24)	(0.20)	(-0.31)	(0.00)
Lh-SVWN	0.34	0.25	0.33	0.18	0.27	0.28	0.27
$g_\sigma = \mathrm{erf}(0.277\,s)$	(-0.18)	(-0.05)	(-0.27)	(-0.16)	(-0.04)	(-0.27)	(-0.13)
Lh-SVWN	0.28	0.22	0.24	0.09	0.24	0.19	0.22
$g_\sigma = 0.48t$	(-0.05)	(0.07)	(-0.13)	(-0.04)	(0.08)	(-0.14)	(0.00)
Lh-SsifPW92	0.28	0.28	0.21	0.24	0.33	0.16	0.27
$g_\sigma = 0.709t$	(0.06)	(0.21)	(0.00)	(0.24)	(0.26)	(-0.03)	(0.15)
Lh-SsirPW92	0.28	0.26	0.21	0.17	0.30	0.16	0.25
$g_\sigma = 0.646t$	(0.03)	(0.18)	(-0.03)	(0.17)	(0.22)	(-0.06)	(0.11)

selected XC functionals (see Sec. 5.1.2) shall be briefly discussed first to serve as background for the comparison to local hybrid functionals. Except for BHLYP and LC-ωPBE, hybrid functionals tend to improve over semi-local functionals for singlet excitations, with

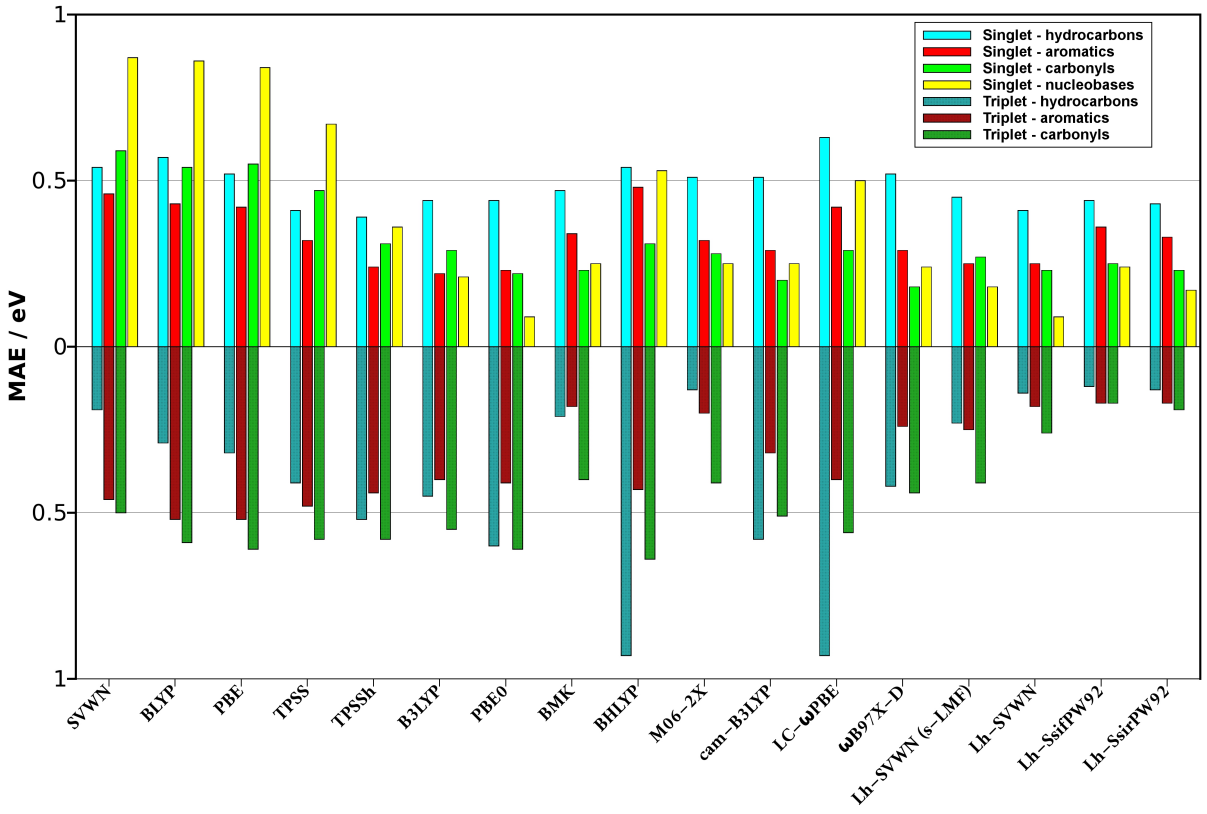

Figure 5.2.: Mean absolute errors (MAEs) in eV of various exchange-correlation functionals for subsets of the vertical valence excitation Thiel test set. Errors for singlet excitations are above, for triplet excitations beneath the axis.

MAEs being closer to 0.3 eV for the latter compared to about 0.5 eV for the former. While global hybrid functionals with an exact-exchange admixture of about 20–25%, e.g. B3LYP and PBE0, exhibit the largest improvement upon the systematic underestimation of singlet valence excitation energies by semi-local functionals, global hybrid functionals with a larger amount of exact exchange, e.g. BHLYP and BMK, tend to overestimate singlet valence excitations. Although the latter holds also true for the investigated range-separated hybrid functionals, most-likely also due to a large average fraction of exact exchange, except LC-ωPBE, the chosen range-separated hybrids exhibit comparable results to the better-performing global hybrids. On the other hand, BHLYP and LC-ωPBE clearly employ too much exact exchange, thus leading to even worse results than the best-performing semi-local functional TPSS. In contrast, negative MSEs, typically around -0.4 eV and -0.5 eV, show that semi-local functionals as well as global and range-separated hybrids systematically underestimate triplet excitation energies,[288,294] except for the better-performing, highly parametrized ωB97X-D, M06-2X and BMK.[286,302] The fact, that BMK with 42%

as well as M06-2X with 54% exact exchange admixture both perform much better than BHLYP with 50% exact exchange, indicates that exact exchange does not play the only major role for an accurate description of triplet valence excitations.

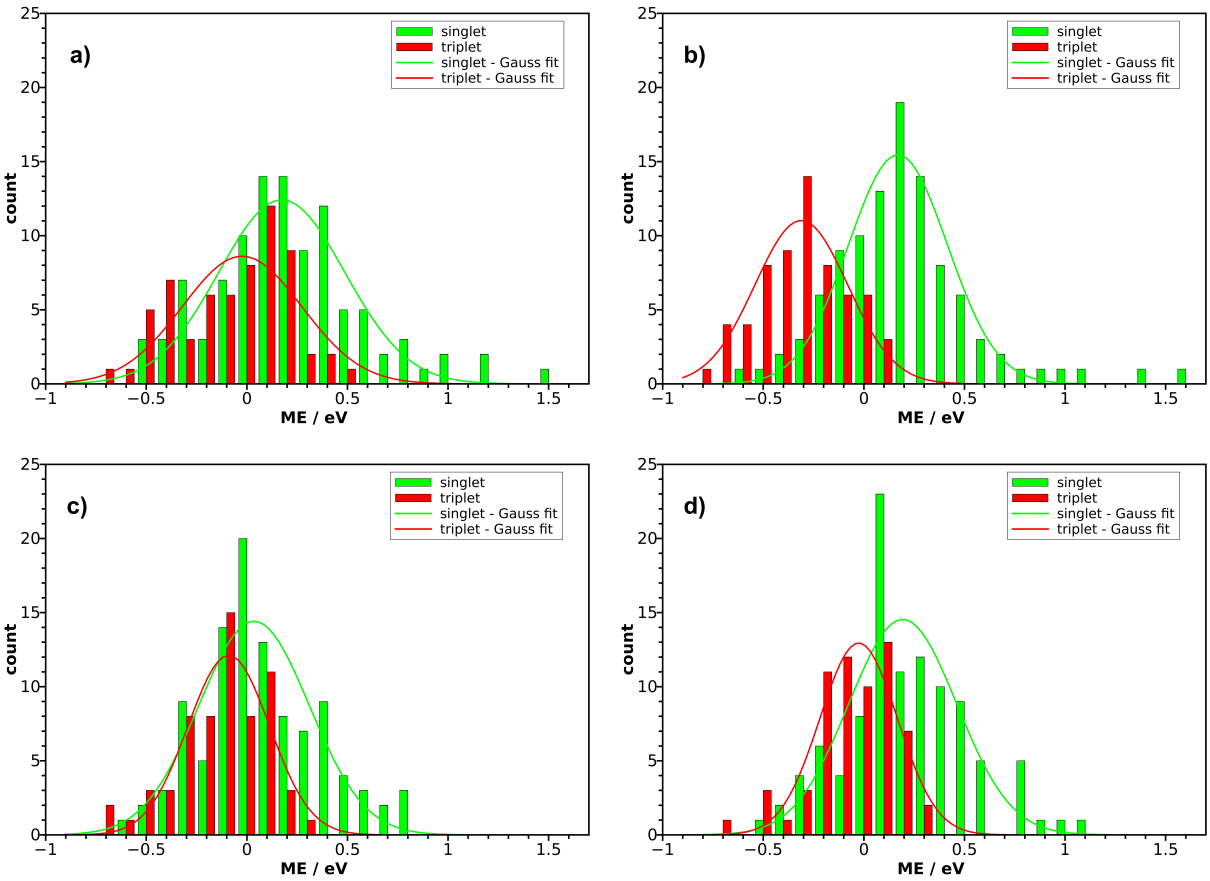

Figure 5.3.: Histograms with respect to the mean signed error (MSE) in electron volt (eV) for four different hybrid functionals, i.e a) M06-2X, b) ωB97X-D, c) *Lh*-SVWN and d) *Lh*-SsirPW92 (both with common t-LMF). Errors are grouped within ranges of 0.1 eV and separately plotted for singlet and triplet excitations of the Thiel test set. The counts w.r.t. MSE are fitted against Gauss distributions.

For singlet excitations, the four investigated local hybrid functionals show a comparable performance to the best global and range-separated hybrids. While the local hybrid employing the s-LMF exhibits no significant systematical error, larger prefactors a of the t-LMF associated with larger exact-exchange admixtures result in more positive MSEs. Accordingly, *Lh*-SsifPW92 and *Lh*-SsirPW92 show a systematic overestimation of singlet valence excitation energies, which nonetheless influences the respective MAEs only moderately. For triplet excitations on the other hand, local hybrids employing the t-LMF clearly outperform all other shown XC functionals, even BMK and M06-2X as best-performing functionals of Ref. 302. This is accompanied with generally reduced MSEs, which in the

Table 5.2.: Mean absolute errors (MAEs) and mean signed errors (MSEs) (in parentheses) in eV for relative energies between the lowest-lying excited states of the Thiel test set, i.e. $S_2 - S_1$, $S_1 - T_1$ and $T_2 - T_1$, calculated with different exchange-correlation functionals. The numbers of excitations included in each subset are given.

Functional	$S_2 - S_1$ 27	$S_1 - T_1$ 19	$T_2 - T_1$ 19	All 65
SVWN	0.43 (0.06)	0.40 (-0.11)	0.24 (-0.03)	0.37 (-0.02)
BLYP	0.40 (0.02)	0.34 (0.02)	0.14 (-0.04)	0.31 (0.00)
PBE	0.41 (0.04)	0.35 (0.06)	0.13 (-0.02)	0.31 (0.03)
TPSS	0.40 (0.05)	0.32 (0.20)	0.13 (0.00)	0.30 (0.08)
TPSSh	0.37 (0.11)	0.36 (0.33)	0.19 (0.04)	0.32 (0.15)
B3LYP	0.39 (0.14)	0.32 (0.25)	0.16 (0.02)	0.30 (0.14)
PBE0	0.41 (0.19)	0.43 (0.41)	0.24 (0.07)	0.37 (0.22)
BMK	0.48 (0.26)	0.30 (0.27)	0.14 (0.09)	0.33 (0.21)
BHLYP	0.55 (0.28)	0.76 (0.73)	0.61 (0.19)	0.63 (0.39)
M06-2X	0.50 (0.28)	0.29 (0.08)	0.12 (-0.01)	0.33 (0.14)
CAM-B3LYP	0.45 (0.23)	0.47 (0.45)	0.27 (0.11)	0.40 (0.26)
LC-ωPBE	0.53 (0.35)	0.80 (0.79)	0.46 (0.31)	0.59 (0.47)
ωB97X-D	0.45 (0.23)	0.37 (0.36)	0.22 (0.09)	0.36 (0.23)
Lh-SVWN $g_\sigma = \mathrm{erf}(0.277\,s)$	0.39 (0.16)	0.29 (0.16)	0.11 (0.03)	0.28 (0.12)
Lh-SVWN $g_\sigma = 0.48t$	0.37 (0.16)	0.28 (0.12)	0.12 (0.02)	0.27 (0.11)
Lh-SsifPW92 $g_\sigma = 0.709t$	0.43 (0.23)	0.27 (0.14)	0.14 (0.03)	0.30 (0.14)
Lh-SsirPW92 $g_\sigma = 0.646t$	0.41 (0.21)	0.28 (0.14)	0.14 (0.03)	0.29 (0.14)

case of *Lh*-SsifPW92 and *Lh*-SsirPW92, give no significant systematic error for triplet valence excitations. The s-LMF based local hybrid exhibits results comparable to ωB97X-D, the best range-separated hybrid.

The good performance of the local hybrids is also reflected by their error histograms, which are shown in Fig. 5.3 for *Lh*-SsirPW92 and *Lh*-SVWN (with t-LMF) in comparison to M06-2X and ωB97X-D, the respectively best-performing global and range-separated hybrid functionals investigated in this work. Singlet and triplet excitations are separately considered. While M06-2X exhibits a relatively broad error distribution for singlet as well as triplet excitations, ωB97X-D is characterized by clear systematic errors, i.e. an underestimation of triplet and an overestimation of singlet excitations. The two local hybrid functionals on the other hand feature relatively sharp distributions with MSE maxima close to 0.0 eV. They thus provide a more balanced description of valence excitations than the chosen reference functionals.

A similar picture as for the fundamental excitations is obtained for the evaluation of energy differences between the lowest-lying excited states, i.e. energies for the $S_1 - S_2$, $T_1 - S_1$ and $T_1 - T_2$ transitions (see Fig. 5.2). Hence, only the main differences will be highlighted. Semi-local functionals perform similarly as global hybrid functionals (except BHLYP) with TPSS and B3LYP, both exhibiting an MAE of 0.3 eV, being the best functionals of each group. Compared to global hybrids, range separated hybrid functionals perform worse than for the fundamental excitations. Although local hybrid functionals also do not improve over standard functionals for the $S_1 - S_2$ transitions, they are among a larger group of well-performing functionals for the $T_2 - T_1$ case and perform best (together with BMK and M06-2X) for the $S_1 - T_1$ energy differences.[286]

In summary, the investigated local hybrid functionals, especially those based on the t-LMF, provide a simultaneously accurate description of singlet and triplet valence excitations, which seems to be more difficult for global and range-separated hybrids despite a large number of empirical parameters in some cases.

5.2.2. Rydberg, Charge-Transfer and Core Excitations: The Tozer Test Sets

While the vertical-excitation test set of Thiel considers solely valence excitations, i.e. excitations of valence electrons into nearby antibonding orbitals, the Tozer test sets additionally include Rydberg, intramolecular charge-transfer and core excitations,[12,290] which shall be discussed in detail in the present section. On the other hand, the renewed discussion of valence excitations on the basis of the Tozer test sets is omitted due to its significantly smaller number and diversity of valence excitations compared to the Thiel test set. Although the number of Rydberg, charge-transfer and core excitations is also limited, it nonetheless allows the identification of weaknesses of the local hybrid func-

tionals, again in comparison to some standard XC functionals. MAEs and MSEs of the investigated functionals for the different excitation types considered in the Tozer test sets are given in Table 5.3 and are visualized in Fig. 5.4.

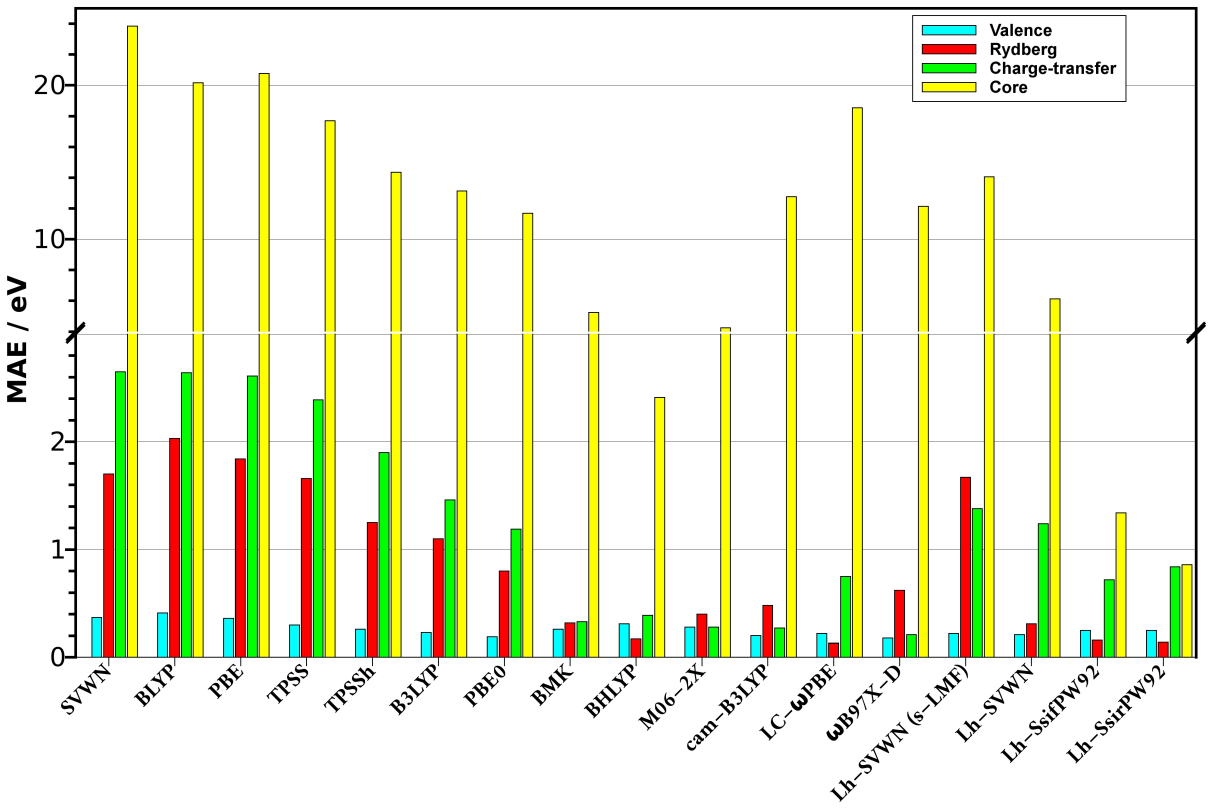

Figure 5.4.: Mean absolute errors (MAEs) in eV of various exchange-correlation functionals for the vertical excitation test sets of Tozer and co-workers. For core excitations, non-corrected reference values are taken.

Difficulties in the treatment of Rydberg excitations arise from the necessity to simultaneously describe the very diffuse Rydberg orbitals, into which electron density is transferred, and the less diffuse valence orbitals, from which the density originates. While the former require a large amount of exact exchange to minimize self-interaction errors, the latter benefit considerably from correlation contributions included in semi-local functionals. As a consequence, the investigated semi-local functionals exhibit systematically too low Rydberg excitation energies with MAEs being close to 2 eV. TPSS and SVWN perform slightly better than the two employed GGA functionals. The inclusion of exact exchange clearly reduces this strong underestimation, which in the case of hybrid functionals with lower amounts of exact exchange, e.g. TPSSh, B3LYP and PBE0, is nonetheless not sufficient for a complete removal. On the other hand, BHLYP as best-performing global

Table 5.3.: Mean absolute errors (MAEs) and mean signed errors (MSEs) (in brackets) in eV for the Tozer test sets calculated with different exchange-correlation functionals. For core excitations, values are given without and with relativistic correction of the 1s orbitals (before and after the slash, respectively). The numbers of excitations are given in addition.

Functional	Valence 32	Rydberg 13	CT 14	Core 28
SVWN	0.37 (-0.35)	1.70 (-1.70)	2.65 (-2.65)	23.85/23.61 (-23.85/-23.61)
BLYP	0.41 (-0.39)	2.03 (-2.03)	2.64 (-2.64)	20.16/19.93 (-20.16/-19.93)
PBE	0.36 (-0.35)	1.84 (-1.84)	2.61 (-2.61)	20.77/20.53 (-20.77/-20.53)
TPSS	0.30 (-0.23)	1.66 (-1.66)	2.39 (-2.39)	17.69/17.45 (-17.69/-17.45)
TPSSh	0.26 (-0.10)	1.25 (-1.25)	1.90 (-1.90)	14.34/14.10 (-14.34/-14.10)
B3LYP	0.23 (-0.17)	1.10 (-1.10)	1.46 (-1.45)	13.14/12.91 (-13.14/-12.91)
PBE0	0.19 (-0.08)	0.80 (-0.80)	1.19 (-1.17)	11.69/11.46 (-11.69/-11.46)
BMK	0.26 (0.00)	0.32 (-0.30)	0.33 (-0.28)	5.24/5.01 (-5.24/-5.01)
BHLYP	0.31 (0.08)	0.17 (0.04)	0.39 (0.10)	2.41/2.18 (-2.41/-2.18)
M06-2X	0.28 (-0.07)	0.40 (-0.38)	0.28 (-0.04)	4.25/4.02 (-4.25/-4.02)
CAM-B3LYP	0.20 (0.02)	0.48 (-0.48)	0.27 (-0.18)	12.76/12.53 (-12.76/-12.53)
LC-ωPBE	0.22 (0.14)	0.13 (-0.03)	0.75 (0.74)	18.54/18.31 (-18.54/-18.31)
ωB97X-D	0.18 (0.04)	0.62 (-0.62)	0.21 (-0.07)	12.14/11.91 (-12.14/-11.91)
Lh-SVWN $g_\sigma = \mathrm{erf}(0.277\,s)$	0.22 (-0.13)	1.67 (-1.67)	1.38 (-1.36)	14.05/13.82 (-14.05/-13.82)
Lh-SVWN $g_\sigma = 0.48t$	0.21 (-0.01)	0.31 (-0.31)	1.24 (-1.21)	6.12/5.89 (-6.12/-5.89)
Lh-SsifPW92 $g_\sigma = 0.709t$	0.25 (0.08)	0.16 (0.07)	0.72 (-0.66)	1.34/1.54 (1.22/1.45)
Lh-SsirPW92 $g_\sigma = 0.646t$	0.25 (0.06)	0.14 (-0.02)	0.84 (-0.79)	0.86/0.74 (-0.71/-0.48)

hybrid provides a very low MAE together with virtually no systematic error. Apparently, 50% exact exchange represents a good compromise between the requirements of valence and Rydberg orbitals. Hence, significantly larger exact-exchange admixtures would gen-

erally result in overestimated Rydberg excitations. Most likely due to the larger number of parameters included in the gradient expansion of the exchange-correlation hole, BMK and M06-2X nonetheless show negative MSEs. Nevertheless, among the studied global hybrids, these two provide the best balance between the demands of Rydberg and valence excitations.

Due to the inclusion of larger fractions of exact exchange, especially in the interelectronic long-range, the three range-separated hybrid functionals significantly improve over global hybrids with lower-exact exchange admixtures. While LC-ωPBE exhibits a very low MAE together with no significant systematic error, the other two range-separated hybrid functionals show MAEs even worse than M06-2X. In addition, all Rydberg excitation energies are underestimated. Especially, the relatively bad performance of ωB97X-D compared to LC-ωPBE is notable, since both functionals employ 100% exact exchange at long range. Here, the main difference lies in the range-separation parameter, which is 0.2 a.u. for ωB97X-D compared to 0.4 a.u. for LC-ωPBE. The latter thus features a faster increase of exact exchange with respect to the interelectronic distance, which suggests, that the Rydberg excitations from the Tozer test set depend to a large extent on an intermediate interelectronic distance and not predominantly on the correct asymptotics.[286] In comparison to a recent TDDFT study of Isegawa *et al.*,[303] where the three investigated range-separated hybrid functionals performed similarly well for Rydberg excitations, larger differences are thus observed in the present work, which with high probability, are related to the fact that the Tozer test set considers more higher-lying Rydberg states than the other studies.[303–305]

Turning to local hybrid functionals, one should first note the different meaning of 'asymptotic region' compared to range-separated hybrid functionals. While in range-separated hybrids, asymptotic regions refer to large interelectronic distances, which is generally the case for Rydberg excitations, the term 'asymptotic region' in local hybrid functionals has a different, real-space meaning, i.e. it refers to regions farther away from the valence (cf. Fig. 5.1), which in fact are sampled by Rydberg excitations. Local hybrid functionals nonetheless show a somewhat similar behavior as range-separated hybrid functionals. That is, *Lh*-SVWN with the s-LMF does not improve the analyzed Rydberg excitation energies, even though it features 100% exact exchange in asymptotic one-electron regions, even compared to SVWN. In contrast, t-LMF-containing local hybrids, which do not exhibit the correct asymptotic behavior, but a steeper change in the intermediate region (cf. Fig. 5.1), perform strikingly better. While *Lh*-SVWN with t-LMF and $a = 0.48$ gives still overall slightly too low Rydberg excitation energies (MSE -0.31 eV), both *Lh*-SsifPW92 and *Lh*-SsirPW92 with their larger a values may be considered to pro-

vide essentially perfect agreement with the reference Rydberg excitation energies (Table 5.3).[286] Compared to the s-LMF with its exact asymptotic behavior, this suggests that in a real-space sense predominantly the intermediate range between valence and asymptotic regions is sampled by the considered Rydberg excitations. This is similar to the finding for range-separated hybrids that the intermediate interelectronic region is most important. Apparently, local hybrids with a scaled t-LMF provide a systematically correct behavior in this region, for which exact properties are, however, largely unknown.[286]

Besides different XC functionals, the influence of the XC potential has been studied for Rydberg excitations by employing the LB94[300] correction to the SVWN potential to ensure the correct asymptotic $-1/r$ behavior. For the Rydberg excitations of the Tozer test set, the MAE of SVWN is dramatically reduced from 1.7 eV to 0.18 eV using the LB94 correction. However, this is accompanied by an increase of the MAE for valence excitations from 0.37 eV to 0.71 eV, which is related to the fact that the LB94 model affects the potential over a large spatial region rather than correcting only distinct regions. More recent developments such as the 'HOMO level depopulation' appear to improve Rydberg excitations without deterioration of valence excitation energies,[306] but have not been investigated in the present work. In this context, it is noteworthy that local hybrid functionals with 100% exact exchange in asymptotic regions guarantee only the correct asymptotic behavior of the energy density, while the potential generally decays as $-c/r$ with $0 < c < 1$, which can be shown easily for a one-electron system, but is not trivial for many electron systems.[97,190] The real-space behavior of the LMFs (e.g. Fig. 5.1) nonetheless remains a useful guideline for the interpretation of the performance of different local hybrid functionals.

Charge-transfer excitations constitute another challenging class of electronic excitations, which is characterized by a charge separation in the excited state, often coming along with a small overlap between the initial and final molecular orbital of the excited electron.[307] Since the interaction between the separated charges exhibits a particularly non-local character, especially for long-range CT excitations,[7,308] large admixtures of non-local exact exchange are essential to reproduce CT excitation energies.[7] Accordingly, semi-local XC functionals perform particularly poorly in this case (Table 5.3), with excitation energies being systematically underestimated by more than 2 eV. Again, TPSS shows slightly smaller errors than the two GGAs and SVWN. Similar to Rydberg excitations, larger exact-exchange admixtures improve the performance of global hybrids for CT excitations, where M06-2X and BMK give clearly the smallest errors (Table 5.3). Nevertheless, the CT excitations of the Tozer test set exhibit only a limited long-range character, so that for CT excitations with more long-range character, larger errors are

expected due to the constant exact-exchange admixture.[309] Among the range-separated hybrid functionals, ωB97X-D and CAM-B3LYP both exhibit a good performance, with MAEs being comparable to those of valence excitations. On the other hand, CT excitation energies are systematically and significantly overestimated by LC-ωPBE, most likely due to the larger range-separation parameter. Although range-separated hybrid functionals are thus generally able to provide improved Rydberg and CT excitation energies,[12,144,293,310] a simultaneously accurate treatment appears to be difficult. Different functionals might perform best for one or the other excitation class.[286]

Concerning CT excitations, the four studied local hybrids can neither compete with the best global nor best range-separated hybrid functionals (Table 5.3).[286] With excitation energies being systematically underestimated, the two *Lh*-SVWN functionals exhibit errors comparable to B3LYP and PBE0, while better results with nonetheless negative MSEs are obtained for *Lh*-SsifPW92 and *Lh*-SsirPW92. This is consistent with larger prefactors a of the t-LMF, leading to an increased average amount of exact exchange. For the subset of CT excitations, a minimal MAE for the *Lh*-SVWN functional is obtained with a reoptimized t-LMF prefactor of $a = 0.88$ (MAE 0.32 eV, MSE 0.01 eV). While such a functional would be competitive to the best-performing functionals studied here, valence excitations as well as thermochemical and other ground-state properties would be deteriorated significantly. In particular, an MAE of 0.50 eV was obtained for the Thiel test set. Despite the limited number of rather simple local hybrids that have been investigated, it appears that local hybrid functionals are generally not able to provide a systematical improvement over conventional global hybrid functionals for the description of CT excitations. In fact, a similar performance as for global hybrids with a certain amount of exact exchange is observed. One possible reason could be the real-space dependence and locality of the LMF. In particular, the non-locality of a CT excitation, and thus the necessity to include excact exchange, is determined by its long-range character in the interelectronic space. In contrast, the LMF distinguishes only between different regions in real space. For example, local hybrid functionals thus do not discriminate between antibonding orbitals of the same bond and antibonding orbitals of an equivalent bond being farther away, which is the inherent difference between valence and CT excitations. Hence, in the case of local hybrids, CT excitations might be more affected by the on average increased amount of exact exchange rather than by a specifically improved exact exchange admixture. A further discussion of the CT problem is provided in Sec. 5.2.3 on the basis of intermolecular CT excitations, which are not considered in the Tozer test sets.

As last excitation class included in the Tozer test sets, 1s core electron excitations of first-row elements shall be discussed. Besides usually non-neglible relativistic shifts of or-

bital energies (cf. Sec. 5.1.1), core orbitals in general feature high electron densities due to their confinement to small volumes. The resulting domination of exchange over correlation thus requires larger amounts of exact exchange to avoid self-interaction errors due to semi-local exchange functionals,[290] which as a consequence, systematically and dramatically underestimate core excitation energies. So far, larger exact-exchange admixtures are realized by increasing the constant prefactor of global hybrids,[290] by introducing an additional, tailored short-range correction within range-separated hybrids[290] or by employing orbital-specific hybrid functionals featuring larger amounts of exact exchange for core orbitals.[135–138,149] In particular, the $BH^{0.58}LYP$ global hybrid functional with a reoptimized constant exact-exchange mixing of $c = 0.58$ has been found to perform best for first-row elements without relativistic corrections.[290] Alternatively, constant semi-empirical shifts to core excitation energies are applied to account for the various errors regarding functional, basis set and relativistic effects.[212,311–313]

MAEs and MSEs (with and without relativistic corrections) for the core excitations of the Tozer test set obtained with all so far discussed XC functionals are given in Table 5.3. As expected, semi-local functionals exhibit a systematic pronounced underestimate of around 17–24 eV, which is reduced to 11–15 eV for 'standard' global hybrid functionals with moderate exact-exchange mixing, such as B3LYP and PBE0, and to 4–6 eV for BMK and M06-2X. Exhibiting an MAE lower than 3 eV, BHLYP shows the best performance. Employing a reoptimized mixing parameter of $c = 0.58$ in the abovementioned $BH^{0.58}LYP$ functional, MAEs even smaller than 1 eV were obtained.[290] While long-range corrected hybrid functionals, as those considered in the present work, do not improve over standard global hybrids, specifically adjusted short-range corrections are able to provide MAEs down to 0.3 eV.[290] Nevertheless, relativistic (see Sec. 5.1.1) effects were not considered in Ref. 290 and thus might be erroneously incorporated into the short-range-separation parameter.

Turning to the local hybrids, *Lh*-SVWN combined with the s-LMF exhibits a similarly pronounced underestimate of core excitation energies as the standard global and range-separated hybrid functionals. This can be explained by a distinct 'dip' of the s-LMF and thus little exact exchange in the core region (Fig. 5.1). In contrast, the t-LMF provides large exact-exchange admixtures in core regions, thus leading to a dramatically reduced MAE of around 6 eV for *Lh*-SVWN with a t-LMF prefactor of $a = 0.48$. The larger a values of the *Lh*-SsifPW92 and *Lh*-SsirPW92 functionals finally provide small positive or negative MSEs and MAEs (Table 5.3) in the range of the abovementioned specialized functionals. Notably, *Lh*-SsifPW92 overshoots somewhat, whereas *Lh*-SsirPW92 is still slightly too low. A t-LMF prefactor between those two values is thus expected to provide

even smaller errors, while the performance for thermochemistry and the other excitation types should be deteriorated only slightly. A specific large admixture of exact exchange in the core region (in real space), as can be ensured by local hybrids employing suitable LMFs, is thus of tremendous importance for core excitations. Compared to other hybrid functionals, this is a particular advantage of the local hybrid approach. In this context, it is noteworthy, that already rather simple local hybrid functionals (with only one or two empirical parameters), optimized only for thermochemical kinetics with no special attention to TDDFT applications, dramatically improve over all other investigated XC functionals, with errors being even competitive to those of specifically designed XC functionals.

Summarizing the performance for the complete Tozer test set, the *Lh*-SsifPW92 and *Lh*-SsirPW92 local hybrids provide the best accuracy over a wide set of difficult excitation classes (core, valence and Rydberg) of any 'non-specialized' studied XC functional, while the improvement for CT-type excitations is insufficient, with performances being inferior to the best available functionals.

5.2.3. Intermolecular Charge-Transfer Excitations

While intramolecular charge-transfer excitations, which usually exhibit only a limited long-range character, already appear to be a great challenge for local hybrid functionals (see Sec. 5.2.2), intermolecular charge-transfer excitations, which often show a more pronounced long-range character, are not included in the Tozer test sets and shall thus be investigated more closely. Therefore, a widely used model case is employed, which is particularly difficult for standard functionals,[8,13] i.e. the shift of the first charge-transfer excitation energy of the ethylene tetrafluoroethylene complex with respect to the intermonomer distance R. Excitation energies relative to an intermonomer distance of $R = 5.0$ Å are shown in Fig. 5.5 for some of the investigated XC functionals. In addition, asymptotic values for an infinite monomer distance are given in parentheses. Besides TPSS, B3LYP, BHLYP and HF, each featuring a different amount of constant exact exchange, three local hybrid functionals are shown, i.e. *Lh*-SsirPW92 ($a = 0.646$), *Lh*-SVWN using the t-LMF and the optimized prefactor of $a = 0.48$ as well as *Lh*-SVWN employing an unscaled t-LMF. Numerical data for the other local hybrid functionals can be found as supplemental information in Ref. 286. The experimental reference value of 12.5 eV for an infinite monomer distance corresponds to the difference between the ionization potential of tetrafluoroethylene and the electron affinity of ethylene.[8,13] Furthermore, the theoretical $1/R$ behavior of the charge-transfer excitation energy is given as reference.

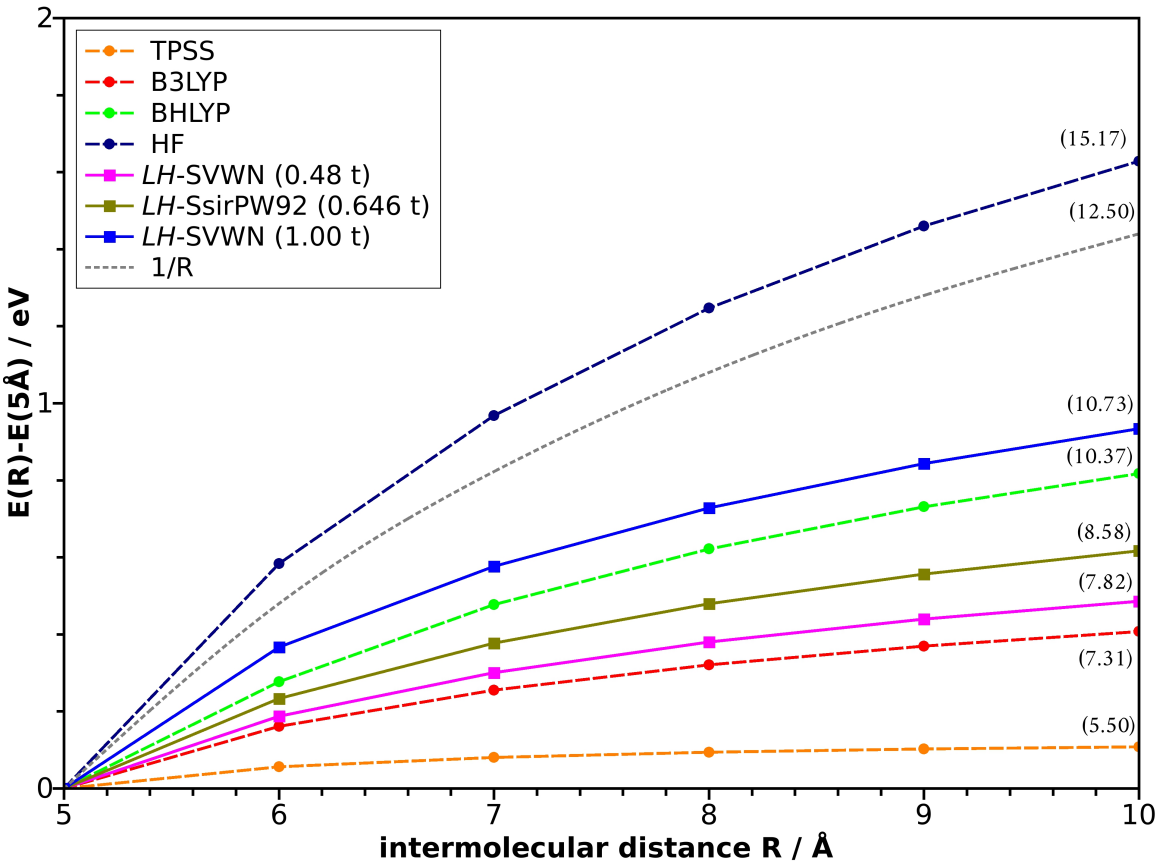

Figure 5.5.: Relative computed lowest charge-transfer excitation energies (in eV) for the ethylene tetrafluoroethylene complex as function of the intermolecular distance compared to the excitation energy at 5.0 Å. The asymptotic values are given in paranthesis below the curves.

Semi-local functionals dramatically underestimate the asymptotic CT excitation energy by more than a factor of 2. Furthermore, the asymptote is reached at too short distances, which reflects the significant deviation from the correct Coulombic $1/R$ behavior of the CT excitation energy.[13] While long-range separated hybrid functionals have been shown to be able to provide accurate asymptotic values,[13] large exact-exchange admixtures are required within global hybrid functionals to get close to the desired behavior. That is, even BHLYP, the best-performing global hybrid for the intramolecular charge-transfer excitations of the Tozer test set, exhibits a too low fraction of exact exchange. On the other hand, HF employs too much exact exchange, although it satisfies the exact $1/R$ increase for longer distances. The employed *Lh*-SVWN ($a = 0.48$) and *Lh*-SsirPW92 local hybrid functionals perform only somewhat better than B3LYP. Even *Lh*-SVWN with an unscaled t-LMF is only slightly better than BHLYP and still more than 1.7 eV below the exact asymptotic value, in spite of 100% exact exchange in one-electron regions and in the low-density limit.[286] Furthermore, also for larger intermonomer distances, the theoretical

$1/R$ increase is not observed, which may be related to the incorrect asymptotic behavior of the local hybrid potential (see Sec. 5.2.2). Regarding the unscaled t-LMF as limiting case, i.e. all meaningful LMFs should provide only less exact exchange, local hybrids without a correlation functional, allowing even more exact exchange, are thus not able to provide accurate intermolecular charge-transfer excitations, which supports the previous argument (see Sec. 5.2.2) that local hybrid functionals in general do not improve over global hybrid functionals with larger fractions of exact exchange. For the chosen example, it can be simply argued that neither the HOMO (highest occupied molecular orbital) of ethylene nor the LUMO (lowest unoccupied molecular orbital) of tetrafluoroethylene are anywhere close to the low-density limit. Hence, the behavior in one-electron regions, as screened by local hybrids, may not be decisive.

Extensions such as range-separated local hybrids[274] and local range-separated hybrids,[314] which combine the ideas of range-separated and local hybrid functionals, represent one possible solution to combine the excellent performance of local hybrids for a wide range of different excitation classes with the benefits of range separation for CT-type excitations.[286]

5.2.4. Additional Effects

In this section, several further aspects important for local hybrid TDDFT calculations, which were disregarded so far, shall be explored in detail. This includes the difference between common LMFs and their spin-channel counterparts as well as effects of the current-density response within the *cLH* functionals, which employ the gauge-invariant kinetic energy density. Furthermore, the effect of the Tamm-Dancoff approximation (TDA) is evaluated, which is frequently used in TDDFT and was suggested to provide improved triplet excitations.[296]

Due to the fact that all studied excitations exhibit a closed-shell ground-state, common LMFs give identical results for singlet excitations as their spin-channel counterparts, provided the same parameters are used. For triplet excitations on the other hand, results differ even with the same parameters. This is shown in Table 5.4 for the triplet excitations of the Thiel test set, for which the common LMFs perform systematically better with MAEs being reduced up to 0.10 eV. This is related to the fact that, due to the use of total rather than spin quantities in common LMFs, the LMF of one spin channel partially includes opposite-spin quantities. According to Eq. (2.75), this results in additional cross-terms simulating some opposite-spin non-dynamical correlation,[18] which is

apparently beneficial for an accurate description of triplet excitations and of open-shell states in general.

Table 5.4.: Mean absolute errors (MAEs) and mean signed errors (MSEs) (in parentheses) in eV for the triplet excitations of the Thiel test set calculated with different local hybrid functionals using spin-channel LMFs and their common-LMF counterparts.

Functional	Hydrocarbons 13	Aromatics 36	Carbonyls 14	Triplets 63
Lh-SVWN	0.37	0.29	0.46	0.35
$g_\sigma = \mathrm{erf}(0.277\, s_\sigma)$	(-0.37)	(-0.29)	(-0.46)	(-0.35)
Lh-SVWN	0.23	0.25	0.41	0.28
$g_\sigma = \mathrm{erf}(0.277\, s)$	(-0.23)	(-0.24)	(-0.41)	(-0.27)
Lh-SVWN	0.27	0.22	0.39	0.27
$g_\sigma = 0.48 t_\sigma$	(-0.27)	(-0.21)	(-0.39)	(-0.26)
Lh-SVWN	0.14	0.18	0.26	0.19
$g_\sigma = 0.48 t$	(-0.07)	(-0.11)	(-0.26)	(-0.14)
Lh-SsifPW92	0.31	0.20	0.37	0.26
$g_\sigma = 0.709 t_\sigma$	(-0.31)	(-0.14)	(-0.37)	(-0.22)
Lh-SsifPW92	0.12	0.17	0.17	0.16
$g_\sigma = 0.709 t$	(-0.01)	(0.02)	(-0.17)	(-0.03)
Lh-SsirPW92	0.31	0.20	0.37	0.26
$g_\sigma = 0.646 t_\sigma$	(-0.31)	(-0.16)	(-0.37)	(-0.24)
Lh-SsirPW92	0.13	0.17	0.19	0.16
$g_\sigma = 0.646 t$	(-0.03)	(-0.01)	(-0.19)	(-0.06)
Lh-SsirPW92 (TDA)	0.12	0.16	0.19	0.16
$g_\sigma = 0.646 t_\sigma$	(0.01)	(-0.03)	(-0.19)	(-0.05)
Lh-SsirPW92 (TDA)	0.22	0.21	0.10	0.19
$g_\sigma = 0.646 t$	(0.18)	(0.08)	(-0.06)	(0.07)

Notably, this systematic improvement for common over spin-channel LMFs does not hold, when the TDA is used (shown in Table 5.4 with *Lh*-SsirPW92 as an example). Here, the spin-channel LMF gives better results than the common LMF, with errors being comparable to those of the common LMF within the full TDDFT scheme. This can be explained by the fact that, in the case of the Thiel test set, the TDA generally leads to systematically upshifted singlet and triplet excitation energies (cf. MSE values in Table 5.5). This can improve the agreement with reference values, if excitation energies are underestimated by the given XC functional, which is indicated by negative MSEs and, for triplet excitations, is the case for most functionals. On the other hand, the performance is obviously deteriorated, if MSEs are small or already positive in the full TDDFT scheme. For example, the latter is the case for singlet excitations calculated with hybrid functionals applying larger amounts of exact exchange (see Table 5.1), also including some

range-separated and local hybrids, as well as for triplet excitations with the *Lh*-SsirPW92 functional employing a common LMF. On the other hand, the systematical upshift is beneficial for the spin-channel counterpart of *Lh*-SsirPW92 (Table 5.4). It is thus clear that the TDA will only improve agreement with benchmark data for certain situations, where an error compensation with other approximations occurs.[286] Compared to most global and range-separated hybrid functionals, all local hybrid functionals considered in the present work nonetheless exhibit smaller MAEs for the triplet excitations of the Thiel set (cf. Table 5.1).

Table 5.5.: Mean absolute errors (MAEs) and mean signed errors (MSEs) (in parentheses) in eV for the Thiel and Tozer test sets calculated with different XC functionals and their current-density dependent counterparts.

	Thiel		Tozer				
Functional	Singlet	Triplet	Valence	Rydberg	CT	Core-valence	Core-Rydberg
	103	63	32	13	14	9	19
TPSS	0.43	0.49	0.30	1.66	2.39	16.31/16.03	18.34/18.13
	(-0.32)	(-0.49)	(-0.23)	(-1.66)	(-2.39)	(-16.31/-16.03)	(-18.34/-18.13)
cTPSS	0.45	0.53	0.33	1.66	2.40	16.34/16.06	18.33/18.12
	(-0.35)	(-0.53)	(-0.29)	(-1.66)	(-2.40)	(-16.34/-16.06)	(-18.33/-18.12)
TPSSh	0.30	0.49	0.26	1.25	1.90	13.32/13.04	14.82/14.61
	(-0.13)	(-0.49)	(-0.10)	(-1.25)	(-1.90)	(-13.32/-13.04)	(-14.82/-14.61)
cTPSSh	0.32	0.52	0.28	1.25	1.93	13.36/13.08	14.81/14.60
	(-0.16)	(-0.52)	(-0.15)	(-1.25)	(-1.92)	(-13.36/-13.08)	(-14.81/-14.60)
Lh-SVWN	0.24	0.19	0.21	0.31	1.24	6.52/6.24	5.93/5.72
$g_\sigma = 0.48t$	(0.08)	(-0.14)	(-0.01)	(-0.31)	(-1.21)	(-6.52/-6.24)	(-5.93/-5.72)
c*Lh*-SVWN	0.23	0.20	0.19	0.57	1.25	6.62/6.34	5.94/5.73
$g_\sigma = 0.48t$	(0.05)	(-0.16)	(-0.05)	(-0.57)	(-1.22)	(-6.62/-6.34)	(-5.94/-5.73)
Lh-SsifPW92	0.33	0.16	0.25	0.16	0.72	0.50/0.67	1.73/1.94
$g_\sigma = 0.709t$	(0.26)	(-0.03)	(0.08)	(0.07)	(-0.66)	(0.14/0.42)	(1.73/1.94)
c*Lh*-SsifPW92	0.32	0.16	0.24	0.35	0.72	0.48/0.63	1.70/1.90
$g_\sigma = 0.709t$	(0.24)	(-0.05)	(0.06)	(-0.34)	(-0.68)	(0.00/0.28)	(1.70/1.90)
Lh-SsirPW92	0.30	0.16	0.25	0.14	0.84	1.60/1.33	0.50/0.46
$g_\sigma = 0.646t$	(0.22)	(-0.06)	(0.06)	(-0.02)	(-0.79)	(-1.60/-1.33)	(-0.29/-0.08)
c*Lh*-SsirPW92	0.28	0.17	0.23	0.38	0.85	1.74/1.46	0.50/0.46
$g_\sigma = 0.646t$	(0.20)	(-0.08)	(0.03)	(-0.38)	(-0.81)	(-1.74/-1.46)	(-0.30/-0.09)
Lh-SsirPW92 (TDA)	0.40	0.19	0.26	0.15	0.84	1.59/1.31	0.50/0.46
$g_\sigma = 0.646t$	(0.37)	(0.07)	(0.18)	(0.00)	(-0.75)	(-1.59/-1.31)	(-0.28/-0.07)

In Table 5.5, effects of using the gauge-invariant kinetic energy density, coming along with an additional response of the current density (see Sec. 3.2), are evaluated for the Thiel and Tozer test sets. Note again, that the current-density-dependent counterparts of the XC functionals are indicated by a prepended 'c'. Obviously, GGAs and the *Lh*-

SVWN functional with the s-LMF are not affected by this current dependence. Hence, the evaluation is restricted to t-LMF containing local hybrids as well as TPSS and TPSSh as reference. For the latter two XC functionals, inclusion of the current-density dependence has only a minor influence. In good agreement with a previous study,[277] individual errors differ by less than 0.04 eV. Local hybrid functionals exhibit a similar picture with the exception of Rydberg and core-valence excitations, which in average, are systematically downshifted by more than 0.25 eV and 0.10 eV, respectively. Those larger deviations for these two excitation classes can be explained by considering the spatial behavior of the LMF for their initial and final state orbitals. As discussed above, the description of low-lying Rydberg excitations requires a balanced treatment of the valence orbitals, from which the electron is excited, and of the target Rydberg orbitals, which predominantly depend on the intermediate spatial region (Fig. 5.1). Similarly, core and valence orbitals are both sampled by core-valence excitations. While the t-LMF gives large exact-exchange admixtures in core and asymptotic regions, few exact exchange is provided in valence regions. In the intermediate regions between the valence and the other two regions, which are in fact sampled by the two excitation classes in question, the t-LMF features steep changes, which appear to cause significant changes in the relative exact-exchange distribution through the additional LMF response term in (3.46) (see also Eq. (3.47)) and thus affect the respective excitation energies significantly. In the case of τ-dependent meta-GGAs, the inhomogeneity parameter t shows the same steep change as the t-LMF of local hybrids. However, it is not multiplied by exact but by local exchange, which does not affect Rydberg and core-valence excitations much. On the other hand, valence, charge-transfer and core-Rydberg excitations do not share this behavior, since intermediate regions with steep changes of the LMF are expected to be less relevant. In the case of core-Rydberg excitations, also a compensation between the steep LMF changes between core and valence regions and between valence and asymptotic regions is possible. Nevertheless, the observed results suggest that the effect of the current-density response for LMFs involving the gauge-invariant kinetic energy density becomes significant for excitations probing widely different LMF values for initial and final state densities.[286]

5.3. Conclusions

The results presented in the current chapter represent the first evaluation of the performance of local hybrid functionals for vertical excitation energies. Besides the ethylene tetrafluoroethylene complex for the investigation of intermolecular charge-transfer excitations, the vertical-excitation test sets of Thiel *et al.* and Tozer *et al.*, which cover valence,

intramolecular CT, Rydberg as well as core excitations, have been employed. For singlet valence excitations, the current local hybrid functionals are on par with state-of-the-art global hybrid functionals, while the best-performing local hybrids exhibit significantly better results for triplet valence excitations. For the latter, especially common LMFs have turned out to give systematically better results, which can be related to the additional inclusion of spin-opposite static correlation contributions. Concerning the other excitation types, local hybrids are able to provide a systematical improvement of Rydberg and core excitations, if the LMF gives an adequate exact-exchange admixture in distinct regions of real space. On the other hand, CT excitations are only comparably well described as with common global hybrid functionals. Regarding other influences, Rydberg and core-valence excitations calculated with local hybrids employing the t-LMF have been identified as the first cases, for which the inclusion of the current-density response to ensure gauge invariance of the kinetic energy density makes a significant difference. In contrast to many other XC functionals, local hybrid functionals appear not to benefit from the TDA, even in the case of triplet excitations, which indicates that local hybrids are generally able to provide accurate vertical excitation energies without the necessity of relying on the error compensation provided by the TDA.

6. Construction of New Calibration Functions

In the current chapter, the development of new calibration functions (CFs), which besides the LMF, represent one of the main building blocks in local hybrid functionals, is presented. First, a new general derivation scheme for calibration functions is introduced, on the basis of which new GGA and meta-GGA based CFs will be derived. For the determination of the free CF parameters, a new optimization procedure is applied, which relies on the correct description of the dissociation of noble gas dimers. Finally, the performance of the new calibration functions is evaluated and analyzed on the basis of the new optimization procedure. The present chapter thus reproduces theory and results already published in Ref. 315.

6.1. Derivation of Calibration Functions

6.1.1. Calibration Functions via Integration by Parts

While previously derived calibration functions (see Sec. 2.3.3) were constructed employing either a coordinate transformation of the exact-exchange hole or the divergence of a vector field, where the vector field is chosen to satisfy known properties of exchange functionals,[21,197] the starting point for the present derivation scheme is the exchange functional itself. Following Eq. (2.55), exchange functionals can usually be written in terms of an integration of exchange energy densities

$$E_{x,\sigma} = \int e_{x,\sigma}(\mathbf{r})\mathrm{d}\mathbf{r} \; . \tag{6.1}$$

As a first step, it is assumed that the energy density in Eq. (6.1) can be partitioned into a scalar product of two vectors, one of which is assumed to be the gradient of a scalar.

The exchange energy and its transformation by a partial integration are then given by

$$\int e_{x,\sigma}(\mathbf{r})\mathrm{d}\mathbf{r} = \int \mathbf{u}^{\mathrm{T}}(\mathbf{r}) \cdot \nabla v(\mathbf{r})\mathrm{d}\mathbf{r} = -\int \nabla^{\mathrm{T}}\mathbf{u}(\mathbf{r}) \cdot v(\mathbf{r})\mathrm{d}\mathbf{r} \; . \tag{6.2}$$

According to the necessary condition (2.84), the subtraction of the last from the middle term in (6.2) allows the construction of a CF by

$$\begin{aligned} \int G_\sigma(\mathbf{r})\mathrm{d}\mathbf{r} &= \int \left[\mathbf{u}^{\mathrm{T}}(\mathbf{r}) \cdot \nabla v(\mathbf{r}) + \nabla^{\mathrm{T}}\mathbf{u}(\mathbf{r}) \cdot v(\mathbf{r})\right] \mathrm{d}\mathbf{r} \\ &= \int \nabla^{\mathrm{T}} \cdot \left[\mathbf{u}(\mathbf{r}) \cdot v(\mathbf{r})\right] \mathrm{d}\mathbf{r} = 0 \; , \end{aligned} \tag{6.3}$$

which coincides with the formula for the divergence of a vector field in Eq. (2.86), with $\mathbf{W}_\sigma(\mathbf{r}) = \mathbf{u}(\mathbf{r}) \cdot v(\mathbf{r})$. Since a partitioning according to Eq. (6.2) is generally possible with GGA and meta-GGA functionals, Eq. (6.3) can be used directly to construct several new semi-local calibration functions embodying the same approximations as the underlying semi-local exchange functional. Hence, in contrast to previously derived CFs, no further assumptions have to be made besides the choice of the underlying exchange functional. The new approach thus reveals the close relationship between the CF and the exchange functional, accompanied by further understanding of the reqired CF properties. In particular, calibration functions based on GGA and τ-dependent meta-GGA exchange will be derived in the present work. For brevity, the space variable $\mathbf{r}$ will be omitted in the following sections of the chapter.

In this context, it should be noted that integration by parts in general is frequently applied in GGA and GEA exchange and correlation functionals to get rid of the density Laplacian. Classical examples are the theoretical determination of the GEA expansion parameter β in Eq. (2.60) on the basis of the gradient expansion of the Fermi hole[86] or the transformation of the original Laplacian-dependent LYP functional[101] into its Laplacian-free version.[102] In recent attempts, even a replacement of a certain fraction of GGA exchange by a Laplacian-dependent energy density has been suggested, arguing that this may suppress oscillations of the corresponding XC potential.[316] Accordingly, the addition of the underlying CF to its related GGA exchange functional may thus also be regarded as a partial step back, which is assumed to improve the compatibility of the resulting exchange energy density with exact exchange.

6.1.2. First-Order GGA Calibration Functions

Following Eq. (2.65), GGA exchange energies can be generally expressed as

$$\begin{aligned} E_{x,\sigma}^{GGA} &= E_{x,\sigma}^{LDA} - \int \rho_\sigma^{4/3} \cdot F\left(s_\sigma\right) \cdot s_\sigma^2 \mathrm{d}\mathbf{r} \\ &= E_{x,\sigma}^{LDA} - \frac{1}{k^2} \int \frac{F\left(s_\sigma\right) \cdot \nabla^{\mathrm{T}} \rho_\sigma}{\rho_\sigma^{4/3}} \cdot \nabla \rho_\sigma \mathrm{d}\mathbf{r} \ , \end{aligned} \tag{6.4}$$

where the reduced spin density gradient s_σ is given by Eq. (2.64) and $F\left(s_\sigma\right)$ denotes the damping function, also known as real-space cut-off function (for details see Sec. 2.2.4). For example, the damping functions for B88[92] and PBE[93] exchange are given by Eqs. (2.66) and (2.67), respectively. While the leading LDA exchange term in (6.4) does not contain any scalar products of vectors and is thus not suited for the construction of a CF via Eq. (6.3), the GGA correction, i.e. the second term on the right-hand side of the equation, can be rewritten according to Eq. (6.2) by taking

$$\mathbf{u} = \frac{1}{k^2} \frac{F\left(s_\sigma\right) \cdot \nabla \rho_\sigma}{\rho_\sigma^{4/3}} \ , \ v = \rho_\sigma \ . \tag{6.5}$$

Introducing a numerical prefactor f_1 for fitting purposes, this provides the CF

$$G_\sigma^{(1)} = \frac{f_1}{k^2} \cdot \nabla^{\mathrm{T}} \left\{ \frac{F\left(s_\sigma\right) \cdot \nabla \rho_\sigma}{\rho_\sigma^{1/3}} \right\} \ , \tag{6.6}$$

which shall be referred to as first-order calibration function (indicated by the superscript in $G_\sigma^{(1)}$), since the integration-by-parts scheme has been applied once. Basically, the numerical prefactor f_1 can be regarded as variable shifting the original exchange energy density to its integration-by-parts transform. In general, it is nonetheless not restricted to values between 0.0 and 1.0.

In an explicit form, Eq. (6.6) reads

$$\begin{aligned} G_\sigma^{(1)} = & \frac{f_1}{k^2} \cdot \left[F\left(s_\sigma\right) \cdot \left(\frac{\nabla^{\mathrm{T}} \nabla \rho_\sigma}{\rho_\sigma^{1/3}} - \frac{1}{3} \frac{\nabla^{\mathrm{T}} \rho_\sigma}{\rho_\sigma^{4/3}} \cdot \nabla \rho_\sigma \right) + \right. \\ & \left. s_\sigma \frac{\mathrm{d}F\left(s_\sigma\right)}{\mathrm{d}s_\sigma} \cdot \left(\frac{\nabla^{\mathrm{T}} \rho_\sigma}{\gamma_{\sigma\sigma}^{1/2} \cdot \rho_\sigma^{1/3}} \cdot \nabla \gamma_{\sigma\sigma}^{1/2} - \frac{4}{3} \frac{\nabla^{\mathrm{T}} \rho_\sigma}{\rho_\sigma^{4/3}} \cdot \nabla \rho_\sigma \right) \right] \ , \end{aligned} \tag{6.7}$$

which can be expressed in a more compact way

$$G_\sigma^{(1)} = f_1 \cdot \rho_\sigma^{4/3} \cdot \left[F\left(s_\sigma\right) \cdot \left(q_\sigma - \frac{1}{3} s_\sigma^2 \right) + s_\sigma \cdot \frac{\mathrm{d}F\left(s_\sigma\right)}{\mathrm{d}s_\sigma} \cdot \left(p_\sigma - \frac{4}{3} s_\sigma^2 \right) \right] \tag{6.8}$$

by introducing the reduced spin density Laplacian and the reduced spin density Hessian

$$q_\sigma = \frac{1}{k^2} \frac{\nabla^{\mathrm{T}} \nabla \rho_\sigma}{\rho_\sigma^{5/3}}, \tag{6.9}$$

$$p_\sigma = \frac{1}{k^2} \frac{\eta_{\sigma,\sigma\sigma}}{\gamma_{\sigma\sigma} \cdot \rho_\sigma^{5/3}} \, , \tag{6.10}$$

respectively. Here, the quantity $\eta_{\sigma,\sigma\sigma}$ is defined as

$$\eta_{\vartheta,\sigma\varsigma} = \nabla^{\mathrm{T}} \rho_\sigma \cdot \nabla \nabla^{\mathrm{T}} \rho_\vartheta \cdot \nabla \rho_\varsigma \tag{6.11}$$

and can be viewed as spin density Hessian projected onto the spin density gradient. Further relations of the reduced spin density Hessian to known DFT quantities as well as necessary extensions of the current local hybrid implementation due to the incorporation of this new semi-local quantity will be disscussed in the Appendix, sections A.1 and A.2, respectively. Note that Eq. (6.11) and the CF of Ref. 197 essentially coincide in the case that the Gaussian damping function (2.92) is employed. Only the definition of the numerical prefactor differs slightly. Hence, the previous CF represents one special case of a first-order GGA calibration function within the present scheme.

6.1.3. Higher-Order GGA Calibration Functions

Considering the explicit formulation of the first-order CF in Eq. (6.8), the integration-by-parts scheme can be applied separately to its individual terms to derive new second-order GGA CFs in the same way as done above for the first-order CF on the basis of the original energy density. The second term of Eq. (6.8) simply represents the original GGA exchange energy density scaled by a factor, so that merely the original first-order GGA CF is obtained again. The same occurs for the first term with the partitioning

$$\mathbf{u} = \frac{f_1}{k^2} \cdot \frac{F\left(s_\sigma\right)}{\rho_\sigma^{1/3}} \nabla \, , \; v = \rho_\sigma \, . \tag{6.12}$$

In contrast, the last two terms of Eq. (6.8) provide new CFs. In particular, a partitioning of the third term into

$$\mathbf{u} = \frac{f_1}{k^2} \cdot s_\sigma \frac{\mathrm{d}F\left(s_\sigma\right)}{\mathrm{d}s_\sigma} \frac{\nabla\rho_\sigma}{\rho_\sigma^{4/3}} \ , \ v = \rho_\sigma \tag{6.13}$$

or equivalently of the fourth term into

$$\mathbf{u} = \frac{f_1}{k^2} \cdot s_\sigma \frac{\mathrm{d}F\left(s_\sigma\right)}{\mathrm{d}s_\sigma} \frac{\nabla\rho_\sigma}{\gamma_{\sigma\sigma}^{1/2} \cdot \rho_\sigma^{1/3}} \ , \ v = \gamma_{\sigma\sigma}^{1/2} \tag{6.14}$$

both result in the same second-order GGA CF

$$G_\sigma^{(2)} = \frac{f_2}{k^2} \cdot \nabla^{\mathrm{T}} \left\{ f_1 \cdot \frac{\nabla\rho_\sigma \cdot s_\sigma}{\rho_\sigma^{1/3}} \frac{\mathrm{d}F\left(s_\sigma\right)}{\mathrm{d}s_\sigma} \right\} \ , \tag{6.15}$$

where prefactors and signs are again absorbed in the empirical parameter f_2. Partitioning the third term of Eq. (6.8) instead into

$$\mathbf{u} = \frac{f_1}{k^2} \cdot s_\sigma \frac{\mathrm{d}F\left(s_\sigma\right)}{\mathrm{d}s_\sigma} \frac{\nabla\gamma_{\sigma\sigma}^{1/2}}{\gamma_{\sigma\sigma}^{1/2} \cdot \rho_\sigma^{1/3}} \ , \ v = \rho_\sigma \tag{6.16}$$

would lead to computationally inefficient third derivatives of the density, which are not considered further here. Hence, in the present work, only the second-order CF (6.15) is considered, which in a more explicit formulation reads

$$\begin{aligned} G_\sigma^{(2)} = f_1 \cdot f_2 \cdot \rho_\sigma^{4/3} \cdot \Bigg[& s_\sigma^2 \cdot \frac{\mathrm{d}^2F\left(s_\sigma\right)}{\mathrm{d}s_\sigma^2} \cdot \left(p_\sigma - \frac{4}{3} s_\sigma^2 \right) + \\ & s_\sigma \cdot \frac{\mathrm{d}F\left(s_\sigma\right)}{\mathrm{d}s_\sigma} \cdot \left(p_\sigma + q_\sigma - \frac{5}{3} s_\sigma^2 \right) \Bigg] \ . \end{aligned} \tag{6.17}$$

Since the second-order GGA CF directly evolves from the first-order GGA CF by application of the new integration-by-parts scheme, $G_\sigma^{(2)}$ can be regarded as first correction term to $G_\sigma^{(1)}$ and should thus be used only in combination with the first-order CF. The same holds also true for higher-order calibration functions, which can be derived easily by subsequently applying the integration-by-parts scheme to terms of higher-order CFs. In particular, one possible Nth-order CF (note that the present derivation scheme would give a large variety of different higher-order CFs) with N free parameters can be derived by generalizing Eqs. (6.6) and (6.15) and summing the individual CF contributions up to

order N

$$G_\sigma = \sum_{m=1}^{N} \left[\prod_{n=1}^{m} f_n \right] \cdot \nabla^{\mathrm{T}} \left\{ \frac{\nabla\rho_\sigma \cdot s_\sigma^{m-1}}{\rho_\sigma^{1/3}} \frac{\mathrm{d}^{m-1} F\left(s_\sigma\right)}{\mathrm{d}s_\sigma^{m-1}} \right\} \mathrm{d}\mathbf{r} \ , \tag{6.18}$$

where the zeroth derivative of the damping function simply refers to the damping function F itself. In this way, the new integration-by-parts scheme provides a theoretically infinite series of successively more flexible CFs based on GGA exchange, which nonetheless is expected to suffer from the same numerical issues for higher orders as GGA or meta-GGA expansions of the exchange hole.[69] To distinguish between CFs of different orders N, the nomenclature 'pig' (partial integration gauge) plus the order of the expansion is introduced. In the present work, only GGA-based CFs to first and second order, i.e pig1 and pig2, respectively, are further investigated.

6.1.4. B98-Based Calibration Functions

Since the above 'pig' calibration functions were derived from GGA exchange, they might not be optimally suited for the calibration of meta-GGA exchange energy densities, that depend on the Kohn-Sham kinetic energy density τ (see Eq. (2.63)). In fact, one of the reasons why semi-local CFs so far were only used for the calibration of GGA exchange energy densities[197] is that attempts to calibrate TPSS exchange[106,107] with the previously derived Gaussian-damped GGA CF (see previous section) deteriorated results.[315] Application of the new integration-by-parts scheme to τ-dependent meta-GGA exchange, thus leading to τ-dependent CFs, represents one possible approach to solve these issues. In particular, the semi-local meta-GGA part of the B98 exchange functional[69]

$$E_{x,\sigma}^{sl} = \int e_{x,\sigma}^{LDA} \cdot \sum_{m=0}^{M} a_m \cdot \left[\frac{w \cdot Q_\sigma}{\left(1 + w^2 \cdot Q_\sigma^2\right)^{1/2}} \right]^m \mathrm{d}\mathbf{r} \tag{6.19}$$

has been used in the present work. Here, a_m denotes the coefficients of the Mth-order inhomogeneity expansion, e_x^{LDA} is the LDA exchange energy density, w represents the damping function coefficient and Q_σ is the meta-GGA inhomogeneity parameter

$$Q_\sigma = 1 + \frac{10}{3} q_\sigma - \frac{\tau_\sigma}{\tau_{TF,\sigma}} + \frac{5}{3} s_\sigma^2 \tag{6.20}$$

with the Thomas-Fermi kinetic energy density

$$\tau_{TF,\sigma} = \frac{3}{40} k^2 \cdot \rho_\sigma^{5/3} \ . \tag{6.21}$$

While the zeroth-order term of the expansion (6.19) corresponds to scaled LDA exchange and is thus not suited for the construction of a CF within the present scheme, CFs can be derived from all higher-order terms. Nonetheless, only the first-order correction term to LDA

$$\Delta e_{x,\sigma}^{B98} = a_1 \cdot F\left(Q_\sigma\right) \cdot Q_\sigma \cdot e_{x,\sigma}^{LDA} \ , \tag{6.22}$$

with the parameter a_1 is considered in the present work for the CF construction, since higher-order terms give only minor improvements in the underlying meta-GGA.[69] F again denotes a damping function

$$F\left(Q_\sigma\right) = \frac{w}{\left(1 + w^2 \cdot Q_\sigma^2\right)^{1/2}} \ , \tag{6.23}$$

which in contrast to the GGA case depends on the inhomogeneity parameter Q_σ instead of s_σ. In a more explicit formulation, Eq. (6.22) reads

$$\begin{aligned} \Delta e_{x,\sigma}^{B98} = &- \frac{3}{2}\left(\frac{3}{4\pi}\right)^{1/3} a_1 \cdot F\left(Q_\sigma\right) \cdot \rho_\sigma^{4/3} - 5\left(\frac{3}{4\pi}\right)^{1/3} \frac{a_1}{k^2} \cdot \frac{F\left(Q_\sigma\right)}{\rho_\sigma^{1/3}} \times \\ &\left[\frac{1}{2}\frac{\nabla^{\mathrm{T}}\rho_\sigma \cdot \nabla\rho_\sigma}{\rho_\sigma} + \nabla^{\mathrm{T}}\nabla\rho_\sigma - 2\sum_k^{occ} \nabla^{\mathrm{T}}\varphi_{k,\sigma}^* \cdot \nabla\varphi_{k,\sigma}\right] \ . \end{aligned} \tag{6.24}$$

While the first term in Eq. (6.24) is again an LDA-like term and is thus disregarded, the remaining three terms all result in the same CF. For the second and third term, this can be easily seen from the fact, that those terms are similar to the first and second term of the first-order GGA CF (6.7), which have been shown to result in the same CF, when used within the integration-by-parts scheme (see Sec. 6.1.3). The differing damping function argument, i.e. Q_σ instead of s_σ, represents only a formal difference. The last term gives the same result due to the relation

$$\nabla\rho_\sigma = \sum_{pq} D_{pq}^\sigma \left(\nabla\varphi_{p,\sigma}^* \cdot \varphi_{q,\sigma} + \varphi_{p,\sigma}^* \cdot \nabla\varphi_{q,\sigma}\right) \ . \tag{6.25}$$

Hence, either of the three remaining terms can be chosen for a partitioning according to Eq. (6.3). Taking exemplarily the second term of Eq. (6.24) (without the numerical

prefactor $5 \cdot a_1 \left(\frac{3}{4\pi}\right)^{1/3}$) and applying the partitioning

$$\mathbf{u} = \frac{1}{k^2} \frac{F\left(Q_\sigma\right) \cdot \nabla \rho_\sigma}{\rho_\sigma^{4/3}} \ , \ v = \rho_\sigma \ , \tag{6.26}$$

results in the first-order meta-GGA CF

$$G_\sigma^{(1)} = \frac{f_1}{k^2} \cdot \nabla^{\mathrm{T}} \left\{ \frac{F\left(Q_\sigma\right) \cdot \nabla \rho_\sigma}{\rho_\sigma^{1/3}} \right\} \ . \tag{6.27}$$

As for the GGA CF, a numerical prefactor f_1, which in the case of the meta-GGA CF has been merged with the numerical prefactors neglected above, is introduced for fitting purpose. Furthermore, Eq. (6.27) differs from the GGA CF (6.6) only by the employed inhomogeneity parameter and a different damping function, which anyway is exchangable in general. Hence, the close relation between GGAs and meta-GGAs is also reflected by the emerging calibration functions.

The evaluation of the divergence in (6.27) with the intermediate result

$$G_\sigma^{(1)} = f_1 \cdot \rho_\sigma^{4/3} \cdot \left[F\left(Q_\sigma\right) \cdot \left(q_\sigma - \frac{1}{3} s_\sigma^2 \right) + \frac{1}{k^2} \frac{\mathrm{d}F\left(Q_\sigma\right)}{\mathrm{d}Q_\sigma} \frac{\nabla^{\mathrm{T}} \rho_\sigma \cdot \nabla Q_\sigma}{\rho_\sigma^{5/3}} \right] \tag{6.28}$$

reveals, that the first-order meta-GGA CF contains the gradient of Q_σ, which itself requires the calculation of the gradient of the spin density Laplacian $\nabla^{\mathrm{T}} \nabla \rho_\sigma$ and thus third basis function derivatives. To avoid third derivatives, the reduced spin density Laplacian can be approximated semi-locally[86] as

$$q_\sigma \approx \frac{9}{20} \frac{\tau_\sigma}{\tau_{TF,\sigma}} - \frac{9}{20} - \frac{1}{12} s_\sigma^2 \ , \tag{6.29}$$

resulting in the approximated inhomogeneity parameter

$$\tilde{Q}_\sigma = \frac{1}{2} \frac{\tau_\sigma}{\tau_{TF,\sigma}} + \frac{25}{18} s_\sigma^2 - \frac{1}{2} \ , \tag{6.30}$$

with its gradient

$$\nabla \tilde{Q}_\sigma = \frac{1}{2} \frac{\nabla \tau_\sigma}{\tau_{TF,\sigma}} - \frac{5}{6} \frac{\tau_\sigma}{\tau_{TF,\sigma}} \frac{\nabla \rho_\sigma}{\rho_\sigma} + \frac{10}{3} s_\sigma^2 \cdot \left[\frac{5}{6} \frac{\nabla \nabla^{\mathrm{T}} \rho_\sigma \nabla \rho_\sigma}{\gamma_{\sigma\sigma}} - \frac{10}{9} \frac{\nabla \rho_\sigma}{\rho_\sigma} \right] \ . \tag{6.31}$$

The approximated meta-GGA CF then reads explicitly

$$G_\sigma^{(1)} = f_1 \cdot \rho_\sigma^{4/3} \cdot \left[F\left(\tilde{Q}_\sigma\right) \cdot \left(q_\sigma - \frac{1}{3} s_\sigma^2 \right) + \frac{10}{3} \cdot \frac{\mathrm{d}F\left(\tilde{Q}_\sigma\right)}{\mathrm{d}\tilde{Q}_\sigma} \times \left(\frac{5}{6} p_\sigma s_\sigma^2 + 2 r_\sigma - \frac{10}{9} s_\sigma^4 - \frac{1}{4} \frac{\tau_\sigma}{\tau_{TF,\sigma}} s_\sigma^2 \right) \right] , \tag{6.32}$$

where r_σ is defined as mixed reduced gradient of the density and the kinetic energy density

$$r_\sigma = \frac{1}{k^4} \frac{\nabla^{\mathrm{T}} \rho_\sigma \cdot \nabla \tau_\sigma}{\rho_\sigma^{10/3}} . \tag{6.33}$$

In analogy to GGA calibration functions, a theoretically infinite series of higher-order meta-GGA CFs can be constructed via

$$G_\sigma = \sum_{m=1}^{N} \left[\prod_{n=1}^{m} f_n \right] \cdot \nabla^{\mathrm{T}} \left\{ \frac{\nabla \rho_\sigma \cdot s_\sigma^{2(m-1)}}{\rho_\sigma^{1/3}} \frac{\mathrm{d}^{m-1} F\left(\tilde{Q}_\sigma\right)}{\mathrm{d}\tilde{Q}_\sigma^{m-1}} \right\} , \tag{6.34}$$

which will be referred to as 'tpig' (τ-dependent partial integration gauge) calibration functions. Nonetheless, to investigate the effect of semi-local τ-dependent CFs, only the first-order meta-GGA CF will be considered further.

Note that the restriction of the power series expansion (6.19) to first order is equivalent to considering the second-order gradient expansion of the exchange hole,[86] additionally imposing exact constraints by introducing the damping function F. Since the meta-GGA calibration function (6.27) directly emerges from such an expansion (and approximately also the GGA CF (6.8)), CFs, either of pig or tpig type, represent the natural formulation for CFs, if the second-order gradient expansion of the exchange hole is assumed. Differences between different pig and tpig CFs only appear in the employed damping function, which thus represents the main component for the construction of new CFs. In cases, in which higher-order gradient expansions of the exchange hole[107] or higher powers of the inhomogeneity parameter[69,95] are considered, as in TPSS or HCTH, respectively, the new integration-by-parts scheme would indeed provide different CFs, if higher-order terms are considered. Nonetheless, it can be hoped that the first-order meta-GGA CF derived from B98 exchange, i.e. tpig1, is already suitable for the calibration of a broader range of meta-GGA exchange functionals. Hence, derivations of calibration functions based on more complicated exchange functionals as TPSS, which is based on a fourth-order gradient expansion, are disregarded in the present work.

6.2. Optimization of Calibration Functions

6.2.1. Optimization Procedure

As in previously proposed calibration functions,[21,197] the newly derived pig and tpig CFs contain empirical parameters, which have to be fixed employing a suitable optimization scheme. So far, two different approaches had been used. Tao *et al.*[21] had optimized the three parameters of their CF (see Eq. (2.87)) by making the semi-local (TPSS) exchange energy density reproduce the exact-exchange energy density for a number of atoms and small diatomics. To some extent, this direct minimization of exchange energy density differences might also eliminate static correlation contributions, required for an accurate description of homogeneous regions in molecules, since no distinction between different regions in real space are made. Hence, this optimization procedure may result in a significant overcalibration. Furthermore, interrelations between the CF and the LMF within the framework of local hybrid functionals (cf. Eq. (2.72)) are completely neglected.

For the calibration of local hybrids, Arbuznikov *et al.*[197] had thus chosen a different approach. Here, the linear prefactor of their CF (see Eq. (2.91)) was optimized together with the LMF parameters and the prefactors of semi-local exchange and correlation corrections to LDA (as in B3LYP, see Eq. (2.70)) with respect to thermochemical test sets, after some preoptimization of the damping function parameter (see Eq. (2.92)). While a balanced description of static correlation contributions is thus retained, it is not guaranteed that gauge issues are directly addressed, since strong interrelations with the other parameters might appear. Furthermore, the fact that the CF itself integrates to 0 (see Eq. (2.84)) suggests that the additional integral $\int g_\sigma(\mathbf{r}) \cdot G_\sigma(\mathbf{r})\mathrm{d}\mathbf{r}$ should not make major contributions to total energies. Hence, thermochemical properties might thus be more affected by other parts of the functional than by the calibration function. It therefore seems more promising to fix the free parameters of a CF to quantities that are most clearly affected by the gauge issue.

In particular, uncalibrated local hybrid functionals generally exhibit unphysical, too repulsive energy curves for weakly bound complexes, such as noble gas dimers. It could be shown[197,200] that even CFs with small linear prefactors are able to appreciably correct this unphysical behavior by removing spurious, typically positive, static correlation contributions (see Eq. (2.75)).[197] Hence, such energy curves may in principle be used to optimize CFs. In the present work, the dissociation curves of several noble gas dimers are thus used to optimize the empirical parameters of the new pig and tpig calibration functions. Therefore, a suitable reference point has to be defined first. At larger distances,

the intermolecular interaction energies between two noble gas atoms can be assumed to be determined by nucleus-nucleus and some remaining Pauli repulsion contributions as well as by dispersion interactions caused exclusively by non-local correlation contributions neither included in simple semi-local nor in hybrid functionals (cf. Sec. 2.2.4).[315] Static correlation is thus negligible. Additionally neglecting the dispersion contributions, Hartree-Fock or exact-exchange-only Kohn-Sham calculations (see Secs. 2.1.2 and 2.2.2, respectively) should accurately reproduce the remaining repulsive interactions and thus provide a suitable reference to identify and subsequently minimize unphysical static correlation contributions (cf. Eq. (2.75)) present in uncalibrated local hybrids. One implicit consequence of this optimization scheme is that, besides the mitigation of the gauge problem, some artifacts inherent to the semi-local exchange functional are also removed. Since the behavior of the reference energy curves nonetheless represents an accurate physical condition (only with the restriction that the minor influence of correlation effects to the orbitals are neglected), the removal of those artifacts can be regarded as an additional feature of the present optimization scheme. Likewise, it can be expected that the obtained calibrated local hybrids form a good basis for the addition of non-local van-der-Waals functionals or other dispersion corrections (see Sec. 2.2.4).[199,200]

Based on these considerations, three optimization schemes are proposed, differing only in the set of orbitals used for the reference and the local hybrid functional. The first method (M1) uses the HF interaction energy as reference, applying the local hybrid of interest without a dynamical correlation functional and orbitals being fully optimized. In the second scheme (M2), the self-consistent HF energy is again used as reference, but the local hybrid orbitals are now optimized in the presence of a dynamical correlation functional, while the local hybrid interaction energy is determined without the dynamical correlation functional to suppress spurious energy contributions. In the third scheme (M3), only one set of self-consistently determined orbitals is used, i.e. orbitals optimized for the local hybrid with dynamical correlation. For this set of orbitals, the static correlation term (2.75) is directly minimized. That is, the exact-exchange-only Kohn-Sham interaction energy is subtracted from the local hybrid interaction energy without dynamical correlation, using an identical set of orbitals.

As a last step, a suitable minimization parameter has to be defined to allow the optimization of the CFs using the proposed schemes. The most natural choice is the use of the absolute area between the local hybrid and the reference energy curve, as illustrated in Fig. 6.1. In practice, n points of the dissociation curves are calculated within a distinct interval and are exactly fitted to an nth order power series expansion. The minimization parameter then corresponds to the absolute integral of the difference between both fit-

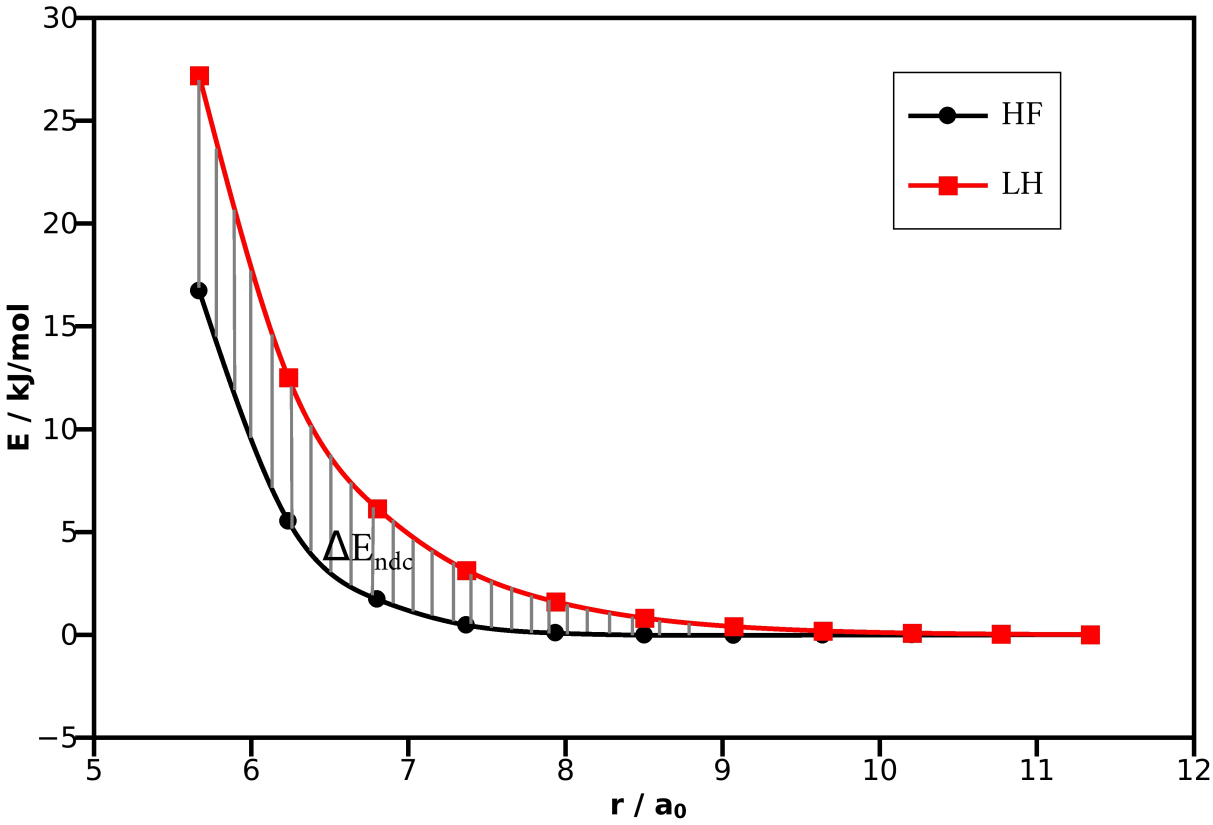

Figure 6.1.: Dissociation curve (energy in kJ/mol and distance in a_0) of the argon dimer calculated with HF and an uncalibrated local hybrid functional with t-LMF (unscaled) and B88 exchange. The difference between both curves (shaded area) represents the spurious (positive) static correlation ΔE_{ndc}, that is minimized by calibration (see text).

ted polynomials. While this scheme is straightforward, its outcome may depend on the applied integration range. A too small lower integration boundary, i.e. a too small interatomic distance, might result in an overcalibration in regions where the chosen reference is not well-behaved anymore, e.g. due to extensive overlap of the two atomic density distributions.[315] On the other hand, a too large upper integration boundary only increases computation time without additional significant contributions to the integral. Besides an integration within real space, i.e. integrating over the interatomic distance r, a second scheme, which applies an integration over the inverse space r^{-1}, is explored. Within the second scheme, contributions from large interatomic distances, which are in fact very small, are lower weighted compared to the first scheme, so that numerical noise might be reduced. Accordingly, shorter distances receive higher weights, which might be advantageous to remove the larger unphysical static correlation contributions in those regions. Considering all possible combinations of proposed integration and reference schemes, six

different procedures are evaluated with respect to their applicability for the optimization of CFs.

6.2.2. Computational Details

All calculations were carried out with the local developer's version of the TURBOMOLE program package,[19] which contains the self-consistent implementation of local hybrid functionals[270] together with the extension to calibration functions of pig and tpig type (cf. Sec. A.2). As basis for the optimizations, a local hybrid functional consisting of LDA exchange,[74,75] self-interaction reduced PW92 correlation (sirPW92)[18,77] (2.83) and a common t-LMF[18] (2.81) was taken. The LMF parameter $a = 0.637$ was obtained by a thermochemical reoptimization with respect to G2-1[317,318] atomization energies and ionization potentials as well as BH76 reaction barriers[319–323] (see Sec. 7.2 for details). For the purpose of comparability, the LMF prefactor has been kept the same for the additionally evaluated B88[92] and TPSS[106,107] exchange functionals. Besides the three CFs pig1, pig2 and tpig1 (cf. Eqs. (6.8), (6.17) and (6.32), respectively), three different damping functions are investigated, i.e. Gaussian damping (2.92) as well as B88- and B98-like damping (2.66) and (6.23), respectively. While in the case of tpig1, the reduced spin density gradient s_σ is simply replaced by the inhomogeneity parameter $\tilde{Q}_\sigma$ for B88 and Gaussian damping, $\tilde{Q}_\sigma$ is equivalently substituted by s_σ for B98 damping with pig type CFs. In all calculations, def2-TZVP basis sets have been employed.[285]

For the optimization of the CF parameters within the proposed scheme (see Sec. 6.2.1), the dissociation curves of the argon-argon (Ar-Ar), the argon-neon (Ar-Ne) and the neon-neon (Ne-Ne) dimer have been chosen. The mean absolute error (MAE) of the measure described in Sec. 6.2.1, i.e. the average over the three dimers, has been used as quality measure and was thus seeked to be minimized. To ensure comparability between the different noble gas dimers, the lower integration boundary was adjusted to give a HF repulsion energy of around 14-16 kJ/mol. Starting from thus-obtained lower distances of 2.2 Å, 2.6 Å and 3.0 Å for Ne-Ne, Ar-Ne and Ar-Ar, respectively, ten additional steps within a range of 3.0 Å have been used for the integration. Since very small interaction energies and even smaller energy differences have to be covered, total energies had to be calculated with high precision. Therefore, an SCF convergence threshold of $10^{-10} E_h$ as well as large molecular grids have been employed to ensure the required accuracy within the semi-numerical integration scheme used in the local hybrid implementation of TURBOMOLE. In particular, a large 1202 point Lebedev spherical grid and a Chebychev radial grid with a large number of 320 and 325 grid points for neon and argon, respectively, are utilized.

This ensures a sufficient number of grid points in the region between the monomers even for larger monomer distances, thus avoiding any oscillations in the dissociation energy curves.[315]

Lacking analytical derivatives with respect to the CF parameters, a Nelder-Mead-Simplex algorithm[324] was used for the optimizations. To accelerate the convergence close to the minimum, which in general is only linear, a quadratically convergent step has been added at the end of the usual optimization (in fact, with a looser threshold), which considers all evaluation points near the actual minimum via a fitting procedure of the parameter surface. Due to the small number of simultaneously treated optimization parameters (at most three), results can be safely assumed to represent global minima.

6.2.3. Results

In a first step, the suitability of the six proposed schemes for the definition of the MAE (see Sec. 6.2.1) shall be evaluated. Therefore, LDA exchange in combination with the pig1 calibration function and B88 damping is employed. The respectively minimized MAEs as well as the corresponding optimized CF parameters are shown in Table 6.1. Since the MAEs for the integration in r and in r^{-1} space exhibit different units, they are not directly comparable. On the other hand, MAEs for a given integration space show only moderate variation for different reference methods (M1-M3), where the exact-exchange-only reference (M3) gives slightly larger deviations compared to the other two methods. Regarding the optimized CF parameters, results obtained with the M2 and the M3 method differ just slightly, in particular in r^{-1} space. While deviations seem to be larger in the r space, the overall prefactor, which is determined by the product of f_1 and β (cf. B88 damping (2.66)), reveals an even better correspondence for r space integration. Although parameters obtained within the M1 scheme exhibit somewhat larger deviations from those of the M2 and M3 method, they differ only moderately, thus illustrating the assumed minor influence of self-consistency on the investigated noble gas dimer dissociation curves (cf. Sec. 6.2.1). Differences between the r and r^{-1} space methods are notable, but also remain moderate, which illustrates the appropriate choice of the integration ranges. In particular, the optimized damping function parameter β exhibits systematically larger values in r space, which however is compensated by slightly smaller values for f_1. Overall, all six methods have been found to be almost equally suited for the optimization of the CF parameters. Nevertheless, the M3 method has the advantage, that the MAE can be directly interpreted as residual static correlation, since the reference is calculated for the same set of orbitals as the local hybrid functional. Hence, in the following discussion only

the M3 method is further used, which in favor of simplicity, is combined with r space integration.

Table 6.1.: Mean absolute errors (MAEs) (in $a_0 \cdot kJ/mol$ for r space and in $a_0^{-1} \cdot kJ/mol$ for r^{-1} space) calculated with a local hybrid functional with LDA exchange and an optimized pig1 CF with B88 damping. Three different evaluation methods (M1-M3) with respect to two different space coordinates (r, r^{-1}) are compared for optimization.

Space	Method	LDA + pig1/B88			
		MAE	f_1	β	$-f_1 \cdot \beta$
r	M1	1.326	-1.009	$2.932 \cdot 10^{-3}$	$2.959 \cdot 10^{-3}$
	M2	1.359	-0.806	$1.246 \cdot 10^{-2}$	$1.005 \cdot 10^{-2}$
	M3	1.473	-0.727	$1.458 \cdot 10^{-2}$	$1.060 \cdot 10^{-2}$
r^{-1}	M1	$4.505 \cdot 10^{-2}$	-1.317	$1.937 \cdot 10^{-3}$	$2.552 \cdot 10^{-3}$
	M2	$4.952 \cdot 10^{-2}$	-1.052	$5.587 \cdot 10^{-3}$	$5.876 \cdot 10^{-3}$
	M3	$5.897 \cdot 10^{-2}$	-1.055	$5.045 \cdot 10^{-3}$	$5.321 \cdot 10^{-3}$

Before comparing different CFs, the influence of the calibration shall be highlighted for the dissociation curves of the individual noble gas dimers. Fig. 6.2 therefore shows the comparison between a calibrated local hybrid functional (LDA exchange with pig1 CF and B88 damping, M3 optimization in r space, cf. Table 6.1) and its corresponding uncalibrated counterpart. The figure plots the unphysical static correlation ΔE_{NDC} as function of the internuclear distance, starting from the selected lower boundary distance value (cf. Sec. 6.2.2) to ensure comparability between the different dimers. Hence, a straight line on the abscissa may be interpreted as a perfectly calibrated local hybrid. The uncalibrated dimer curves exhibit the expected large unphysical repulsion,[197,200] with the curvature varying somewhat between the complexes. The Ne-Ne dimer shows the fastest decay, the Ar-Ar dimer the slowest. Obviously, even the simple pig1 CF used for Fig. 6.2 reduces ΔE_{NDC} appreciably, i.e. from an MAE of 12.664 $a_0 \cdot kJ/mol$ for the uncalibrated curves to a MAE of 1.473 $a_0 \cdot kJ/mol$ for the calibrated ones. Reflecting the differences between the uncalibrated curves, the calibrated curves also exhibit a variable behavior for the three dimers, from a small undercorrection for Ne-Ne via essentially perfect calibration for Ar-Ne to a slight overcalibration for Ar-Ar. It is these variations and thus the quality and universality of the CF, that the MAE expresses.[315] In this context, it should be noted that, beyond $\Delta r > 2.0 a_0$, the calibrated local hybrid exhibits essentially negligible static correlation contributions for all noble gas dimers, which shows the effectiveness of the calibration at larger distances.

As a next step, the ability of the various CFs derived in Sec. 6.1 to universally minimize ΔE_{NDC} in conjunction with different semi-local exchange energy densities and different damping functions shall be analyzed. Table 6.2 provides the CF parameters f_1, f_2 and

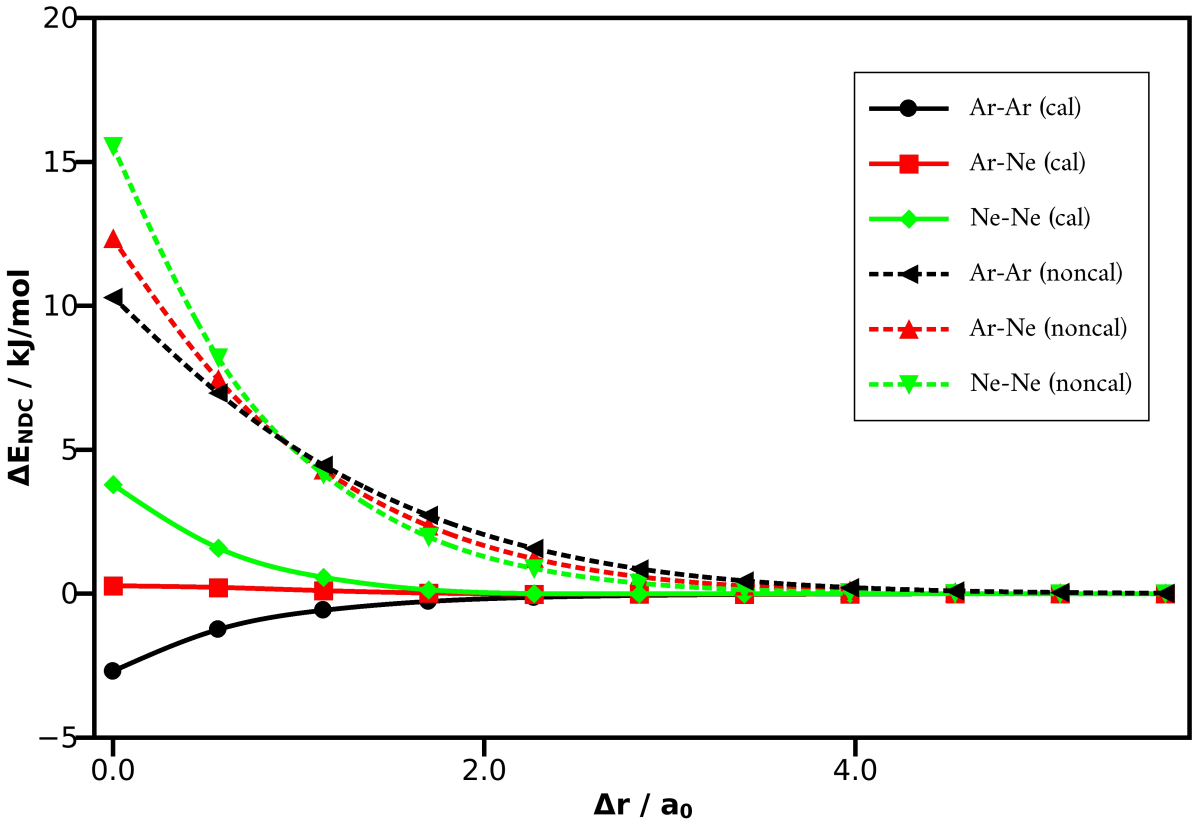

Figure 6.2.: Static correlation contributions ΔE_{NDC} in kJ/mol calculated for distances Δr in a_0 relative to the lowest boundary distance (depending on noble gas dimer, see Sec. 6.2.2). The dotted and full lines represent non-calibrated and calibrated local hybrid functionals, respectively.

β optimized for different combinations of exchange energy densities, basic CF forms and damping functions together with the obtained MAEs. Regarding the various damping functions, simple Gaussian damping exhibits the largest MAEs in combination with LDA exchange, irrespective of the chosen CF. On the other hand, Gaussian damping provides the lowest MAEs for B88 and TPSS exchange with the pig1 form. With the more sophisticated pig2 and tpig1 CFs, B88 and particularly B98 damping perform better. In contrast to the other two damping functions, Gaussian damping does not benefit from the second-order correction term introduced in pig2, thus simply reducing the CF to pig1 form. B98 damping slightly outperforms B88 damping for pig2 and tpig1, which is most pronounced for TPSS exchange. Although this might reflect the better match of meta-GGA damping with a meta-GGA exchange energy density, differences are small compared to the benefit with respect to the uncalibrated local hybrid.

The performance of the different calibration functions for different exchange energy densities varies relatively little. Only for the simple pig1 CF, MAEs increase significantly for

Table 6.2.: Minimized mean absolute errors (MAEs) in $a_0 \cdot kJ/mol$ and corresponding CF parameters (f_1, f_2, β) in a.u. calculated with local hybrid functionals using different semi-local exchange energy densities $e^{sl}_{x,\sigma}$ in combination with the pig1, pig2 and tpig1 CFs and different damping functions F. The integration method M3 in r space has been used.

$e^{sl}_{x,\sigma}$	F	pig1			pig2				tpig1		
		MAE	f_1	β	MAE	f_1	f_2	β	MAE	f_1	β
LDA	B88	1.47	-0.73	$1.46 \cdot 10^{-2}$	1.41	-1.97	0.61	$3.56 \cdot 10^{-3}$	1.47	-14.11	$2.28 \cdot 10^{-4}$
	B98	1.59	-0.23	2.09	1.37	-0.49	0.66	$6.39 \cdot 10^{-1}$	1.47	-2.05	$8.34 \cdot 10^{-2}$
	Gauss	1.60	-0.19	$9.13 \cdot 10^{-2}$	1.60	-0.19	0.00	$9.13 \cdot 10^{-2}$	1.73	-0.15	$1.08 \cdot 10^{-3}$
B88	B88	1.82	-0.58	$1.91 \cdot 10^{-2}$	1.53	-2.24	0.82	$3.67 \cdot 10^{-3}$	1.51	-7.53	$5.14 \cdot 10^{-4}$
	B98	1.93	-0.19	2.08	1.48	-0.54	0.86	$6.87 \cdot 10^{-1}$	1.48	-1.28	$1.54 \cdot 10^{-1}$
	Gauss	1.60	-0.20	$1.44 \cdot 10^{-1}$	1.60	-0.20	0.00	$1.44 \cdot 10^{-1}$	1.68	-0.15	$2.06 \cdot 10^{-3}$
TPSS	B88	1.83	-0.54	$2.38 \cdot 10^{-2}$	1.57	-2.41	0.81	$6.89 \cdot 10^{-3}$	1.48	-5.77	$8.46 \cdot 10^{-4}$
	B98	2.03	-0.19	2.99	1.47	-0.59	0.93	$7.10 \cdot 10^{-1}$	1.44	-1.08	$2.24 \cdot 10^{-1}$
	Gauss	1.53	-0.23	$1.96 \cdot 10^{-1}$	1.53	-0.23	0.00	$1.96 \cdot 10^{-1}$	1.60	-0.17	$3.34 \cdot 10^{-3}$

B88 and TPSS exchange, with the exception of Gaussian damping. In contrast, pig2 and tpig1 calibration perform comparably well for all investigated exchange energy densities and, except for simple Gaussian damping, which anyhow is disfavored due to its too fast decay, exhibit clearly smaller MAEs than the previous pig1 CF. Besides the effectiveness of the second linear parameter f_2 in the pig2 CF, this illustrates the potential of a tpig-like calibration, especially for the calibration of non-LDA exchange energy densities. In particular, even the tpig1 CF, although also containing only one linear parameter, exhibits significantly lower MAEs for the calibration of B88 and TPSS exchange than pig1, which might be related to the meta-GGA background of the tpig1 CF. Giving the lowest MAEs for the calibration of LDA and TPSS exchange, respectively, pig2 and tpig1 calibration thus clearly improve over the simple pig1 CF.

Going from LDA to TPSS exchange, the damping function parameters of the calibration functions turned out to increase systematically, thus indicating an increasingly faster decay of the damping. Within the present scheme, this means that different semi-local exchange energy densities require slightly different calibration in the long range. Most notably, the optimized damping function parameters β are in good agreement with the values of the exchange functionals, upon which the CFs are based. That is, for B88 exchange, the pig2 CF with B88 damping exhibits a damping parameter of $\beta = 0.0037$, while $\beta = 0.0042$ for the B88 exchange functional.[92] Likewise, tpig1 with B98 damping used for the calibration of B88 exchange and the B98 exchange functional have damping parameters of $\beta = 0.15$ and $\beta = 0.11$, respectively.[69] Besides a well-behaved optimization procedure, this underlines again the close relationship between the CFs of this work and

the underlying exchange functionals, from which they have been derived. In this context, it should be noted that, due to different inhomogeneity parameters used in pig and tpig CFs, i.e. the reduced density gradient s_σ and $\tilde{Q}_\sigma$, which is proportional to s_σ^2, respectively, damping function parameters represent different orders of magnitude for pig and tpig CFs. Hence, the damping function parameter based on a distinct exchange functional is not simply transferable to calibration functions with other underlying exchange functionals.

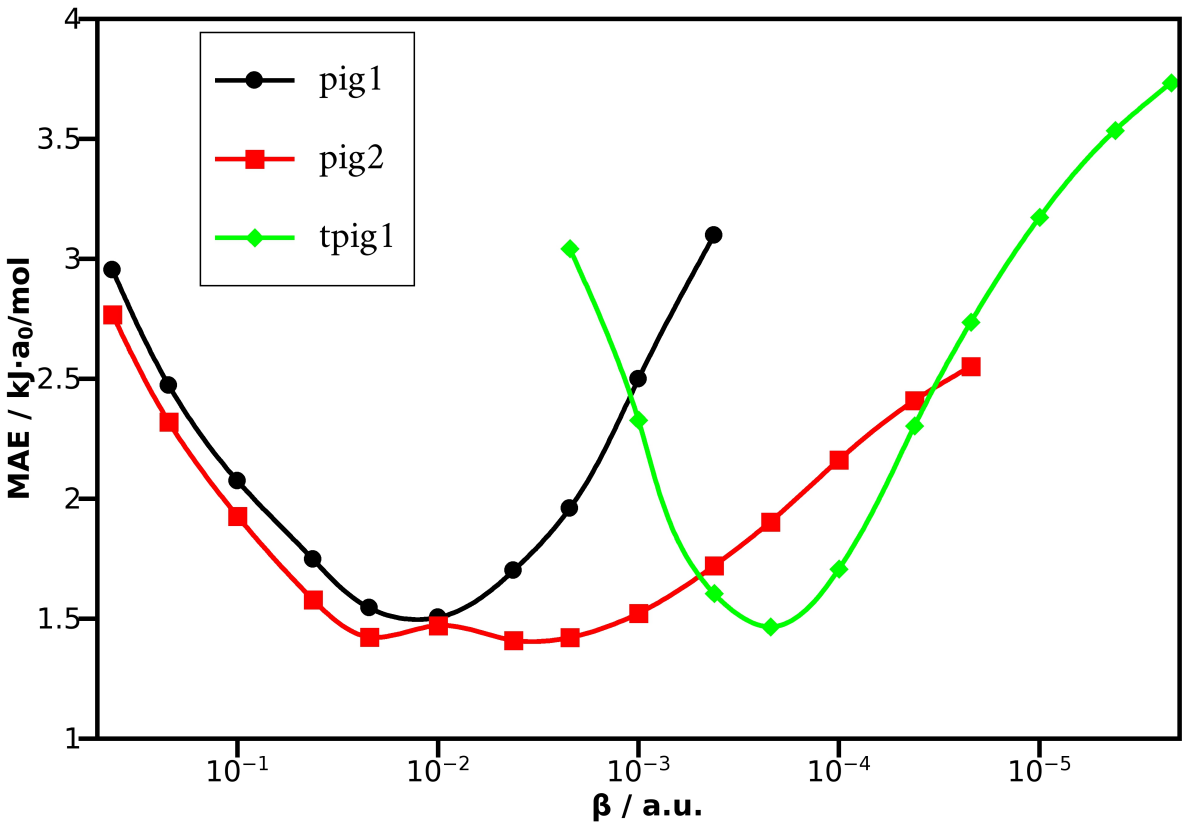

Figure 6.3.: Scan of the mean absolute error (MAE) in $a_0 \cdot kJ/mol$ over the damping function parameter β of the B88 damping function calculated with calibrated (pig1, pig2 or tpig1) local hybrid functionals with LDA exchange. For each value of β, the other CF parameters have been optimized.

While calibration functions optimized within the present scheme (see Sec. 6.2.1) thus effectively minimize the unphysical static correlation in weak interaction curves, as e.g. for the dissociation of noble gas dimers, it was previously observed that the optimal CF parameters determined with respect to thermochemical properties may differ considerably.[197,200] Besides small MAEs, a sufficient flexibility of CFs is thus very desirable. For the evaluation of the flexibility of the three investigated CF types, mean absolute errors within the present optimization scheme have been determined for different fixed values

of the damping parameter β, while the remaining parameters of the CF are reoptimized. Therefore, LDA exchange was used together with B88-like damping. Fig. 6.3 plots the resulting MAEs as a function of β for the three different types of CFs, i.e. pig1, pig2 and tpig1. While the curves for the pig1 and tpig1 CFs each exhibit a distinct minimum with steep curvature, the pig2 CF shows a much more shallow double-minimum curve with low MAEs over a larger range of β. As discussed above, the optimal damping parameter for tpig1 is two orders of magnitude smaller than the one for pig1 due to the different employed inhomogeneity parameters. Although the lowest MAE with pig2 is only slightly better than with the other two CFs, the larger range of β with low MAEs and thus a higher flexibility of the CF might be advantageous for a simultaneous accurate treatment of weak interactions and thermochemistry. The reason for this higher flexibility is the additional linear prefactor introduced within the second-order correction term of pig2. The addition of higher-order corrections might provide even more flexibility. This shows the potential of the new integration-by-parts scheme, which besides the construction of CFs on the basis of an arbitrary GGA or meta-GGA exchange functional, allows the systematical development of higher-order CFs.

6.3. Conclusions

Besides the search for suitable models for the local mixing function, the development of calibration functions to mitigate the gauge origin problem (see Sec. 2.3.3 for details) represents the most difficult task in the construction of local hybrid functionals. In the present chapter, a novel general derivation scheme for the construction of CFs based on an integration by parts of exchange functionals has been presented. Besides the illustration of the close relation between CFs and approximations to the exchange functional, the new scheme thus provides the opportunity to construct a large variety of different new CFs. In particular, new CFs have been derived on the basis of GGA as well as the semi-local part of B98 exchange, leading to the pig and tpig type CFs, respectively. While the first-order pig type CF, i.e. pig1, has been identified as the previously proposed CF of Arbuznikov *et al.* and thus provides a more detailed theoretical understanding of the previous model, the second-order pig and first-order tpig CFs, i.e. pig2 and tpig1, respectively, represent fundamentally new calibration functions. For the determination of their intrinsic empirical parameters, a novel optimization procedure, minimizing the unphysical static correlation contributions in dissociation curves of noble gas dimers, which are known to be significantly affected by the calibration of exchange energy densities, has been additionally proposed. In contrast to previous approaches, the gauge problem is thus

more directly tackled and an overcalibration is avoided to a large extent. Concerning the new CFs, it could be shown that tpig1 performs significantly better than the previous pig1, although both CFs contain only one linear parameter. The additional parameter provided by the second-order CF pig2 turned out to dramatically enhance the flexibility of the calibration function, if an appropriate damping is applied. Hence, the present chapter provides the methodology for the construction of novel, more flexible calibration functions as well as a general methodology for their optimization. In conjunction with the usual thermochemical optimization of XC functionals, as will be used in the next chapter for the development of local hybrids employing a new LMF and correlation functional, the new optimization procedure thus opens the way for the general development of calibrated local hybrid functionals, which are expected to be better suited for the addition of semi-empirical dispersion corrections.

7. Construction of a New Local Mixing Function

While the last chapter was concerned with the construction of new calibration functions (CFs) to mitigate the gauge problem inherent to local hybrid functionals, the present chapter deals with the development of a new local mixing function (LMF). In the first section, the theoretical model used for the construction of the new gt-LMF is elucidated in detail. This also includes a modified version of the self-interaction reduced PW92 correlation functional. Subsequently, the thermochemically optimized local hybrid functionals containing the modified correlation functional either in combination with the new gt-LMF or the standard t-LMF are evaluated with respect to common thermochemical and vertical-excitation test sets.

7.1. Theoretical Model

Although being the first proposed and one of the simplest approaches for modeling the local mixing function,[15,185] the scaled t-LMF

$$g_\sigma(\mathbf{r}) = a \cdot t_\sigma(\mathbf{r}) = a \cdot \frac{1}{8}\frac{\gamma_{\sigma\sigma}(\mathbf{r})}{\tau_\sigma(\mathbf{r})\,\rho_\sigma(\mathbf{r})} \tag{7.1}$$

still represents one of the most successful models for the construction of new local hybrid functionals.[17,18,197] The t-LMF nonetheless exhibits several undesirable properties. That is, it violates the correct behavior in one-electron regions for prefactors $a < 1.0$, which is usually the case for thermochemically optimized prefactors,[18,185,197] the single empirical parameter allows only a limited flexibility in intermediate regions between valence and one-electron regions, which have been shown to be responsible for accurate Rydberg excitation energies, and the maximum amount of exact exchange in core regions is limited to a certain fraction determined by a irrespective of the atom type, which results in an unbalanced performance for core excitations of atoms from different periods. Nevertheless,

the t-LMF represents a suitable starting point for the construction of new local mixing functions, that are able to satisfy the above mentioned conditions.

Within the new approach of the current work, the constant scaling factor a is simply replaced by a real-space-dependent function $\tilde{g}_\sigma(\mathbf{r})$, which is similar to the step from global to local hybrid functionals. This then leads to the new local mixing function

$$g_\sigma(\mathbf{r}) = \tilde{g}_\sigma(\mathbf{r}) \cdot t_\sigma(\mathbf{r}) = \tilde{g}_\sigma(\mathbf{r}) \cdot \frac{1}{8} \frac{\gamma_{\sigma\sigma}(\mathbf{r})}{\tau_\sigma(\mathbf{r})\,\rho_\sigma(\mathbf{r})} , \tag{7.2}$$

referred to as gt-LMF, where the function $\tilde{g}_\sigma(\mathbf{r})$ is responsible for the downscaling of the t-LMF in different regions of real space and thus has to satisfy the condition

$$0.0 \leq \tilde{g}_\sigma(\mathbf{r}) \leq 1.0 . \tag{7.3}$$

In particular, $\tilde{g}_\sigma(\mathbf{r})$ should provide a distinct downscaling in valence regions to ensure an adequate description of thermochemical properties. In homogeneous regions, the LMF value is already fixed to 0.0 due to the inhomogeneity parameter $t_\sigma(\mathbf{r})$, so that $\tilde{g}_\sigma(\mathbf{r})$ generally may take arbitrary values between 0.0 and 1.0. While in one-electron regions, $\tilde{g}_\sigma(\mathbf{r})$ has to be 1.0 to guarantee 100% exact exchange, the downscaling in core regions should account for the demand of heavier elements for larger fractions of exact exchange due to their higher electron density at the atomic cores. Taking those considerations into account, $\tilde{g}_\sigma(\mathbf{r})$ can be modeled in a similar way as the local mixing function itself. Therefore, the simple approach

$$\tilde{g}_\sigma(\mathbf{r}) = \frac{h_\sigma(\mathbf{r})}{1 + h_\sigma(\mathbf{r})} \tag{7.4}$$

has been chosen, where the dimensionless function

$$h_\sigma(\mathbf{r}) = a + b \cdot s_\sigma^2(\mathbf{r}) + c \cdot q_\sigma^2(\mathbf{r}) + d \cdot p_\sigma^2(\mathbf{r}) \tag{7.5}$$

contains a constant, the reduced spin density gradient $s_\sigma(\mathbf{r})$, the reduced spin density Laplacian $q_\sigma(\mathbf{r})$ and the reduced spin density Hessian $p_\sigma(\mathbf{r})$ (see Eqs. (2.64), (6.9) and (6.10), respectively), each scaled by an individual parameter ($a - d$) that should be positive to satisfy condition (7.3).

The parameter a defines the minimal value of $\tilde{g}_\sigma(\mathbf{r})$ and thus the maximum downscaling of the t-LMF. For example, a value of $a = 0.0$ allows the $h_\sigma(\mathbf{r})$ function to become 0.0, if the reduced quantities exhibit zero values, which would result in $\tilde{g}_\sigma(\mathbf{r}) = 0.0$. On the other hand, $a = 1.0$ provides a scaling factor of at least 50%, while $a = \infty$

would simply result in an unscaled t-LMF. Hence, the parameter a is comparable to the linear prefactor of the t-LMF and thus able to provide an adequate downscaling in valence regions, where the reduced quantities might not be effective. The remaining parameters b, c and d determine the influence of the reduced quantities. Since the latter all have infinite values in the low-density limit, the condition $\tilde{g}_\sigma(\mathbf{r}) = 1.0$ in one-electron regions is automatically satisfied, if one of their parameters is non-zero. Only the regions identified as one-electron regions might change with different parameter sets. Due to the antisymmetry of the spin density gradient with respect to atomic centers, the reduced spin density gradient is zero at the atomic centers. On the other hand, $p_\sigma(\mathbf{r})$ and $q_\sigma(\mathbf{r})$ exhibit non-zero values at the atomic centers, since the spin density Hessian is a symmetric quantity. The combination of the three reduced quantities within the $h_\sigma(\mathbf{r})$ function thus generally allows an adjustment of the amount of exact exchange in core regions depending on the atom as well as a fine-tuning in intermediate regions. The presented gt-LMF is thus generally able to eliminate the abovementioned deficiencies of the t-LMF, supposed a suitable parameter set is provided. In fact, $h_\sigma(\mathbf{r})$ can be simply extended by other reduced quantities, as e.g. the reduced kinetic energy density gradient (see Sec. A.1), to further improve the present model. Nevertheless, for simplicity only the three abovementioned reduced quantities are further considered in the present work.

Since common LMFs are generally known to give improved results compared to their spin-channel counterparts (see Sec. 2.3.2), a common LMF version of the gt-LMF shall be constructed, too. While a mixed gt-LMF

$$g_\sigma(\mathbf{r}) = \frac{1}{8} \cdot \frac{h_\sigma(\mathbf{r})}{1 + h_\sigma(\mathbf{r})} \cdot \frac{\gamma_{\sigma\sigma}(\mathbf{r}) + 2\gamma_{\sigma\sigma'}(\mathbf{r}) + \gamma_{\sigma'\sigma'}(\mathbf{r})}{[\tau_\sigma(\mathbf{r}) + \tau_{\sigma'}(\mathbf{r})] \cdot [\rho_\sigma(\mathbf{r}) + \rho_{\sigma'}(\mathbf{r})]} \,, \tag{7.6}$$

in which the common t-LMF is scaled by the spin-channel $\tilde{g}_\sigma(\mathbf{r})$ function, is generally conceivable, only the 'complete' common gt-LMF shall be used in the present work. Hence, $h_\sigma(\mathbf{r})$ in Eq. (7.6) has to be additionally replaced by

$$h(\mathbf{r}) \equiv h_\sigma(\mathbf{r}) = a + b \cdot s^2(\mathbf{r}) + c \cdot q^2(\mathbf{r}) + d \cdot p^2(\mathbf{r}) \,, \tag{7.7}$$

where

$$s(\mathbf{r}) \equiv s_\sigma(\mathbf{r}) = \frac{1}{k'} \cdot \frac{\left[\gamma_{\sigma\sigma}(\mathbf{r}) + 2\gamma_{\sigma\sigma'}(\mathbf{r}) + \gamma_{\sigma'\sigma'}(\mathbf{r})\right]^{1/2}}{\left[\rho_\sigma(\mathbf{r}) + \rho_{\sigma'}(\mathbf{r})\right]^{4/3}} , \tag{7.8}$$

$$q(\mathbf{r}) \equiv q_\sigma(\mathbf{r}) = \frac{1}{k'^2} \cdot \frac{\nabla^{\mathrm{T}}\nabla\rho_\sigma(\mathbf{r}) + \nabla^{\mathrm{T}}\nabla\rho_{\sigma'}(\mathbf{r})}{\left[\rho_\sigma(\mathbf{r}) + \rho_{\sigma'}(\mathbf{r})\right]^{5/3}} , \tag{7.9}$$

$$p(\mathbf{r}) \equiv p_\sigma(\mathbf{r}) = \frac{1}{k'^2} \cdot \frac{\eta_{\sigma,\sigma\sigma} + 2\cdot\eta_{\sigma,\sigma\sigma'} + \eta_{\sigma,\sigma'\sigma'} + \eta_{\sigma',\sigma\sigma} + 2\cdot\eta_{\sigma',\sigma\sigma'} + \eta_{\sigma',\sigma'\sigma'}}{\left[\gamma_{\sigma\sigma}(\mathbf{r}) + 2\gamma_{\sigma\sigma'}(\mathbf{r}) + \gamma_{\sigma'\sigma'}(\mathbf{r})\right]\cdot\left[\rho_\sigma(\mathbf{r}) + \rho_{\sigma'}(\mathbf{r})\right]^{5/3}} \tag{7.10}$$

denote the reduced density gradient, the reduced density Laplacian and the reduced density Hessian, respectively, which represent the total quantity counterparts of the spin quantities employed in the spin-channel gt-LMF (7.4).

Considering the arguments for the construction of the self-interaction-reduced PW92 correlation functional (2.83), i.e. self-correlation in the correlation functional should be reduced to the same extent as self-interaction within the exchange functional by the local admixture of exact exchange, the self-interaction-reduced PW92 (sirPW92)[18] functional has to be adjusted, if it is combined with the new common gt-LMF. In particular, a modified version of the sirPW92 correlation functional, referred to as sirPW92*, is proposed

$$E_c^{sirPW92^*}[\rho_\alpha(\mathbf{r}),\rho_\beta(\mathbf{r})] = E_c^{PW92}[\rho_\alpha(\mathbf{r}),\rho_\beta(\mathbf{r})] - \sum_\sigma \int g_\sigma(\mathbf{r}) \cdot e_c^{srPW92}[\rho_\sigma(\mathbf{r}),0]\mathrm{d}\mathbf{r} , \tag{7.11}$$

which employs the same LMF g_σ (also with the same parameters) as used in the local hybrid exchange functional in the self-correlation reduction scheme. Besides an enhanced compatibility with LMFs that are not of t-LMF type, the new sirPW92* correlation thus also differs from the previous sirPW92 scheme, if a common t-LMF is used in the local hybrid exchange functional. Wheras in sirPW92*, the common t-LMF would also be employed in the self-correlation reduction, a spin-channel t-LMF would be used within the previous sirPW92 scheme.

7.2. Computational Details

Based on the newly proposed theoretical models for the local mixing function and the correlation functional (see Sec. 7.1), two new local hybrid functionals have been constructed. Besides Slater-Dirac exchange,[74,75] both employ the new sirPW92* correlation functional and are thus labelled as *Lh*-SsirPW92*. While one functional contains the common t-LMF and thus differs from the previous *Lh*-SsirPW92[18] only in the correlation

functional, which employs the common t-LMF instead of the spin-channel t-LMF for the self-correlation correction, the second local hybrid uses the new common gt-LMF. The free empirical parameters within both local hybrids, i.e. one with the common t-LMF and four with the common gt-LMF, are optimized with respect to thermochemical test sets. In particular, G2-1[317,318] atomization energies (G2-1 AE) and ionization potentials (G2-1 IP) as well as the BH76 test set,[319–323] consisting of 38 hydrogen transfer (HTBH38) and 38 non-hydrogen transfer barrier heights (NHTBH38), are used for that purpose. The weighted mean absolute error over the mentioned test sets is optimized, where atomization energies and barrier heights are equally weighted with 25%, while for ionization potentials, a weighting factor of 50% is chosen due to the generally lower sensititvity of ionization potentials with respect to the choice of the XC functional, as will be seen later. G2-1 electron affinities (G2-1 EA) are not included, to reduce the calculation cost of the optimization, and since electron affinities appear to be reasonably well described without being included in the optimization test set (see Sec. 7.3). For all optimizations, Ahlrichs' def2-TZVP basis sets[295] as well as the modified Nelder-Mead Simplex algorithm described in Sec. 6.2.2 are employed. To ensure positive parameter values, adequate boundary conditions are included in the optimization algorithm.

The performance of the optimized functionals is evaluated with respect to thermochemical as well as vertical excitation test sets. For thermochemistry, MAEs for G2-1 atomization energies, ionization potentials and electron affinities as well as for the barrier heights of the HTBH38 and NHTBH38 test sets are calculated. For comparison, the semi-local functionals SVWN,[74–76] BLYP,[92,101] PBE[93] and TPSS[106,107] as well as the global hybrid functionals TPSSh,[124] B3LYP,[126,127] PBE0[125] and BHLYP[120] are additionally considered. Besides, four existing local hybrid functionals, i.e. *Lh*-SVWN with spin-channel t-LMF ($a = 0.48$)[185] and spin-channel s-LMF ($\beta = 0.277$)[186] as well the *Lh*-SsirPW92 and *Lh*-SsifPW92 functionals with common t-LMF and empirical prefactors of $a = 0.646$ and $a = 0.709$,[18] respectively, are employed as well. All calculations of thermochemical properties are done with the def2-QZVPPD basis set.[285] For the evaluation of the performance for vertical excitations, the test sets of Thiel[287–289] and Tozer,[12,290] which were already used in chapter 5, are employed. Hence, the same basis sets are used as described in Sec. 5.1.2.

All calculations were done with the local developers' version of the TURBOMOLE program package,[19] which contains the DFT[270] and the linear-response TDDFT implementation[272] of local hybrid functionals as well as their extensions to the new common gt-LMF and sirPW92* correlation. Modifications of the existing implementations caused by the reduced density Laplacian and the reduced density Hessian are explained in detail

in Sec. A.2. In all calculations, the RI-J approximation for Coulomb integrals (see Sec. 2.5.2) has been used. Numerical integration of the semi-local XC energy densities as well as semi-numerical integration (see Sec. 2.5.3) of exact exchange within global and local hybrid functionals were done on the TURBOMOLE m3 grid.

7.3. Results

The thermochemically optimized prefactor of the common t-LMF within the *Lh*-SsirPW92* functional is $a = 0.637$, which is very close to the prefactor in the previous *Lh*-SsirPW92 functional.[18] Besides a well-behaved optimization procedure, this also indicates an adequate definition of the optimization parameter (see Sec. 7.2). For the common gt-LMF, only three non-zero parameters remained after optimization, i.e. $a = 1.04357$, $b = 0.09032$ and $d = 0.02607$. The optimal prefactor for the reduced density Laplacian is $c = 0.00000$, so that this term has no influence on the resulting LMF. This can be explained by the fact that the reduced density Laplacian exhibits similar properties as the reduced density Hessian. While the reduced density Laplacian considers the trace of the density Hessian, the reduced density Hessian contains information about the complete density Hessian by projecting it onto the density gradient. Apparently, only one of those two quantities is required to effectively reduce errors with respect to thermochemical test sets. Although the reduced density Hessian seems to be the natural choice, since the complete density Hessian is considered, the reduced density Laplacian might be preferred within other setups. Nevertheless, in the optimized common gt-LMF within the *Lh*-SsirPW92* functional, only three empirical parameters are retained.

The spatial behavior of both optimized local mixing functions is illustrated in Fig. 7.1 along the molecular axis of the CO molecule. The common t-LMF shows the usual behavior, i.e. low LMF values in valence regions combined with LMF values of $g_\sigma(\mathbf{r}) = 0.637$ in core and asymptotic regions and steep changes in-between. In valence regions, the common gt-LMF exhibits essentially the same behavior as the common t-LMF, which indicates that those regions are of high importance for an accurate description of thermochemical properties. On the other hand, the common gt-LMF provides only around 50% exact exchange in core regions, which coincides with the downscaling of the common t-LMF provided by the constant parameter a in the common gt-LMF. Hence, the reduced quantities, although generally being able to provide more flexibility in core regions, do not affect the behavior of the common gt-LMF here. In fact, this might be an artefact of the thermochemical optimization procedure, which does not consider properties depending on core regions. In the intermediate region between the valence and the asymptotic

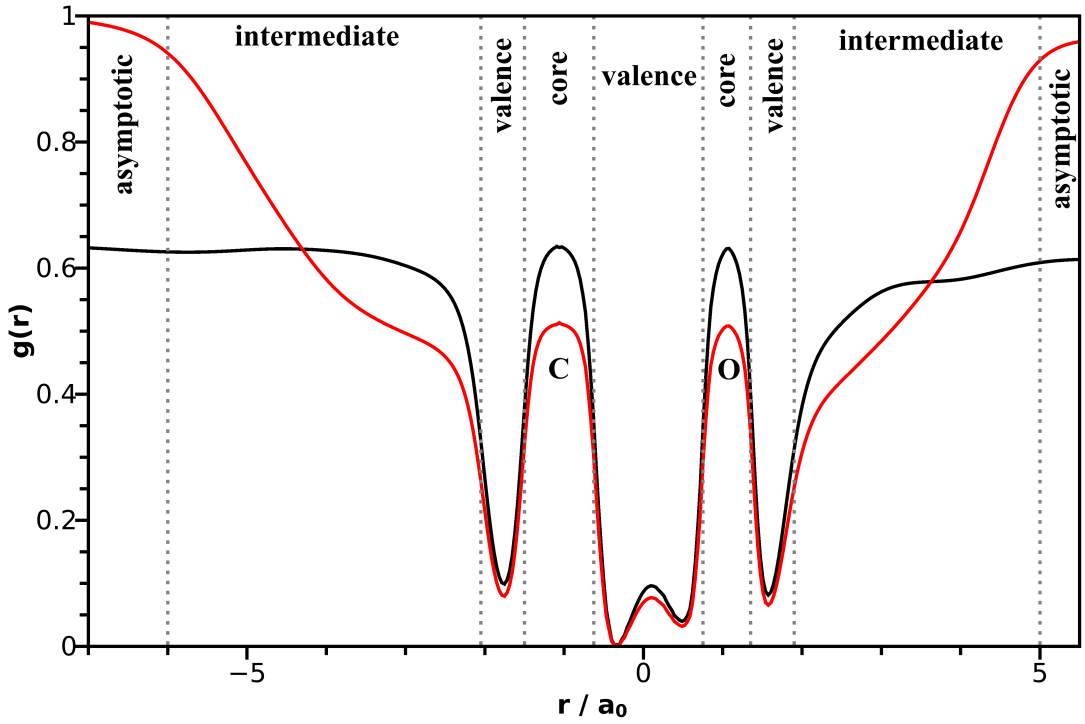

Figure 7.1.: LMF values $g_\sigma(\mathbf{r})$ of the common t-LMF (black) and the common gt-LMF (red) plotted for the CO molecule along the molecular axis with LMF parameters (see text) being optimized for the *Lh*-SsirPW92* functional with respect to the combined thermochemical test set (see Sec. 7.2). Different real-space regions are classified as described in Sec. 5.1.2.

region, the common gt-LMF shows a distinctly different behavior from the common t-LMF. Instead of one single steep change, the common gt-LMF exhibits two changes in the intermediate region, where the first, steeper change is caused by the parameter a and the common t-LMF part, while the second change, which leads to $g_\sigma(\mathbf{r}) = 1.0$ in the asymptotics, is a direct result of the new terms containing the reduced density gradient and the reduced density Hessian. Apparently, less exact exchange is required in intermediate regions close to the valence, while more exact exchange is needed with an increasing distance. Astonishingly, the common t-LMF and the common gt-LMF intersect each other approximately in the center of the intermediate region, which indicates that the average amount of exact exchange in these regions do not differ between both LMFs. Hence, the common gt-LMF at least mitigates two deficiencies of the common t-LMF (see Sec. 7.1). That is, it provides the correct behavior in one-electron regions as well as more flexibility in the intermediate region. While the common gt-LMF in general also provides a higher flexibility in core regions, the thermochemically optimized gt-LMF simply reduces to a

scaled common t-LMF in core regions. Nevertheless, this might be related to the employed optimization test set and might thus be accomplished by considering properties that are more sensitive with respect to core regions.

First, the performance of the optimized local hybrid functionals shall be evaluated with respect to the employed thermochemical test sets (see Sec. 7.2). Results for all considered XC functionals are given in Table 7.1. Although the performance of the considered conventional XC functionals[62] and local hybrids[17,18] for the calculation of thermochemical properties has already been studied extensively, they shall be briefly discussed first to serve as background for the comparison to the optimized new local hybrid functionals. Besides a systematic strong overestimation of atomization energies and underestimation of barrier heights, SVWN systematically exhibits too large ionization potentials and electron affinities. Turning to GGA and meta-GGA functionals, these problems are significantly mitigated, although not completely removed. With an increasing amount of exact exchange in global hybrid functionals, MSEs become more negative for atomization energies and more positive for barrier heights. Up to B3LYP and PBE0, this also results in generally smaller MAEs compared to the semi-local functionals. The trend is partially reversed for larger exact-exchange admixtures, as e.g. in BHLYP. Here, atomization energies and electron affinities are significantly underestimated due to the large exact-exchange admixture, while barrier heights exhibit even smaller MAEs than with the other global hybrids. This indicates, that a simultaneously good description of atomization energies and barrier heights remains difficult for the simple global hybrid functionals considered in the present work. More complicated schemes are nonetheless able to provide both.[62] Electron affinities and ionization potentials appear to be weakly influenced by the admixture of exact exchange.

Local hybrid functionals, on the other hand, are able to provide simultaneously accurate atomization energies and barrier heights as well as electron affinities and ionization potentials. While the *Lh*-SVWN functional employing the s-LMF exhibits MAEs more comparable to less well-performing global hybrids, the picture changes upon turning to local hybrids using LMFs of t-LMF type. Here, the best results are obtained with the common t-LMF within the *Lh*-SsirPW92 and the *Lh*-SsifPW92 functional. Besides low MAEs for electron affinities close to 2.0 kcal/mol, especially barrier heights are well described by both functionals, which can be attributed to the larger prefactor in comparison to the t-LMF within the *Lh*-SVWN functional. While hydrogen transfer barrier heights exhibit very small MAEs close to 1.0 kcal/mol with almost no systematic error, non-hydrogen transfer barriers, although being better described than by most other XC functionals, are systematically overestimated. Atomization energies and ionization potentials on the other

Table 7.1.: Mean absolute errors (MAEs) and mean signed errors (MSEs) (in parentheses) in kcal/mol for the G2-1, G2-1 IP, G2-1 EA, HTBH38 and NHTBH38 test sets calculated with several XC functionals, including some existing and the new optimized local hybrid functionals.

Functional	G2-1 55	G2-1 IP 38	G2-1 EA 25	HTBH38 38	NHTBH38 38
SVWN	35.74 (35.74)	5.23 (3.98)	5.57 (5.57)	17.43 (-17.43)	12.18 (-11.99)
BLYP	4.60 (2.88)	4.80 (-1.65)	3.43 (-0.47)	7.40 (-7.40)	8.29 (-8.26)
PBE	7.94 (6.51)	3.90 (0.23)	2.29 (0.98)	9.22 (-9.22)	8.19 (-8.09)
TPSS	4.62 (3.63)	4.23 (-0.62)	2.43 (-1.25)	7.57 (-7.57)	8.65 (-8.60)
TPSSh	4.84 (0.96)	4.34 (-0.44)	2.94 (-2.14)	5.83 (-5.83)	6.61 (-6.54)
B3LYP	2.66 (-0.44)	3.88 (0.20)	2.68 (-1.17)	4.10 (-3.99)	4.44 (-4.31)
PBE0	3.02 (-1.69)	4.30 (0.41)	2.68 (-1.84)	4.13 (-4.13)	3.33 (-2.85)
BHLYP	11.80 (-11.06)	5.53 (-1.10)	6.27 (-5.64)	2.79 (1.04)	2.34 (0.69)
Lh-SVWN $g_\sigma = \mathrm{erf}(0.277\, s_\sigma)$	5.00 (1.81)	4.48 (3.08)	2.79 (1.86)	3.37 (-3.25)	3.62 (-2.03)
Lh-SVWN $g_\sigma = 0.48 t_\sigma$	3.88 (1.14)	5.17 (4.37)	3.52 (2.93)	2.40 (-1.94)	2.67 (-1.50)
Lh-SsirPW92 $g_\sigma = 0.646 t$	3.45 (2.06)	4.49 (3.73)	2.50 (2.10)	1.12 (0.13)	2.32 (1.49)
Lh-SsifPW92 $g_\sigma = 0.709 t$	3.45 (1.64)	4.03 (2.76)	2.01 (1.16)	1.09 (0.60)	2.84 (2.40)
Lh-SsirPW92* $g_\sigma = 0.637 t$	3.33 (1.45)	4.35 (3.38)	2.41 (1.73)	1.25 (-0.14)	2.23 (1.23)
Lh-SsirPW92* $g_\sigma = \tilde{g} \cdot t$	2.01 (0.78)	4.02 (2.54)	2.08 (1.04)	1.22 (-0.26)	2.42 (1.20)

hand are significantly overestimated, with MAEs being more comparable to standard global hybrid functionals with low exact exchange.

Concerning the different test sets, two facts become obvious. While atomization energies and barrier heights exhibit large deviations between the distinct XC functionals and are strongly affected by the admixture of exact exchange, the MAEs for the G2-1 ionization potentials and electron affinities vary much less. Electron affinities on the one hand appear to be well described by most functionals with MAEs around 2.0 to 3.0 kcal/mol. Considering the fact that the local hybrid functionals with the smallest MAEs for electron

affinities are only optimized with respect to atomization energies and barrier heights suggests that electron affinities are not a necessary part of the optimization test set (cf. Sec. 7.2). On the other hand, ionization potentials exhibit relatively large MAEs of around 4.0 to 5.0 kcal/mol and thus remain the considered property described worst within the current work. Regarding the optimization procedure (see Sec. 7.2), a larger weight of the ionization potentials compared to the other properties thus appears a reasonable choice.

Turning to the optimized new *Lh*-SsirPW92* local hybrid functionals, the performance of the common t-LMF shall be discussed first. Despite the very similar linear prefactor of $a = 0.637$ compared to the previous *Lh*-SsirPW92 functional with $a = 0.646$, the new *Lh*-SsirPW92* functional shows distinct differences. That is, G2-1 atomization energies are less overestimated, with the MSE being more than 0.6 kcal/mol lower. Since the t-LMF prefactor a deviates only by around 0.01 from the *Lh*-SsirPW92 functional, this large decrease is most likely due to the modification in the sirPW92* correlation, which indicates that using the same LMF in the self-correlation correction scheme as in the local hybrid functional provides some benefits compared to the previous sirPW92 scheme. Besides, the MAEs for all considered properties except hydrogen transfer barrier heights are slightly lowered, which can be related to the slightly smaller prefactor of the common t-LMF. In combination with the new common gt-LMF, *Lh*-SsirPW92* exhibits even better results. While barrier heights remain well described, with errors comparable to those of the *Lh*-SsirPW92* functional with common t-LMF, electron affinities and ionization potentials are almost equally well treated as with the so far best local hybrid functional *Lh*-SsifPW92. G2-1 atomization energies on the other hand are dramatically improved compared to the other investigated XC functionals, with the MAE being close to 2.0 kcal/mol. Furthermore, the mean signed errors for all test sets are significantly lowered compared to *Lh*-SsirPW92* with common t-LMF. The new *Lh*-SsirPW92* functional employing the common gt-LMF thus represents a significant improvement over many standard XC functionals and, in particular, over the currently best performing local hybrid functionals.

Besides the performance for thermochemical properties, the optimized new local hybrid functionals are additionally evaluated with respect to their performance for vertical excitations. For that purpose, the Thiel and Tozer test sets employed in chapter 5 are used again. Since many XC functionals have already been discussed in Sec. 5.2, the discussion is restricted to a comparison to existing local hybrid functionals, which is shown in Table 7.2. Concerning the *Lh*-SsirPW92* functional employing the common t-LMF, results are, as expected, very similar to those of the *Lh*-SsirPW92 functional. Larger deviations are only apparent for triplet valence excitations, where *Lh*-SsirPW92* exhibits a slightly

Table 7.2.: Mean absolute errors (MAEs) and mean signed errors (MSEs) (in parentheses) in eV for the Thiel and Tozer test sets calculated with existing as well as the optimized new local hybrid functionals. For core excitations, results are given with and without relativistic correction (before and after the slash).

	Thiel		Tozer				
Functional	Singlet	Triplet	Valence	Rydberg	CT	Core-valence	Core-Rydberg
	103	63	32	13	14	9	19
Lh-SVWN	0.26	0.35	0.22	1.67	1.38	13.38/13.10	14.37/14.16
$g_\sigma = \mathrm{erf}(0.277\, s_\sigma)$	(-0.03)	(-0.35)	(-0.13)	(-1.67)	(-1.36)	(-13.38/-13.10)	(-14.37/-14.16)
Lh-SVWN	0.24	0.27	0.21	0.31	1.24	6.52/6.24	5.93/5.72
$g_\sigma = 0.48 t_\sigma$	(0.08)	(-0.26)	(-0.01)	(-0.31)	(-1.21)	(-6.52/-6.24)	(-5.93/-5.72)
c*Lh*-SVWN	0.23	0.30	0.19	0.57	1.25	6.62/6.34	5.94/5.73
$g_\sigma = 0.48 t_\sigma$	(0.05)	(-0.29)	(-0.05)	(-0.57)	(-1.22)	(-6.62/-6.34)	(-5.94/-5.73)
Lh-SsirPW92	0.30	0.16	0.25	0.14	0.84	1.60/1.33	0.50/0.46
$g_\sigma = 0.646 t$	(0.22)	(-0.06)	(0.06)	(-0.02)	(-0.79)	(-1.60/-1.33)	(-0.29/-0.08)
c*Lh*-SsirPW92	0.28	0.17	0.23	0.38	0.85	1.74/1.46	0.50/0.46
$g_\sigma = 0.646 t$	(0.20)	(-0.08)	(0.03)	(-0.38)	(-0.81)	(-1.74/-1.46)	(-0.30/-0.09)
Lh-SsifPW92	0.33	0.16	0.25	0.16	0.72	0.50/0.67	1.73/1.94
$g_\sigma = 0.709 t$	(0.26)	(-0.03)	(0.08)	(0.07)	(-0.66)	(0.14/0.42)	(1.73/1.94)
c*Lh*-SsifPW92	0.32	0.16	0.24	0.35	0.72	0.48/0.63	1.70/1.90
$g_\sigma = 0.709 t$	(0.24)	(-0.05)	(0.06)	(-0.34)	(-0.68)	(0.00/0.28)	(1.70/1.90)
Lh-SsirPW92*	0.29	0.19	0.24	0.14	0.86	1.54/1.41	0.82/0.76
$g_\sigma = 0.637 t$	(0.21)	(-0.13)	(0.06)	(-0.04)	(-0.82)	(-1.54/-1.27)	(-0.22/-0.01)
c*Lh*-SsirPW92*	0.28	0.20	0.23	0.40	0.87	1.67/1.53	0.82/0.76
$g_\sigma = 0.637 t$	(0.19)	(-0.16)	(0.02)	(-0.40)	(-0.83)	(-1.67/-1.39)	(-0.23/-0.02)
Lh-SsirPW92*	0.25	0.19	0.22	0.41	1.09	4.64/4.36	4.05/3.84
$g_\sigma = \tilde{g} \cdot t$	(0.13)	(-0.14)	(0.02)	(-0.41)	(-1.06)	(-4.64/-4.36)	(-4.05/-3.84)
c*Lh*-SsirPW92*	0.24	0.20	0.22	1.00	1.10	4.73/4.45	4.06/3.85
$g_\sigma = \tilde{g} \cdot t$	(0.11)	(-0.16)	(-0.04)	(-1.00)	(-1.07)	(-4.73/-4.45)	(-4.06/-3.85)

more pronounced underestimation, and for core excitations, where core-Rydberg excitations are most affected. Although parts of the deviations might be also related to the lower exact-exchange admixture in the *Lh*-SsirPW92* functional, it appears that those excitations are most sensitive to spurious self-correlation contributions, which differ between *Lh*-SsirPW92 and *Lh*-SsirPW92*. This is in accordance with the previous finding that triplet valence excitations are significantly influenced by the change from spin-channel to common LMFs and by the introduction of a self-correlation correction (see Sec. 5.2.4). For the core excitations, it is noteworthy that the MSEs for the *Lh*-SsirPW92* functional are more positive than those of *Lh*-SsirPW92 despite the fact that the lower LMF prefactor would suggest more negative MSEs due to less exact exchange and thus higher-lying core orbitals. It appears that self-correlation in the core region significantly affects core excitations, and that the new sirPW92* scheme performs distinctly differently than the previous

sirPW92 scheme. Since the quality of core excitations is nonetheless mostly determined by the choice of the LMF, no clear decision between both schemes can be made.

Turning to the *Lh*-SsirPW92* functional with the new common gt-LMF, valence excitations are similarly well described as with the other local hybrid functionals, with the MAE for singlet excitations being closer to the *Lh*-SVWN functionals. On the other hand, Rydberg and charge-transfer excitations are described worse than with the best-performing local hybrid and are more comparable with *Lh*-SVWN employing the t-LMF. Compared to the latter, CT excitations are slightly better described, which indicates a larger average fraction of exact exchange, while Rydberg excitations exhibit a stronger underestimation. This shows, that in the relevant parts of the intermediate region less exact exchange is provided (cf. Fig. 7.1) and that these parts are quite close to the valence, since mainly lower-lying Rydberg states were considered. Nevertheless, for higher-lying Rydberg states, it can be speculated that the new common gt-LMF gives better results due to the correct behavior in one-electron regions. Most notably, the consideration of the current-density response dramatically worsens results for Rydberg excitations, while the effect on core-valence excitations remains similar to functionals with t-LMF. One possible reason for this is the more pronounced change of the LMF in the intermediate region. While the t-LMF exhibits one steep change up to the value fixed by the LMF prefactor, the common gt-LMF goes up to $g_\sigma(\mathbf{r}) = 1.0$ within two steep changes (see Fig. 7.1), so that, according to the discussion in Sec. 5.2.4, the influence of the current-density response is expected to be larger compared to a scaled t-LMF. Although it appears that the inclusion of the current-density response thus generally deteriorates the performance for Rydberg excitations, it might be different in combination with other LMFs and XC functionals as well as for the inclusion of calibration functions. Due to the lower amount of exact exchange in the core region, core excitations are also less well described than with the best local hybrid.

7.4. Conclusions

In this chapter, a new model for the local mixing function, i.e. the gt-LMF, as well as a modified version of the sirPW92 functional, referred to as sirPW92*, have been presented. Additionally containing terms depending on the density gradient and the density Hessian, respectively, the gt-LMF provides a more flexible approach than the so far most successful local mixing function, the t-LMF. Relying on a thermochemical optimization of the four empirical parameters of the common gt-LMF within the new *Lh*-SsirPW92* functional, this has been illustrated by evaluating the performance for various thermo-

chemical and vertical-excitation test sets. While for thermochemical properties, the new local hybrid functional is generally on par with the so far most successful local hybrids, G2-1 atomization energies are improved in comparison to other successful functionals such as B3LYP. On the other hand, vertical excitation energies for charge-transfer, Rydberg and core excitations of the Tozer test sets are described significantly worse than with the *Lh*-SsirPW92* functional containing the common t-LMF. This shows, that the usual thermochemical optimization of XC functionals does not automatically provide parametrizations suitable for the description of response properties such as vertical excitation energies. Hence, a common optimization procedure, simultaneously considering thermochemical and vertical-excitation test sets, might be desirable, to make efficient use of the high flexibility provided by the gt-LMF model. In fact, so far only three of the four proposed empirical parameters have been effectively used within the optimized common gt-LMF, which indicates a potentially higher flexibility of the new approach. In this sense, the present work can be regarded as only a first step towards new local hybrid functionals that are able to describe a wide range of different chemically relevant properties.

8. Conclusions and Outlook

In the present work, the development of local hybrid functionals has been extended into two major directions. The first one is concerned with the conjunction of local hybrids with time-dependent density functional theory, which constitutes the most widely used tool for the calculation of excited states of large molecules. To that end, the current work provides the first detailed derivation and formulation of the adiabatic local hybrid XC kernel integrals within the generalized KS formalism as well as the corresponding matrix-vector products, which are required for an implementation into modern quantum chemical programs. Since local hybrids belong to the class of explicit orbital-dependent functionals, so that explicit derivatives with respect to the electron density are not possible, a derivation scheme directly based on density matrix derivatives has been used. Concerning the previously employed FDO scheme for the derivation of the local hybrid XC potential, the present work establishes a direct link to the density-matrix-based scheme, leading to a reformulation of the conventional FDO, which is needed for the derivation of adiabatic XC kernels within a FDO framework.

On this theoretical basis, the present work also features a detailed description of the first implementation of the adiabatic local hybrid XC kernel into the common quantum chemical program package TURBOMOLE. Concerning the employed semi-numerical integration scheme, which exhibits a formal cubic scaling with respect to system size, special attention has been paid to the efficiency of the implementation. Besides an efficient computation of the **A** matrix, realized by the introduction of S- and P-junctions, where P-junctions were adjusted for the special requirements of TDDFT, an efficient matrix vector multiplication has been established. Thus leading to a formal linear scaling in the limit of large molecules, the new implementation together with the RI-J approximation outperforms the conventional global hybrid TDDFT implementation of TURBOMOLE already for small molecules and medium-sized basis sets. Due to the formal quadratic scaling with basis set size, even larger time savings were obtained for large basis sets. In combination with the additionally implemented SMP parallelization, the present local hybrid TDDFT implementation thus allows the calculation of a large number of excitations for larger molecules with at least medium-sized basis sets and therefore provides

an efficient tool for routine TDDFT calculations with local hybrid functionals. Nevertheless, the semi-numerical integration, especially in the case of local hybrids, can engender enhanced requirements on the numerical integration grid. While for most excitations, a relatively small numerical grid is sufficient, more diffuse grids are required, when diffuse states are sampled in conjunction with diffuse basis functions, as it is the case, e.g., in Rydberg excitations. Since similar problems might also occur for other cases, accuracy issues concerning the molecular grid have to be excluded first. Here, the incremental protocol, used in the present work, represents one particular tool for the identification of such numerical issues. Regarding other semi-numerical methods like the PS and the COSX method, a reevaluation of the numerical accuracy concerning the molecular grid with special attention to diffuse states, e.g. by following the presented protocol, is thus recommended.

Based on the new efficient implementation, the present work also provides the first evaluation of local hybrid functionals with respect to their performance for vertical excitations. Making use of the common Thiel and Tozer test sets as well as a model system covering intermolecular CT excitations, the performance of several existing local hybrids has been assessed. While for singlet valence excitations, the overall best-performing local hybrid functional *Lh*-SsirPW92 is on par with other state-of-the-art hybrid functionals, local hybrids are generally able to provide a significantly enhanced accuracy for triplet valence excitations as well as for core and Rydberg excitations. CT excitations, on the other hand, appear to be less well described with the investigated local hybrids than with some other hybrid functionals, especially certain range-separated hybrids. Besides, it could be shown that the TDA does not generally enhance the accuracy for triplet excitations, especially in the case of local hybrids employing common LMFs. Likewise, Rydberg and core-valence excitations calculated with local hybrids employing the t-LMF have been identified as first cases, for which the response of the current density within functionals containing the current-dependent gauge-invariant kinetic energy density have a major influence. Although common representive test sets have been employed for the first evaluation of local hybrids, only a small part of possible electronic configurations is covered. Hence, further studies using more diverse test sets, containing, e.g., transition metal complexes, radical excitations, strongly correlated complexes or core excitations of second row elements, which have been excluded in the present work due to particular basis set issues, are desirable. Concerning the investigated local hybrid functionals, only a small set of different functionals have been explored so far. Besides the predominant use of the t-LMF, all explored local hybrids only considered Slater-Dirac exchange and employed LDA correlation, which was at best self-correlation corrected. In fact, some

possible candidates for further investigations are the recently developed calibrated local hybrids of Arbuznikov *et al.*,[197] which use only the simple t-LMF, but employ semi-local exchange and correlation functionals, as well as local hybrids containing more advanced LMFs, such as some of those shown in Sec. 2.3.2.

Besides the combination of local hybrid functionals with TDDFT, the present work also features a more general development of local hybrids. In particular, novel approaches for the construction of the two exclusive local hybrid building blocks, i.e. the LMF and the CF, are proposed. In the case of calibration functions, a new derivation scheme, which is based on integration by parts of exchange functionals, has been introduced. Application of this scheme to GGA exchange as well as to the semi-local part of B98 exchange has led to calibration functions of pig and tpig type, where both are theoretically given to an infinite order. In this context, a previously reported semi-local CF[197] has been identified as first-order pig type CF, illustrating the universality of the new derivation scheme. For the determination of the introduced empirical parameters, a novel optimization procedure has been used, which aims at minimizing unphysical static correlation contributions in the dissociation curves of noble gas dimers, which are known to be directly related to the gauge problem. Although not exclusively correcting for gauge issues, the new method thus provides an effective approach for the calibration of local hybrids. Concerning the proposed new CFs, it could be shown that the introduction of a second linear parameter through pig2 significantly enhances the flexibility of the CF, while tpig1 provides comparably good results within the new optimization scheme with only one empirical linear parameter. Beyond those CFs that have been explicitly investigated in the present work, the novel derivation scheme allows, e.g., the derivation of further higher-order calibration functions based on the so far employed exchange functionals, as well as the development of CFs on the basis of more advanced exchange functionals such as TPSS. In particular, the tpig2 CF represents a promising candidate for future investigations, since it combines the flexibility of a second-order CF with the more advanced functional form of tpig type calibration functions. Also, the construction of CFs containing quantities beyond second basis function derivatives is possible. The pig2 and tpig1 CF, which have been investigated in the present work, thus represent only a first step towards a new generation of calibrated local hybrid functionals.

For the local mixing function, a novel *ad hoc* model has been proposed, the gt-LMF. Relying on the beneficial properties of the scaled t-LMF, several of its shortcomings, e.g. the wrong behaviour in one-electron regions, have been eliminated by substituting the constant prefactor by a real-space-dependent function, which includes additional information about the density gradient and the density Hessian. To retain the balanced self-correlation

reduction of the self-interaction-reduced PW92 functional also with the new gt-LMF, the sirPW92 functional was additionally modified to use the same LMF as in the exchange functional also for the screening of one-electron regions in the self-correlation correction. For the thermochemical optimization, the *Lh*-SsirPW92* functional in combination with the common gt-LMF containing four empirical parameters, has been chosen. While most of the investigated thermochemical properties, such as reaction barriers, ionization potentials and electron affinities calculated with the optimized new local hybrid are on par with the so far most successful local hybrid functionals, atomization energies, evaluated using the G2-1 test set, were significantly improved, e.g. compared to the succesful global hybrid B3LYP. On the other hand, vertical excitation energies of some excitation classes were significantly deteriorated with the new local hybrid, e.g. Rydberg, CT and core excitations. This indicates, that a pure thermochemical optimization does not automatically provide a good description of response properties, such as vertical excitation energies. One possibility to overcome this shortcoming is the inclusion of vertical excitation energies in the optimization test set, e.g. those of Rydberg and core excitations, which sample distinct regions in real space. This potentially leads to local hybrid functionals that treat ground-state thermochemistry and vertical excitations similarly well. Due to its higher flexibility compared to other LMFs, the new gt-LMF represents one promising candidate for such an optimization. Besides those quantities that are already included, further reduced quantities (see Sec. A.1), e.g. the kinetic energy density gradient, could be also incorporated in the gt-LMF to further enhance its flexibility. Concerning the correlation functional, self-correlation-reduced GGA correlation functionals might be one option for future local hybrid functionals.

While as a first step, the new approaches for the LMF and the correlation functional, and the CF have been investigated separately in the present work, the combination of these approaches represents a promising way for future developments on the field of local hybrid functionals. In particular, a large variety of calibrated new local hybrids can be constructed on the basis of these new approaches. Suitable parameter sets may then be obtained by combining the conventional thermochemical optimization strategy for LMFs, which in fact, can be enhanced by vertical excitation energies, with the new optimization procedure for CFs. In particular, both schemes could be performed subsequently, until a self-consistent set of LMF and CF parameters is obtained. Finally, this might lead to local hybrid functionals featuring an improved and balanced description of thermochemical properties and vertical excitation energies as well as being better suited for the addition of semi-empirical dispersion corrections, while only a couple of empirical parameters has to be included.

Providing the theoretical and technical basis for the use of local hybrid functionals within linear-response TDDFT, as well as illustrating several new directions in the development of novel local hybrid functionals, the present work thus represents another important step towards the routine use of local hybrid functionals in quantum chemistry.

A. Appendix

In the first section of the appendix, a brief discussion of reduced quantities, which have been extensively used for the expression of the new CFs and LMFs developed in chapters 6 and 7, respectively, is provided. Besides, the extension of the existing local hybrid implementation of TURBOMOLE enabling self-consistent DFT and TDDFT calculations with the new CFs and LMFs will be presented in the second section. In both cases, parts are taken from Ref. 315. For clarity, the space variable $\mathbf{r}$ is generally omitted.

A.1. Reduced Quantities

Although semi-local XC functionals can be generally expressed in terms of fundamental quantities that directly emerge from the contraction of the density matrix with the basis function vector as the electron density ρ, the kinetic energy density τ and their spatial derivatives, most XC functionals make use of auxilliary quantities to enhance comprehensibility and clarity. One particular class of auxilliary quantities, that is widely used for the definition of exchange functionals, are so-called reduced quantities, which represent a scalar measure of a particular fundamental quantity on the scale of the Thomas-Fermi wavelength[325] and are made dimensionless through division with the electron density. The two most commonly used reduced quantities[93,107,186] are the reduced spin density gradient and the reduced spin density Laplacian

$$s_\sigma = \frac{1}{k} \cdot \frac{\gamma_{\sigma\sigma}^{1/2}}{\rho_\sigma^{4/3}} \,, \tag{A.1}$$

$$q_\sigma = \frac{1}{k^2} \cdot \frac{\nabla^{\mathrm{T}}\nabla\rho_\sigma}{\rho_\sigma^{5/3}} \,, \tag{A.2}$$

respectively, which both go to infinity in the low-density limit due to the slower decay of $\gamma_{\sigma\sigma}^{1/2}$ and $\nabla^{\mathrm{T}}\nabla\rho_\sigma$ compared to the respective powers of the spin density. While the reduced spin density gradient exhibits a value of $s_\sigma = 0$ in homogeneous regions and thus at the atomic centers, q_σ constitutes non-zero values at the atomic cores. In a similar fashion,

the reduced kinetic energy density

$$v_\sigma = \frac{1}{k^2} \cdot \frac{\tau_\sigma}{\rho_\sigma^{5/3}} = \frac{3}{40} \cdot \frac{\tau_\sigma}{\tau_{TF,\sigma}} \,, \tag{A.3}$$

may be defined. Although it is not commonly used due to its rexpressability into the ration between the kinetic energy density and the Thomas-Fermi kinetic energy density, together with Eq. (A.1), it allows a reformulation of the inhomogeneity parameter t_σ of Eq. (2.68) into

$$t_\sigma = \frac{\tau_{W,\sigma}}{\tau_\sigma} = \frac{5}{3} \cdot s_\sigma^2 \cdot \frac{\tau_{TF,\sigma}}{\tau_\sigma} = \frac{1}{8} \cdot \frac{s_\sigma^2}{v_\sigma} \,, \tag{A.4}$$

which illustrates the universal applicability of reduced quantities.

Besides the so far mentioned reduced quantities, two others have been introduced in the present work. The first one is the reduced spin density Hessian

$$p_\sigma = \frac{1}{k^2} \frac{\eta_{\sigma,\sigma\sigma}}{\gamma_{\sigma\sigma} \cdot \rho_\sigma^{5/3}} \,, \tag{A.5}$$

where the normalization with respect to $\gamma_{\sigma\sigma}$ ensures, that information about the spin density gradient, on which the spin density Hessian is projected, is not included. Hence, p_σ exhibits similar properties as the reduced spin density Laplacian, i.e. an infinite value in the low-density limit and non-zero values at atomic cores. Although the reduced density Hessian has not been directly defined so far, other Hessian-dependent quantities commonly used for the expression of XC functionals may be reexpressed in terms of p_σ. For example, the dimensionless parameter

$$u_\sigma = \frac{1}{k^3} \cdot \frac{\nabla^{\mathrm{T}} \rho_\sigma \nabla \gamma_{\sigma\sigma}^{1/2}}{\rho_\sigma^3} \tag{A.6}$$

represents one important building block for GGA XC potentials.[326] Applying the substitution

$$\nabla \gamma_{\sigma\sigma}^{1/2} = \frac{\nabla \nabla^{\mathrm{T}} \rho_\sigma \nabla \rho_\sigma}{\gamma_{\sigma\sigma}^{1/2}} \,, \tag{A.7}$$

results in the alternative formulation

$$u_\sigma = \frac{1}{k^3} \cdot \frac{\eta_{\sigma,\sigma\sigma}}{\gamma_{\sigma\sigma}^{1/2} \cdot \rho_\sigma^3} \,. \tag{A.8}$$

Finally using Eqs. (A.5) and (A.1), defining the reduced spin density Hessian and the reduced spin density gradient, respectively, gives

$$u_\sigma = p_\sigma \cdot s_\sigma \ , \tag{A.9}$$

which illustrates, that the reduced spin density Hessian p_σ is in accordance with existing reduced quantities and able to facilitate commonly used expressions.

Another quantity, that is closely related to p_σ, is the Θ_σ function used in the DORI,[189] the related meta-GGA[104] and the Θ-LMF (2.79).[188] While in the original notation, Θ_σ is defined in terms of a local wave vector

$$\Theta_\sigma = \frac{\left[\nabla \left(\frac{\nabla\rho_\sigma}{\rho_\sigma}\right)^2\right]^2}{\left(\frac{\nabla\rho_\sigma}{\rho_\sigma}\right)^6} \ , \tag{A.10}$$

the explicit application of the ∇ operator results in

$$\Theta_\sigma = 4 - 8 \cdot \frac{\rho_\sigma \cdot \eta_{\sigma,\sigma\sigma}}{\gamma_{\sigma\sigma}^2} + 4 \cdot \frac{\rho_\sigma^2}{\gamma_{\sigma\sigma}^3} \cdot \nabla^{\mathrm{T}}\rho_\sigma \nabla\nabla^{\mathrm{T}}\rho_\sigma \nabla\nabla^{\mathrm{T}}\rho_\sigma \nabla\rho_\sigma \ . \tag{A.11}$$

The introduction of another reduced quantity, i.e. the reduced quadratic spin density Hessian

$$\tilde{p}_\sigma = \frac{\nabla^{\mathrm{T}}\rho_\sigma \nabla\nabla^{\mathrm{T}}\rho_\sigma \nabla\nabla^{\mathrm{T}}\rho_\sigma \nabla\rho_\sigma}{k^4 \cdot \gamma_{\sigma\sigma} \cdot \rho_\sigma^{10/3}} \ , \tag{A.12}$$

results in a simple formulation of the Θ_σ function in terms of reduced quantities

$$\Theta_\sigma = 4 + 4\frac{\tilde{p}_\sigma}{s_\sigma^4} - 8\frac{p_\sigma}{s_\sigma^2} \ . \tag{A.13}$$

In contrast to the reduced spin density Hessian, in Eq. (A.12), the square of the spin density Hessian is projected onto the spin density gradients. Hence, $\tilde{p}_\sigma$ generally does not contain additional information about the system compared to $\tilde{p}_\sigma$ and can thus be approximated to good accuracy, as numerically tested within the local developers' version of TURBOMOLE,[315] by the square of the reduced spin density Hessian

$$\tilde{p}_\sigma \approx p_\sigma^2 \ . \tag{A.14}$$

Accordingly, the Θ_σ function (A.13) can be approximated as

$$\Theta_\sigma \approx 4 \cdot \left(1 - \frac{p_\sigma}{s_\sigma^2}\right)^2 , \tag{A.15}$$

thus avoiding second powers of the spin density Hessian. Besides revealing the close relation between the reduced spin density Hessian and the DORI, the proposed simplified Θ_σ function represents a simpler object than the original one (A.13), since only one quantity including the density Hessian appears. This may simplify self-consistent implementations of such quantities (cf. also Sec. A.2 below), without loss of information.

The second reduced quantity, that has been newly defined in the present work, is the mixed reduced density kinetic energy density gradient

$$r_\sigma = \frac{1}{k^4} \frac{\iota_{\sigma\sigma}}{\rho_\sigma^{10/3}} , \tag{A.16}$$

where

$$\iota_{\sigma\varsigma} = \nabla^{\mathrm{T}} \rho_\sigma \cdot \nabla \tau_\varsigma \tag{A.17}$$

represents the kinetic energy density gradient projected onto the spin density gradient. While r_σ in fact contains information about the kinetic energy density gradient, it partially also incorporates the spin density gradient. Hence, it is desirable to define a quantity that exclusively contains information about the kinetic energy density gradient. Accordingly, the reduced kinetic energy density gradient may be defined by

$$w_\sigma = \frac{1}{k^3} \cdot \frac{\vartheta_{\sigma\sigma}^{1/2}}{\rho_\sigma^2} , \tag{A.18}$$

with

$$\vartheta_{\sigma\varsigma} = \nabla^{\mathrm{T}} \tau_\sigma \nabla \tau_\varsigma \tag{A.19}$$

being the square of the kinetic energy density gradient. To avoid redundancy, again for the sake of a simplified possible self-consistent implementation, the reduced kinetic energy density gradient can be approximated using the relation

$$\vartheta_{\sigma\sigma} \cdot \gamma_{\sigma\sigma} = \nabla^{\mathrm{T}} \tau_\sigma \nabla \tau_\sigma \cdot \nabla^{\mathrm{T}} \rho_\sigma \nabla \rho_\sigma \approx \nabla^{\mathrm{T}} \rho_\sigma \nabla \tau_\sigma \cdot \nabla^{\mathrm{T}} \tau_\sigma \nabla \rho_\sigma = \iota_{\sigma\sigma}^2 . \tag{A.20}$$

For the reduced kinetic energy density gradient then follows

$$w_\sigma \approx \frac{1}{k^3} \cdot \frac{\iota_{\sigma\sigma}}{\gamma_{\sigma\sigma}^{1/2} \cdot \rho_\sigma^2} = \frac{r_\sigma}{s_\sigma} \,, \tag{A.21}$$

which shows that, in general, the information contained in w_σ and r_σ is similar.

Last, the usefulness of reduced quantities shall be illustrated for the example of the dimensionless parameter

$$x_\sigma = \frac{\nabla^{\mathrm{T}} \rho_\sigma \nabla \tau_{W,\sigma}}{\nabla^{\mathrm{T}} \rho_\sigma \nabla \tau_\sigma} = \frac{1}{8} \cdot \frac{2 \cdot \eta_{\sigma,\sigma\sigma} \cdot \rho_\sigma - \gamma_{\sigma\sigma}^2}{\rho_\sigma^2 \cdot \iota_{\sigma\sigma}} \,, \tag{A.22}$$

which represents the ratio between the von-Weizsäcker kinetic energy density gradient projected on to the spin density gradient and the kinetic energy density gradient projected on to the spin density gradient. While Eq. (A.22) constitutes the most suitable formulation regarding the implementation, as will be seen in Sec. A.2, the reformulation in terms of reduced quantities

$$x_\sigma = \frac{1}{8} \cdot s_\sigma^2 \cdot \frac{2 \cdot p_\sigma - s_\sigma^2}{r_\sigma} = t_\sigma \cdot \frac{v_\sigma \cdot [2 \cdot p_\sigma - s_\sigma^2]}{r_\sigma} \tag{A.23}$$

provides a simpler formulation with respect to subsequent transformations. In particular, the dimensionless quantitiy x_σ can be easily partitioned into the inhomogeneity parameter t_σ and an additional scaling factor, whose identification would be more difficult within the conventional formulation (A.22).

In summary, reduced quantities represent a suitable set of auxilliary quantities to facilitate formulations of complicated XC functionals and to enable the identification of interrelations with other quantities. Concerning local hybrid functionals, reduced quantities, being dimensionless by default, may represent a better starting point for the construction of new local mixing functions than fundamental quantities. For example, this has been shown in Chapter 7 for the new gt-LMF. Other dimensionless quantities proposed in the present section might also be suitable ingredients for future LMFs. Note that all relations shown for the reduced spin quantities are also valid for the corresponding total quantities, with the only difference that $k = 2\left(6\pi^2\right)^{1/3} \approx 7.79555$ has to be replaced by $k' = 2\left(3\pi^2\right)^{1/3} \approx 6.18734$.

A.2. Extension of the Implementation

Besides those quantities already incorporated in conventional τ-dependent meta-GGAs, the new calibration and local mixing functions introduce an additional dependence on several additional ingredients. This holds in particular for quantities that explicitly depend on second basis function derivatives, such as e.g. the reduced spin density Hessian (A.5) and the reduced spin density Laplacian (A.2). While these quantities are formally already considered in the derivation of the local hybrid potential and kernel integrals (see Sec. 3.2.3) through the general definition of the semi-local potential operator $\hat{d}_{mn}$ (see Eq. (3.17)), they were initially not considered within the existing TURBOMOLE implementation of local hybrid functionals. To allow self-consistent DFT and TDDFT calculations with the new CFs and LMFs, the existing code thus had to be extended.

As a first step, a suitable definition of the set $\mathbb{Q}$, which contains all quantities considered by the respective XC functional, has to be given (cf. Sec. 3.2.1). Besides the projected spin density Hessian $\eta_{\sigma,\sigma\sigma}$ and the spin density Laplacian $\nabla^{\mathrm{T}}\nabla\rho_\sigma$, the scalar product of the gradients of the spin density and the kinetic energy density $\iota_{\sigma\sigma}$ shall be added to the set of τ-dependent meta-GGA ingredients (3.16). Additionally replacing the conventional kinetic energy density (2.63) by the gauge-invariant kinetic energy density (3.22) and accordingly $\iota_{\sigma\varsigma}$ by its gauge-invariant version

$$\tilde{\iota}_{\sigma\varsigma} = \nabla^{\mathrm{T}}\rho_\sigma\nabla\tilde{\tau}_\varsigma = \nabla^{\mathrm{T}}\rho_\sigma\nabla\tau_\varsigma + \frac{1}{2}\frac{\mathbf{j}_\varsigma^2\cdot\gamma_{\sigma\varsigma}}{\rho_\varsigma^2} - \frac{\nabla^{\mathrm{T}}\rho_\sigma\nabla\mathbf{j}_\varsigma^{\mathrm{T}}\cdot\mathbf{j}_\varsigma}{\rho_\varsigma}\ , \tag{A.24}$$

leads to an additional dependence of the XC functional on the current density $\mathbf{j}$ and on the current-density gradient $\nabla\mathbf{j}^{\mathrm{T}}$ (which is a matrix). Furthermore, all spin permutations of the additional quantities shall be included in $\mathbb{Q}$ to allow the construction of total spin quantities, which are required e.g. by common LMFs (see Sec. 2.3.2). For example, the projected total density Hessian and the total spin version of $\iota_{\sigma\sigma}$ are given by

$$\eta = \eta_{\alpha,\alpha\alpha} + 2\cdot\eta_{\alpha,\alpha\beta} + \eta_{\alpha,\beta\beta} + \eta_{\beta,\alpha\alpha} + 2\cdot\eta_{\beta,\alpha\beta} + \eta_{\beta,\beta\beta}\ , \tag{A.25}$$

$$\iota = \iota_{\alpha\alpha} + \iota_{\beta\alpha} + \iota_{\alpha\beta} + \iota_{\beta\beta}\ , \tag{A.26}$$

respectively. Considering all of these dependencies of the semi-local potential operator, the set $\mathbb{Q}$ can be generally defined as

$$\begin{aligned}\mathbb{Q} = \big\{&\rho_\alpha, \rho_\beta, \gamma_{\alpha\alpha}, \gamma_{\alpha\beta}, \gamma_{\beta\beta}, \tau_\alpha, \tau_\beta, \nabla^{\mathrm{T}}\nabla\rho_\alpha, \nabla^{\mathrm{T}}\nabla\rho_\beta, \mathbf{j}_\alpha, \mathbf{j}_\beta,\\ &\eta_{\alpha,\alpha\alpha}, \eta_{\alpha,\alpha\beta}, \eta_{\alpha,\beta\beta}, \eta_{\beta,\alpha\alpha}, \eta_{\beta,\alpha\beta}, \eta_{\beta,\beta\beta}, \iota_{\alpha\alpha}, \iota_{\beta\alpha}, \iota_{\alpha\beta}, \iota_{\beta\beta}, \nabla\mathbf{j}_\alpha^{\mathrm{T}}, \nabla\mathbf{j}_\beta^{\mathrm{T}}\big\}\ ,\end{aligned} \tag{A.27}$$

which in the case of a current-free ground state, then leads to the explicit formulation of the semi-local potential operator

$$\begin{aligned}\hat{d}_{mn,\sigma} e_{xc} =& \varphi^*_{m,\sigma}\varphi_{n,\sigma}\frac{\partial e_{xc}}{\partial \rho_\sigma} + \frac{1}{2}\nabla^{\mathrm{T}}\varphi^*_{m,\sigma}\nabla\varphi_{n,\sigma}\frac{\partial e_{xc}}{\partial \tau_\sigma} + \nabla^{\mathrm{T}}\nabla\left(\varphi^*_{p,\sigma}\varphi_{q,\sigma}\right)\frac{\partial e_{xc}}{\partial \nabla^{\mathrm{T}}\nabla\rho_\sigma} + \\ & \nabla^{\mathrm{T}}\left(\varphi^*_{p,\sigma}\varphi_{q,\sigma}\right)\cdot\left[2\nabla\rho_\sigma\frac{\partial e_{xc}}{\partial \gamma_{\sigma\sigma}} + \nabla\rho_{\sigma'}\frac{\partial e_{xc}}{\partial \gamma_{\sigma\sigma'}} + \nabla\tau_\sigma\frac{\partial e_{xc}}{\partial \iota_{\sigma\sigma}} + \nabla\tau_{\sigma'}\frac{\partial e_{xc}}{\partial \iota_{\sigma\sigma'}}\right] + \\ & 2\cdot\nabla^{\mathrm{T}}\left(\varphi^*_{p,\sigma}\varphi_{q,\sigma}\right)\cdot\left[\nabla\nabla^{\mathrm{T}}\rho_\sigma\nabla\rho_\sigma\frac{\partial e_{xc}}{\partial \eta_{\sigma,\sigma\sigma}} + \nabla\nabla^{\mathrm{T}}\rho_{\sigma'}\nabla\rho_\sigma\frac{\partial e_{xc}}{\partial \eta_{\sigma',\sigma\sigma}}\right] + \\ & \nabla^{\mathrm{T}}\left(\varphi^*_{p,\sigma}\varphi_{q,\sigma}\right)\left[\nabla\nabla^{\mathrm{T}}\rho_\sigma\nabla\rho_{\sigma'}\frac{\partial e_{xc}}{\partial \eta_{\sigma,\sigma\sigma'}} + \nabla\nabla^{\mathrm{T}}\rho_{\sigma'}\nabla\rho_{\sigma'}\frac{\partial e_{xc}}{\partial \eta_{\sigma',\sigma\sigma'}}\right] + \\ & \nabla^{\mathrm{T}}\rho_\sigma\nabla\nabla^{\mathrm{T}}\left(\varphi^*_{p,\sigma}\varphi_{q,\sigma}\right)\cdot\left[\nabla\rho_\sigma\frac{\partial e_{xc}}{\partial \eta_{\sigma,\sigma\sigma}} + \nabla\rho_{\sigma'}\frac{\partial e_{xc}}{\partial \eta_{\sigma,\sigma\sigma'}}\right] + \\ & \nabla^{\mathrm{T}}\rho_{\sigma'}\nabla\nabla^{\mathrm{T}}\left(\varphi^*_{p,\sigma}\varphi_{q,\sigma}\right)\nabla\rho_{\sigma'}\frac{\partial e_{xc}}{\partial \eta_{\sigma,\sigma'\sigma'}} + \\ & \frac{1}{2}\left[\nabla^{\mathrm{T}}\varphi^*_{p,\sigma}\nabla^{\mathrm{T}}\nabla\varphi_{q,\sigma} + \nabla^{\mathrm{T}}\varphi_{q,\sigma}\nabla^{\mathrm{T}}\nabla\varphi^*_{p,\sigma}\right]\cdot\left[\nabla\rho_\sigma\frac{\partial e_{xc}}{\partial \iota_{\sigma\sigma}} + \nabla\rho_{\sigma'}\frac{\partial e_{xc}}{\partial \iota_{\sigma'\sigma}}\right] . \end{aligned} \tag{A.28}$$

While the corresponding semi-local kernel operator can be simply obtained by concatenating two semi-local potential operators (see Eq. (3.20)), for current-free ground states, second derivatives with respect to the current density and its gradient can be reexpressed as

$$\frac{\delta^2 e_{xc}}{\delta \mathbf{j}_\sigma^2} = -\frac{\delta e_{xc}}{\delta \tilde{\tau}_\sigma}\frac{1}{\rho_\sigma} + \frac{\delta e_{xc}}{\delta \tilde{\iota}_{\sigma\sigma}}\frac{\gamma_{\sigma\sigma}}{\rho_\sigma^2} + \frac{\delta e_{xc}}{\delta \tilde{\iota}_{\sigma'\sigma}}\frac{\gamma_{\sigma\sigma'}}{\rho_\sigma^2} , \tag{A.29}$$

$$\frac{\delta^2 e_{xc}}{\delta \nabla\mathbf{j}_\sigma^{\mathrm{T}}\delta \mathbf{j}_\sigma} = -\frac{\delta e_{xc}}{\delta \tilde{\iota}_{\sigma\sigma}}\frac{\nabla\rho_\sigma}{\rho_\sigma} - \frac{\delta e_{xc}}{\delta \tilde{\iota}_{\sigma'\sigma}}\frac{\nabla\rho_{\sigma'}}{\rho_\sigma} , \tag{A.30}$$

similar to Eq. (3.26) for the case of τ-dependent meta-GGAs employing only the gauge-invariant kinetic energy density $\tilde{\tau}_\sigma$ (cf. Sec. 3.2.1). Accordingly, the derivatives (A.29) and (A.30) also give non-vanishing contributions only to the anti-symmetric matrix-vector product (3.47).

In a second step, the additional semi-local quantities have to be made available within the TURBOMOLE implementation of local hybrid functionals. Besides the basis function vector and its first derivatives, second basis function derivatives are additionally required. Together with the **B** vector (4.1) and its gradient, the spin density Hessian and the

gradient of the kinetic energy density can be calculated via

$$\nabla\nabla^{\mathrm{T}}\rho_\sigma = 2\cdot\sum_\mu \left[\nabla B_\mu^\sigma\cdot\nabla^{\mathrm{T}}X_\mu + \nabla\nabla^{\mathrm{T}}X_\mu\cdot B_\mu^\sigma\right] \ , \tag{A.31}$$

$$\nabla\tau_\sigma = \sum_\mu \nabla\nabla^{\mathrm{T}}X_\mu\cdot\nabla B_\mu^\sigma \ , \tag{A.32}$$

respectively, finally allowing the determination of the spin density Laplacian $\nabla^{\mathrm{T}}\nabla\rho_\sigma$ as trace of the spin density Hessian as well as $\eta_{\sigma,\sigma\sigma}$ and $\iota_{\sigma\sigma}$ through Eqs. (6.11) and (A.17). Based on those quantities, the local hybrid matrix-vector products can then be calculated using the same procedure as the one described in detail in Sec. 4.2.1. Due to the inclusion of the new quantities within the semi-local potential operator, the semi-local parts of the symmetric and anti-symmetric local matrix-vector products take a slightly different form, i.e.

$$\begin{aligned} v_{\sigma,\mu\nu}^{sl,+} =& X_\mu X_\nu\cdot G_{xx,\mu}^{\sigma,+} + \nabla^{\mathrm{T}}\left[X_\mu X_\nu\right]\cdot\mathbf{G}_{dxx,\mu}^{\sigma,+} + \nabla^{\mathrm{T}}X_\mu\nabla X_\nu\cdot G_{dxdx,\mu}^{\sigma,+} + \\ & \nabla^{\mathrm{T}}\nabla\left[X_\mu X_\nu\right]\cdot G_{d2xx,\mu}^{\sigma,+} + \sum_\varsigma \nabla^{\mathrm{T}}\rho_\varsigma\nabla\nabla^{\mathrm{T}}\left[X_\mu X_\nu\right]\cdot\mathbf{G}_{hxx,\mu}^{\sigma\varsigma,+} + \\ & \left[\nabla^{\mathrm{T}}X_\nu\nabla\nabla^{\mathrm{T}}X_\mu + \nabla^{\mathrm{T}}X_\mu\nabla\nabla^{\mathrm{T}}X_\nu\right]\cdot\mathbf{G}_{d2xdx,\mu}^{\sigma,+} \ , \end{aligned} \tag{A.33}$$

$$\begin{aligned} v_{\sigma,\mu\nu}^{sl,-} =& \left[\nabla^{\mathrm{T}}X_\mu X_\nu - X_\mu\nabla^{\mathrm{T}}X_\nu\right]\cdot\mathbf{G}_{cdx,\mu}^{\sigma,-} + \\ & \left[\mathbf{G}_{cd2x,\mu}^{\sigma,-}\right]^{\mathrm{T}}\cdot\left[\nabla\nabla^{\mathrm{T}}X_\mu X_\nu - X_\mu\nabla\nabla^{\mathrm{T}}X_\nu\right]\cdot\mathbf{G}_{cd2x',\mu}^{\sigma,-} \ , \end{aligned} \tag{A.34}$$

respectively. Here $G_{d2xx,\mu}^{\sigma,+}$, $\mathbf{G}_{hxx,\mu}^{\sigma\varsigma,+}$ and $\mathbf{G}_{d2xdx,\mu}^{\sigma,+}$ denote those contributions to the symmetric local matrix-vector product arising from the density Laplacian, the density Hessian and the gradient of the kinetic energy density, respectively. Terms arising in the anti-symmetric local matrix-vector product due to the gradient of the current density are collected within terms $\mathbf{G}_{cd2x,\mu}^{\sigma,-}$ and $\mathbf{G}_{cd2x',\mu}^{\sigma,-}$. Since the implementation of the local hybrid potential is similar to the determination of the symmetric local hybrid matrix-vector product, it will be not discussed further.

In the actual state of the local developers' version of TURBOMOLE, all new calibration functions and LMFs are implemented within the *ridft* and *dscf* module, thus allowing self-consistent DFT calculations. In the *escf* module, only the response of the density Hessian and the density Laplacian are additionally implemented so far, so that only calibration functions of pig type as well as the new LMFs are accessible. Response terms of the kinetic energy density gradient and the current density gradient will be included in a later version.

Bibliography

[1] A. Dreuw and M. Head-Gordon, *Chem. Rev.* **105**, 4009 (2005).

[2] H. Weiss, R. Ahlrichs and M. Häser, *J. Chem. Phys.* **99**, 1262 (1993).

[3] L. Reining, V. Olevano, A. Rubio and G. Onida, *Phys. Rev. Lett.* **88**, 066404 (2002).

[4] G. Onida, L. Reining and A. Rubio, *Rev. Mod. Phys.* **74**, 601 (2002).

[5] S. Sharma, J. K. Dewhurst, A. Sanna and E. K. U. Gross, *Phys. Rev. Lett.* **107**, 186401 (2011).

[6] S. Sharma, J. K. Dewhurst, S. Shallcross, G. K. Madjarova and E. K. U. Gross, *J. Chem. Theory Comput.* **11**, 1710 (2015).

[7] A. Dreuw and M. Head-Gordon, *J. Am. Chem. Soc.* **126**, 4007 (2004).

[8] A. Dreuw, J. L. Weisman and M. Head-Gordon, *J. Chem. Phys.* **119**, 2943 (2003).

[9] S. Grimme and M. Parac, *Chem. Phys. Chem.* **3**, 292 (2003).

[10] D. J. Tozer and N. C. Handy, *J. Chem. Phys.* **109**, 10180 (1998).

[11] D. J. Tozer and N. C. Handy, *Phys. Chem. Chem. Phys.* **2**, 2117 (2000).

[12] M. J. G. Peach, P. Benfield, T. Helgaker and D. J. Tozer, *J. Chem. Phys.* **128**, 044118 (2008).

[13] Y. Tawada, T. Tsuneda, S. Yanagisawa, T. Yanai and K. Hirao, *J. Chem. Phys.* **120**, 8425 (2004).

[14] M. Dierksen and S. Grimme, *J. Phys. Chem. A* **108**, 10225 (2004).

[15] J. Jaramillo, G. E. Scuseria and M. Ernzerhof, *J. Chem. Phys.* **118**, 1068 (2003).

[16] K. Burke, F. G. Cruz and K.-C. Lam, *J. Chem. Phys.* **109**, 8161 (1998).

[17] M. Kaupp, H. Bahmann and A. V. Arbuznikov, *J. Chem. Phys.* **127**, 194102 (2007).

[18] A. V. Arbuznikov and M. Kaupp, *J. Chem. Phys.* **136**, 014111 (2012).

[19] TURBOMOLE V7.0 2015, a development of university of karlsruhe and Forschungszentrum Karlsruhe GmbH, 1989-2007, TURBOMOLE GmbH, since 2007; available from `http://www.turbomole.com`.

[20] H. Weiss, R. Ahlrichs and M. Häser, *J. Chem. Phys.* **99**, 1262 (1993).

[21] J. Tao, V. N. Staroverov, G. E. Scuseria and J. P. Perdew, *Phys. Rev. A* **77**, 012509 (2008).

[22] E. Schrödinger, *Phys. Rev.* **28**, 1049 (1926).

[23] B. Podolsky, *Phys. Rev.* **32**, 812 (1928).

[24] W. Koch and M. C. Holthausen. *A Chemist's Guide to Density Functional Theory*, p. 3. John Wiley & Sons (2001).

[25] M. Born and R. Oppenheimer, *Ann. Phys.* **389**, 457 (1927).

[26] J. Reinhold. *Quantentheorie der Moleküle*, p. 124 ff. Vieweg + Teubner (2006).

[27] H. B. Schlegel, *J. Comput. Chem.* **24**, 1514 (2003).

[28] L. S. Cederbaum, *J. Chem. Phys.* **128**, 124101 (2008).

[29] G. A. Wort and L. S. Cederbaum, *Annu. Rev. Phys. Chem.* **55**, 127 (2004).

[30] A. Szabo and N. S. Ostlund. *Modern Quantum Chemistry*, chapter 3. Dover Publications Inc. (1996).

[31] W. Pauli jr., *Z. Phys.* **31**, 765 (1925).

[32] T. Helgaker, P. Jørgensen and J. Olsen. *Molecular Electronic-Structure Theory*, p. 20 f. John Wiley & Sons (2000).

[33] R. McWeeny, *Rev. Mod. Phys.* **32**, 335 (1960).

[34] A. Szabo and N. S. Ostlund. *Modern Quantum Chemistry*, p. 31 ff. Dover Publications Inc. (1996).

[35] J. A. Pople and R. K. Nesbet, *J. Chem. Phys.* **22**, 571 (1954).

[36] C. C. J. Roothaan, *Rev. Mod. Phys.* **23**, 69 (1951).

[37] G. G. Hall, *Proc. R. Soc. A* **205**, 541 (1951).

[38] P.-O. Löwdin, *Phys. Rev.* **97**, 1509 (1955).

[39] T. Helgaker, P. Jørgensen and J. Olsen. *Molecular Electronic-Structure Theory*, p. 158 ff. John Wiley & Sons (2000).

[40] E. Fermi and E. Amaldi, *Accad. Ital. Rome* **6**, 119 (1934).

[41] J. P. Perdew and A. Zunger, *Phys. Rev. B* **23**, 5048 (1981).

[42] T. Helgaker, P. Jørgensen and J. Olsen. *Molecular Electronic-Structure Theory*, chapter 5. John Wiley & Sons (2000).

[43] H. Koch and P. Jørgensen, *J. Chem. Phys.* **93**, 3333 (1990).

[44] P. E. M. Siegbahn, *J. Chem. Phys.* **72**, 1647 (1980).

[45] B. O. Roos, K. Andersson and M. P. Fülscher, *Chem. Phys. Lett.* **192**, 5 (1992).

[46] R. G. Parr and W. Yang. *Density-Functional Theory of Atoms and Molecules*, chapter 3. Oxford University Press (1989).

[47] P. Hohenberg and W. Kohn, *Phys. Rev.* **136**, 864 (1964).

[48] M. Levy, *Proc. Natl. Acad. Sci. USA* **76**, 6062 (1979).

[49] E. Fermi, *Rend. Accad., Lincei* **6**, 602 (1927).

[50] L. H. Thomas, *Proc. Camb. Phil. Soc.* **23**, 542 (1927).

[51] R. G. Parr and W. Yang. *Density-Functional Theory of Atoms and Molecules*, chapter 6. Oxford University Press (1989).

[52] W. Kohn and L. J. Sham, *Phys. Rev.* **140**, 1133 (1965).

[53] R. G. Parr and W. Yang. *Density-Functional Theory of Atoms and Molecules*, chapter 7. Oxford University Press (1989).

[54] W. Koch and M. C. Holthausen. *A Chemist's Guide to Density Functional Theory*, chapter 5. John Wiley & Sons (2001).

[55] A. Seidl, A. Görling, P. Vogl, J. A. Majewski and M. Levy, *Phys. Rev. B* **53**, 3764 (1996).

[56] T. L. Gilbert, *Phys. Rev. B* **12**, 2111 (1975).

[57] R. T. Sharp and G. K. Horton, *Phys. Rev.* **90**, 317 (1953).

[58] J. Harris, *Phys. Rev. A* **29**, 1648 (1984).

[59] J. Harris and R. O. Jones, *J. Phys. F* **4**, 1170 (1974).

[60] D. C. Langreth and J. P. Perdew, *Phys. Rev. B* **15**, 2884 (1977).

[61] O. Gunnarsson and B. I. Lundqvist, *Phys. Rev. B* **13**, 4274 (1976).

[62] A. D. Becke, *J. Chem. Phys.* **140**, 18A301 (2014).

[63] W. Koch and M. C. Holthausen. *A Chemist's Guide to Density Functional Theory*, p. 24 ff. John Wiley & Sons (2001).

[64] K. Burke, J. P. Perdew and M. Ernzerhof, *J. Chem. Phys.* **109**, 3760 (1998).

[65] J. P. Perdew and W. Yue, *Phys. Rev. B* **33**, 8800 (1986).

[66] J. C. Kimball, *Phys. Rev. A* **7**, 1648 (1973).

[67] M. J. G. Peach, A. M. Miller, A. M. Teale and D. J. Tozer, *J. Chem. Phys.* **129**, 064105 (2008).

[68] A. V. Arbuznikov and M. Kaupp, *J. Chem. Phys.* **128**, 214107 (2008).

[69] A. D. Becke, *J. Chem. Phys.* **109**, 2092 (1998).

[70] A. J. Cohen, P. Mori-Sánchez and W. Yang, *Chem. Rev.* **112**, 289 (2012).

[71] J. P. Perdew and K. Schmidt, *AIP Conf. Proc.* **577**, 1 (2001).

[72] B. G. Janesko, *Int. J. Quant. Chem.* **113**, 83 (2013).

[73] M. Kaupp, A. V. Arbuznikov and H. Bahmann, *Z. Phys. Chem.* **224**, 545 (2010).

[74] J. C. Slater, *Phys. Rev.* **81**, 385 (1951).

[75] P. A. M. Dirac, *Proc. Cambridge Phil. Roy. Soc.* **26**, 376 (1930).

[76] S. H. Vosko, L. Wilk and M. Nusair, *Can. J. Phys.* **58**, 1200 (1980).

[77] J. P. Perdew and Y. Wang, *Phys. Rev. B* **45**, 13244 (1992).

[78] D. M. Ceperly and B. J. Alder, *Phys. Rev. Lett.* **45**, 566 (1980).

[79] E. Wigner and F. Seitz, *Phys. Rev.* **43**, 804 (1933).

[80] M. Levy and J. P. Perdew, *Phys. Rev. A* **32**, 2010 (1985).

[81] M. Levy, *Phys. Rev. A* **43**, 4637 (1991).

[82] L. A. Curtiss, K. Raghavachari, P. C. Redfern and J. A. Pople, *J. Chem. Phys.* **106**, 1063 (1997).

[83] A. D. Becke, *Phys. Rev. A* **33**, 2786 (1986).

[84] J. P. Perdew, D. C. Langreth and V. Sahni, *Phys. Rev. Lett.* **38**, 1030 (1977).

[85] F. Herman, J. P. Van Dyke and I. B. Ortenburger, *Phys. Rev. Lett.* **22**, 807 (1969).

[86] A. D. Becke, *Int. J. Quant. Chem.* **23**, 1915 (1983).

[87] C. F. von Weizsäcker, *Z. Physik* **96**, 431 (1935).

[88] L. Kleinman, *Phys. Rev. B* **39**, 2223 (1984).

[89] A. D. Becke, *J. Chem. Phys.* **85**, 7184 (1986).

[90] J. P. Perdew, *Phys. Rev. Lett.* **55**, 1665 (1985).

[91] A. D. Becke, *J. Chem. Phys.* **84**, 4524 (1986).

[92] A. D. Becke, *Phys. Rev. A* **38**, 3098 (1988).

[93] J. P. Perdew, K. Burke and M. Ernzerhof, *Phys. Rev. Lett.* **77**, 3865 (1996).

[94] E. H. Lieb and S. Oxford, *Int. J. Quant. Chem.* **19**, 427 (1981).

[95] A. D. Boese, N. L. Doltsinis, N. C. Handy and M. Sprik, *J. Chem. Phys.* **112**, 1670 (2000).

[96] A. D. Boese and N. C. Handy, *J. Chem. Phys.* **114**, 5497 (2001).

[97] E. Engel, J. A. Chevary, L. D. Macdonald and S. H. Vosko, *Z. Phys. D - Atoms, Molecules and Clusters* **23**, 7 (1992).

[98] J. P. Perdew, *Phys. Rev. B* **33**, 8822 (1986).

[99] D. C. Langreth and M. J. Mehl, *Phys. Rev. B* **28**, 1809 (1983).

[100] J. P. Perdew, J. A. Chevary, S. H. Vosko, K. A. Jackson, M. R. Pederson, D. J. Singh and C. Fiolhais, *Phys. Rev. B* **46**, 6671 (1992).

[101] C. Lee, W. Yang and R. G. Parr, *Phys. Rev. B* **37**, 785 (1988).

[102] B. Miehlich, A. Savin, H. Stoll and H. Preuss, *Chem. Phys. Lett.* **157**, 200 (1989).

[103] R. Colle and D. Salvetti, *Theor. Chem. Acta.* **37**, 329 (1975).

[104] P. de Silva and C. Corminboeuf, *J. Chem. Phys.* **143**, 111105 (2015).

[105] J. P. Perdew, S. Kurth, A. Zupan and P. Blaha, *Phys. Rev. Lett.* **82**, 2544 (1999).

[106] J. Tao, J. P. Perdew, V. N. Staroverov and G. E. Scuseria, *Phys. Rev. Lett.* **91**, 146401 (2003).

[107] J. P. Perdew, J. Tao, V. N. Staroverov and G. E. Scuseria, *J. Chem. Phys.* **120**, 6898 (2004).

[108] J. Sun, J. P. Perdew and A. Ruzsinszky, *Proc. Natl. Acad. Sci. USA* **112**, 685 (2015).

[109] J. Sun, A. Ruzsinszky and J. P. Perdew, *Phys. Rev. Lett.* **115**, 036402 (2015).

[110] A. D. Becke, *J. Chem. Phys.* **138**, 074109 (2013).

[111] A. D. Becke, *J. Chem. Phys.* **138**, 161101 (2013).

[112] A. D. Becke, *J. Chem. Phys.* **88**, 1053 (1988).

[113] A. D. Becke, *J. Chem. Phys.* **104**, 1040 (1996).

[114] S. Grimme, *J. Comput. Chem.* **27**, 1787 (2006).

[115] A. D. Boese and N. C. Handy, *J. Chem. Phys.* **116**, 9559 (2002).

[116] Y. Zhao and D. G. Truhlar, *J. Chem. Phys.* **125**, 194101 (2006).

[117] R. Peverati and D. G. Truhlar, *J. Phys. Chem. Lett.* **3**, 117 (2012).

[118] A. D. Becke and M. R. Roussel, *Phys. Rev. A* **39**, 3761 (1989).

[119] F. F. and J. P. Perdew, *J. Chem. Phys.* **124**, 044103 (2006).

[120] A. D. Becke, *J. Chem. Phys.* **98**, 1372 (1993).

[121] J. P. Perdew, M. Ernzerhof and K. Burke, *J. Chem. Phys.* **105**, 9982 (1996).

[122] P. Cortona, *J. Chem. Phys.* **136**, 086101 (2012).

[123] G. I. Csonka, J. P. Perdew and A. Ruzsinszky, *J. Chem. Theory Comput.* **6**, 3688 (2010).

[124] V. N. Staroverov, G. E. Scuseria, J. Tao and J. P. Perdew, *J. Chem. Phys.* **119**, 12129 (2003).

[125] C. Adamo and V. Barone, *J. Phys. Chem.* **110**, 6158 (1999).

[126] A. D. Becke, *J. Chem. Phys.* **98**, 5648 (1993).

[127] P. J. Stephens, F. J. Devlin, C. F. Chabalowski and M. J. Frisch, *J. Phys. Chem.* **98**, 11623 (1994).

[128] A. D. Boese and J. M. L. Martin, *J. Chem. Phys.* **121**, 3405 (2004).

[129] Y. Zhao, N. E. Schultz and D. G. Truhlar, *J. Chem. Phys.* **123**, 161103 (2005).

[130] Y. Zhao and D. G. Truhlar, *Theor. Chem. Account* **120**, 215 (2008).

[131] Y. Zhao and D. G. Truhlar, *J. Phys. Chem. A* **110**, 13126 (2006).

[132] Y. Zhao and D. G. Truhlar, *J. Chem. Theory Comput.* **4**, 1849 (2008).

[133] A. D. Becke, *J. Chem. Phys.* **119**, 2972 (2003).

[134] A. D. Becke, *J. Chem. Phys.* **122**, 064101 (2005).

[135] Y. Imamura, R. Kobayashi and H. Nakai, *J. Chem. Phys.* **134**, 124113 (2011).

[136] Y. Imamura, R. Kobayashi and H. Nakai, *Chem. Phys. Lett.* **513**, 130 (2011).

[137] A. Nakata, Y. Imamura, T. Otsuka and H. Nakai, *J. Chem. Phys.* **124**, 094105 (2006).

[138] A. Nakata, Y. Imamura and H. Nakai, *J. Chem. Phys.* **125**, 064109 (2006).

[139] H. Stoll and A. Savin. *Density Functional Methods in Physics*, p. 177. Plenum, New York (1985).

[140] A. Savin and H.-J. Flad, *Int. J. Quantum Chem.* **56**, 327 (1995).

[141] J. Toulouse, F. Colonna and A. Savin, *Phys. Rev. A* **70**, 062505 (2004).

[142] H. Iikura, T. Tsuneda, T. Yanai and K. Hirao, *J. Chem. Phys.* **115**, 3540 (2001).

[143] O. A. Vydrov and G. E. Scuseria, *J. Chem. Phys.* **125**, 234109 (2006).

[144] N. Mardirossian, J. A. Parkhill and M. Head-Gordon, *Phys. Chem. Chem. Phys.* **13**, 19325 (2011).

[145] J. Heyd, G. E. Scuseria and M. Ernzerhof, *J. Chem. Phys.* **118**, 8207 (2003).

[146] R. Peverati and D. G. Truhlar, *Phys. Chem. Chem. Phys.* **14**, 16187 (2012).

[147] N. Besley, M. J. G. Peach and D. J. Tozer, *Phys. Chem. Chem. Phys.* **11**, 10350 (2009).

[148] T. Yanai, D. P. Tew and N. C. Handy, *Chem. Phys. Lett.* **393**, 51 (2004).

[149] Y. Imamura, R. Kobayashi and H. Nakai, *Int. J. Quant. Chem.* **113**, 245 (2013).

[150] D. Jacquemin, B. Moore II, A. Planchat, C. Adamo and J. Autschbach, *J. Chem. Theory Comput.* **10**, 1677 (2014).

[151] T. Körzdörfer, J. S. Sears, C. Sutton and J. Brédas, *J. Chem. Phys.* **135**, 204107 (2011).

[152] A. Karolewski, L. Kronik and S. Kümmel, *J. Chem. Phys.* **138**, 204115 (2013).

[153] J.-D. Chai and M. Head-Gordon, *J. Chem. Phys.* **128**, 084106 (2008).

[154] J.-D. Chai and M. Head-Gordon, *Phys. Chem. Chem. Phys.* **10**, 6615 (2008).

[155] R. Peverati and D. G. Truhlar, *J. Phys. Chem. Lett.* **2**, 2810 (2011).

[156] S. Grimme, *J. Comput. Chem.* **27**, 1787 (2006).

[157] T. Sato and H. Nakai, *J. Chem. Phys.* **131**, 224104 (2009).

[158] T. Sato and H. Nakai, *J. Chem. Phys.* **133**, 194101 (2010).

[159] M. Dion, H. Rydberg, E. Schröder, D. C. Langreth and B. I. Lundqvist, *Phys. Rev. Lett.* **92**, 246401 (2004).

[160] K. Lee, É. D. Murray, L. Kong, B. I. Lundqvist and D. C. Langreth, *Phys. Rev. B* **82**, 081101 (2010).

[161] A. D. Becke and E. R. Johnson, *J. Chem. Phys.* **127**, 154108 (2007).

[162] S. N. Steinmann and C. Corminboeuf, *J. Chem. Theory Comput.* **7**, 3567 (2011).

[163] O. A. Vydrov and T. van Voorhis, *Phys. Rev. Lett* **103**, 063004 (2009).

[164] S. Grimme, *J. Chem. Phys.* **124**, 034108 (2006).

[165] L. Goerigk, J. Moellmann and S. Grimme, *Phys. Chem. Chem. Phys.* **11**, 4611 (2009).

[166] A. Karton, A. Tarnopolsky, J.-F. Lamère, G. C. Schatz and J. M. L. Martin, *J. Phys. Chem. A* **112**, 12868 (2008).

[167] J. M. Pitarke and A. G. Eguiluz, *Phys. Rev. B* **57**, 6329 (1998).

[168] J. F. Dobson and J. Wang, *Phys. Rev. Lett.* **82**, 2123 (1999).

[169] S. Kurth and J. P. Perdew, *Phys. Rev. B* **59**, 10461 (1999).

[170] F. Furche, *Phys. Rev. B* **64**, 195120 (2001).

[171] F. Furche, *J. Chem. Phys.* **129**, 114105 (2008).

[172] J. Toulouse, I. C. Gerber, G. Jansen, A. Savin and J. G. Ángyán, *Phys. Rev. Lett.* **102**, 096404 (2009).

[173] J. G. Ángyán, R.-F. Liu, J. Toulouse, and G. Jansen, *J. Chem. Theory Comput.* **7**, 3116 (2011).

[174] A. Grüneis, M. Marsman, J. Harl, L. Schimka and G. Kresse, *J. Chem. Phys.* **131**, 154115 (2009).

[175] X. Ren, P. Rinke, C. Joas and M. Scheffler, *J. Mater. Sci.* **47**, 7447 (2012).

[176] X. Ren, A. Tkatchenko, P. Rinke and M. Scheffler, *Phys. Rev. Lett.* **106**, 153003 (2011).

[177] X. Ren, P. Rinke, G. E. Scuseria and M. Scheffler, *Phys. Rev. B* **88**, 035120 (2013).

[178] P. Bleiziffer, M. Krug and A. Görling, *J. Chem. Phys.* **142**, 244108 (2015).

[179] P. Bleiziffer, A. Heßelmann and A. Görling, *J. Chem. Phys.* **139**, 084113 (2013).

[180] R. J. Bartlett, V. F. Lotrich and I. V. Schweigert, *J. Chem. Phys.* **123**, 062205 (2005).

[181] F. G. Cruz, K.-C. Lam and K. Burke, *J. Phys. Chem. A* **102**, 4911 (1998).

[182] A. V. Arbuznikov, H. Bahmann and M. Kaupp, *J. Phys. Chem. A* **113**, 11898 (2009).

[183] J. P. Perdew, V. N. Staroverov, J. Tao and G. E. Scuseria, *Phys. Rev. A* **78**, 052513 (2008).

[184] A. V. Arbuznikov, M. Kaupp and H. Bahmann, *J. Chem. Phys.* **124**, 204102 (2006).

[185] H. Bahmann, A. Rodenberg, A. V. Arbuznikov and M. Kaupp, *J. Chem. Phys.* **126**, 011103 (2007).

[186] A. V. Arbuznikov and M. Kaupp, *Chem. Phys. Lett.* **440**, 160 (2007).

[187] E. R. Johnson, *J. Chem. Phys.* **141**, 124120 (2014).

[188] P. de Silva and C. Corminboeuf, *J. Chem. Phys.* **142**, 074112 (2015).

[189] P. de Silva and C. Corminboeuf, *J. Chem. Theory Comput.* **10**, 3745 (2014).

[190] T. Schmidt, E. Kraisler, L. Kronik and S. Kümmel, *Phys. Chem. Chem. Phys.* **16**, 14357 (2014).

[191] R. Haunschild, B. G. Janesko and G. E. Scuseria, *J. Chem. Phys.* **131**, 154112 (2009).

[192] T. Schmidt, E. Kraisler, A. Makmal, L. Kronik and S. Kümmel, *J. Chem. Phys.* **140**, 18A510 (2014).

[193] A. Görling and M. Levy, *Phys. Rev. B* **47**, 13105 (1993).

[194] Y. Zhou, H. Bahmann and M. Ernzerhof, *J. Chem. Phys.* **143**, 124103 (2015).

[195] B. G. Janesko and G. E. Scuseria, *J. Chem. Phys.* **127**, 164117 (2007).

[196] B. G. Janesko and G. E. Scuseria, *J. Chem. Phys.* **128**, 084111 (2008).

[197] A. V. Arbuznikov and M. Kaupp, *J. Chem. Phys.* **141**, 204101 (2014).

[198] J. Tao, M. Springborg and J. P. Perdew, *J. Chem. Phys.* **119**, 6457 (2003).

[199] K. Theilacker, A. V. Arbuznikov, H. Bahmann and M. Kaupp, *J. Phys. Chem. A* **115**, 8990 (2011).

[200] K. Theilacker, A. V. Arbuznikov and M. Kaupp, *Mol. Phys.* **114**, 1118 (2016).

[201] L. Goerigk and S. Grimme, *J. Chem. Theory Comput.* **6**, 107 (2010).

[202] L. Goerigk and S. Grimme, *J. Chem. Theory Comput.* **7**, 291 (2011).

[203] U. von Barth, *Phys. Rev. A* **20**, 1693 (1979).

[204] T. Ziegler, A. Rauk and E. J. Baerends, *Theoret. Chim. Acta* **43**, 261 (1977).

[205] F. A. Evangelista, P. Shushkov and J. C. Tully, *J. Phys. Chem. A* **117**, 7378 (2013).

[206] H. Zhekove, M. Krykunov, J. Autschbach and T. Ziegler, *J. Chem. Theory Comput.* **10**, 3299 (2014).

[207] M. E. Casida, *J. Mol. Struct. (Theochem.)* **914**, 3 (2009).

[208] E. Runge and E. K. U. Gross, *Phys. Rev. Lett.* **52**, 997 (1984).

[209] R. van Leeuwen, *Phys. Rev. Lett.* **80**, 1280 (1998).

[210] G. Vignale, *Phys. Rev. A* **77**, 062511 (2008).

[211] R. van Leeuwen, *Int. J. Mod. Phys. B* **15**, 1969 (2001).

[212] K. Lopata, B. E. van Kuiken, M. Khalil and N. Govind, *J. Chem. Theory Comput.* **8**, 3284 (2012).

[213] K. Yabana and G. F. Bertsch, *Phys. Rev. A* **60**, 1271 (1999).

[214] A. Zangwill and P. Soven, *Phys. Rev. A* **21**, 1561 (1980).

[215] M. J. Stott and E. Zaremba, *Phys. Rev. A* **21**, 12 (1980).

[216] M. E. Casida. *Recent Advances in Density Functional Methods, Part I*, pp. 155–192. World Scientific: Singapore (1995).

[217] E. K. U. Gross and N. T. Maitra. *Fundamentals of Time-Dependent Density Functional Theory*, chapter 4. Springer (2012).

[218] R. M. Sternheimer, *Phys. Rev.* **96**, 951 (1954).

[219] K. Pernal, O. Gritsenko and E. J. Baerends, *Phys. Rev. A* **75**, 012506 (2007).

[220] F. Furche, *J. Chem. Phys.* **114**, 5982 (2001).

[221] A. D. McLachlan and M. A. Ball, *Rev. Mod. Phys.* **36**, 844 (1964).

[222] P. Jørgensen and J. Linderberg, *Int. J. Quant. Chem.* **4**, 587 (1970).

[223] M. Hellgren and U. von Barth, *Phys. Rev. B* **78**, 115107 (2008).

[224] S. Hirata and M. Head-Gordon, *Chem. Phys. Lett.* **314**, 291 (1999).

[225] F. A. Bischoff, R. J. Harrison and E. F. Valeev, *J. Chem. Phys.* **137**, 104103 (2012).

[226] D. Sundholm, *J. Chem. Phys.* **122**, 194107 (2005).

[227] J. J. Mortensen, L. B. Hansen and K. W. Jacobsen, *Phys. Rev. B* **71**, 035109 (2005).

[228] J. Hafner, *J. Comput. Chem.* **29**, 2044 (2008).

[229] A. D. Becke, *Int. J. Quantum Chem., Quantum Chem. Symp.* **23**, 599 (1989).

[230] T. Helgaker, P. Jørgensen and J. Olsen. *Molecular Electronic-Structure Theory*, chapter 9. John Wiley & Sons (2000).

[231] T. Helgaker, P. Jørgensen and J. Olsen. *Molecular Electronic-Structure Theory*, p. 361 ff. John Wiley & Sons (2000).

[232] T. Helgaker, P. Jørgensen and J. Olsen. *Molecular Electronic-Structure Theory*, p. 381 ff. John Wiley & Sons (2000).

[233] T. Helgaker, P. Jørgensen and J. Olsen. *Molecular Electronic-Structure Theory*, p. 372 ff. John Wiley & Sons (2000).

[234] A. K. H. Weiss and C. Ochsenfeld, *J. Comput. Chem.* **36**, 1390 (2015).

[235] M. Primorac, *Int. J. Quant. Chem.* **68**, 305 (1998).

[236] T. Helgaker, P. Jørgensen and J. Olsen. *Molecular Electronic-Structure Theory*, p. 366 ff. John Wiley & Sons (2000).

[237] J. Rys, M. Dupuis and H. F. King, *J. Comput. Chem.* **4**, 154 (1983).

[238] M. Dupuis, J. Rys and H. F. King, *J. Chem. Phys.* **65**, 111 (1976).

[239] R. P. Sagar and V. H. Smith Jr., *Int. J. Quant. Chem.* **42**, 827 (1992).

[240] H. F. King and M. Dupuis, *J. Comput. Phys.* **21**, 144 (1976).

[241] W. Gautschi, *Math. Comp.* **22**, 251 (1968).

[242] M. Häser and R. Ahlrichs, *J. Comput. Chem.* **10**, 104 (1989).

[243] C. Ochsenfeld, C. A. White and M. Head-Gordon, *J. Chem. Phys.* **109**, 1663 (1998).

[244] O. Treutler and R. Ahlrichs, *J. Chem. Phys.* **102**, 346 (1995).

[245] A. D. Becke, *J. Chem. Phys.* **88**, 2547 (1988).

[246] P. M. W. Gill, B. G. Johnson and J. A. Pople, *Chem. Phys. Lett.* **209**, 506 (1993).

[247] C. W. Murray, N. C. Handy and G. J. Laming, *Mol. Phys.* **78**, 997 (1993).

[248] V. I. Lebedev, *Zh. Vychisl. Mat. Mat. Fiz.* **15**, 48 (1975).

[249] M. Abramowitz and I. A. Stegun, editors. *Handbook Of Mathematical Functions With Formulas, Graphs, And Mathematical Tables*, p. 888. Dover Publications (1972).

[250] K. Eichkorn, O. Treutler, H. Öhm, M. Häser and R. Ahlrichs, *Chem. Phys. Lett.* **240**, 283 (1995).

[251] F. Weigend, *J. Comput. Chem.* **29**, 167 (2008).

[252] F. Weigend, *Phys. Chem. Chem. Phys.* **4**, 4285 (2002).

[253] E. J. Baerends, D. E. Ellis and P. Ros, *Chem. Phys.* **2**, 41 (1973).

[254] J. L. Whitten, *J. Chem. Phys.* **58**, 4496 (1973).

[255] B. I. Dunlap, J. W. D. Connolly and J. R. Sabin, *J. Chem. Phys.* **71**, 3396 (1979).

[256] O. Vahtras, J. Almlöf and M. W. Feyereisen, *Chem. Phys. Lett.* **213**, 514 (1993).

[257] H.-J. Werner, F. R. Manby and P. J. Knowles, *J. Chem. Phys.* **118**, 8149 (2003).

[258] P. Bleiziffer, A. Heßelmann and A. Görling, *J. Chem. Phys.* **136**, 134102 (2012).

[259] R. Bauernschmitt, M. Häser, O. Treutler and R. Ahlrichs, *Chem. Phys. Lett.* **264**, 573 (1997).

[260] D. Rappoport and F. Furche, *J. Chem. Phys.* **122**, 064105 (2005).

[261] R. A. Friesner, *Chem. Phys. Lett.* **116**, 39 (1985).

[262] R. A. Friesner, *J. Chem. Phys.* **86**, 3522 (1987).

[263] R. A. Friesner, *J. Phys. Chem.* **92**, 3091 (1988).

[264] C. Ko, D. K. Malick, D. A. Braden, R. A. Friesner and T. J. Martínez, *J. Chem. Phys.* **128**, 104103 (2008).

[265] F. Neese, F. Wennmohs, A. Hansen and U. Becker, *Chem. Phys.* **356**, 98 (2009).

[266] T. Petrenko, S. Kossmann and F. Neese, *J. Chem. Phys.* **134**, 054116 (2011).

[267] R. Izsák, F. Neese and W. Klopper, *J. Chem. Phys.* **139**, 094111 (2013).

[268] C. van Wüllen, *Chem. Phys. Lett.* **245**, 648 (1995).

[269] F. Della Sala and A. Görling, *J. Chem. Phys.* **115**, 5718 (2001).

[270] H. Bahmann and M. Kaupp, *J. Chem. Theory Comput.* **11**, 1540 (2015).

[271] P. Plessow and F. Weigend, *J. Comput. Chem.* **33**, 810 (2012).

[272] T. M. Maier, H. Bahmann and M. Kaupp, *J. Chem. Theory Comput.* **11**, 4226 (2015).

[273] F. Zahariev, S. S. Leang and M. S. Gordon, *J. Chem. Phys.* **138**, 244108 (2013).

[274] B. G. Janesko, A. V. Krukau and G. E. Scuseria, *J. Chem. Phys.* **129**, 124110 (2008).

[275] R. Neumann, R. H. Nobes and N. C. Handy, *Mol. Phys.* **87**, 1 (1996).

[276] R. Bauernschmitt and R. Ahlrichs, *Chem. Phys. Lett.* **256**, 454 (1996).

[277] J. E. Bates and F. Furche, *J. Chem. Phys.* **137**, 164105 (2012).

[278] T. Burnus, M. A. L. Marques and E. K. U. Gross, *Phys. Rev. A* **72**, 010501 (2005).

[279] F. Furche, B. T. Krull, B. D. Nguyen and J. Kwon, *J. Chem. Phys.* **144**, 174105 (2016).

[280] E. R. Davidson, *J. Comput. Phys.* **17**, 87 (1975).

[281] J. Olsen, H. J. A. Jensen and Jørgensen, *J. Comput. Phys.* **74**, 265 (1988).

[282] B. O. Roos and P. E. M. Siegbahn. *Modern Theoretical Chemistry, Methods of Electronic Structure*, volume 3, chapter 7. Plenum, New York, (1977).

[283] T. H. Dunning Jr., *J. Chem. Phys.* **90**, 1007 (1989).

[284] T. H. Dunning Jr., *J. Chem. Phys.* **53**, 2823 (1970).

[285] F. Weigend and R. Ahlrichs, *Phys. Chem. Chem. Phys.* **7**, 3297 (2005).

[286] T. M. Maier, H. Bahmann, A. V. Arbuznikov and M. Kaupp, *J. Chem Phys.* **144**, 074106 (2016).

[287] M. Schreiber, M. R. Silva-Junior, S. P. A. Sauer and W. Thiel, *J. Chem. Phys.* **128**, 134110 (2008).

[288] M. R. Silva-Junior, M. Schreiber, S. P. A. Sauer and W. Thiel, *J. Chem. Phys.* **129**, 104103 (2008).

[289] M. R. Silva-Junior, M. Schreiber, S. P. A. Sauer and W. Thiel, *J. Chem. Phys.* **133**, 174318 (2010).

[290] N. A. Besley, M. J. G. Peach and D. J. Tozer, *Phys. Chem. Chem. Phys.* **11**, 10350 (2009).

[291] D. Hofmann and S. Kümmel, *J. Chem. Phys.* **137**, 064117 (2012).

[292] J. Messud, P. M. Dinh, P.-G. Reinhard and E. Suraud, *Ann. Phys.* **324**, 955 (2009).

[293] A. D. Laurent and D. Jacquemin, *Int. J. Quantum Chem.* **113**, 2019 (2013).

[294] D. Jacquemin, V. Wathelet, E. A. Perpete and C. Adamo, *J. Chem. Theory Comput.* **5**, 2420 (2009).

[295] A. Schäfer, C. Huber and R. Ahlrichs, *J. Chem. Phys.* **100**, 5829 (1994).

[296] M. J. G. Peach and D. J. Tozer, *J. Phys. Chem. A* **116**, 9783 (2012).

[297] W. A. de Jong, R. J. Harrison and D. A. Dixon, *J. Chem. Phys.* **114**, 48 (2001).

[298] D. Peng and M. Reiher, *Theor. Chem. Acc.* **131**, 1081 (2012).

[299] D. Peng, N. Middendorf, F. Weigend and M. Reiher, *J. Chem. Phys.* **138**, 184105 (2013).

[300] R. van Leeuwen and E. J. Baerends, *Phys. Rev. A* **49**, 2421 (1994).

[301] M. J. Frisch, G. W. Trucks, H. B. Schlegel, G. E. Scuseria, M. A. Robb, J. R. Cheeseman, G. Scalmani, V. Barone, B. Mennucci, G. A. Petersson, H. Nakatsuji, M. Caricato, X. Li, H. P. Hratchian, A. F. Izmaylov, J. Bloino, G. Zheng, J. L. Sonnenberg, M. Hada, M. Ehara, K. Toyota, R. Fukuda, J. Hasegawa, M. Ishida, T. Nakajima, Y. Honda, O. Kitao, H. Nakai, T. Vreven, J. A. Montgomery, Jr., J. E. Peralta, F. Ogliaro, M. Bearpark, J. J. Heyd, E. Brothers, K. N. Kudin, V. N. Staroverov, R. Kobayashi, J. Normand, K. Raghavachari, A. Rendell, J. C. Burant, S. S. Iyengar, J. Tomasi, M. Cossi, N. Rega, J. M. Millam, M. Klene, J. E. Knox, J. B. Cross, V. Bakken, C. Adamo, J. Jaramillo, R. Gomperts, R. E. Stratmann, O. Yazyev, A. J. Austin, R. Cammi, C. Pomelli, J. W. Ochterski, R. L. Martin, K. Morokuma, V. G. Zakrzewski, G. A. Voth, P. Salvador, J. J. Dannenberg, S. Dapprich, A. D. Daniels, D. Farkas, J. B. Foresman, J. V. Ortiz, J. Cioslowski

and D. J. Fox. Gaussian 09 Revision D.01. Gaussian Inc. Wallingford CT 2009.

[302] D. Jacquemin, E. A. Perpete, I. Ciofini and C. Adamo, *J. Chem. Theory Comput.* **6**, 1532 (2010).

[303] M. Isegawa, R. Peverati and D. G. Truhlar, *J. Chem. Phys.* **137**, 244104 (2012).

[304] K. B. Wiberg, A. E. de Oliveira and G. Trucks, *J. Phys. Chem. A* **106**, 4192 (2002).

[305] M. Caricato, G. W. Trucks, M. J. Frisch and K. B. Wiberg, *J. Chem. Theory Comput.* **6**, 370 (2010).

[306] A. P. Gaiduk and V. N. S. D. S. Firaha, *Phys. Rev. Lett.* **108**, 253005 (2012).

[307] M. J. G. Peach, C. R. Le Sueur, K. Ruud, M. Guillaume and D. J. Tozer, *Phys. Chem. Chem. Phys.* **11**, 4465 (2009).

[308] D. J. Tozer, *J. Chem. Phys.* **119**, 12697 (2003).

[309] R. J. Magyar and S. Tretiak, *J. Chem. Theory Comput.* **3**, 976 (2007).

[310] K. A. Nguyen, P. N. Day and R. Pachter, *J. Chem. Phys.* **135**, 074109 (2011).

[311] F. A. Lima, R. Bjornsson, T. Weyhermüller, P. Chandrasekaran, P. Glatzel, F. Neese and S. DeBeer, *Phys. Chem. Chem. Phys.* **15**, 20911 (2013).

[312] N. Schmidt, R. Fink and W. Hieringer, *J. Chem. Phys.* **133**, 054703 (2010).

[313] N. A. Besley and F. A. Asmuruf, *Phys. Chem. Chem. Phys.* **12**, 12024 (2010).

[314] A. V. Krukau, G. E. Scuseria, J. P. Perdew and A. Savin, *J. Chem. Phys.* **129**, 124103 (2008).

[315] T. M. Maier, M. Haasler, A. V. Arbuznikov and M. Kaupp, *Phys. Chem. Chem. Phys.* **18**, 21133 (2016).

[316] A. C. Cancio, C. E. Wagner and S. A. Wood, *Int. J. Quantum Chem.* **112**, 3796 (2012).

[317] J. A. Pople, M. Head-Gordon, D. J. Fox, K. Raghavachari and L. A. Curtiss, *J. Chem. Phys.* **90**, 5622 (1989).

[318] L. A. Curtiss, C. Jones, G. W. Trucks, K. Raghavachari and J. A. Pople, *J. Chem. Phys.* **93**, 2537 (1990).

[319] Y. Zhao, B. J. Lynch and D. G. Truhlar, *Phys. Chem. Chem. Phys.* **7**, 43 (2005).

[320] Y. Zhao, N. E. Schultz and D. G. Truhlar, *J. Chem. Theory Comput.* **2**, 364 (2006).

[321] Y. Zhao, N. González-García and D. G. Truhlar, *J. Phys. Chem. A* **109**, 2012 (2005).

[322] J. Zheng, Y. Zhao and D. G. Truhlar, *J. Chem. Theory Comput.* **5**, 808 (2009).

[323] A. Karton, A. Tarnopolsky, J.-F. Lemère, G. C. Schatz and J. M. L. Martin, *J. Phys. Chem. A* **112**, 12868 (2008).

[324] J. A. Nelder and R. Mead, *Computer Journal* **7**, 308 (1965).

[325] J. P. Perdew, K. Burke and W. Yue, *Phys. Rev. B* **54**, 16533 (1996).

[326] J. P. Perdew and W. Yue, *Phys. Rev. B* **33**, 8800 (1986).